

Synthesis, structure formation, charge
transport and applications of semiconducting
copolymers based on thieno[3,4-c]pyrrole-4,6-
dione

DISSERTATION

zur Erlangung des akademischen Grades

einer Doktorin der Naturwissenschaften (Dr. rer. nat.)

in der Bayreuther Graduiertenschule für Mathematik und Naturwissenschaften

(BayNAT)

der Universität Bayreuth

vorgelegt von

Tina Elisabeth Weller

aus München

Bayreuth, 2018

Die vorliegende Arbeit wurde in der Zeit von September 2013 bis Mai 2018 in Bayreuth am Lehrstuhl für Makromolekulare Chemie I der Universität Bayreuth unter der Betreuung von Herrn Professor Dr. Mukundan Thelekkat angefertigt.

Vollständiger Ausdruck der von der Bayreuther Graduiertenschule für Mathematik und Naturwissenschaften (BayNAT) der Universität Bayreuth genehmigten Dissertation zur Erlangung des akademischen Grades einer Doktorin der Naturwissenschaften (Dr. rer. Nat.).

Dissertation eingereicht am: 04.05.2018

Zulassung durch das Leitungsgremium: 16.05.2018

Wissenschaftliches Kolloquium: 18.10.2018

Amtierender Direktor: Prof. Dr. Dirk Schüler

Prüfungsausschuss:

Prof. Dr. Mukundan Thelekkat (Gutachter)

Prof. Dr. Seema Agarwal (Gutachterin)

Prof. Dr. Carlo Unverzagt (Vorsitz)

Prof. Dr. Anna Köhler

Für meine Familie

“Was wir wissen, ist ein Tropfen – was wir nicht wissen, ein Ozean.”

Isaac Newton

Table of Contents

Summary	1
Zusammenfassung.....	5
1 Introduction	9
2 Objective of the thesis	47
3 Overview of the thesis	49
Individual contributions to joint publications	61
4 Influence of the edge-on or face-on alignment of thieno[3,4- <i>c</i>]pyrrole-4,6-dione based copolymer films achieved by processing on devices	65
5 Highly efficient and balanced charge transport in thieno[3,4- <i>c</i>]pyrrole-4,6-dione copolymers: Dramatic influence of thieno[3,2- <i>b</i>]thiophene comonomer on alignment and charge transport	103
6 Fluorination in thieno[3,4- <i>c</i>]pyrrole-4,6-dione copolymers leading to electron transport, high crystallinity and end-on alignment	143
7 Influence of fluorination and backbone extension in thieno[3,4- <i>c</i>]pyrrole-4,6-dione based copolymers carrying thiophene and terthiophene comonomers.....	175
8 List of publications	211
Danksagung	213

Summary

This thesis deals with new semiconducting copolymers based on thieno[3,4-c]pyrrole-4,6-dione (TPD) for the application in organic electronics. These polymers were designed by the donor-acceptor concept, whereby all polymers have TPD as the common acceptor unit. Charge transport properties were systematically tuned by structural variation of the comonomers, especially with regards to donor strength. In order to gain a deeper understanding of structure-property relations, the thin film alignment was elucidated in grazing incidence wide angle X-ray scattering (GIWAXS) measurements. Conjugated polymers often are semicrystalline materials with a rigid polymer backbone, which interact with one another via π - π stacking and alkyl stacking. Therefore, the polymer chains can assemble into stacks, which can orient to the substrate in an edge-on, face-on or end-on manner. While an edge-on alignment corresponds to an orientation of the planar π -system perpendicular to the substrate, an alignment parallel to the substrate is referred to as face-on. The alignment in an end-on fashion is only rarely observed because here the polymer chains stand on the substrate. Consequently, the device performance can depend on the thin film alignment since the charge transport along the π - π stacking direction is more efficient than along the alkyl stacking direction. An edge-on alignment favors charge transport in an organic field effect transistor (OFET), whereas a face-on alignment promotes charge transport in a diode configuration.

In the first part of this thesis, we investigate the influence of fluorination following two different concepts. First, we studied the influence of thiophene fluorination in p-type materials based on TPD and terthiophene. In detail, the thiophenes attached to the TPD unit were decorated with additional solubilizing side chains. Upon fluorination, the energy levels are lowered due to the decreased donor strength allowing a higher open-circuit voltage in organic solar cells. Indeed, the open-circuit voltage could be increased for the fluorinated polymer/PCBM blend. However, the fill factor suffered losses resulting only in an identical power conversion efficiency compared to the non-fluorinated polymer system. More important, we additionally studied the influence of processing on thin film alignment and device performance. Both materials show a high degree of crystallinity and strongly aggregate in solution as shown in temperature dependent UV-Vis measurements. Furthermore, the nature of aggregates depends on the solvent used. Processing from chloroform results in predominantly face-on alignment, whereas processing from

dichlorobenzene suppresses the formation of these face-on stacks. Consequently, higher charge transport in OFET was achieved for films processed from dichlorobenzene, while the performance in organic solar cells benefits from processing from chloroform.

The second concept of fluorination was used to facilitate electron transport by decreasing the electron density along the polymer backbone stabilizing the radical anion. Therefore, we incrementally decreased the donor strength of the 1,4-di(2-thienyl)benzene comonomer by di- and tetrafluorination of the phenyl moiety. In fact, we achieved exclusively n-channel operation in OFETs upon tetrafluorination, whereas the non- and difluorinated polymers show ambipolar charge transport behavior. Interestingly, all polymers show an end-on alignment, which is rarely observed without any grafting of the polymer chains to the substrate surface. In addition to fluorination of the phenyl group, we wanted to prove this concept for thiophene. Therefore, we synthesized a series of four copolymers containing TPD and non-fluorinated as well as fluorinated thiophene. Besides the copolymerization of TPD with thiophene derivatives, we used a TPD monomer additionally flanked with thiophene. Next to the influence of fluorination, we also studied the impact of the extended backbone. In fact, fluorination of thiophene leads to exclusively n-channel operation in OFET for the copolymer without extended backbone. All other polymers show ambipolar charge transport, whereby fluorination improves the efficiency of charge transport, especially of electrons.

The second part of the thesis deals with the incorporation of the very rigid, planar and electron-rich thienothiophene (TT) moiety into TPD copolymers in order to compare it with the simple thiophene (T) moiety. In addition to the influence of the nature of comonomer, the influence of the molecular weight in TPD copolymers carrying thiophene was studied. All polymers show highly balanced ambipolar charge transport. The charge carrier mobilities could be improved by increasing the molecular weight in TPD copolymers carrying thiophene and by substitution of thiophene with thienothiophene by one order of magnitude each. This trend correlates well with the observed thin film alignment. Whereas PTPDT with low molecular weight showed no preferential ordering of the polymer chains to the substrate, a face-on alignment could be achieved for PTPDT with higher molecular weight. A dramatic change in alignment towards edge-on fashion was caused by the thienothiophene moiety yielding very high and balanced charge transport.

In summary, we designed and synthesized p-type, ambipolar as well as n-type materials by variation of the donor strength of the comonomer. For each class of materials, a series of copolymers was systematically studied regarding thermal, optical and electrochemical properties. More important, the charge transport properties were correlated with the thin film alignment of these polymers. Therefore, insights into structure-property relations in TPD based copolymer were gained.

Zusammenfassung

Die vorliegende Arbeit behandelt halbleitende Polymere basierend auf Thieno[3,4-c]pyrrol-4,6-dion (TPD) für die Anwendung in organischer Elektronik. Diese Polymere wurden nach dem Donor-Akzeptor Konzept entworfen, wobei alle Polymere TPD als Akzeptorbaustein gemeinsam haben. Die Ladungsträgertransporteigenschaften wurden systematisch durch strukturelle Variation der Comonomere, insbesondere deren Donorstärke, beeinflusst. Um ein tieferes Verständnis hinsichtlich deren Struktur-Eigenschafts-Beziehungen zu erzeugen, wurde die Orientierung der Polymerketten in dünnen Filmen mittels Weitwinkelstreuung mit streifendem Einfall (GIWAXS) analysiert. Konjugierte Polymere sind oft teilkristalline Materialien mit einem steifen Polymerrückgrat, die untereinander durch π - π und Alkyl-Wechselwirkungen interagieren. Dies führt zum Zusammenschluss von mehreren Polymerketten zu Polymerstapeln, die eine *edge-on*, *face-on* oder *end-on* Ausrichtung zum Substrat einnehmen können. Eine *edge-on* Ausrichtung umfasst die Orientierung der planaren π -Systeme senkrecht zum Substrat, während sich die Polymerstapel bei *face-on* parallel zum Substrat anordnen. Eine *end-on* Orientierung, bei der die Polymerketten senkrecht auf dem Substrat stehen, tritt nur selten auf. Diese unterschiedlichen Orientierungen können die Leistung des elektronischen Bauteils maßgeblich beeinflussen, da der Ladungsträgertransport entlang der π - π Wechselwirkungen effizienter ist als entlang der Alkyl-Wechselwirkungen. Eine *edge-on* Ausrichtung begünstigt den Ladungsträgertransport in organischen Feldeffekttransistoren (OFET), wohingegen der Ladungsträgertransport in einer Diodenkonfiguration durch eine *face-on* Orientierung gefördert werden kann.

Im ersten Teil der Arbeit wird der Einfluss der Fluorierung basierend auf zwei unterschiedlichen Konzepten untersucht. Zunächst haben wir den Einfluss der Fluorierung in p-Halbleitern basierend auf TPD und Terthiophen studiert, wobei die Thiophene, die an den TPD-Baustein angebunden sind, mit zusätzlichen löslichkeitsvermittelnden Seitenketten funktionalisiert wurden. Die Fluorierung bewirkt ein Absenken der Energieniveaus aufgrund der durch sie verringerten Donorstärke, was wiederum zu einer höheren Leerlaufspannung in organischen Solarzellen führen kann. In der Tat konnte an dieser Stelle die Leerlaufspannung in dem Blendesystem aus fluoriertem Polymer und PCBM erhöht werden. Jedoch ging dies mit Verlusten im Füllfaktor einher, wodurch nur ein identischer Wirkungsgrad im Vergleich zum nicht-

fluorierten Polymersystem erzielt werden konnte. Zusätzlich haben wir den Einfluss der Prozessierung auf die Orientierung der Polymerketten im dünnen Film sowie auf die Leistung im Bauteil untersucht. Beide Materialien zeigen eine hohe Kristallinität und aggregieren stark in Lösung, wie in temperaturabhängigen UV-Vis Messungen gezeigt werden konnte. Des Weiteren hängt die Art der Aggregate vom verwendeten Lösungsmittel ab. Die Prozessierung aus Dichlorbenzol verhindert die Entstehung von *face-on* Polymerstapeln. Daraus resultierte ein höherer Ladungsträgertransport in OFETs für die Filme, die aus Dichlorbenzol prozessiert wurden, während die Leistung der organischen Solarzelle von der Prozessierung aus Chloroform profitiert.

Das zweite Konzept der Fluorierung beruht auf der Verringerung der Elektronendichte entlang des Polymerrückrats, was zu einer Stabilisierung des Radikalanions sowie zu Elektronentransport führen kann. Hierfür haben wir inkrementell die Donorstärke des Comonomers 1,4-Di(2-thienyl)benzol (TPT) durch Di- und Tetrafluorierung der Phenylgruppe verringert. Tetrafluorierung führt tatsächlich ausschließlich zu n-Kanal-Betrieb in OFETs, während die nicht- und difluorierten Polymere ambipolaren Ladungsträgertransport aufweisen. Interessanterweise zeigen alle Polymere die *end-on* Orientierung, die nur selten ohne Verankerung der Polymerketten auf die Substratoberfläche beobachtet wird. Zusätzlich zur Fluorierung der Phenylgruppe wollten wir dieses Konzept auch auf Thiophen übertragen. Hierzu haben wir eine Reihe von vier Copolymeren basierend auf TPD und Thiophen sowie fluoriertem Thiophen synthetisiert. In dieser Copolymerisation haben wir zusätzlich auch ein TPD Monomer flankiert mit Thiophen eingesetzt, um nicht nur den Einfluss der Fluorierung, sondern auch den Einfluss eines erweiterten Polymerrückrats zu untersuchen. Auch hier konnte ausschließlich Elektronentransport durch die Fluorierung von Thiophen für das Polymer ohne erweitertes Polymerrückgrat erreicht werden. Alle anderen Polymere zeigten ambipolaren Ladungsträgertransport, wobei die Fluorierung den Ladungsträgertransport vor allem von Elektronen erhöht.

Der zweite Teil der Arbeit behandelt die Verwendung der sehr steifen, planaren und elektronreichen Thienothiophen-Einheit (TT) in TPD Copolymeren im Vergleich zum einfachen Thiophen-Baustein (T). Zusätzlich zum Einfluss der Art des Comonomers wurde der Einfluss des Molekulargewichts in Copolymeren basierend auf TPD und Thiophen untersucht. Alle Polymere zeigen sehr ausgeglichenen ambipolaren Ladungsträgertransport, wobei die Effizienz durch

Erhöhung des Molekulargewichts in Copolymeren basierend auf TPD und Thiophen und weiter durch Verwendung von Thienothiophen anstelle von Thiophen um jeweils eine Größenordnung verbessert werden konnte. Dieser Trend korreliert mit der beobachteten Orientierung der Polymerketten im dünnen Film. Während PTPDT mit niedrigerem Molekulargewicht keine bevorzugte Orientierung der Polymerketten zum Substrat zeigte, konnte eine *face-on* Orientierung für PTPDT mit höherem Molekulargewicht erreicht werden. Eine drastische Änderung in der Ausrichtung der Polymerketten hin zu einer *edge-on* Orientierung wurde für die Thienothiophen-Einheit beobachtet, wodurch ein sehr hoher und ausgeglichener Ladungsträgertransport erreicht werden konnte.

Zusammenfassend ist es uns gelungen p-typ, ambipolar und n-typ Materialien durch die Variation der Donorstärke des Comonomers zu entwerfen und zu synthetisieren. Für jede Klasse von Materialien wurde eine Reihe von Copolymeren systematisch hinsichtlich ihrer thermischen, optischen und elektrochemischen Eigenschaften untersucht. Die Ladungsträgertransporteigenschaften wurden mit der Orientierung der Polymerketten im dünnen Film korreliert, wodurch Kenntnisse über Struktur-Eigenschafts-Beziehungen in TPD basierten Copolymeren erlangt wurden.

1 Introduction

In 2016, the first steps against climate change were agreed upon in Paris by almost all countries of the world. In order to mitigate global warming, the energy revolution needs to be promoted by expanding the renewable energy sector and promoting zero CO₂ emission. In the year 2017, the overall electricity of Germany was generated to about 29.0% by renewable energies including 11.9% wind power, 7.0% biomass, 5.9% photovoltaics and 3.2% hydropower (status: March 2017).^[1] Especially the photovoltaic sector is in the focus as in one hour the sun provides sufficient energy to cover the one-year energy demand of all living people. Most solar modules are based on silicon and can deliver efficiencies of over 26% up to date.^[2] In mass production, the efficiencies of commercially available solar modules lie rather around 17%.^[3] However, these solar panels require silicon in ultra-high purity, which requires an energy-intensive production process. Therefore, the energy payback time is nowadays at around 2.5 years when located in Northern Europe.^[3] Additionally, thick layers are needed due to the low absorption of sun light and due to the lack of technologies to slice the monocrystalline silicon in very thin layers. Usually, such solar modules are opaque, rigid, and heavy since they are encapsulated with glass plates.

One alternative emerging technology could be organic solar cells. Here, inexpensive high-absorbing materials require only very thin active layers and allow for flexible and lightweight devices. Throughput large-area modules are accessible by low-temperature processing, for example roll-to-roll printing techniques. As active material, organic semiconductors including small molecules as well as polymers are applied. Besides their application as organic semiconductors in solar cells, these materials are also used in transistors, diodes, sensors and light-emitting devices (LED). Regarding photovoltaics, these materials show efficiencies up to 13% on lab-scale.^[4] Instead of the high energy payback times required for silicon solar cells, organic solar cells have a payback time of just around 90 days.^[5] A first step towards commercialization is made by the chemical company Heliatek. They hold the world record efficiency of 13.2% for tandem solar cells fabricated by vacuum processing of small molecules. In production using the roll-to-roll printing technique (Figure 1.1a), efficiencies of 7-8% are achieved for opaque devices and 6% for devices with different degrees of transparency of up to 30%. These solar panels can be integrated in building facades and roofs, especially when they are transparent (Figure 1.1b). At the Expo 2015, the roof of the German pavilion was decorated

with organic solar cell panels as shown in Figure 1.1c and d. Further possible applications are irregular shaped products such as backpacks and tents due to the flexibility of these devices.^[6]

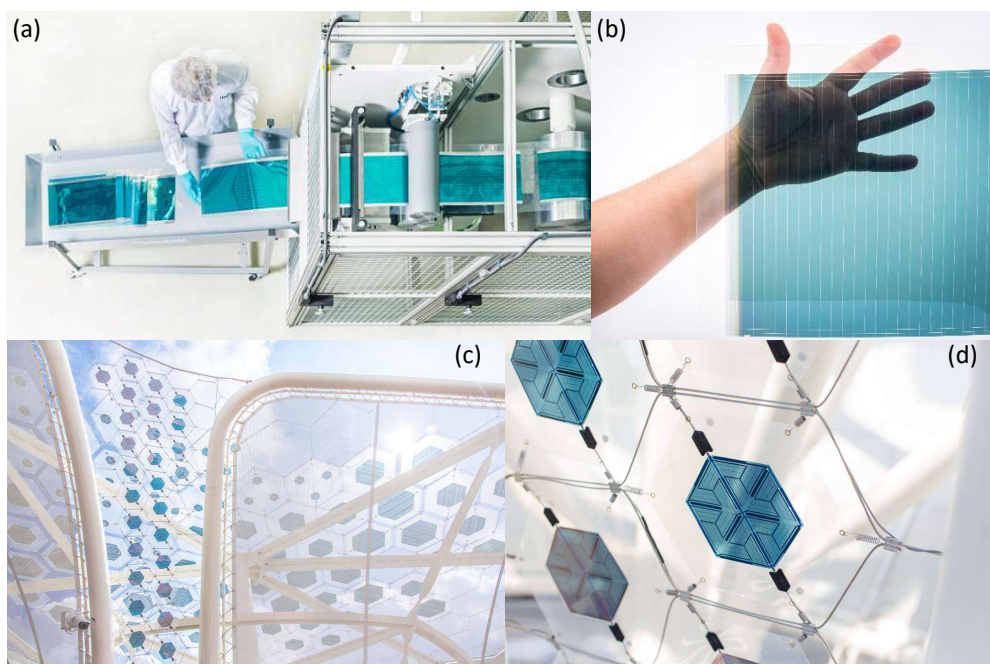


Figure 1.1. (a) Production of organic solar cells by the roll-to-roll printing technique at Heliatek GmbH.^[7] (b) Example for a transparent flexible solar cell having transparencies of up to 50% developed by the Heliatek GmbH.^[7] (c) Integration of organic solar cells into the roof of the German pavilion at the Expo 2015.^[8] (d) Enlarged section of the integrated organic solar cells shown in (c).^[8]

1.1 Organic solar cells

In 1986, Tang published the first heterojunction photovoltaic device achieving a power conversion efficiency of about 1%.^[9] As active layer, a bilayer of copper phthalocyanine and a perylene tetracarboxylic derivative was used. A scheme of a bilayer architecture is given in Figure 1.2a, where the red material represents the electron transporting material (acceptor) and the blue one the hole transporting material (donor). Photoconversion takes place only at the interface of the donor and acceptor material and in organics the generated excitons have a very small exciton diffusion length in the range of some 10 nm. Therefore, the efficiency of a bilayer solar cell is absorption limited and bulk heterojunction (BHJ) solar cells were developed to increase the interface area and domain sizes in the range of exciton diffusion length which paved for higher efficiencies (Figure 1.2b).^[10,11] Here, in the simplest system, the donor and acceptor materials are mixed in a blend system in order to increase the interfacial area between the donor and acceptor domains. Thus, the BHJ architecture became the standard device geometry for solar cell research if at least one component is a polymer. An alternative concept is the block copolymer strategy, where the donor and acceptor materials are covalently linked. Due to

microphase separation small domain sizes and very large defined interfaces can be achieved. The optimal geometry would be achieved by a lamellar phase separation perpendicular to the substrate surface as shown in Figure 1.2c.^[12]

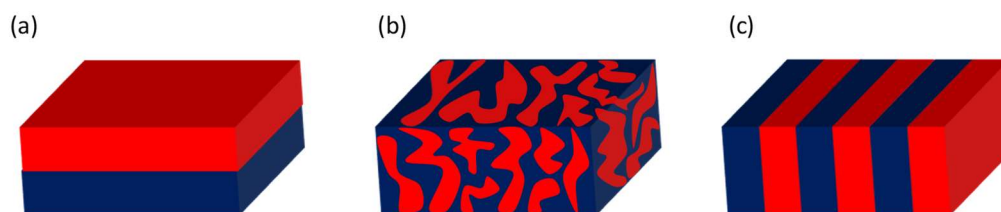


Figure 1.2. Active layer architectures comprising a donor (blue) and acceptor (red) material: (a) Bilayer architecture, (b) blend system where the materials are highly mixed (bulk heterojunction) and (c) phase separation of a block copolymer (donor and acceptor material covalently linked) in order to achieve a lamellar orientation perpendicular to the substrate.

In the following two sections, the physical processes in organic solar cells are described followed by the methods of characterization of the devices.

1.1.1 Physical processes in organic solar cells

The most promising architecture for effective photoconversion is the BHJ solar cell and a schematic setup of the complete device is illustrated in Figure 1.3. As front electrode, indium tin oxide (ITO) on glass or a flexible plastic substrate is used due to its transparency. The back contact comprises metals such as aluminum and calcium. In order to improve charge extraction, interlayers between the electrodes and the active layer are often introduced. For example, PEDOT:PSS is often used as hole extraction layer.

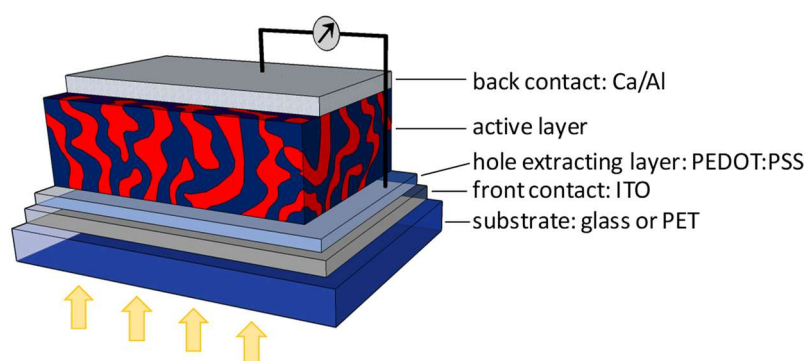


Figure 1.3. Schematic setup of a bulk-heterojunction solar cell. The active layer is sandwiched between two electrodes.

The photogeneration in organic solar cells fundamentally differs from a silicon-based solar cell, which is mainly caused by the difference in dielectric constants and the magnitude of exciton binding energy. Whereas silicon has a dielectric constant of 12, that for organic materials is in

the range of 2-4.^[13] Additionally, the exciton binding energy in organics is very high and therefore, photoexcitation does not result in the generation of a free electron-hole pair as it is the case in silicon-based solar cells, but rather in a strongly coulombically bound electron-hole pair, also called exciton.^[14] The physical processes leading to photocurrent can be divided into four fundamental steps as shown in Figure 1.4: (i) Photon absorption and exciton generation, (ii) exciton diffusion, (iii) exciton dissociation and (iv) charge collection.

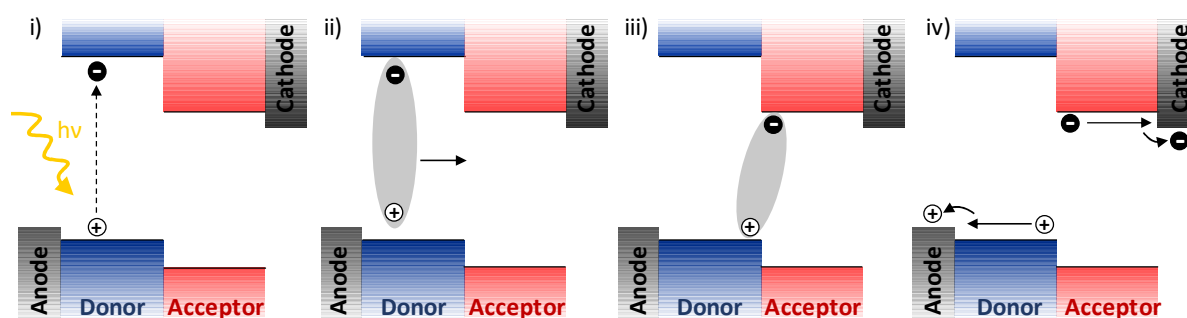


Figure 1.4. Physical processes in an organic solar cell: (i) Photon absorption and exciton generation, (ii) exciton diffusion until the D/A interface is reached, (iii) exciton dissociation at the D/A interface into free charge carriers and (iv) charge collection to the respective electrodes.

Upon light absorption an exciton is generated in the active layer, typically within the donor material due to its usually higher absorption coefficient. Diffusion of the exciton through the domain occurs until either the donor-acceptor interface is reached, or recombination takes place. The exciton diffusion length L_D is limited to 5-10 nm due to its short life-time of only nanoseconds and small diffusion coefficient.^[15-19] If an exciton reaches the donor-acceptor interface, a charge transfer state is generated due to the energy level offset of the donor and acceptor material. The electron is transferred to the lower lying LUMO (lowest unoccupied molecular orbital) of the acceptor material and the hole remains in the HOMO (highest occupied molecular orbital) of the donor material. After charge dissociation, the free charge carriers migrate to the electrodes under the internal field. Charge separation at the D-A interface is the key process in order to target high efficiencies. Therefore, a closer understanding of these processes is of high importance in respect of device optimization and detailed information can be found in several reviews.^[20-24] Charge separation can be described based on electronic orbital energies or on state energies and both descriptions are shown in Figure 1.5.

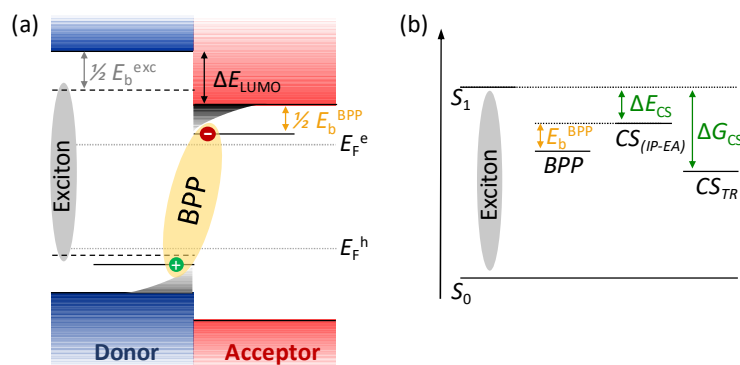


Figure 1.5. (a) Electronic orbital energy diagram and (b) state energy diagram of a D/A interface during photoconversion. E_b^{exc} is the exciton binding energy and E_b^{BPP} the equivalent binding energy of the bound polaron pair (BPP). ΔE_{LUMO} is the D/A LUMO-LUMO offset. Splitting of the electron as well as hole quasi-Fermi levels E_F^e and E_F^h of the blend under device operation corresponds to the free energy of charges after thermalization. This thermally relaxed charge separated state CS_{TR} is also illustrated in (b). ΔE_{CS} is the enthalpy difference between the S_1 state and the charge separated polaron, which is given by IP-EA. ΔG_{CS} is the total energy loss during the overall charge separation process. Adapted from Durrant et al.^[23]

Due to the low dielectric constant of organic semiconductors, the binding energies E_b^{exc} of the coulombically bound charges can amount to several hundred meV, which exceeds the thermal energy $k_B T$. These bound states are called charge transfer states as mentioned above or bound polaron pair (BPP) states. As driving force for charge separation, an energy offset between the LUMO levels of donor and acceptor material (ΔE_{LUMO}) is required. An offset value greater than 0.3 eV is often described in the literature to overcome the exciton binding energy.^[25–27] This exciton binding energy is considered to be the reason for the lower electronic bandgap in relation to its optical gap.^[28] Alternatively, the charge separation process can be viewed in terms of state energies as illustrated in Figure 1.5b. The state energies of the bound polaron pair and separated charges are shown in relation to the energy state of the polymer exciton S_1 . Here, the energy offset needed for charge separation is given as ΔE_{CS} , which is the energy difference between the charge separated polaron (given by the energies IP (of the donor) and EA (of the acceptor)) and the exciton energy E_{S_1} : $\Delta E_{\text{CS}} = (\text{IP-EA}) - E_{S_1}$. With the exciton binding energy, ΔE_{CS} can be described in relation to ΔE_{LUMO} : $\Delta E_{\text{CS}} = \Delta E_{\text{LUMO}} - E_b^{\text{exc}}$. On the contrary, the free energies of electrons and holes in the blend differ from their individual polaron energies. They are defined by the electron and hole quasi-Fermi levels E_F , which lie within the electronic bandgap. Charge separation leads to an increase in entropy and by that, thermalization with these Fermi levels results in a less energetic state CS_{TR} . This energy represents the voltage output of the device in the absence of losses. Losses can be attributed to recombination of charge carriers during photoconversion. As mentioned above, an exciton can decay after excitation without approaching the donor-acceptor interface upon which the absorbed energy is released as heat.

This mechanism is called geminate recombination, which also includes recombination of the bound charges through the CT state. Additionally, a further recombination mechanism is of quite significance. It is called non-geminate recombination and includes bimolecular recombination as well as trap-assisted recombination. In the case of bimolecular recombination, the free charge carriers generated from different excitons recombine before being collected by the electrodes. Trap-assisted recombination occurs when a trapped charge carrier recombines. Details about the recombination processes and their effects on solar cell performance are provided in several reviews.^[29,30]

Solar cell fabrication includes a high degree of device optimization, especially regarding the morphology of the active layer. Due to the small exciton diffusion length, an interpenetrating network of the donor and acceptor material is required. A high degree of charge extraction can only be achieved by intercalation of both materials suppressing large, pure domains of either one, but providing enough nanodomains of each capable of charge transport.^[31] This nanostructure morphology can be optimized by the processing parameters and is mainly influenced by the solvent used for film processing.^[32] Furthermore, solvent additives like 1,8-diiodo-octane (DIO) can help to achieve the desired blend morphology in specific systems.^[33]

1.1.2 Characterization of organic solar cells

The performance of a solar cell device is characterized by several parameters, which are described in the following. In order to elucidate the efficiency of a solar cell, current-voltage characteristics are measured in the dark and under illumination with a defined light source. Such current-voltage characteristics are exemplarily shown in Figure 1.6a.

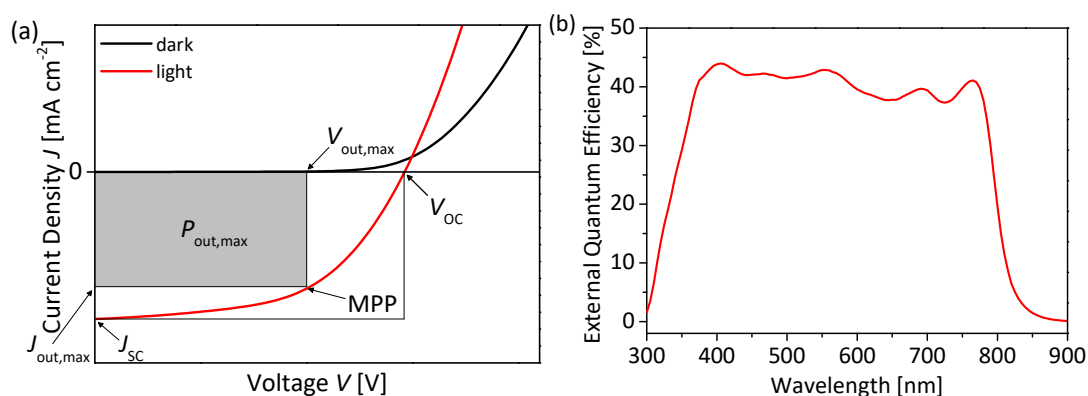


Figure 1.6. (a) Current-voltage characteristics of a solar cell in the dark and under illumination. Parameters describing the performance are open-circuit voltage (V_{OC}), short-circuit current (J_{SC}) and maximum power point (MPP). (b) External quantum efficiency (EQE) spectrum of a solar cell.

Important characteristic values for comparison with other devices are, besides the power conversion efficiency, the short-circuit current density J_{SC} , the open circuit voltage V_{OC} and the fill factor FF. The short-circuit current density is defined as the current at zero bias and depends on the number of absorbed photons as well as on the charge carrier mobilities of the active layer materials. Correspondingly, the voltage at zero current is called open-circuit voltage and directly relates to the offset between the HOMO energy level of the donor material and the LUMO energy level of the acceptor material. The fill factor describes the shape of the current-voltage characteristics and provides a measure of the maximum power output $P_{out,max}$ in relation to the maximum attainable power. For the calculation of FF, the maximum power point MMP need to be determined as the peak value of current times voltage. The quotient of $P_{out,max}$ divided by the product of V_{OC} and J_{SC} gives the fill factor. Furthermore, the organic solar cell is operated at the MMP.

$$FF = \frac{P_{out,max}}{J_{SC} \cdot V_{OC}} = \frac{J_{out,max} \cdot V_{out,max}}{J_{SC} \cdot V_{OC}} \quad (1)$$

The power conversion efficiency η is defined as the ratio of the maximum electrical power delivered by the PV cell to the incident light power and reads as follows:

$$\eta = \frac{P_{out,max}}{P_{in}} = \frac{J_{SC} \cdot V_{OC} \cdot FF}{P_{in}} \quad (2)$$

A further definition of the device efficiency is given by the external quantum efficiency (EQE) and internal quantum efficiency (IQE). Both terms describe how efficiently the incident light is converted into electrical energy as a function of a specific wavelength. The EQE, also called incident photon-to-current conversion efficiency (IPCE), describes the electron flux in the external circuit per incident photon flux on the PV cell at a specific wavelength. An example of an EQE measurement is shown in Figure 1.6b. The electron flux J_e is given by the short-circuit current density divided by the charge of one electron e . Analogously, the incident photon flux J_{ph} can be calculated by the incident light intensity P_{in} divided by the energy of one photon. This leads to the following definition of the EQE:

$$EQE = \frac{J_e}{J_{ph}} = \frac{J_{SC}/e}{P_{in}/(h\nu)} = \frac{J_{SC} h\nu}{P_{in} e} \quad (3)$$

In contrast to the EQE, the IQE is defined as the number of electrons flowing in the external circuit per actually absorbed photon. This gives the photoconversion properties of the active layer including the efficiency of exciton diffusion, charge transfer and charge collection.

1.2 Semiconducting polymers

In 2000 the Nobel Prize in Chemistry was awarded to Alan J. Heeger, Alan G. MacDiarmid and Hideki Shirakawa “*for the discovery and development of conductive polymers*”. In order to achieve conductivity in a polymer, a conjugated π -system is required, which is then oxidized to create charge carriers. The first report is dated back to 1862, where Henry Letheby describes the anodic oxidation of aniline in sulphuric acid.^[34] He received a partly conductive material, which was probably doped polyaniline. A further conductive material was found in polypyrroles, which were first published in 1963 by Weiss and coworkers.^[35] The breakthrough was achieved by the discovery of doped polyacetylene as conductive polymer. In 1974, Shirakawa successfully synthesized well-defined films with relatively modest conductivities.^[36] By collaboration with MacDiarmid and Heeger, a tremendous improvement of conductivity was achieved by the doping of the material with halides.^[37] Further studies on polyacetylene followed.^[38,39] In the following early 1980s up to the end of 90s similar conjugated polymers were extensively studied including polypyrrole, polythiophene, polyphenylenevinylene and polyaniline. In the late 1980s, solubility was introduced to the polymers by attaching alkyl side chains making the polymers processable.

1.2.1 Low band gap (LBG) polymers

One requirement for a semiconducting polymer in OPV applications is a high absorption coefficient over a wide range of the visible light. The absorption edge can be shifted to higher wavelengths by decreasing the optical gap. In general, five structural factors contribute to the optical gap, where the bond length alternation represents the major contribution. Further contributions are planarity, substitution, aromaticity as well as intra- and intermolecular interactions as shown in Figure 1.7a for polythiophene. By introducing rigid building blocks, the torsion angle between two aromatic moieties are reduced and planarization occurs. Consequently, the conjugation is extended und delocalization is facilitated, which leads to a decreased optical gap. Very rigid polymers can be achieved by covalent linkage of the aromatic moieties. By introduction of electron donating or withdrawing groups at the aromatic moiety, the HOMO or LUMO energy levels can be adjusted.^[40] Further reduction of the optical gap can

be achieved using low band gap polymers. These polymers can either be designed by the quinoid or donor-acceptor approach.^[41–43]

The quinoid approach is based on the two different resonance structures of the aromatic building block. Besides the aromatic resonance structure, conversion to the less stable quinoid form can occur. The quinoid form has a smaller band gap and therefore, the ratio of aromatic to quinoid population influences the bond length alternation. A more enhanced quinoid character results in a decreased optical gap and can be implemented by fused aromatic units. Examples for such building blocks in combination with their resonance structure are shown in Figure 1.7b. Here, the quinoid resonance structure is stabilized by the formation of for example an aromatic benzene unit in poly(benzo[*c*]thiophene). Thereby, the loss of aromaticity of the thiophene unit is accompanied by a gain in aromaticity of the benzene unit, which benefits from a higher aromatic stabilization resonance energy than thiophene.^[44–46]

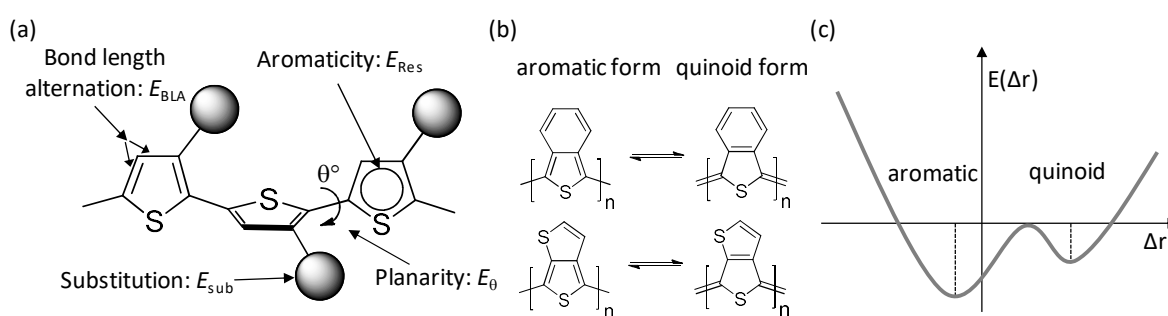


Figure 1.7. (a) The five structural contributions influencing the optical gap of polymeric semiconductors. (b) Aromatic and quinoid form of poly(benzo[*c*]thiophene) and poly(thieno[3,4-*b*]thiophene) and (c) its respective energy diagram.

A more powerful strategy to alter the optical gap is the donor-acceptor (D-A) approach, where an electron-rich donor unit and an electron-poor acceptor unit are arranged in an alternating way in the polymer backbone.^[47] This D-A arrangement generates a push-pull driving force facilitating the electron delocalization. Moreover, intramolecular charge transfer (ICT) is enhanced resulting in two resonance forms: D-A and $D^+=A^-$. In this model, the quinoid form is stabilized by the increased double bond character between the repeating units. The hybridization of molecular orbitals provides a better understanding of the decrease in optical gap. As shown in Figure 1.8, the LUMO as well as the HOMO level of both acceptor and donor unit recombine resulting in two new respective energy levels. By redistribution of the electrons, an energetically increased HOMO as well as decreased LUMO level of the D-A array is achieved

forming a reduced optical gap E_g . Examples for electron-rich donor units as well as for electron-deficient acceptor units are shown in Figure 1.8.^[48]

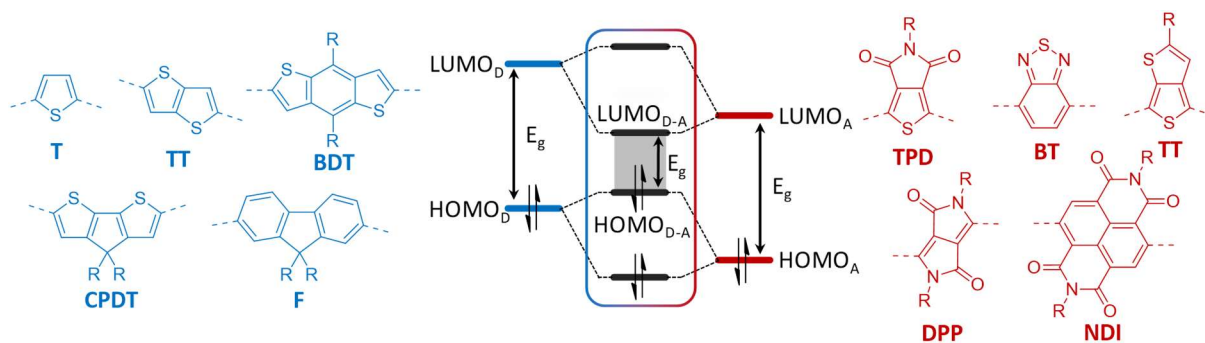


Figure 1.8. Energy level hybridization of a donor unit with an acceptor unit giving the new $HOMO_{D-A}$ and $LUMO_{D-A}$ levels in the D-A copolymer together with examples of the respective units. Donor units: thiophene (T), thieno[3,2-b]thiophene (TT), benzo[1,2-b:4,5-b']dithiophene (BDT), cyclopentadithiophene (CPDT), fluorene (F). Acceptor units: thieno[3,4-c]pyrrole-4,6-dione (TPD), 2,1,3-benzothiadiazole (BT), thieno[3,4-b]thiophene (TT), diketopyrrolopyrrole (DPP), naphthalene diimide (NDI).

Copolymers designed by the donor-acceptor approach predominantly show hole-transporting properties and are referred to as donor materials. The two terms, donor unit and donor material, need to be distinguished strictly (as well as acceptor unit and acceptor material). Whereas the donor unit describes the inherent electron donating moiety in the low-band copolymer, the term donor material refers to the properties of the whole copolymer. Besides the low band gap of around 1.5 eV, which is ideal to harvest most of the incident sun light for maximizing J_{SC} , a comparable low-lying HOMO level is required to ensure a high V_{OC} . Additionally, the LUMO energy offset of the donor and acceptor material needs to be maintained in order to promote efficient charge separation. Therefore, the optical gap and the energy levels of the polymeric donor material can be adjusted by tuning the donor as well as acceptor strength of the corresponding units.^[49] By this concept also electron transporting materials can be achieved by decreasing the electron density along the polymer backbone in order to stabilize the radical anion. This can be achieved by decreasing the donor strength of the electron-rich unit and/or increasing the acceptor strength of the electron-poor unit. Consequently, the optical gap is increased.

1.2.2 Hole transporting materials

Among the intensively studied semiconducting polymers are polythiophenes.^[50,51] By introducing solubilizing alkyl side chains to achieve poly(3-hexylthiophene) (P3HT), these homopolymers became processable and up to now the best studied hole transporting material.

Beneficial of these types of polymers are their controlled synthetic accessibility,^[52,53] high crystallinity and high charge carrier mobility^[54]. However, their device performance in organic solar cells is inhibited due to their limited range of sun light absorption. In combination with PCBM as acceptor material, average power conversion efficiencies of about 3%^[55] and a maximal PCE of 5.5%^[56] could be realized. Using other fullerene derivatives such as the indene-C₆₀ bisadduct (IC₆₀BA) more than 6% were achieved,^[57–59] which could even be improved to over 7% using the C₇₀ analogue.^[60] In order to achieve power conversion efficiencies beyond 7%, new donor polymers based on thiophene featuring a smaller band gap were developed. As shown in Chapter 1.2.1, various monomer combinations, substituents as well as side chains can be used to create a huge library of D-A copolymers. An overview of the different classes of polymers along with their performance in solar cells was published in 2016 by W.H. Jo *et al.*^[61] The molecular structure of selected LBG polymers as well as P3HT are summarized in Figure 1.9. Highest efficiencies in combination with PC₇₁BM as acceptor material are highlighted in the following. In the branch of TPD based copolymers, an efficiency of 9.2% was achieved by PT-ttTPD.^[62] Polymers with fluorinated thieno[3,4-*b*]thiophene as acceptor unit in combination with a benzodithiophene derivative (PTB7-Th) showed a PCE value of 10.6%.^[63] Whereas DPP based copolymers show very high mobilities in organic field effect transistors,^[64] their solar cell performance is inferior and a maximal efficiency of 8.8% could be measured for C3-DPPTT-t.^[65] Efficiencies of more than 10% are reported for fluorinated benzothiadiazole based polymers^[66] as well as naphtho[1,2-*c*:5,6-*c'*]bis[1,3,5]thiadiazole (NT) based polymers.^[67]

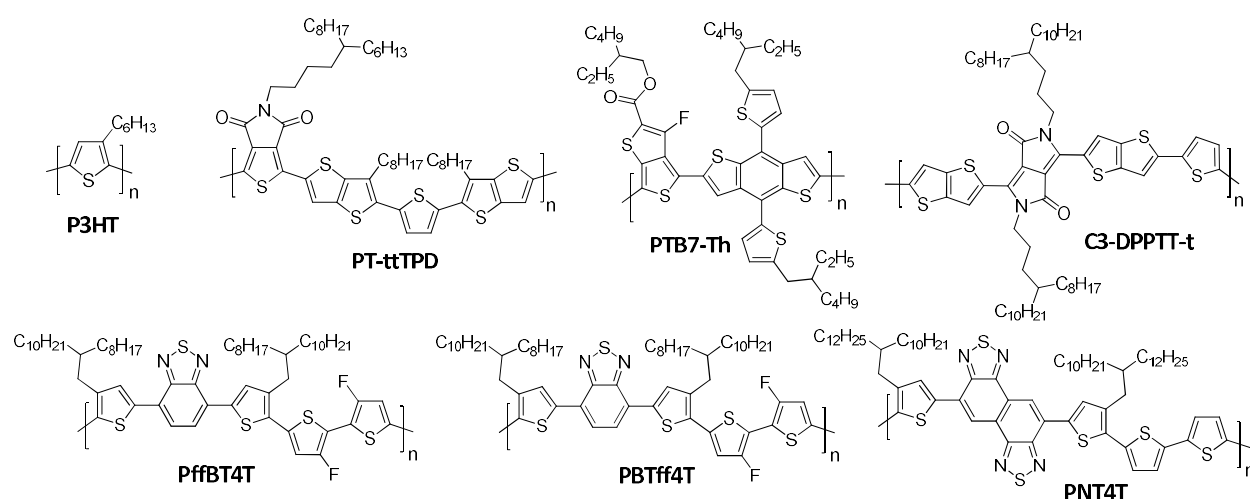


Figure 1.9. Examples for polymers used as donor materials in organic solar cells.

1.2.3 Electron transporting materials

The first and still most widely used electron transporting material is fullerene and its derivatives. By functionalization of C₆₀, highly soluble fullerene derivatives are achieved, out of which especially fullerene phenyl-C₆₁-butyric acid methyl ester should be noted.^[68] The limited light absorption could be overcome by the corresponding C₇₀ derivatives.^[69] These class of materials are intensively studied and widely applied in blends together with a polymer donor due to its outstanding properties. Fullerenes reveal a high electron affinity,^[70] fast electron transfer from donor materials^[71] and high electron transport characteristics.^[72] By intensive optimization of the polymer-fullerene blend, in some cases a desired optimum morphology could be achieved.^[73] However, fullerenes suffer from several drawbacks such as poor light absorption, high production costs and a relatively low-lying LUMO level limiting the open-circuit voltage. Additionally, blend morphologies comprising fullerenes are not very stable and PCBM diffuses through the active layer.^[74,75] Therefore, the interest in alternative materials arose and small molecule as well as polymers came into spotlight. Regarding small molecule acceptor materials, several reviews give an overview about the scientific progress and deal with many different classes including perylene bisimides (PBI).^[76–78] An example for a small molecule acceptor based on PBI is given in Figure 1.10. The bay-linked PBI dimer SdiPBI-Se shows a high efficiency of 8.4% in combination with a wide band gap polymer (PDBT-T1) as donor.^[79] Very high efficiencies of 11.4% were achieved by the indacenodithieno[3,2-*b*]thiophene based small molecule ITIC.^[80] By introducing fluorine substituents to ITIC, a new record efficiency of over 13% was published just recently.^[4] The first polymers showing electron transport were based on cyanated PPV and their performance in all-polymer solar cells was limited to a PCE of 2%.^[81–83] A tremendous increase in performance was achieved using NDI based copolymers reaching efficiencies of more than 8%.^[84] The major challenge in all-polymer solar cells is taking control of the blend morphology as a mixture of two different polymers tends to show macrophase separation. In general, the blend morphology can be optimized by solvent engineering, thermal annealing and adjusting polymer molecular weights or the D/A blending ratio. Additionally, it is crucial to choose acceptor and donor materials with complementary absorption spectra and partial miscibility, which can be influenced by side-chain engineering or varying substituents. An overview of the research progress of all-polymer solar cells is given in the reviews of Benten *et al.*^[85] and Kim *et al.*^[86]

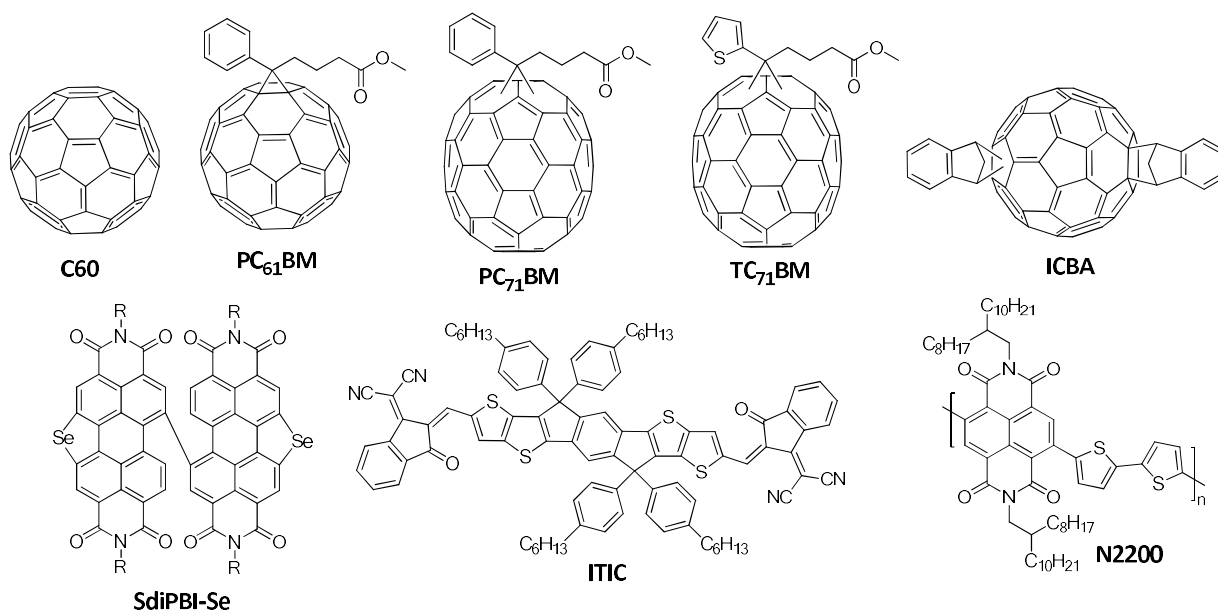


Figure 1.10. Overview of various acceptor materials.

1.3 Polymerization methods

The formation of a carbon-carbon bond is essential for the polymerization of conjugated polymers and can be achieved by metal catalyzed cross-coupling reactions. In 2010, the Nobel Prize in chemistry was awarded to Heck, Negishi, and Suzuki “for palladium-catalyzed cross-couplings in organic synthesis”.^[87,88] Besides their pioneering work, further cross-coupling reactions have been developed and applied for the polymerization of conjugated copolymers. For the polycondensation of two different monomers arranged in an alternating way, bifunctional monomers with two different functional groups are necessary depending on the type of cross-coupling reaction. An overview of all these reactions are given in Figure 1.11. The three most widely applied polycondensation types are Stille,^[89] Suzuki^[90] and Direct Heteroarylation (DHA)^[91] cross-coupling reactions. Sonogashira^[92] and Heck^[93] reactions are only seldom used due to the electronically less favorable triple or double bond, respectively. A further method is the Yamamoto cross-coupling reaction between two halogen functionalized aryl units.^[94] However, this reaction is only suitable for electron-rich homopolymers or statistic copolymers.

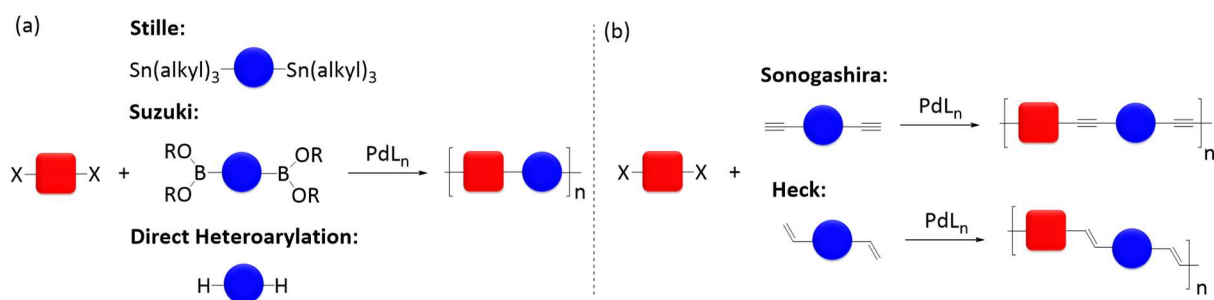


Figure 1.11. Polycondensation via palladium-catalyzed cross-coupling reactions achieving copolymers in an alternating way. A dihalogen functionalized monomer is copolymerized with a second monomer carrying different functional groups depending on the type of reaction: (a) Direct coupling of two aromatic moieties by Stille, Suzuki or Direct Heteroarylation reactions and (b) coupling via triple or double bonds by Sonogashira or Heck reaction, respectively.

The majority of copolymers are synthesized by Stille polycondensation due to the tolerance of many functional groups and mild reaction conditions. Furthermore, the organotin monomers are less sensitive to oxygen and moisture. On the downside, they are highly toxic. A more environmentally friendly alternative may be found in boronic acids as used in Suzuki polycondensation, which also tolerates a broad range of functional groups. One exception are functional groups, which are unstable under basic conditions and therefore, cannot be used in Suzuki reactions. An additional drawback is that the polymerization is hindered in the case of thiophene based monomers, which are widely present in high-performance polymers. For the Direct Heteroarylation polymerization, no functionalization of the second monomer is necessary making this technique very economically compatible. Additionally, the synthetic effort is diminished and the purification of the monomer, which is often difficult for stannylated as well as borylated compounds, is simple since the non-functionalized monomers can be easily purified. In general, highly pure monomers are necessary to maintain a 1:1 stoichiometry in order to achieve high molecular weights. In contrast to the easy accessibility of monomers, the polymerization needs to be optimized for each monomer combination in terms of catalyst, solvent and additives.^[95] Furthermore, side reactions generating defects along the polymer backbone need to be suppressed, especially when additional aromatic protons are present, which may take part in the coupling reaction.^[96] In this work, the polymers were synthesized via Stille polycondensation and therefore, this reaction is viewed in more detail in the following. Further information regarding Stille,^[97] Suzuki^[98] and DHA^[99,100] polycondensation can be found in the corresponding reviews.

The reaction of organostannanes and electrophilic partners is described as Stille coupling.^[89] In 1993, the Stille coupling was first used as a tool for polycondensation reactions developed by Yu

and co-workers.^[101,102] The reaction mechanism of the palladium catalyzed Stille coupling is shown in Figure 1.12 including oxidative addition, transmetalation and reductive elimination. In the first step, the Pd(0) catalyst is oxidatively inserted into the C-X bonding forming a Pd(II) intermediate. Thereby, X is typically a halide, where the reactivity is increased from chlorine over bromine to iodine. By oxidative addition, the 14-electron Pd(0) complex is converted to the *cis*-tetravalent 16-electron Pd(II) complex. This *cis*-intermediate is in equilibrium with its thermodynamically more stable *trans*-form. The consequent transmetalation is the rate determining step and involves ligand substitution. In detail, one of the C-Sn bonds is cleaved by the electrophilic Pd(II) complex followed by substitution under elimination of XSn(alkyl)₃. Reductive elimination under regeneration of the catalyst yields the cross-coupling product. As catalyst Pd(0) as well as Pd(II) species can be used. The most commonly used Pd(0) catalyst is Pd(PPh₃)₄. Due to its sensitivity against oxygen, the more stable catalyst [Pd₂(dba)₃] was developed. Examples for Pd(II) sources are benzyl(chloro)bis(triphenylphosphine)palladium (II) and bis(acetonitrile)palladium(II) dichloride. In these cases, the catalyst needs to be reduced to Pd(0) prior to the reaction with the organohalides.^[103] The cross-coupling reaction takes place between an electron-poor and electron-rich monomer and therefore, the functional groups should be chosen carefully. According to the catalytic cycle, electron withdrawing compounds can facilitate the oxidative addition, while electron-rich moieties promote the transmetalation. Therefore, the reaction can be accelerated by decorating the D monomer with tin groups and the A monomer with halogen groups.^[95]

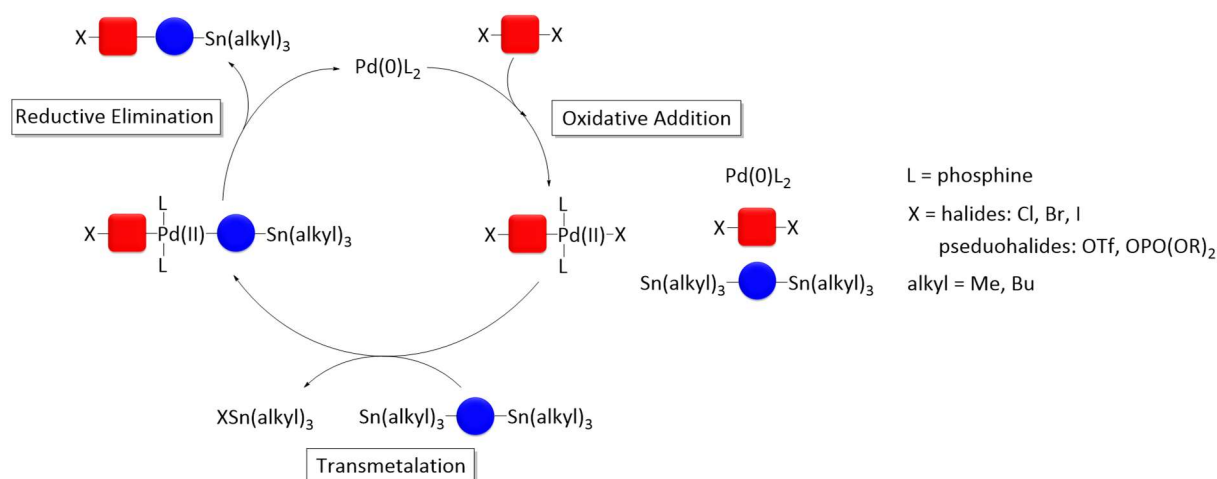


Figure 1.12. Catalytic cycle of Stille cross coupling including oxidative addition, transmetalation and reductive elimination.

The polymerization of alternating copolymers is in the most cases achieved via the AA/BB approach by a step-growth mechanism as shown before. According to the polymerization method, comonomers are symmetrically functionalized by A and B groups, respectively. It is also possible to combine the two different functional groups in one monomer either in single or combined aromatic moieties. This AB polycondensation approach involves high synthetic effort for the monomers, but the resulting asymmetric monomer can then be homopolymerized. For some monomers, polymerization towards the chain-growth mechanism is realized gaining control of molecular weight, dispersity and end-groups. An overview of the two different approaches is shown in Figure 1.13.

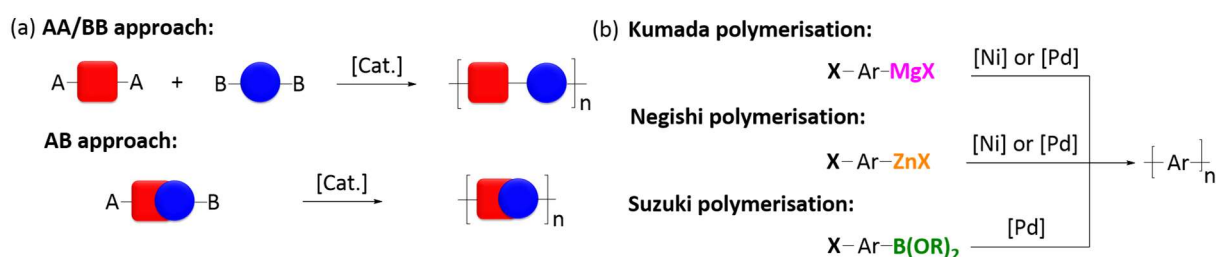


Figure 1.13. (a) Polycondensation via the AA/BB and AB approach. (b) Three types of catalyst transfer polymerization requiring asymmetric monomer units.

The propagation of the polymer chain along with coordination of the catalyst to the chain end is called catalyst transfer polymerization (CTP). Three types of CTPs are prominent: Kumada,^[104,105] Negishi^[106] and Suzuki polymerization. First investigations were made on the Kumada cross-coupling reaction (KCTP) between aryl-halides and Grignard reagents based on thiophenes.^[107] McCullough achieved regio-regular head-to-tail poly(3-hexylthiophene), which was also demonstrated for zinc-based monomers by Rieke.^[108] Further studies gave evidence that the monomers can be prepared by Grignard metathesis (GRIM) starting from the dibromoalkylthiophene.^[109] Control over molecular weight, dispersities and regioregularity via KCTP were demonstrated independently by McCullough and Yokozawa.^[110–112] CTP was limited to alkylthiophenes until Yokozawa demonstrated the catalyst-transfer polycondensation for poly(*p*-phenylene).^[113] The scope of monomers was then extended to fluorenes^[114] and carbazoles,^[115] which could be polymerized via the chain-growth mechanism based on the Suzuki-Miyaura coupling reaction. Further electron-rich as well as electron-deficient monomers are accessible and an overview of the progress can be found in the review of Grisorio and Suranna.^[116] Still the incorporation of any electron-deficient moiety into a D-A copolymer approach using CTP is not generally available.

1.4 Charge transport in organic semiconducting polymers

Organic semiconductors do not possess intrinsic charge carriers. Therefore, charge carriers need to be generated by electrical injection or photoinduced charge separation. The motion of these charge carriers is driven by the electric field, i.e. an electrostatic potential gradient. Therefore, the current flow is drift controlled. The motion of charge carriers is described by their mobility μ , which is defined as the drift velocity v per unit electric field F .^[117]

$$\mu = \frac{v}{F} \quad (4)$$

In most cases, the charge carrier mobility depends on the electric field. The mobility can be related to the conductivity by considering the current density j , which is defined as the number N of charges e that flow per unit time t and unit area A :

$$j = \frac{eN}{At} \quad (5)$$

By expansion of equation (5) with the unit length l , this equation can be rewritten by means of the number density of charges $n = \frac{N}{A \cdot l}$. With the mean drift velocity $v = \frac{l}{t}$ that charges explore within an electric field as well as equation (4), the following expression emerges:

$$j = \frac{eNl}{Atl} = en \frac{l}{t} = env = en\mu F \quad (6)$$

With Ohm's law ($j = \sigma F$, where σ is the conductivity) the following relation between conductivity and mobility can be established:

$$\sigma = en\mu \quad (7)$$

In comparison to inorganic semiconductors, where charge transport can be described via band transport, the charge transport mechanism in organic semiconductors is more complex requiring alternative models taking into account the disorder of these materials. Here, the charge transport is better described by a hopping mechanism. Among several proposed models, the two most important ones are the polaronic transport and the disorder-controlled transport.^[117] The latter one has been introduced by Bässler and describes the charge transport by hopping within a gaussian distribution of density of states.^[118,119]

Various experimental techniques are available to measure the charge carrier mobility, such as the time of flight (ToF) technique,^[120] space-charge-limited current (SCLC) measurements^[121] and organic field effect transistors (OFETs). Whereas the ToF as well as SCLC techniques yield the bulk mobility of the semiconductor, only interfacial charge transport in very thin layers close to the dielectric is studied in OFETs. Since the charge carrier concentrations in the OFET method is very high, the mobilities obtained by OFET are usually about three orders of magnitude higher than their corresponding bulk mobilities.^[122] In the following, the work principle of an organic field effect transistor (OFET) is described in detail.^[123–125]

An organic field effect transistor is suited for measuring charge carrier mobilities of an organic semiconductor. Various transistor architectures are available. In this work, transistors with a bottom gate/bottom contact architecture are used and the schematic setup is shown in Figure 1.14a. The transistor consists of a source, a drain and a gate electrode. Here, the gate electrode is separated by a dielectric material while the source and drain electrodes contact the semiconductor. The semiconductor is deposited on top of the device and its charge carrier mobility is measured between the source and drain electrodes creating a comparable narrow channel. This channel is defined in terms of width W (1-20 μm) and length L (1-20 μm). Further common transistor architectures are bottom gate/top contact, top gate/bottom contact and top gate/top contact. The major advantage of the bottom gate/bottom contact architecture is that the semiconductor can be applied on pre-prepared substrates and no further post-deposition of electrodes is necessary. OFET devices used in this work consist of gold source and drain electrodes. Highly doped silicon is used as gate electrode and simultaneously functions as substrate, which is coated by silicon dioxide as dielectric.^[126]

In general, a transistor operates as a capacitor. When applying a voltage at the gate electrode V_G , charge carriers accumulate at the interface of the semiconductor and the dielectric material as shown in Figure 1.14b in red. Depending on the sign of the gate voltage, holes or electrons can be accumulated. The gate voltage needs to exceed a certain threshold V_{th} to first of all inject charges and fill up any traps before a current can be detected. Therefore, the gate voltage minus the threshold voltage is called the effective voltage. When simultaneously to the gate voltage a voltage between source and drain V_{ds} is applied, current can flow from source to drain. The drain current I_{ds} linearly depends on the drain voltage V_{ds} by Ohm's law as long as the effective voltage exceeds V_{ds} (linear regime). By reaching the effective voltage, the charge carrier density is

depleted close to the drain electrode and the transistor is pinched off (see Figure 1.14b ii)). The resulting gradient leads to a saturation of the drain current. Upon further increase of V_{ds} , the pinch-off point is shifted towards the source and the charges are pulled over the depletion zone by the electric field. The transistor operates in the saturation regime.^[123–125]

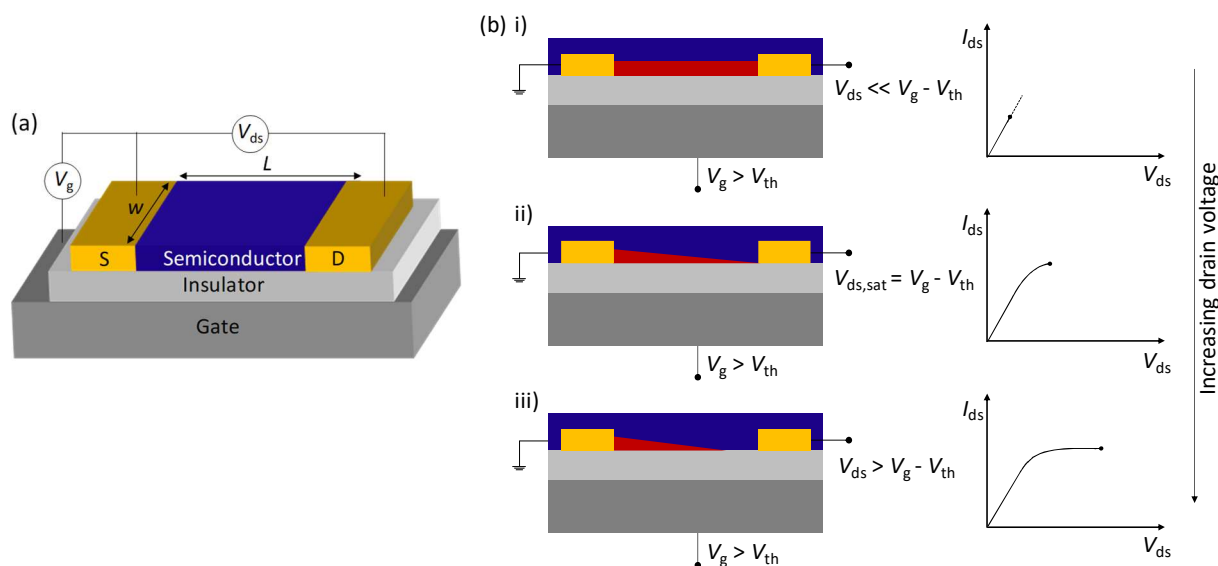


Figure 1.14. (a) Schematic setup of a bottom gate/bottom contact organic field effect transistor. (b) Operation principle of an OFET at an applied gate voltage V_G and drain voltage V_{ds} . The red layer presents the charge carrier density. Impact on the current-voltage characteristic by increasing the drain voltage: i) linear regime, ii) start of saturation regime at pinch-off point and iii) saturation regime. Adapted from^[123,125].

The measurement of the drain current in dependency on the drain voltage at a fixed gate voltage is repeated for several gate voltages and is called output characteristic (Figure 1.15a). Determination of the charge carrier mobility is possible in the linear as well as the saturation regime. Therefore, the drain current is measured under variation of the gate voltage at a fixed drain voltage, which is called transfer characteristic. For the mobility determination in the saturation regime, the drain voltage needs to lie in this region. The saturation drain current is then defined as:

$$I_{ds,sat} = \frac{W}{2L} \mu_{sat} C_i (V_g - V_{th})^2 \quad (8)$$

An example for a transfer characteristic is shown in Figure 1.15. From the square root plot of the drain current, the charge carrier mobility can be calculated using the slope of the graph (see Figure 1.15b red line):

$$\mu_{sat} = \left(\frac{\partial \sqrt{I_{ds}}}{\partial V_g} \right)^2 \cdot \frac{2L}{WC_i} \quad (9)$$

Additionally, the threshold voltage can be determined from the linear plot. It is obtained from the intercept with the x-axis. A further parameter for the characterization of a transistor is the on-off ratio, which is defined as the difference in drain current between the “off” state (no current flows) and the “on” state (maximum current).^[123–125]

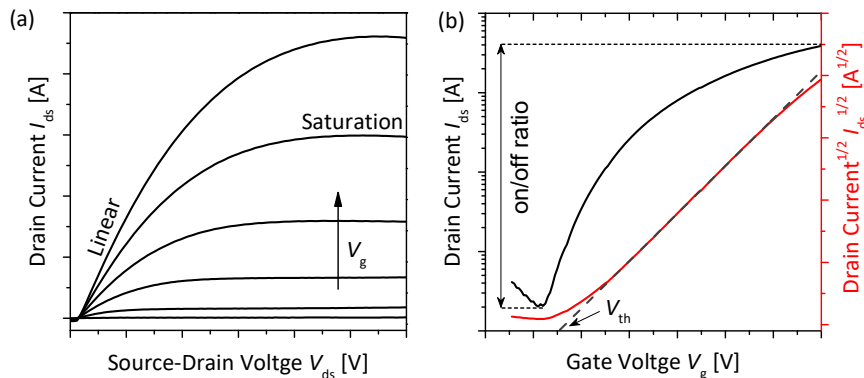


Figure 1.15. Representative current-voltage characteristics. (a) Output characteristics and (b) transfer characteristic in the saturation regime together with the linear fit. The on/off ratio and threshold voltage are displayed in the graph. Adapted from^[125].

The electric current in a device depends on the efficiency of charge injection as well as on the ability of the material to transport charges. Therefore, the electrodes have a strong impact on charge injection and should be selected according to the material’s HOMO level regarding hole transport or LUMO level in terms of electron transport. For an acceptable transistor performance, the material should be as pure as possible. Oxygen as well as water traces should be diminished to avoid trap sites, especially for n-channel operation.^[127] As mentioned above, the charge transport measured in an OFET takes place only at the semiconductor/dielectric interface. Therefore, the surface modification of the dielectric by a self-assembled monolayer (SAM) is often achieved by silanes prior to deposition of the semiconductor and is considered a crucial step to avoid traps and leakage current.^[128] Otherwise, alternative gate insulators can be used to improve the performance, which is of course also depending on the device architecture.^[129] Additionally, the morphology, orientation as well as crystallinity of the semiconductor influences the performance of OFETs and is discussed in the following chapter.

1.5 Thin film alignment of semiconducting polymers

Due to the conjugated, aromatic backbone of semiconducting polymers, the majority of these materials exhibits some level of crystallinity. In thin films, intermolecular interactions between the polymer chains by alkyl stacking and π - π stacking can be observed. So formed stacks can assemble on the substrate in three different ways, which are shown schematically in Figure 1.16. In the edge-on conformation, the polymer backbones orient perpendicular to the substrate surface. An alignment parallel to the substrate meaning the conjugated π -systems lie flat on the substrate, is called face-on orientation. A third, rather rarely observed alignment is end-on, where the polymer chains are standing upright on the substrate.^[130–132]

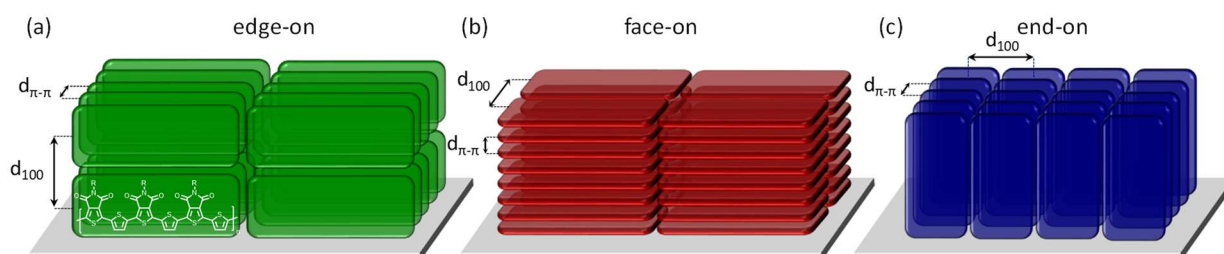


Figure 1.16. Schematic illustration of the three possible thin film alignments: (a) edge-on, (b) face-on and (c) end-on. The π - π stacking distances $d_{\pi-\pi}$ and lamellar stacking distances d_{100} are marked.

The different thin film alignments affect the charge carrier mobilities of the material depending on the device geometry, which can be either a diode or transistor configuration. In general, three different charge transport pathways are possible in polymer stacks, which are schematically illustrated in Figure 1.17. The most effective charge transport takes place along the polymer backbone (1), which is called intrachain transport. For interchain transport, charge transport from chain to chain via the π - π stacking (2) or alkyl stacking (3) is necessary. Along the π - π direction, charge transport takes place moderately, whereas long distances need to be travelled across the alkyl stacking, which makes the charge transport less effective.^[133] When correlating the thin film alignment to the different device geometries, it becomes clear that edge-on alignment is favorable for charge transport in OFETs,^[133] while face-on alignment is rather suited for diodes^[134]. In a diode configuration, the end-on alignment can achieve very high charge carrier mobilities, which is for example presented in the literature for P3HT.^[135] However, this alignment is only rarely observed without structural modification of the substrate. Therefore, only face-on and edge-on alignment are considered in the following. The correlation between crystallite orientation and performance in organic electronic devices is repeatedly shown

throughout the literature.^[136–139] Control over the thin film alignment can not only be achieved by variation of the molecular structure, but also by adjusting the processing conditions.^[140–143]

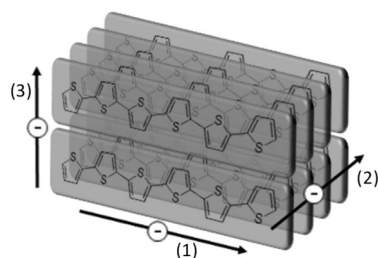


Figure 1.17. Possible charge transport pathways: (1) Intrachain transport, (2) interchain transport along π - π stacking and (3) alkyl stacking direction.

For probing the crystallinity as well as the molecular packing structure and orientation of crystalline domains in the bulk, X-ray diffraction measurements are the method of choice. Due to the low scattering strength of the polymers, more intensive synchrotron radiation is necessary. Since the polymers are analyzed in form of thin films, the sample scattering volume is small. Therefore, grazing incidence wide angle X-ray scattering (GIWAXS) is applied and a schematic setup is shown in Figure 1.18. Small incident angles α_i of 0.05° - 0.35° are applied in order to enhance the sample scattering volume. By grazing the sample under different incident angles, the penetration depth of the X-ray beam is varied and by that, information of the alignment at different depths can be gained. At very small angles only the surface of the sample is probed and by sequentially increasing the angle, deeper-lying slices of the sample can be scanned. Highest scattering intensities are achieved at the critical angle α_c . The scattering patterns are recorded on a 2D detector, which is placed about 10 cm behind the sample, and expressed as a function of the scattering vector Q . Here, Q_{xy} describes the scattering vector along the sample surface (in-plane) and Q_z perpendicular to the sample surface (out-of-plane).

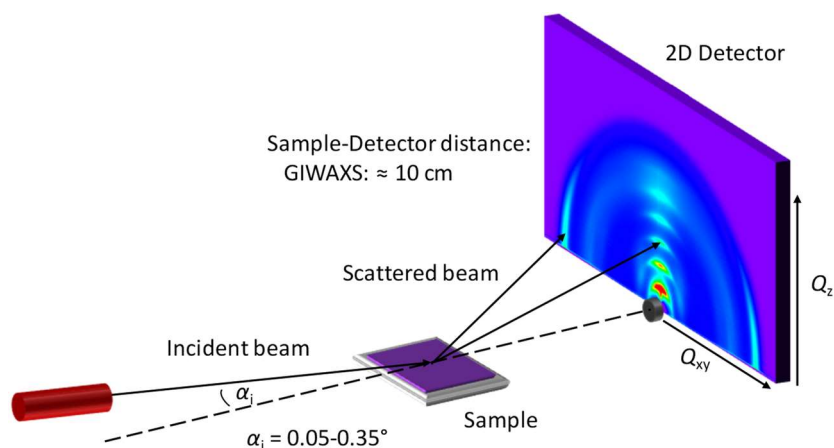


Figure 1.18. Schematic setup of a grazing incidence wide angle X-ray scattering (GIWAXS) experiment. The incident beam grazes the sample deposited on a silicon substrate in angles α_i . By a 2D detector, the scattering intensities in the out-of-plane (Q_z) and in-plane (Q_{xy}) direction is collected. The typical sample-detector distance is given.

Edge-on and face-on alignment can be distinguished based on the scattering patterns, which are summarized in Figure 1.19. In the case of edge-on alignment, the π - π stacking refraction peak is observed in-plane and the lamellar stacking peaks out-of-plane (Figure 1.19a). When the polymer backbone is oriented in-plane (face-on), the alkyl stacking peak appears in xy-direction and the π - π stacking in z-direction (Figure 1.19b). A large degree of disorder leads to equal intensity over all polar angles and continuous rings are observed (Figure 1.19c). In many samples, the different orientation motifs coexist, and mixed scattering patterns are observed (Figure 1.19d).

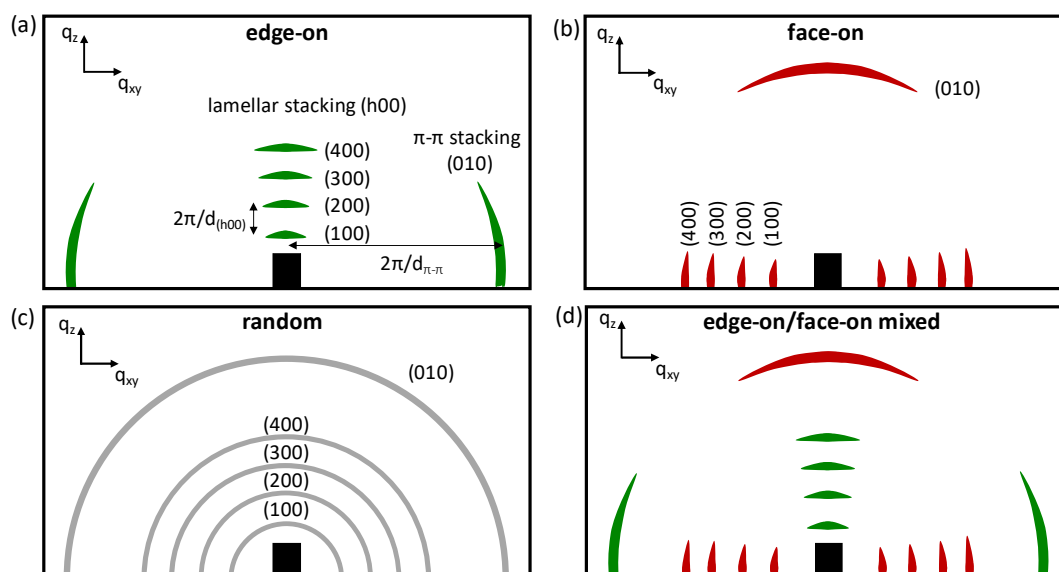


Figure 1.19. Model 2D scattering patterns received by GIWAXS measurements for (a) edge-on alignment, (b) face-on alignment, (c) random orientation and (d) mixture of edge-on and face-on orientation. The lamellar stacking peaks (h00) and π - π stacking peak (010) is indicated. Adapted from^[144].

From the 2D scattering images, line profiles along xy- ($\chi = 90^\circ$) and z-direction ($\chi = 0^\circ$) are generated for in-depth analysis. From the peak position, the Bragg spacing d can be calculated as:

$$d = \frac{2\pi}{q} \quad (10)$$

The full width at half maximum (FWHM) of the scattering peaks provides information about the sample's microstructure. Not only the crystallite size affects the width of Bragg reflections, which is described by the Scherrer equation. Additionally, the crystallite shape, shape distribution and distortion of the crystal structure influence the FWHM. The most important distortions of the crystal lattice are microstrain and dislocations. Using the FWHM the coherence length can be calculated, which gives a rough indication of the distance of order.^[145]

$$\xi = \frac{2\pi}{FWHM} \quad (11)$$

In order to quantify the degree of thin film alignment, the Herman's Orientation Parameter S can be calculated.^[146,147] Therefore, the first order alkyl stacking peak (100) is analyzed regarding its intensity distribution over all polar angles χ . For every incident angle, the respective line cut of the scattering intensity depended on the polar angles χ is plotted. From these plots, the molecular orientation parameter f_{\perp} can be calculated as:

$$f_{\perp} = \frac{\int_0^{\pi/2} I(\chi) \cos^2 \chi \sin \chi d\chi}{\int_0^{\pi/2} I(\chi) \sin \chi d\chi} \quad (12)$$

where $I(\chi)$ is the total scattered intensity and $\sin \chi$ is a geometric intensity correction factor.

The S parameter is now calculated as follows:

$$S = \frac{1}{2}(3f_{\perp} - 1) \quad (13)$$

Thereby, values between -0.5 and 1 are obtained. $S = 1$ corresponds to perfect edge-on orientation, whereas $S = -0.5$ represents 100% face-on. If the S parameter amounts a value of 0, either no orientation or a 1:1 mixture of edge-on and face-on orientation is present. Furthermore, information about the different layers of the bulk are examined by variation of the incident angle. Therefore, the S -Parameter can be plotted dependent on the grazing angle as schematically illustrated in Figure 1.20.

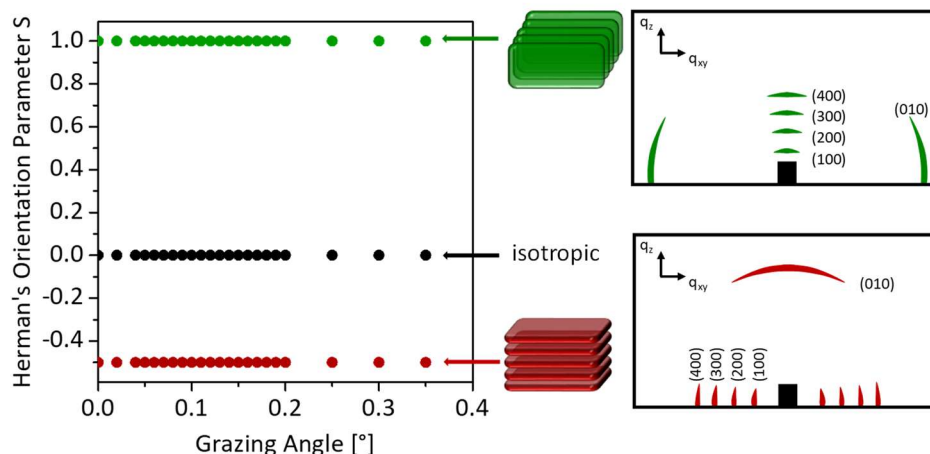


Figure 1.20. Schematic plot of the Herman's Orientation Parameter S vs. grazing angle for a perfectly edge-on ($S = 1$) and face-on ($S = -0.5$) orientation as well as for an isotropic orientation ($S = 0$).

1.6 Copolymers based on thieno[3,4-*c*]pyrrole-4,6-dione (TPD)

For the design of donor-acceptor polymers, thieno[3,4-*c*]pyrrole-4,6-dione (TPD) represents an interesting acceptor unit due to its high electron-deficient properties. Moreover, copolymers containing TPD have been proven to show high photostability, which is crucial in long-term applications.^[148] Its rigidity as well as planarity favors intermolecular interactions allowing for good packing in the solid state. The planarity of the TPD moiety was studied for TPD dimers. By the X-ray crystal structure an anti-coplanar confirmation could be confirmed involving a short O-S non-bonded distance of 2.9 Å, which is much smaller than the sum of van der Waals radii.^[149] To the TPD moiety, solubilizing side chains can easily be attached providing high solubility of the polymers. The majority of polymers are synthesized by Stille, Suzuki or Direct Heteroarylation polycondensation. For that, the TPD moiety is often halogen functionalized, because the corresponding tin or boron derivatives are not accessible. In the following, the synthesis of the TPD monomer is given followed by relevant examples for TPD polymers from the literature. A detailed overview of TPD based polymers can be found in two reviews.^[150,151]

The first report about unsubstituted thieno[3,4-*c*]pyrrole-4,6-dione is dated back to 1954.^[152] In 1970, BASF patented a series of TPD based compounds for the dyeing of polyesters.^[153] For the synthesis of TPD several approaches are available starting from 3,4-thiophene dicarboxylic acid as shown in Figure 1.21. This starting reagent is either commercially available or can be synthesized from the corresponding 3,4-dibromo derivative via 3,4-dicyanothiophene.^[154] An alternative pathway for the synthesis of 3,4-thiophene dicarboxylic acid is published by Leclerc

and coworkers starting from methyl 2-oxopropanoate and ethyl cyanoacetate. In combination with sulfur, the amino-thiophene derivative is formed in a Gewald reaction.^[155] Finally, the unsubstituted compound can be achieved by a Sandmeyer-type reaction.^[156] The most widespread route for the synthesis of the TPD moiety is shown in Figure 1.21. on the top right.^[154,157,158] Formation of the thiophene anhydride is followed by a condensation reaction with an alkyl amine. For the ring-closure reaction, thionyl chloride is required yielding the TPD moiety. The corresponding bromo compound can be obtained by bromination with NBS. Recently, a new synthetic route with enhanced atom economy and mild conditions allowing the incorporation of functionalized side chains was published (Figure 1.21. on the bottom right).^[159] In the first step, the imide is directly formed from 3,4-thiophene dicarboxylic acid, which could be brominated under mild reaction conditions. Various side chains carrying different functionalities could be successfully introduced. By this approach the number of synthetic steps could be reduced and hazardous and toxic reagents are avoided.^[159]

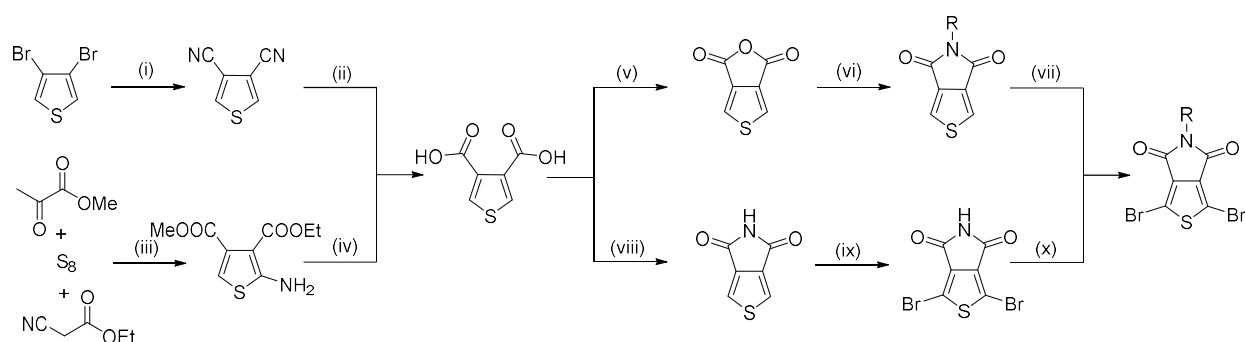


Figure 1.21. Synthesis of the bromo-TPD monomer via different routes. Reaction conditions: (i) CuCN; (ii) KOH; (iii) Et₃N, DMF; (iv) *t*-BuONO, THF, Δ; or: 2M NaOH, Δ; (v) Ac₂O, Δ; (vi) RNH₂, toluene, Δ; or: SOCl₂, Δ (vii) NBS, TFA/H₂SO₄; (viii) 28% NH₃/H₂O, 260 °C; (ix) NBS, H₂SO₄; (x) R-X, K₂CO₃, DMF.

The first TPD homopolymer was prepared by Pomerantz via the Ullmann approach.^[158] A similar polymer was synthesized by Nielsen and Bjornholm.^[154] However, the degree of polymerization was limited to about ten repeating units due to the poor solubility of the linear side chains of the TPD moiety. In order to maintain solubility, Leclerc introduced long, branched alkyl chains to the TPD moiety and prepared homopolymers via DHAP.^[156] High molecular weights were achieved and the influence of the side-chain on optical properties and solid-state packing were studied showing that a balance of solubility and solid-state packing is crucial.

Zhang and Tour published the first example of a D-A copolymer in 1997, which was obtained via Stille polymerization of dibromo-TPD and distannyl-diaminothiophene.^[157,160] The interest in the TPD acceptor unit rose again in 2010, when Leclerc and coworkers combined TPD with

benzodithiophene as a donor unit (see Figure 1.22. PTPDBDT).^[161] Almost at the same time this donor-acceptor polymer was published by the groups of Jen,^[162] Xie^[163] and Fréchet^[164]. Whereas Leclerc achieved a PCE of 5.5% in combination with PCBM,^[161] Fréchet was able to reach a higher efficiency of 6.8%^[164]. Further improvement was realized by processing the blend together with co-additives to control the active layer morphology reaching a PCE of 7.1%.^[165] By intense side chain engineering of both units, a highest PCE of 8.5% could be obtained.^[166] These promising results proved that TPD is a suitable acceptor unit in D-A copolymers for the application as donor material in BHJ solar cells. In order to push the efficiencies further, other donor units were incorporated such as cyclopentadithiophene (CPDT) reaching efficiencies of 6.4%.^[167] By substitution of the bridging carbon with silicon (dithienosilole, DTS) or germanium (dithienogermole, DTG) the efficiencies could be improved to 7.3%^[168] and 8.5%,^[169] respectively. The most common donor unit is thiophene and therefore, corresponding copolymers based on TPD were widely studied including thiophene, bi-, ter- and quaterthiophene derivatives.^[170,171] From these series of copolymers, bi- as well as terthiophenes exhibit best PCEs of 7.3%^[172] and 7.9%,^[173] respectively. Additionally, high hole mobilities in OFETs were achieved, which are for both polymers in the range of $0.2 \text{ cm}^2 \text{ V}^{-1} \text{ s}^{-1}$.^[170] By incorporating vinyl linkers in TPD copolymers with bithiophene (PTPDVT), even higher hole mobilities of $0.4 \text{ cm}^2 \text{ V}^{-1} \text{ s}^{-1}$ were reached.^[174] Best performances in transistors as well as organic solar cells were achieved by incorporating thieno[3,4-c]thiophene in the polymer backbone. Using PtTPDTT hole mobilities of $1.3 \text{ cm}^2 \text{ V}^{-1} \text{ s}^{-1}$ could be achieved.^[175] Power conversion efficiencies exceeding 9% have been realized with the donor polymers PttTPDT and Pt2TPDTT in combination with PCBM^[176,177]. Recently, the benchmark of 10% was crossed with the polymer PttTPDBDTT in combination with a small molecule acceptor.^[178] Additionally, D-A copolymers based on TPD were efficiently applied as donor material in all-polymer solar cells^[179,180]

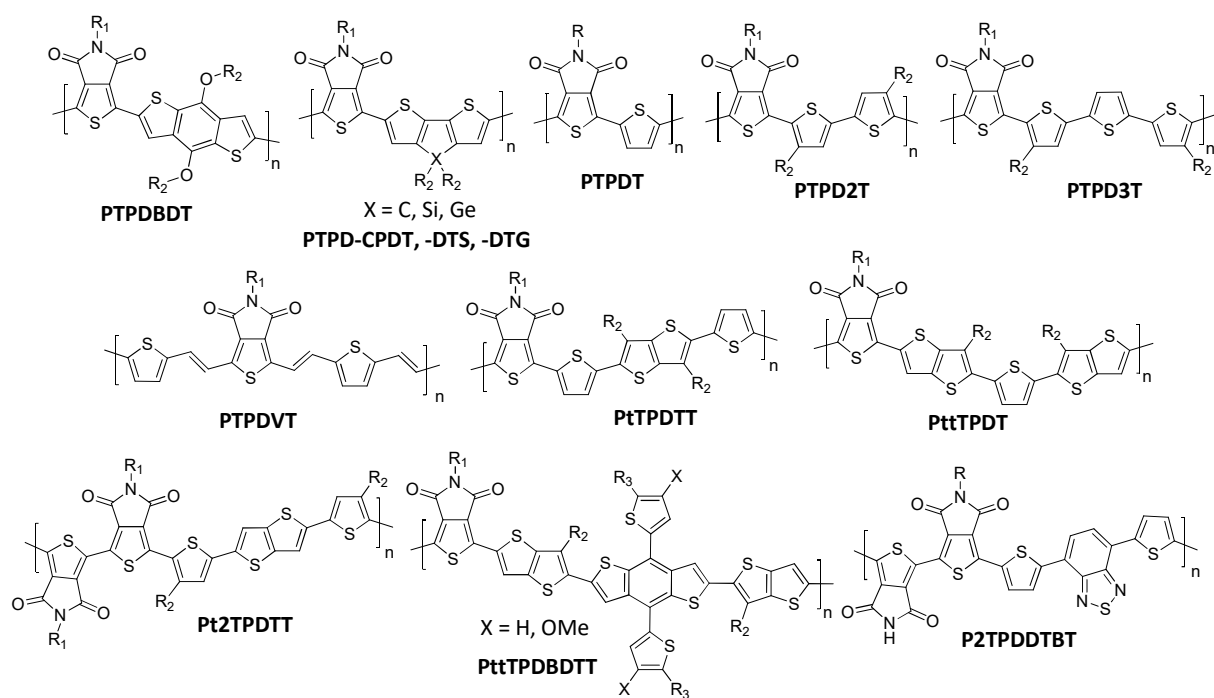


Figure 1.22. Examples for TPD based copolymers showing p-type behavior as well as ambipolar charge transport.

Regarding ambipolar charge transport and electron transport only a few examples of TPD based copolymers are known to date although the TPD moiety is strongly electron-deficient. In OFET devices, polymer P2TPDDBT showed highly balanced ambipolar transistor behavior with an electron mobility of $1.02 \text{ cm}^2 \text{ V}^{-1} \text{ s}^{-1}$ and a hole mobility of $0.33 \text{ cm}^2 \text{ V}^{-1} \text{ s}^{-1}$.^[181] Ambipolar transistor behavior was also reported for a TPD based copolymer carrying thiophene (PTPDT). However, the charge carrier mobilities of these devices were only in the range of 10^{-3} - $10^{-4} \text{ cm}^2 \text{ V}^{-1} \text{ s}^{-1}$.^[170] By combination of TPD with a second acceptor unit, isoindigo (PTPDIIG), unipolar n-type transistor behavior could be achieved with maximal electron mobilities of $0.01 \text{ cm}^2 \text{ V}^{-1} \text{ s}^{-1}$.^[182,183] Recently, the first polymer based on TPD was applied as an acceptor material in all-polymer solar cells followed by the publication of two additional polymers. As shown in Figure 1.23, all these polymers carry besides TPD, difluorothiophene as comonomer and feature moderate efficiencies up to 4.8% in combination with appropriate donor polymers.^[184,185]

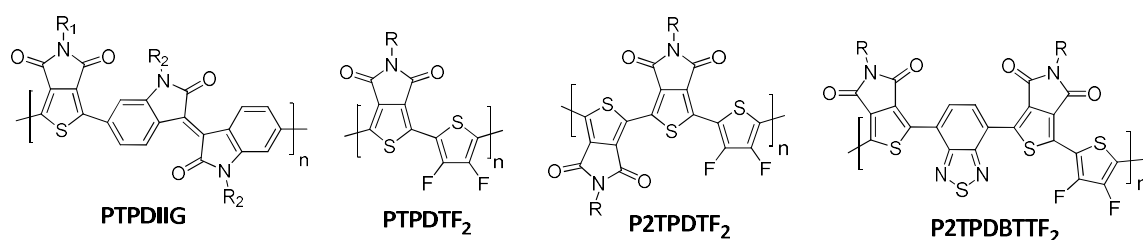


Figure 1.23. Copolymers based on TPD showing n-type behavior.

1.7 References

- [1] <https://www.bmwi.de/Redaktion/EN/Dossier/renewable-energy.html> (accessed on 20.09.2017).
- [2] K. Yoshikawa, H. Kawasaki, W. Yoshida, T. Irie, K. Konishi, K. Nakano, T. Uto, D. Adachi, M. Kanematsu, H. Uzu, K. Yamamoto, *Nat. Energy* **2017**, *2*, 17032.
- [3] Fraunhofer Institute for Solar Energy Systems, ISE, *Photovoltaics Report 2017*, <https://www.ise.fraunhofer.de/content/dam/ise/de/documents/publications/studies/Photovoltaics-Report.pdf> (accessed on 20.09.2017).
- [4] W. Zhao, S. Li, H. Yao, S. Zhang, Y. Zhang, B. Yang, J. Hou, *J. Am. Chem. Soc.* **2017**, *139*, 7148.
- [5] F. C. Krebs, N. Espinosa, M. Hösel, R. R. Søndergaard, M. Jørgensen, *Adv. Mater.* **2014**, *26*, 29.
- [6] <http://www.opvius.com/en/applications.html> (accessed on 20.09.2017).
- [7] <http://www.heliatek.com/de/presse/downloads> (accessed on 20.09.2017).
- [8] <http://www.aktuelle-wochenschau.de/main-navi/archiv/chemie-und-licht-2015/kw21-materialien-der-organischen-photovoltaik-auf-der-expo-2015-in-mailand.html> (accessed on 20.09.2017).
- [9] C. W. Tang, *Appl. Phys. Lett.* **1986**, *48*, 183.
- [10] N. S. Sariciftci, D. Braun, C. Zhang, V. I. Srdanov, A. J. Heeger, G. Stucky, F. Wudl, *Appl. Phys. Lett.* **1993**, *62*, 585.
- [11] G. Yu, J. Gao, J. C. Hummelen, F. Wudl, A. J. Heeger, *Science* **1995**, *270*, 1789.
- [12] P. D. Topham, A. J. Parnell, R. C. Hiorns, *J. Polym. Sci. B Polym. Phys.* **2011**, *49*, 1131.
- [13] B. A. Gregg, M. C. Hanna, *J. Appl. Phys.* **2003**, *93*, 3605.
- [14] M. Knupfer, *Appl. Phys. A* **2003**, *77*, 623.
- [15] S. Cook, A. Furube, R. Katoh, L. Han, *Chem. Phys. Lett.* **2009**, *478*, 33.
- [16] J. J. M. Halls, K. Pichler, R. H. Friend, S. C. Moratti, A. B. Holmes, *Appl. Phys. Lett.* **1996**, *68*, 3120.
- [17] A. J. Lewis, A. Ruseckas, O. Gaudin, G. R. Webster, P. L. Burn, I. Samuel, *Org. Electron.* **2006**, *7*, 452.
- [18] P. E. Shaw, A. Ruseckas, I. D. W. Samuel, *Adv. Mater.* **2008**, *20*, 3516.
- [19] A. J. Ward, A. Ruseckas, I. D. W. Samuel, *J. Phys. Chem. C* **2012**, *116*, 23931.
- [20] J.-L. Brédas, J. E. Norton, J. Cornil, V. Coropceanu, *Acc. Chem. Res.* **2009**, *42*, 1691.

- [21] T. M. Clarke, J. R. Durrant, *Chem. Rev.* **2010**, *110*, 6736.
- [22] C. Deibel, V. Dyakonov, *Rep. Prog. Phys.* **2010**, *73*, 96401.
- [23] S. D. Dimitrov, J. R. Durrant, *Chem. Mater.* **2014**, *26*, 616.
- [24] B. M. Savoie, N. E. Jackson, T. J. Marks, M. A. Ratner, *Phys. Chem. Chem. Phys.* **2013**, *15*, 4538.
- [25] J. J. M. Halls, J. Cornil, D. A. dos Santos, R. Silbey, D.-H. Hwang, A. B. Holmes, J. L. Bredas, R. H. Friend, *Phys. Rev. B* **1999**, *60*, 5721.
- [26] M. C. Scharber, D. Mühlbacher, M. Koppe, P. Denk, C. Waldauf, A. J. Heeger, C. J. Brabec, *Adv. Mater.* **2006**, *18*, 789.
- [27] J.-L. Brédas, D. Beljonne, V. Coropceanu, J. Cornil, *Chem. Rev.* **2004**, *104*, 4971.
- [28] J.-L. Bredas, *Mater. Horiz.* **2014**, *1*, 17.
- [29] C. M. Proctor, M. Kuik, T.-Q. Nguyen, *Prog. Polym. Sci.* **2013**, *38*, 1941.
- [30] J. D. Servaites, M. A. Ratner, T. J. Marks, *Energy Environ. Sci.* **2011**, *4*, 4410.
- [31] N. C. Cates, R. Gysel, J. E. P. Dahl, A. Sellinger, M. D. McGehee, *Chem. Mater.* **2010**, *22*, 3543.
- [32] S. E. Shaheen, C. J. Brabec, N. S. Sariciftci, F. Padinger, T. Fromherz, J. C. Hummelen, *Appl. Phys. Lett.* **2001**, *78*, 841.
- [33] H.-C. Liao, C.-C. Ho, C.-Y. Chang, M.-H. Jao, S. B. Darling, W.-F. Su, *Mater. Today* **2013**, *16*, 326.
- [34] H. Letheby, *J. Chem. Soc.* **1862**, *15*, 161.
- [35] B. A. Bolto, R. McNeill, D. E. Weiss, *Aust. J. Chem.* **1963**, *16*, 1090.
- [36] T. Ito, H. Shirakawa, S. Ikeda, *J. Polym. Sci. Polym. Chem. Ed.* **1974**, *12*, 11.
- [37] H. Shirakawa, E. J. Louis, A. G. MacDiarmid, C. K. Chiang, A. J. Heeger, *J. Chem. Soc., Chem. Commun.* **1977**.
- [38] C. K. Chiang, C. R. Fincher, Y. W. Park, A. J. Heeger, H. Shirakawa, E. J. Louis, S. C. Gau, A. G. MacDiarmid, *Phys. Rev. Lett.* **1977**, *39*, 1098.
- [39] C. K. Chiang, M. A. Druy, S. C. Gau, A. J. Heeger, E. J. Louis, A. G. MacDiarmid, Y. W. Park, H. Shirakawa, *J. Am. Chem. Soc.* **1978**, *100*, 1013.
- [40] J. Roncali, *Macromol. Rapid Commun.* **2007**, *28*, 1761.
- [41] J. L. Brédas, A. J. Heeger, F. Wudl, *J. Chem. Phys.* **1986**, *85*, 4673.
- [42] J. Roncali, *Chem. Rev.* **1997**, *97*, 173.
- [43] H. van Mullekom, *Mater. Sci. Eng. R Rep.* **2001**, *32*, 1.

- [44] Y.-J. Cheng, S.-H. Yang, C.-S. Hsu, *Chem. Rev.* **2009**, *109*, 5868.
- [45] C. L. Chochos, S. A. Choulis, *Prog. Polym. Sci.* **2011**, *36*, 1326.
- [46] C. Winder, N. S. Sariciftci, *J. Mater. Chem.* **2004**, *14*, 1077.
- [47] E. E. Havinga, W. ten Hoeve, H. Wynberg, *Polym. Bull.* **1992**, *29*, 119.
- [48] Z. Zhang, J. Wang, *J. Mater. Chem.* **2012**, *22*, 4178.
- [49] H. Zhou, L. Yang, W. You, *Macromolecules* **2012**, *45*, 607.
- [50] T. Yamamoto, K. Sanechika, A. Yamamoto, *J. Polym. Sci. B Polym. Lett. Ed.* **1980**, *18*, 9.
- [51] J. W.-P. Lin, L. P. Dudek, *J. Polym. Sci. Polym. Chem. Ed.* **1980**, *18*, 2869.
- [52] R. D. McCullough, R. D. Lowe, M. Jayaraman, D. L. Anderson, *J. Org. Chem.* **1993**, *58*, 904.
- [53] T. A. Chen, R. D. Rieke, *J. Am. Chem. Soc.* **1992**, *114*, 10087.
- [54] H. Sirringhaus, P. J. Brown, R. H. Friend, M. M. Nielsen, K. Bechgaard, B. M. W. Langeveld-Voss, A. J. H. Spiering, R. A. J. Janssen, E. W. Meijer, P. Herwig, D. M. de Leeuw, *Nature* **1999**, *401*, 685.
- [55] M. T. Dang, L. Hirsch, G. Wantz, *Adv. Mater.* **2011**, *23*, 3597.
- [56] B. Kadem, A. Hassan, W. Cranton, *J Mater Sci. Mater. Electron.* **2016**, *27*, 7038.
- [57] G. Zhao, Y. He, Y. Li, *Adv. Mater.* **2010**, *22*, 4355.
- [58] F. Cheng, G. Fang, X. Fan, H. Huang, Q. Zheng, P. Qin, H. Lei, Y. Li, *Sol. Energy Materials and Sol. Cells* **2013**, *110*, 63.
- [59] X. Guo, M. Zhang, C. Cui, J. Hou, Y. Li, *ACS Appl. Mater. Interfaces* **2014**, *6*, 8190.
- [60] X. Guo, C. Cui, M. Zhang, L. Huo, Y. Huang, J. Hou, Y. Li, *Energy Environ. Sci.* **2012**, *5*, 7943.
- [61] J. W. Jung, J. W. Jo, E. H. Jung, W. H. Jo, *Organic Electronics* **2016**, *31*, 149.
- [62] J.-H. Kim, J. B. Park, I. H. Jung, A. C. Grimsdale, S. C. Yoon, H. Yang, D.-H. Hwang, *Energy Environ. Sci.* **2015**, *8*, 2352.
- [63] Z. He, B. Xiao, F. Liu, H. Wu, Y. Yang, S. Xiao, C. Wang, T. P. Russell, Y. Cao, *Nat. Photonics* **2015**, *9*, 174.
- [64] I. Kang, H.-J. Yun, D. S. Chung, S.-K. Kwon, Y.-H. Kim, *J. Am. Chem. Soc.* **2013**, *135*, 14896.
- [65] Y. Liu, J. Zhao, Z. Li, C. Mu, W. Ma, H. Hu, K. Jiang, H. Lin, H. Ade, H. Yan, *Nat. Commun.* **2014**, *5*, 5293.
- [66] R. S. Ashraf, I. Meager, M. Nikolka, M. Kirkus, M. Planells, B. C. Schroeder, S. Holliday, M. Hurhangee, C. B. Nielsen, H. Sirringhaus, I. McCulloch, *J. Am. Chem. Soc.* **2015**, *137*, 1314.
- [67] V. Vohra, K. Kawashima, T. Kakara, T. Koganezawa, I. Osaka, K. Takimiya, H. Murata, *Nat. Photonics* **2015**, *9*, 403.

- [68] J. C. Hummelen, B. W. Knight, F. LePeq, F. Wudl, J. Yao, C. L. Wilkins, *J. Org. Chem.* **1995**, *60*, 532.
- [69] M. M. Wienk, J. M. Kroon, W. J. H. Verhees, J. Knol, J. C. Hummelen, P. A. van Hal, R. A. J. Janssen, *Angew. Chem. Int. Ed.* **2003**, *42*, 3371.
- [70] Q. Xie, E. Perez-Cordero, L. Echegoyen, *J. Am. Chem. Soc.* **1992**, *114*, 3978.
- [71] N. S. Sariciftci, L. Smilowitz, A. J. Heeger, F. Wudl, *Science* **1992**, *258*, 1474.
- [72] P. H. Wöbkenberg, D. D. Bradley, D. Kronholm, J. C. Hummelen, D. M. de Leeuw, M. Cölle, T. D. Anthopoulos, *Synth. Met.* **2008**, *158*, 468.
- [73] N. C. Cates, R. Gysel, Z. Beiley, C. E. Miller, M. F. Toney, M. Heeney, I. McCulloch, M. D. McGehee, *Nano Lett.* **2009**, *9*, 4153.
- [74] N. D. Treat, M. A. Brady, G. Smith, M. F. Toney, E. J. Kramer, C. J. Hawker, M. L. Chabiny, *Adv. Energy Mater.* **2011**, *1*, 82.
- [75] B. A. Collins, E. Gann, L. Guignard, X. He, C. R. McNeill, H. Ade, *J. Phys. Chem. Lett.* **2010**, *1*, 3160.
- [76] C. B. Nielsen, S. Holliday, H.-Y. Chen, S. J. Cryer, I. McCulloch, *Acc. Chem. Res.* **2015**, *48*, 2803.
- [77] D. M. Stoltzfus, J. E. Donaghey, A. Armin, P. E. Shaw, P. L. Burn, P. Meredith, *Chem. Rev.* **2016**, *116*, 12920.
- [78] W. Chen, Q. Zhang, *J. Mater. Chem. C* **2017**, *5*, 1275.
- [79] D. Meng, D. Sun, C. Zhong, T. Liu, B. Fan, L. Huo, Y. Li, W. Jiang, H. Choi, T. Kim, J. Y. Kim, Y. Sun, Z. Wang, A. J. Heeger, *J. Am. Chem. Soc.* **2016**, *138*, 375.
- [80] H. Bin, L. Gao, Z.-G. Zhang, Y. Yang, Y. Zhang, C. Zhang, S. Chen, L. Xue, C. Yang, M. Xiao, Y. Li, *Nat. Commun.* **2016**, *7*, 13651.
- [81] R. H. Friend, M. Granström, K. Petritsch, A. C. Arias, A. Lux, M. R. Andersson, *Nature* **1998**, *395*, 257.
- [82] T. W. Holcombe, J. E. Norton, J. Rivnay, C. H. Woo, L. Goris, C. Piliago, G. Griffini, A. Sellinger, J.-L. Brédas, A. Salleo, J. M. J. Fréchet, *J. Am. Chem. Soc.* **2011**, *133*, 12106.
- [83] T. W. Holcombe, C. H. Woo, D. F. J. Kavulak, B. C. Thompson, J. M. J. Fréchet, *J. Am. Chem. Soc.* **2009**, *131*, 14160.
- [84] L. Gao, Z.-G. Zhang, L. Xue, J. Min, J. Zhang, Z. Wei, Y. Li, *Adv. Mater.* **2016**, *28*, 1884.
- [85] H. Benten, D. Mori, H. Ohkita, S. Ito, *J. Mater. Chem. A* **2016**, *4*, 5340.
- [86] H. Kang, W. Lee, J. Oh, T. Kim, C. Lee, B. J. Kim, *Acc. Chem. Res.* **2016**, *49*, 2424.

- [87] "The Nobel Prize in Chemistry 2010". Nobelprize.org. Nobel Media AB 2014. Web. 27 Jun 2017. <http://www.nobelprize.org/nobel_prizes/chemistry/laureates/2010/>.
- [88] A. Suzuki, *Angew. Chem. Int. Ed.* **2011**, *50*, 6722.
- [89] J. K. Stille, *Angew. Chem. Int. Ed.* **1986**, *25*, 508.
- [90] N. Miyaura, A. Suzuki, *J. Chem. Soc., Chem. Commun.* **1979**.
- [91] M. Lafrance, K. Fagnou, *J. Am. Chem. Soc.* **2006**, *128*, 16496.
- [92] K. Sonogashira, Y. Tohda, N. Hagihara, *Tetrahedron Lett.* **1975**, *16*, 4467.
- [93] R. F. Heck, J. P. Nolley, *J. Org. Chem.* **1972**, *37*, 2320.
- [94] T. Yamamoto, A. Morita, Y. Miyazaki, T. Maruyama, H. Wakayama, Z. H. Zhou, Y. Nakamura, T. Kanbara, S. Sasaki, K. Kubota, *Macromolecules* **1992**, *25*, 1214.
- [95] F. Huang, H.-L. Yip, Y. Cao (Eds.), *Polymer photovoltaics: Materials, physics, and device engineering*, Royal Society of Chemistry, Cambridge **2016**.
- [96] A. E. Rudenko, B. C. Thompson, *J. Polym. Sci. Part A: Polym. Chem.* **2015**, *53*, 135.
- [97] B. Carsten, F. He, H. J. Son, T. Xu, L. Yu, *Chem. Rev.* **2011**, *111*, 1493.
- [98] J. Sakamoto, M. Rehahn, G. Wegner, A. D. Schlüter, *Macromol. Rapid Commun.* **2009**, *30*, 653.
- [99] L. G. Mercier, M. Leclerc, *Acc. Chem. Res.* **2013**, *46*, 1597.
- [100] A. Facchetti, L. Vaccaro, A. Marrocchi, *Angew. Chem. Int. Ed.* **2012**, *51*, 3520.
- [101] Z. Bao, W. Chan, L. Yu, *Chem. Mater.* **1993**, *5*, 2.
- [102] Z. Bao, W. K. Chan, L. Yu, *J. Am. Chem. Soc.* **1995**, *117*, 12426.
- [103] P. Espinet, A. M. Echavarren, *Angew. Chem. Int. Ed.* **2004**, *43*, 4704.
- [104] K. Tamao, K. Sumitani, M. Kumada, *J. Am. Chem. Soc.* **1972**, *94*, 4374.
- [105] K. Tamao, S. Kodama, I. Nakajima, M. Kumada, A. Minato, K. Suzuki, *Tetrahedron* **1982**, *38*, 3347.
- [106] E. Negishi, *Acc. Chem. Res.* **2002**, *15*, 340.
- [107] R. D. McCullough, S. P. Williams, S. Tristram-Nagle, M. Jayaraman, P. C. Ewbank, L. Miller, *Synth. Met.* **1995**, *69*, 279.
- [108] T.-A. Chen, X. Wu, R. D. Rieke, *J. Am. Chem. Soc.* **1995**, *117*, 233.
- [109] R. S. Loewe, S. M. Khersonsky, R. D. McCullough, *Adv. Mater.* **1999**, *11*, 250.
- [110] E. E. Sheina, J. Liu, M. C. Iovu, D. W. Laird, R. D. McCullough, *Macromolecules* **2004**, *37*, 3526.
- [111] A. Yokoyama, R. Miyakoshi, T. Yokozawa, *Macromolecules* **2004**, *37*, 1169.

- [112] I. Osaka, R. D. McCullough, *Acc. Chem. Res.* **2008**, *41*, 1202.
- [113] R. Miyakoshi, K. Shimono, A. Yokoyama, T. Yokozawa, *J. Am. Chem. Soc.* **2006**, *128*, 16012.
- [114] A. Yokoyama, H. Suzuki, Y. Kubota, K. Ohuchi, H. Higashimura, T. Yokozawa, *J. Am. Chem. Soc.* **2007**, *129*, 7236.
- [115] M. C. Stefan, A. E. Javier, I. Osaka, R. D. McCullough, *Macromolecules* **2009**, *42*, 30.
- [116] R. Grisorio, G. P. Suranna, *Polym. Chem.* **2015**, *6*, 7781.
- [117] V. Coropceanu, J. Cornil, D. A. da Silva Filho, Y. Olivier, R. Silbey, J.-L. Brédas, *Chem. Rev.* **2007**, *107*, 926.
- [118] H. Bässler, *phys. stat. sol. (b)* **1993**, *175*, 15.
- [119] F. Laquai, G. Wegner, H. Bässler, *Philosophical transactions. Series A, Mathematical, physical, and engineering sciences* **2007**, *365*, 1473.
- [120] D. Hertel, H. Bässler, U. Scherf, H. H. Hörhold, *J. Chem. Phys.* **1999**, *110*, 9214.
- [121] J. C. Blakesley, F. A. Castro, W. Kylberg, G. F. Dibb, C. Arantes, R. Valaski, M. Cremona, J. S. Kim, J.-S. Kim, *Organic Electronics* **2014**, *15*, 1263.
- [122] C. Tanase, E. J. Meijer, P. W. M. Blom, D. M. de Leeuw, *Phys. Rev. Lett.* **2003**, *91*, 216601.
- [123] C. R. Newman, C. D. Frisbie, D. A. da Silva Filho, J.-L. Brédas, P. C. Ewbank, K. R. Mann, *Chem. Mater.* **2004**, *16*, 4436.
- [124] A. Köhler, H. Bässler, *Electronic processes in organic semiconductors: An introduction*, Wiley-VCH Verlag GmbH & Co, Weinheim **2015**.
- [125] J. Zaumseil, H. Sirringhaus, *Chem. Rev.* **2007**, *107*, 1296.
- [126] S. Holliday, J. E. Donaghey, I. McCulloch, *Chem. Mater.* **2014**, *26*, 647.
- [127] A. Facchetti, *Mater. Today* **2007**, *10*, 28.
- [128] L.-L. Chua, J. Zaumseil, J.-F. Chang, E. C.-W. Ou, P. K.-H. Ho, H. Sirringhaus, R. H. Friend, *Nature* **2005**, *434*, 194.
- [129] A. Facchetti, M.-H. Yoon, T. J. Marks, *Adv. Mater.* **2005**, *17*, 1705.
- [130] P. M. Beaujuge, J. M. J. Fréchet, *J. Am. Chem. Soc.* **2011**, *133*, 20009.
- [131] M. A. Ruderer, P. Müller-Buschbaum, *Soft Matter* **2011**, *7*, 5482.
- [132] P. Müller-Buschbaum, *Adv. Mater.* **2014**, *26*, 7692.

- [133] H. Siringhaus, P. J. Brown, R. H. Friend, M. M. Nielsen, K. Bechgaard, B. M. W. Langeveld-Voss, A. J. H. Spiering, R. A. J. Janssen, E. W. Meijer, P. Herwig, D. M. de Leeuw, *Nature* **1999**, *401*, 685.
- [134] J. Guo, Y. Liang, J. Szarko, B. Lee, H. J. Son, H. J. Son, B. S. Rolczynski, L. Yu, L. X. Chen, *J. Phys. Chem. B* **2010**, *114*, 742.
- [135] J. Ma, K. Hashimoto, T. Koganezawa, K. Tajima, *J. Am. Chem. Soc.* **2013**, *135*, 9644.
- [136] Z. B. Henson, K. Müllen, G. C. Bazan, *Nat. Chem.* **2012**, *4*, 699.
- [137] L. H. Jimison, M. F. Toney, I. McCulloch, M. Heeney, A. Salleo, *Adv. Mater.* **2009**, *21*, 1568.
- [138] A. Salleo, R. J. Kline, D. M. DeLongchamp, M. L. Chabinyc, *Adv. Mater.* **2010**, *22*, 3812.
- [139] H. N. Tsao, D. Cho, J. W. Andreasen, A. Rouhanipour, D. W. Breiby, W. Pisula, K. Müllen, *Adv. Mater.* **2009**, *21*, 209.
- [140] L. Hartmann, K. Tremel, S. Uttiya, E. Crossland, S. Ludwigs, N. Kayunkid, C. Vergnat, M. Brinkmann, *Adv. Funct. Mater.* **2011**, *21*, 4047.
- [141] A. M. Hiszpanski, Y.-L. Loo, *Energy Environ. Sci.* **2014**, *7*, 592.
- [142] J. Rivnay, R. Steyrleuthner, L. H. Jimison, A. Casadei, Z. Chen, M. F. Toney, A. Facchetti, D. Neher, A. Salleo, *Macromolecules* **2011**, *44*, 5246.
- [143] K. Vakhshouri, B. H. Smith, E. P. Chan, C. Wang, A. Salleo, C. Wang, A. Hexemer, E. D. Gomez, *Macromolecules* **2016**, *49*, 7359.
- [144] I. Osaka, K. Takimiya, *Polymer* **2015**, *59*, A1-A15.
- [145] M. Birkholz, P. F. Fewster, *Thin film analysis by X-Ray scattering*, WILEY-VCH, Weinheim **2009**.
- [146] L. A. Perez, P. Zalar, L. Ying, K. Schmidt, M. F. Toney, T.-Q. Nguyen, G. C. Bazan, E. J. Kramer, *Macromolecules* **2014**, *47*, 1403.
- [147] R.-J. Roe, *Methods of X-ray and neutron scattering in polymer science*, Oxford Univ. Press, New York, NY **2000**.
- [148] A. Tournebize, J.-L. Gardette, C. Taviot-Guého, D. Bégué, M. A. Arnaud, C. Dagron-Lartigau, H. Medlej, R. C. Hiorns, S. Beaupré, M. Leclerc, A. Rivaton, *Polym. Degrad. Stab.* **2015**, *112*, 175.
- [149] M. Pomerantz, *Tetrahedron Lett.* **2003**, *44*, 1563.
- [150] A. Pron, P. Berrouard, M. Leclerc, *Macromol. Chem. Phys.* **2013**, *214*, 7.
- [151] X. Guo, A. Facchetti, T. J. Marks, *Chem. Rev.* **2014**, *114*, 8943.

- [152] J. SICE, *J. Org. Chem.* **1954**, *19*, 70.
- [153] M. D. Dimmler, H. D. Eilingsfeld, BASF SE, *Thiophene derivs. for dyeing synthetic fibres and plastics - prepd. from opt. substd. (2,5)-diphenyl-thiophene-(3,4)-dicarboxylic acid anhydrides and prim. amines*, DE2538951A1, Sep 02, **1977**.
- [154] C. B. Nielsen, T. Bjørnholm, *Org. Lett.* **2004**, *6*, 3381.
- [155] P. Berrouard, F. Grenier, J.-R. Pouliot, E. Gagnon, C. Tessier, M. Leclerc, *Org. Lett.* **2011**, *13*, 38.
- [156] P. Berrouard, S. Dufresne, A. Pron, J. Veilleux, M. Leclerc, *J. Org. Chem.* **2012**, *77*, 8167.
- [157] Q. T. Zhang, J. M. Tour, *J. Am. Chem. Soc.* **1997**, *119*, 5065.
- [158] M. Pomerantz, A. S. Amarasekara, *Synth. Met.* **2003**, *135-136*, 257.
- [159] R. M. W. Wolfe, J. R. Reynolds, *Org. Lett.* **2017**, *19*, 996.
- [160] Q. T. Zhang, J. M. Tour, *J. Am. Chem. Soc.* **1998**, *120*, 5355.
- [161] Y. Zou, A. Najari, P. Berrouard, S. Beaupré, B. R. Aïch, Y. Tao, M. Leclerc, *J. Am. Chem. Soc.* **2010**, *132*, 5330.
- [162] Y. Zhang, S. K. Hau, H.-L. Yip, Y. Sun, O. Acton, A. K.-Y. Jen, *Chem. Mater.* **2010**, *22*, 2696.
- [163] G. Zhang, Y. Fu, Q. Zhang, Z. Xie, *Chem. Commun.* **2010**, *46*, 4997.
- [164] C. Piliego, T. W. Holcombe, J. D. Douglas, C. H. Woo, P. M. Beaujuge, J. M. J. Fréchet, *J. Am. Chem. Soc.* **2010**, *132*, 7595.
- [165] B. R. Aïch, J. Lu, S. Beaupré, M. Leclerc, Y. Tao, *Organic Electronics* **2012**, *13*, 1736.
- [166] C. Cabanetos, A. El Labban, J. A. Bartelt, J. D. Douglas, W. R. Mateker, J. M. J. Fréchet, M. D. McGehee, P. M. Beaujuge, *J. Am. Chem. Soc.* **2013**, *135*, 4656.
- [167] Z. Li, S.-W. Tsang, X. Du, L. Scoles, G. Robertson, Y. Zhang, F. Toll, Y. Tao, J. Lu, J. Ding, *Adv. Funct. Mater.* **2011**, *21*, 3331.
- [168] T.-Y. Chu, J. Lu, S. Beaupré, Y. Zhang, J.-R. Pouliot, S. Wakim, J. Zhou, M. Leclerc, Z. Li, J. Ding, Y. Tao, *J. Am. Chem. Soc.* **2011**, *133*, 4250.
- [169] C. E. Small, S. Chen, J. Subbiah, C. M. Amb, S.-W. Tsang, T.-H. Lai, J. R. Reynolds, F. So, *Nat. Photonics* **2011**, *6*, 115.
- [170] X. Guo, R. P. Ortiz, Y. Zheng, M.-G. Kim, S. Zhang, Y. Hu, G. Lu, A. Facchetti, T. J. Marks, *J. Am. Chem. Soc.* **2011**, *133*, 13685.
- [171] N. Zhou, X. Guo, R. Ponce Ortiz, T. Harschneck, E. F. Manley, S. J. Lou, P. E. Hartnett, X. Yu, N. E. Horwitz, P. Mayorga Burrezo, T. J. Aldrich, J. T. López Navarrete, M. R.

- Wasielewski, L. X. Chen, R. P. H. Chang, A. Facchetti, T. J. Marks *J. Am. Chem. Soc.* **2015**, *137*, 12565.
- [172] M.-S. Su, C.-Y. Kuo, M.-C. Yuan, U.-S. Jeng, C.-J. Su, K.-H. Wei, *Adv. Mater.* **2011**, *23*, 3315.
- [173] X. Guo, N. Zhou, S. J. Lou, J. Smith, D. B. Tice, J. W. Hennek, R. P. Ortiz, J. T. L. Navarrete, S. Li, J. Strzalka, L. X. Chen, R. P. H. Chang, A. Facchetti, T. J. Marks, *Nat. Photonics* **2013**, *7*, 825.
- [174] W. Qing, X. Gong, X. Liang, Y. Wang, S. Yang, L. Tan, Y. Ma, Z. Liu, J. Li, *Macromol. Rapid Commun.* **2016**, *37*, 1357.
- [175] Q. Wu, M. Wang, X. Qiao, Y. Xiong, Y. Huang, X. Gao, H. Li, *Macromolecules* **2013**, *46*, 3887.
- [176] J.-H. Kim, J. B. Park, I. H. Jung, A. C. Grimsdale, S. C. Yoon, H. Yang, D.-H. Hwang, *Energy Environ. Sci.* **2015**, *8*, 2352.
- [177] X. Qiao, W. Chen, Q. Wu, S. Zhang, H. Wu, Z. Liu, R. Yang, H. Li, *Chem. Commun.* **2017**, *53*, 3543.
- [178] F. Lin, W. Huang, H. Sun, J. Xin, H. Zeng, T. Yang, M. Li, X. Zhang, W. Ma, Y. Liang, *Chem. Mater.* **2017**, *29*, 5636.
- [179] T. Kim, J.-H. Kim, T. E. Kang, C. Lee, H. Kang, M. Shin, C. Wang, B. Ma, U. Jeong, T.-S. Kim, B. J. Kim, *Nat. Commun.* **2015**, *6*, 8547.
- [180] J. Yuan, W. Ma, *J. Mater. Chem. A* **2015**, *3*, 7077.
- [181] X. Qiao, Q. Wu, H. Wu, J. Zhang, H. Li, *Adv. Funct. Mater.* **2017**, *27*, 1604286.
- [182] F. Grenier, P. Berrouard, J.-R. Pouliot, H.-R. Tseng, A. J. Heeger, M. Leclerc, *Polym. Chem.* **2013**, *4*, 1836.
- [183] G. Kim, A.-R. Han, H. R. Lee, J. Lee, J. H. Oh, C. Yang, *Chem. Commun.* **2014**, *50*, 2180.
- [184] S. Liu, Z. Kan, S. Thomas, F. Cruciani, J.-L. Brédas, P. M. Beaujuge, *Angew. Chem. Int. Ed.* **2016**, *55*, 12996.
- [185] S. Liu, X. Song, S. Thomas, Z. Kan, F. Cruciani, F. Laquai, J.-L. Bredas, P. M. Beaujuge, *Adv. Energy Mater.* **2017**, *376*, 1602574.

2 Objective of the thesis

The aim of this thesis is the synthesis of novel semiconducting polymers based on thieno[3,4-c]pyrrole-4,6-dione (TPD) for the application in optoelectronic devices. These polymers are designed via the donor-acceptor approach and have TPD as the acceptor unit in common. We chose TPD as acceptor unit due to the high photostability of the corresponding polymers. By variation of the comonomer, the polarity of charge transport should be tuned in order to systematically generate p-type, ambipolar and n-type materials. A key objective of this work is to reveal the structure-property relations of these polymers. In organic field effect transistors (OFETs) as well as organic photovoltaics, the efficiency of charge transport is crucial for the device performance and not only depends on the molecular structure, but also on the thin film alignment of polymer chains to the substrate. The correlation between charge transport properties in OFETs and thin film alignment revealed by grazing incidence wide angle X-ray scattering (GIWAXS) measurements should be addressed in this thesis in detail. On the one hand, the consequences of systematic variation of the chemical structure on the thin film alignment and charge transport should be investigated and on the other hand, the influence of the processing parameters used for the device preparation. Furthermore, we have been interested to generate electron transport in TPD copolymers due to the limited choice of acceptor materials for the application in organic solar cells. For this purpose, the donor strength of the comonomers should be decreased by fluorination in order to facilitate electron transport. Here, not only the influence of charge transport but also on crystallinity, energy levels and solid-state packing should be studied. Furthermore, fluorine substituents should be introduced into p-type materials in order to study the influence on the material's properties. By fluorination, the HOMO energy level can be lowered allowing a higher open-circuit voltage and a possibly higher performance in organic solar cells.

3 Overview of the thesis

In this thesis, semiconducting copolymers based on thieno[3,4-c]pyrrole-4,6-dione (TPD) were designed, synthesized and studied in order to elucidate structure-property relations. As mentioned in the introduction, semiconducting polymers are designed by the donor-acceptor concept requiring a combination of an electron-deficient and electron-rich comonomer. For all copolymers, we chose TPD as acceptor unit due to its remarkable thermal stability and coplanar structure, which facilitates intra- and intermolecular interactions. TPD was combined with different comonomers with varying donor strength in order to tune especially the polarity of charge transport. This thesis embraces four chapters and a graphical overview is given in Figure 3.1.

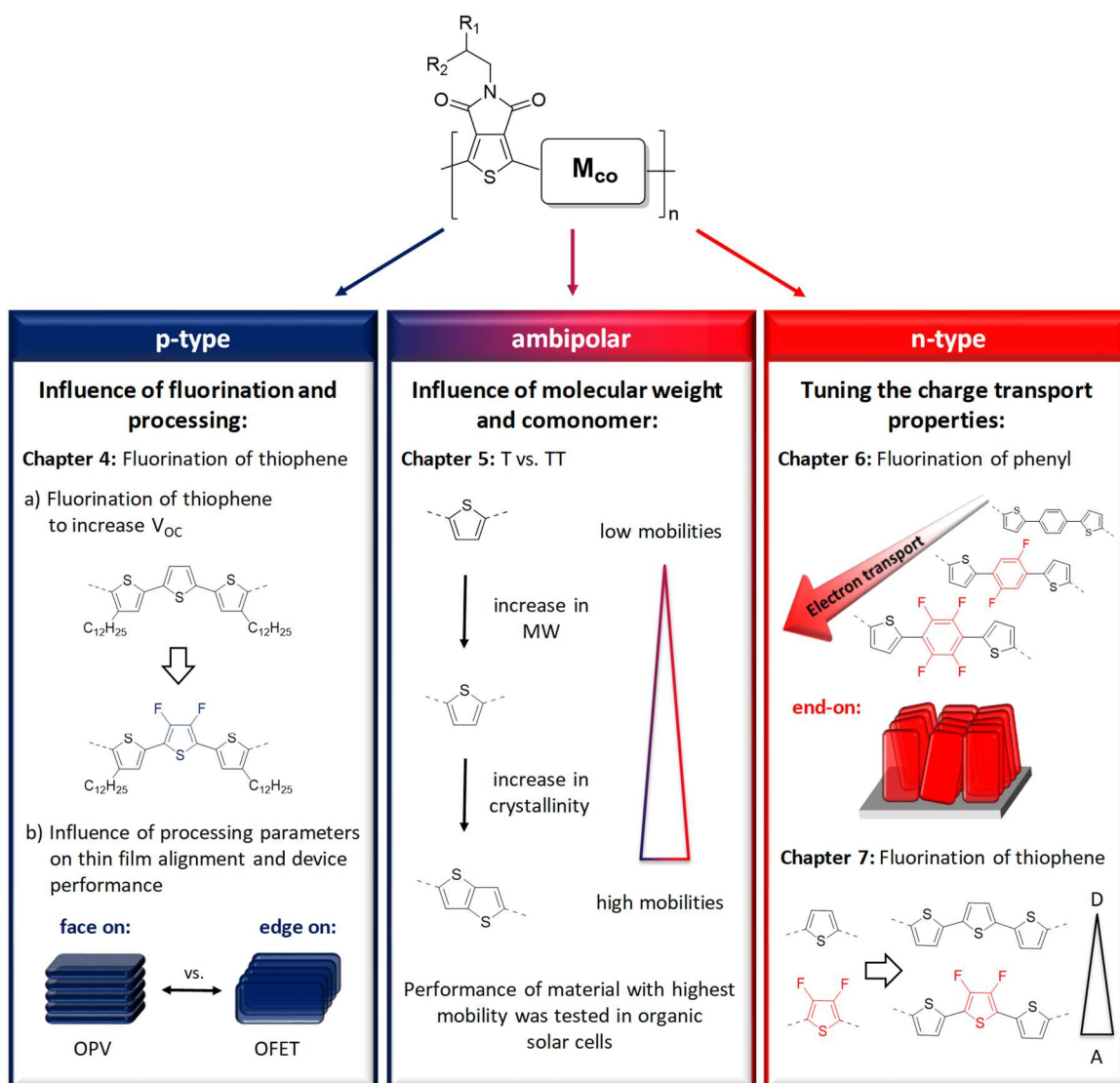


Figure 3.1. Overview of the thesis: By structural variation of the comonomer in TPD copolymers, p-type, ambipolar and n-type materials are obtained.

The synthesis of all copolymers designed by the donor-acceptor concept was carried out with Stille polymerization via the AA/BB approach. Therefore, the TPD monomer was dibromo functionalized and bis(trimethyl tin) groups were attached to the corresponding comonomers. An overview of all monomers used in the Stille polycondensation is given in Figure 3.2. In order to maintain solubility of the resulting polymers, the TPD monomers were decorated with branched and long alkyl chains – either octyldodecyl or decyltetradecyl. For the synthesis of copolymers carrying terthiophene, the TPD was flanked with thiophene as well as thiophene carrying additional solubilizing alkyl chains and copolymerized with 2,5-bis(trimethylstannyl)thiophene (or the corresponding fluorinated derivative). Detailed synthetic procedures for the TPD monomers as well as comonomers are given in the Supporting Information of each chapter. Stille polycondensation was carried out with tris(dibenzylideneacetone)dipalladium as a catalyst and tri(*o*-tolylphosphine) as a ligand. The molecular weights were analyzed by size exclusion chromatography (SEC).

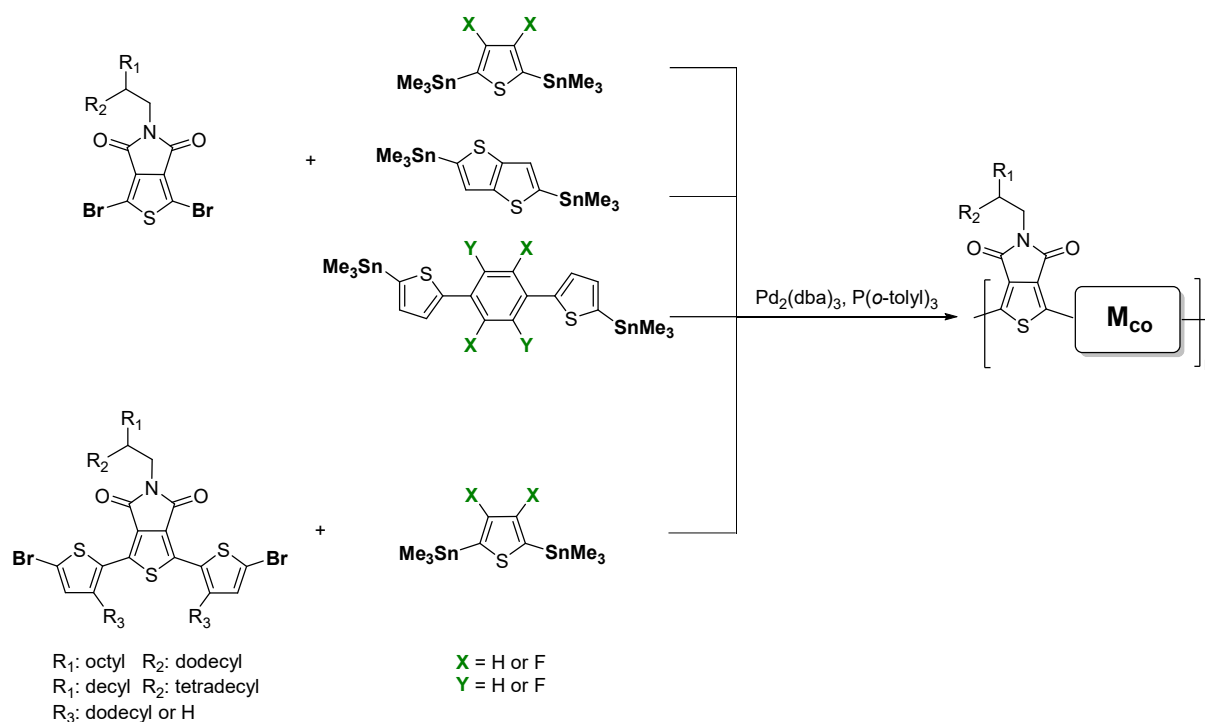


Figure 3.2. Synthesis of the TPD copolymers via Stille polycondensation.

By structural variation of the comonomer in TPD copolymers, the extent and nature of charge transport properties could be tuned and evaluated using organic field effect transistors (OFETs). We managed to achieve materials showing p-type, ambipolar and n-type behavior. In each chapter, a series of copolymers was systematically studied to understand the influence of structural changes on the material's properties. Besides the thermal, optical and electrochemical

characterization of the polymers, the charge transport in OFET was studied in detail. For the different device performances, the thin film alignment plays a crucial role. In principle, polymer chains can align either in an edge-on or face-on manner (see also Chapter 1.5). In an OFET, charge transport takes only place at the interface of the device involving only a few nm of the semiconducting material. Therefore, an edge-on orientation where the planar π -faces are perpendicular to the substrate favors charge transport in OFETs. In contrast, orientation of the polymer chains parallel to substrate, which is called face-on orientation, promotes charge transport in a vertical direction as it is the case in a vertical sandwich configuration. In this thesis, the interplay between charge transport and thin film alignment was studied in detail. Therefore, the structural elucidation of thin films via grazing incidence wide angle X-ray scattering (GIWAXS) analysis was performed at the Australian Synchrotron in collaboration with Prof. Dr. Chris McNeill at the Monash University in Melbourne. Additionally, the performance of selected materials in organic solar cells was tested in Melbourne (Chapter 4 & 5).

In this thesis, particularly the influence of fluorination on the efficiency as well as polarity of charge transport was intensively studied. On the one hand, incorporation of fluorine in the polymer backbone can lead to planarization of the polymer backbone by non-covalent interactions, which can promote crystallization and therefore, improve charge transport. A higher charge carrier mobility can improve the short circuit current in an organic solar cell and therefore, the overall performance in organic solar cells. Furthermore, fluorination can lead to an enhanced open-circuit voltage, which is limited by the difference of the HOMO level of the donor and the LUMO level of the acceptor. Fluorination in p-type materials was proven to lower the energy levels and therefore, the open-circuit voltage can be increased. This concept was addressed in Chapter 4, which focuses on p-type materials based on TPD and terthiophene. Here, the thiophene comonomer was replaced with difluorothiophene and the consequences on the material's property were investigated. On the other hand, fluorine is strongly electronegative and decreases the electron density along the backbone. Therefore, fluorination can not only influence the efficiency, but also the polarity of charge transport by stabilization of the radical anion. In Chapter 6 and 7, fluorination was used to reduce the donor strength in order to facilitate electron transport in OFET. This concept was proven for comonomers based on fluorinated phenyl (Chapter 6) and thiophene (Chapter 7).

Polymers can not only transport either holes or electrons, also the charge transport of both charge carriers can be realized in one material. These ambipolar materials were obtained by copolymerization of TPD with thiophene as well thieno[3,2-*b*]thiophene, which constitute the content of Chapter 5. In the first part, the influence of the molecular weight in copolymers based on TPD and thiophene was investigated regarding thin film alignment and charge transport. Secondly, thiophene was replaced by the very rigid and planar thienothiophene moiety, which has a significant impact on the solid-state packing in thin films. In OFETs, all polymers show high and balanced hole and electron mobilities and the efficiency of charge transport could be correlated with the individual thin film alignment obtained from GIWAXS. The orientation of the polymer chains to the substrate in thin films can not only be influenced by the molecular structure, but also the processing parameters have a significant impact. In Chapter 4, the influence of the processing on the thin film alignment and therefore, the performance in OFETs as well as in organic photovoltaics (OPVs) was studied in addition to the consequences of fluorination.

An overview of the main results of each chapter is given in the following. In the individual chapters, the detailed description of the experiments as well as results can be found. The main focus of the thesis lies throughout all chapters on the variation of the chemical structure of TPD containing copolymers and their structure property correlations.

Chapter 4: Influence of the edge-on or face-on alignment of thieno[3,4-*c*]pyrrole-4,6-dione based copolymer films achieved by processing on devices

This chapter focuses on p-type materials based on TPD and terthiophene, where we addressed two main questions. How does processing influence the alignment of polymer chains in thin films and consequently the performance of these materials in OFET as well as OPV? Can fluorination be beneficial for improving the performance of these materials? For this, we copolymerized TPD flanked with thiophene carrying additional solubilizing side chains with thiophene (PTPDTTT) and difluorothiophene (PTPDTF₂T) via Stille polycondensation. Highly crystalline materials as shown in DSC measurements were obtained. Upon fluorination, the melting as well as crystallization temperature are increased while the melt enthalpy stays almost constant. Due to the high crystallinity, these polymers strongly aggregate in solution, which was studied by temperature dependent UV-Vis measurements in chloroform and dichlorobenzene, respectively. As shown in Figure 3.3, the nature and quality of aggregates depends on the comonomer unit as well as on

the solvent used. Therefore, the influence of processing from these two solvents as well as of thermal annealing on polymer chain alignment was studied using GIWAXS measurements.

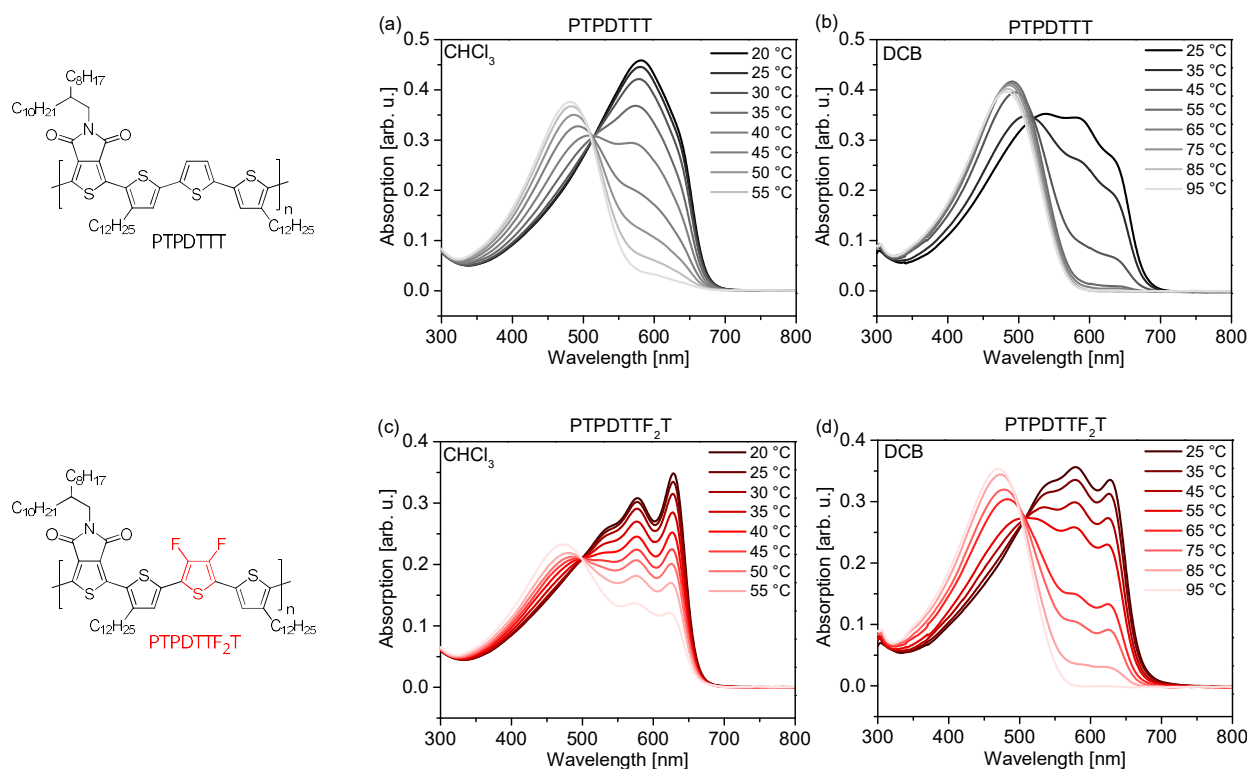


Figure 3.3. Temperature dependent UV-Vis measurements of the two polymers, PTPD(TTT and TF₂)T in chloroform (a and c) and dichlorobenzene (b and d) solution, respectively.

Films processed from chloroform give predominately face-on orientation after thermal annealing, whereas processing from DCB suppresses the formation of these face-on stacks. The degree of alignment is quantified by the Herman's orientation parameter S , which can take values between -0.5 (edge-on) and +1.0 (face-on). As shown in Figure 3.4, the swapping effect of alignment in annealed films is more pronounced for PTPD(TTT) than for the corresponding fluorinated copolymer. Accordingly, the charge carrier mobilities in OFETs are influenced by processing and higher hole mobilities are achieved for films cast from DCB for both polymers. In comparison to the non-fluorinated polymer, the hole mobility of the fluorinated polymer is slightly lower. However, the fluorinated polymer showed ambipolar charge transport after thermal annealing, especially when processed from DCB. In contrast, the solar cell performance of these materials in combination with PC₇₁BM was improved by processing from chloroform, which cannot be justified by the thin film alignment, but rather by the different blend morphologies. The TPD copolymers deliver a PCE of 5.3% in combination with fullerene. Fluorination indeed leads to a higher open-circuit voltage due to the lowered ionization potential

and compensates the loss in fill factor leading to identical PCE values of 5.3% for both copolymers.

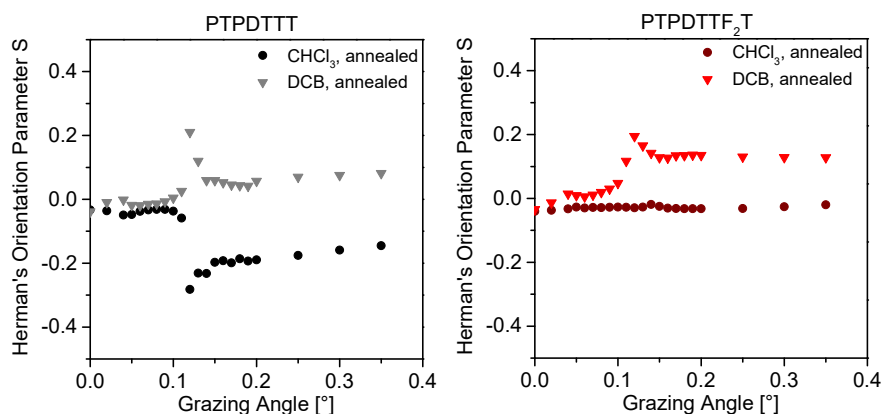


Figure 3.4. Herman's orientation parameter S for annealed films of PTPDTT and PTPDTF₂T processed from chloroform and dichlorobenzene showing the suppression of face-on stacks by processing from DCB.

Chapter 5: Highly efficient and balanced charge transport in thieno[3,4-*c*]pyrrole-4,6-dione copolymers: Dramatic influence of thieno[3,2-*b*]thiophene comonomer on alignment and charge transport

This work shows how the thin film alignment of conjugated polymers can be influenced by the molecular structure, which nicely correlates with the charge transport properties observed in OFETs. We studied a series of copolymers based on the electron-deficient TPD building block, copolymerized with either thiophene (PTPDT) or thieno[3,2-*b*]thiophene (PTPDTT). For the polymer PTPDTT, high molecular weights were achieved with Stille polycondensation in contrast to polymer PTPDT featuring low molecular weights (PTPDT-1). We optimized the Stille polymerization conditions obtaining a second sample with a higher molecular weight (PTPDT-2). Therefore, we addressed the question, if there is any dependence of charge transport on molecular weight by comparing PTPDT-1 and PTPDT-2 or the nature of comonomer used by comparing PTPDT-2 and PTPDTT. The charge carrier mobilities of this series of copolymers was studied in OFET devices as-cast and after thermal annealing at 100 °C as well as 250 °C. In Figure 3.5, the results are summarized graphically. All polymers showed ambipolar transistor behavior with highly balanced hole and electron mobilities. The highest OFET mobilities, both for holes and electrons were reached in PTPDTT with the very rigid aromatic moiety thieno[3,2-*b*]thiophene as comonomer. After thermal annealing at 250 °C a hole mobility of 0.11 cm² V⁻¹ s⁻¹ and an electron mobility of 0.17 cm² V⁻¹ s⁻¹ evolved.

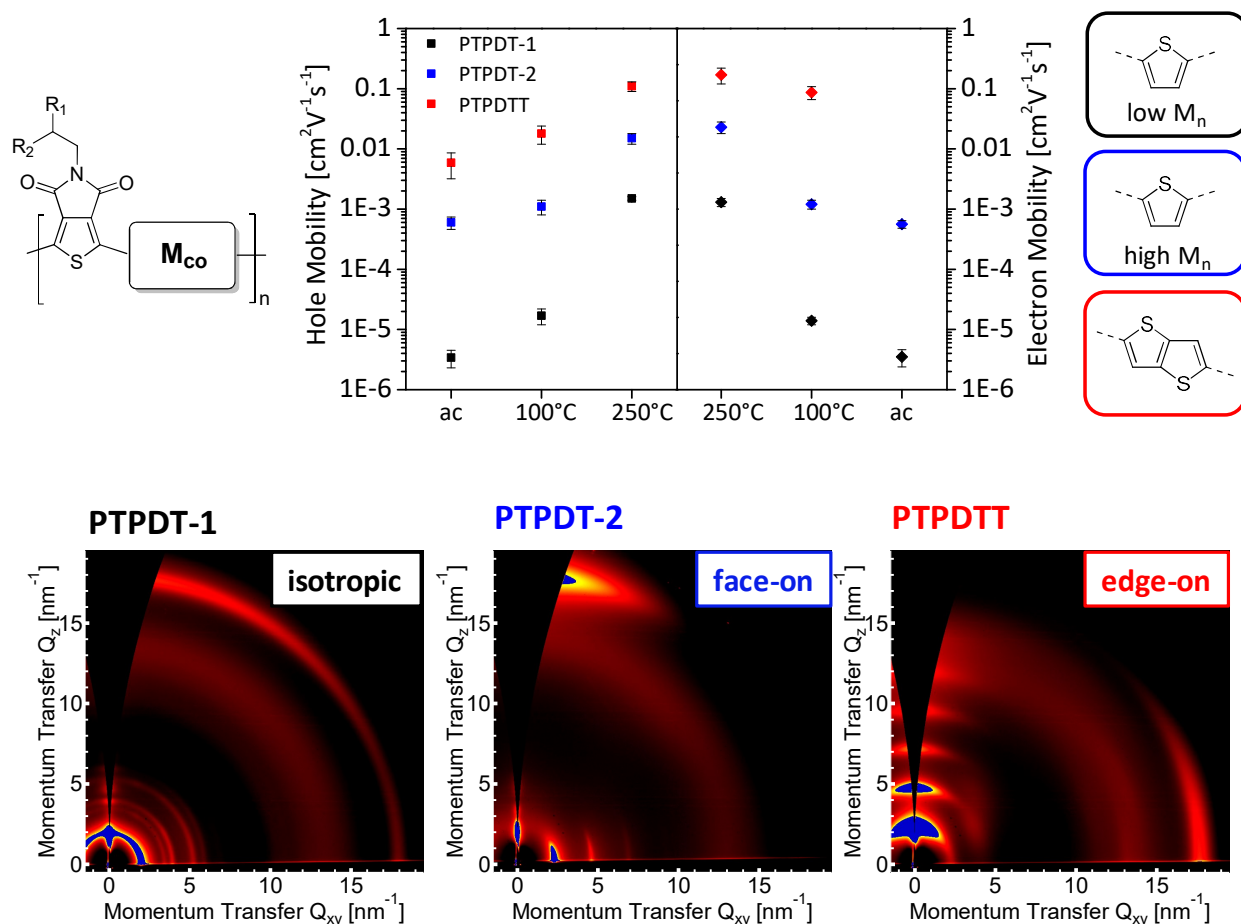


Figure 3.5. Summary of hole and electron mobilities obtained from OFET measurements of PTPDT-1, PTPDT-2 and PTPDTT (top); and 2D GIWAXS scattering images of the corresponding films annealed at 250 °C (bottom).

The results were correlated with the thin film microstructure analyzed by GIWAXS in as-cast and annealed films. In Figure 3.5 the 2D scattering patterns for the films annealed at 250 °C are depicted. Annealing has a very pronounced effect on the nature and degree of crystallization of all copolymers. Especially, thin films of PTPDTT show four orders of lamellar stacking in the as-cast sample and even five orders after thermal annealing. Polymer PTPDT-1 with low molecular weights shows no preferential orientation in thin films, and therefore exhibited the lowest charge carrier mobilities. Charge transport could be improved in PTPDT-2 by increasing the molecular weight resulting in enhanced structural ordering. Additionally, the face-on alignment was favored by increasing the molecular weight. A shift of comonomer from simple thiophene to the planar and electron-dense thienothiophene in PTPDTT drastically changes the alignment from face-on to edge-on fashion. Consequently, the charge carrier mobilities increased by one order of magnitude. Due to the high mobilities of PTPDTT, this material was applied as a donor as well as an acceptor material in organic solar cells by suitable combination with an acceptor or donor material, respectively. However, the device performance of PTPDTT used as an acceptor

material in combination with the polymer donor PBDTTT-EFT in an all-polymer solar cell was very poor. In contrast, the application of PTPDTT as a donor material in combination with PC₇₁BM delivered a solar cell device with a power conversion efficiency of 4.3%.

Chapter 6: Fluorination in thieno[3,4-c]pyrrole-4,6-dione copolymers leading to electron transport, high crystallinity and end-on alignment

In this chapter, fluorination was used to increase the electron affinity along the polymer backbone in order to facilitate electron injection and transport. The influence of fluorination on the properties regarding structure formation and OFET mobilities are systemically studied. Therefore, a series of copolymers based on thieno[3,4-c]pyrrole-4,6-dione and 1,4-di(2-thienyl)benzene (TPT) with different degrees of fluorination on the phenyl unit was synthesized by Stille polycondensation (Figure 3.6). The comonomer TPT was di- and tetrafluorinated (TPF₂T and TPF₄T) in order to gradually increase the degree of fluorination. Analysis of the three polymers by high-temperature SEC gave number-average molecular weights between 7.90-13.6 kg mol⁻¹ with dispersities of 1.1-1.3. In Flash DSC measurements, melting as well as crystallization could be observed for all polymers. Fluorination leads to higher melting as well as crystallization temperatures due to the stronger intermolecular interactions facilitated by planarization of the polymer backbone. However, the increase in degree of fluorination from the difluoro- to the tetrafluoro-derivative has almost no influence on the thermal properties. Whereas the optical properties are almost not affected by fluorination, the energy levels, both the ionization potential (IP) and electron affinity (EA), which are determined by cyclic voltammetry, are considerably altered. As shown in Figure 3.6, the energy levels are gradually lowered upon fluorination due to the incremental decrease of the donor strength.

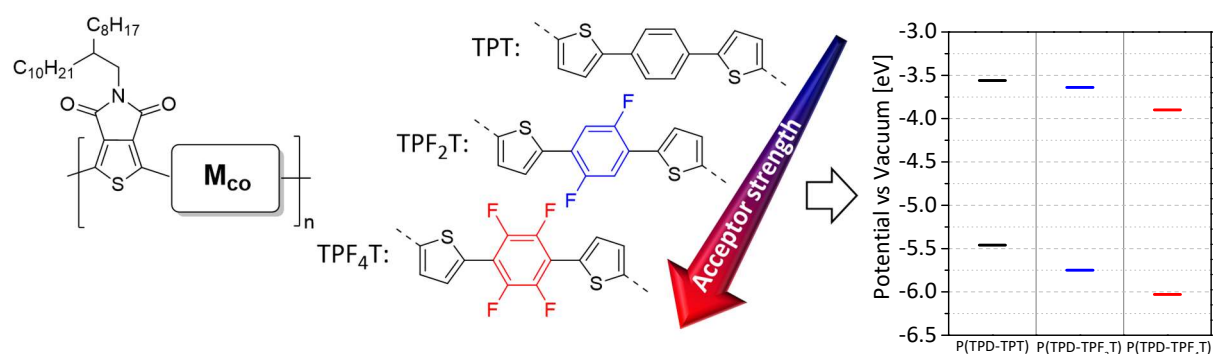


Figure 3.6. Molecular structure of the three polymers and energy levels determined by cyclic voltammetry.

The charge transport properties of this series of copolymers were studied in OFETs and the corresponding output characteristics are shown in Figure 3.7. After thermal annealing, the non-fluorinated as well as difluorinated polymers show ambipolar channel operation, whereby the efficiency of charge transport is enhanced by fluorination. In contrast, tetrafluorination results in exclusively n-type behavior with an electron mobility of $3.7 \times 10^{-4} \text{ cm}^2 \text{ V}^{-1} \text{ s}^{-1}$.

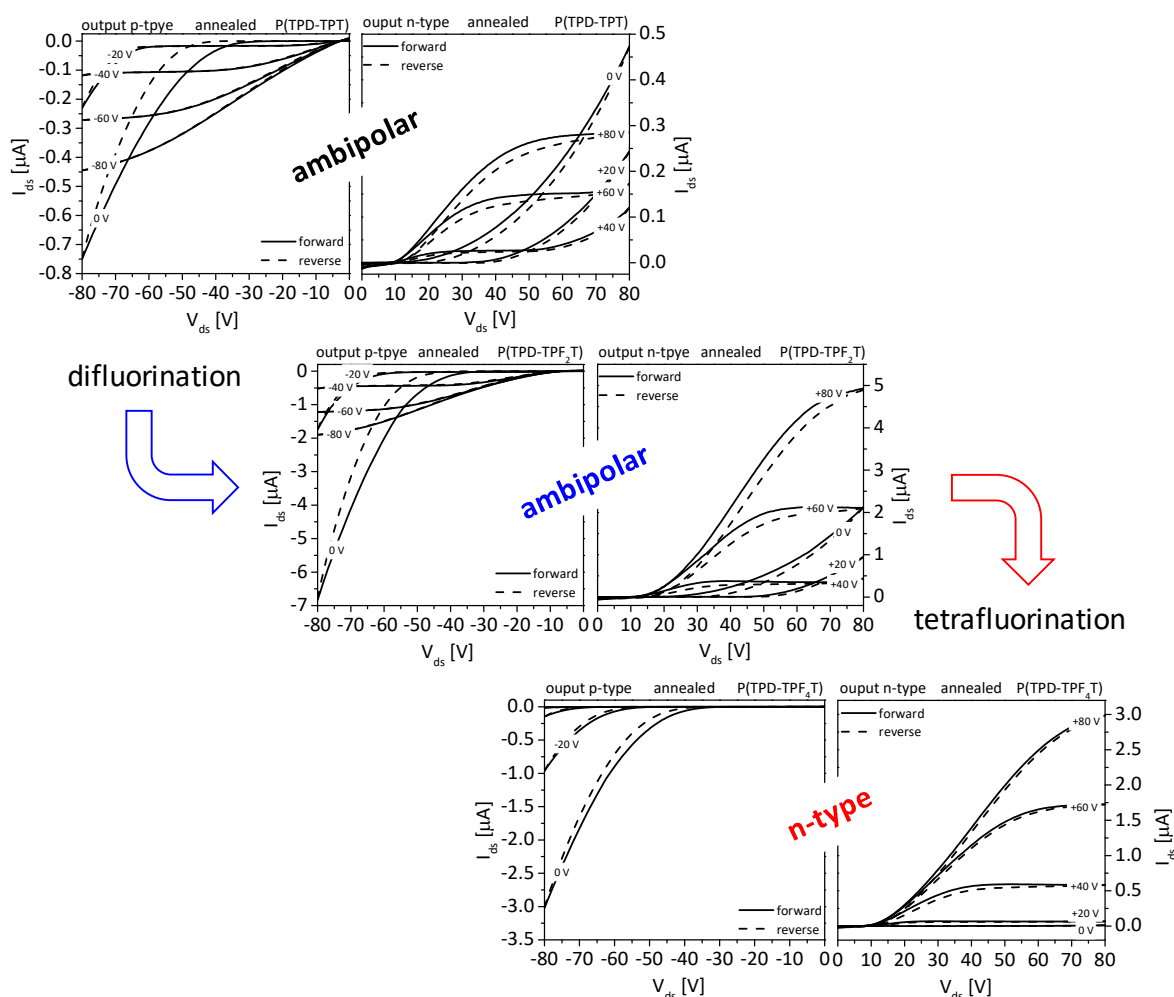


Figure 3.7. Both p- and n-type OFET output curves after annealing at 250 °C for P(TPD-TPT) (top), P(TPD-TPF₂T) (middle) and P(TPD-TPF₄T) (bottom).

GIWAXS measurements of as-cast and annealed films reveal a very interesting structural alignment in thin films. Very surprisingly, these polymers show end-on alignment, where the polymer chains stand on the substrate. This alignment is only rarely observed in the case of conjugated polymer films obtained just by solution casting. Usually it is achieved by chemical grafting of the chains onto a substrate. This may be partially explained as due to the low molecular weights of these polymers in relation to the film thickness. Fluorination does not influence the microstructural properties, only the propensity of crystallization is increased.

Chapter 7: Influence of fluorination and backbone extension in thieno[3,4-c]pyrrole-4,6-dione based copolymers carrying thiophene and terthiophene comonomers

In the latter chapter, electron transport was facilitated by fluorination of the phenyl moiety in the TPT comonomer. Instead of fluorinating the phenyl moiety, we used here thiophene as comonomer and the influence of thiophene fluorination is studied in a series of four copolymers based on thieno[3,4-c]pyrrole-4,6-dione (Figure 3.8). Besides the copolymerization of TPD with fluorinated (PTPDTF₂) and non-fluorinated thiophene (PTPDT), a TPD monomer flanked with thiophene was additionally applied in the Stille polycondensation (PTPD[2T]T and PTPD[2T]TF₂). Thus, the influence of the extended backbone is studied in addition to the comparison of the fluorinated and non-fluorinated polymers.

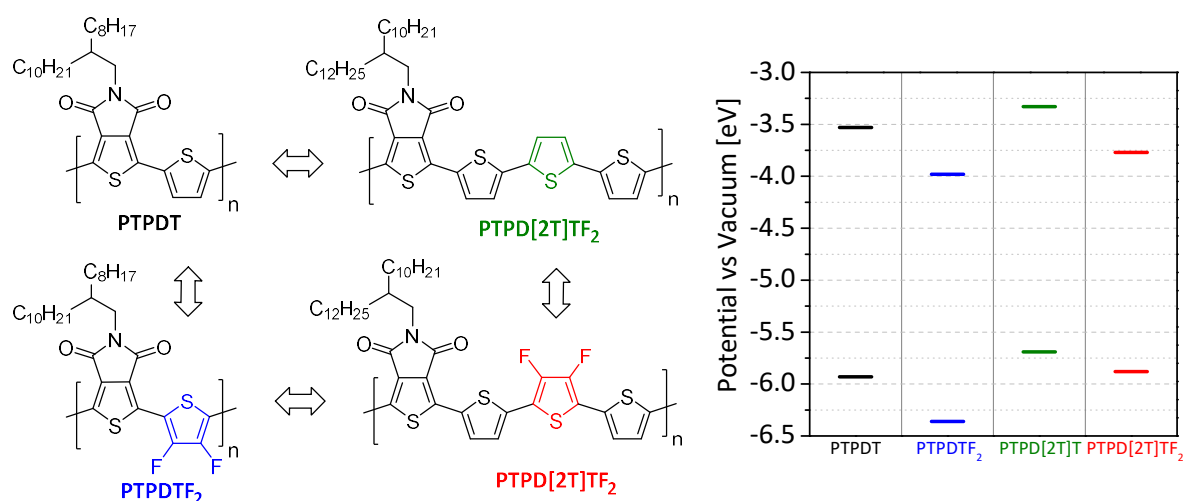


Figure 3.8. Molecular structures of the fluorinated as well as non-fluorinated polymers (left) and energy levels determined by cyclic voltammetry (right).

All polymers are crystalline and show thermal transitions in Flash DSC measurements. By fluorination the melting as well as crystallization temperatures are shifted to higher temperatures. In contrast, extension of the backbone has no influence on the thermal properties. Due to the electron withdrawing character of fluorine, the optical gap is slightly enlarged by fluorination. The energy levels were determined by cyclic voltammetry measurements and the resulting IPs and EAs are summarized in Figure 3.8. Upon fluorination the energy levels, IP as well as EA, are lowered, whereas the effect is more pronounced for the polymer PTPDTF₂. The energy levels of the polymers with extended backbone PTPD[2T]T or PTPD[2T]TF₂ are overall increased in comparison to the polymers PTPDT or PTPDTF₂.

The charge carrier mobilities of this series of copolymers were studied in organic field effect transistors and the results are graphically summarized in Figure 3.9. Additionally, GIWAXS measurements were performed in order to elucidate structure-property relations. For polymer PTPDFT₂, exclusively n-channel operation with an electron mobility in the range of 10⁻³ cm² V⁻¹ s⁻¹ was achieved. All other polymers show ambipolar charge transport properties. In comparison to the non-fluorinated polymer PTPDT, the electron mobility of polymer PTPDFT₂ is one order of magnitude lower. In GIWAXS measurements, both polymers show predominantly face-on orientation, but only the first order of alkyl stacking is observed for PTPDFT₂ in comparison to PTPDT showing three orders of alkyl stacking. Therefore, fluorination in this structure leads to a less crystalline material and a lower electron mobility. Nevertheless, a n-type material was obtained, and a more efficient charge transport would be expected in a diode configuration making PTPDFT₂ an interesting acceptor material for all-polymer solar cells. For the polymers with extended backbone, fluorination improves charge transport and especially the electron mobility is positively affected. The thin film alignment is almost not affected by fluorination as revealed from the GIWAXS analysis.

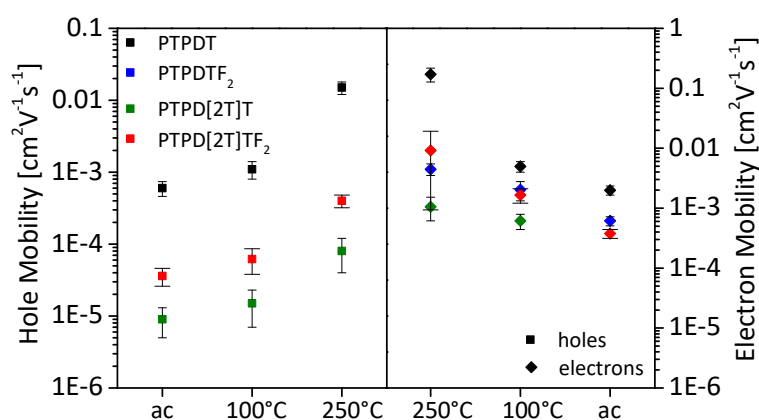


Figure 3.9. Summary of the OFET hole and electron mobilities of the polymers PTPDT, PTPDFT₂, PTPD[2T]T, PTPD[2T]TF₂ measured as-cast and at different annealing temperatures.

This overview clearly depicts the structural variation of TPD containing donor-acceptor polymers leading to p-type or n-type or ambipolar semiconductors, which can be understood from the electron affinity or electron richness variation in structure as well as orientation effects.

Individual contributions to joint publications

The following section specifies the individual contributions of the authors.

Chapter 4

This chapter is prepared for submission to *ACS Applied Materials and Interfaces* under the title:

“Influence of the edge-on or face-on alignment of thieno[3,4-*c*]pyrrole-4,6-dione based copolymer films achieved by processing on devices”

by **Tina Weller**, Kira Rundel, Adam Welford, Christopher R. McNeill and Mukundan Thelakkat.

I synthesized the monomers as well as polymers and characterized the materials regarding their thermal, optical and electrochemical properties. Further, I studied the charge transport in OFET and performed the GIWAXS experiments of the neat polymers during the beamtime of the group of Prof. McNeill at the Australian Synchrotron. I evaluated and analyzed the GIWAXS data and wrote the corresponding parts of the manuscript.

Adam Welford performed the AFM measurements. Kira Rundel prepared and characterized the solar cell devices and analyzed the blends in GIWAXS and TEM experiments. She wrote the device part of the manuscript and was involved in scientific discussions.

Christopher R. McNeill organized and supervised the beamtime, helped with the GIWAXS analysis, was involved in the scientific discussions and corrected the manuscript.

Mukundan Thelakkat supervised the project, was involved in the scientific discussion and corrected the manuscript.

Chapter 5

This chapter is published in *Journal of Physical Chemistry C*, **2018**, *122*, 7565-7574 under the title:

“Highly Efficient and Balanced Charge Transport in Thieno[3,4-*c*]pyrrole-4,6-dione Copolymers: Dramatic Influence of Thieno[3,2-*b*]thiophene Comonomer on Alignment and Charge Transport”

by **Tina Weller**, Kira Rundel, Gert Krauss, Christopher R. McNeill and Mukundan Thelakkat.

I synthesized the monomers as well as polymers and characterized the materials regarding their thermal, optical and electrochemical properties. Further, I studied the charge transport in OFET and performed the GIWAXS experiments of the neat polymers during the beamtime of the group of Prof. McNeill at the Australian Synchrotron. I evaluated and analyzed the GIWAXS data and wrote the corresponding parts of the manuscript.

Kira Rundel prepared and characterized the solar cell devices and analyzed the blends in UV-Vis and GIWAXS experiments. She wrote the device part of the manuscript and was involved in scientific discussions.

Gert Krauss synthesized comonomer **3** as well as polymer PTPDTT during his six-week internship under my supervision.

Christopher R. McNeill organized and supervised the beamtime, helped with the GIWAXS analysis, was involved in the scientific discussions and corrected the manuscript.

Mukundan Thelakkat supervised the project, was involved in the scientific discussion and corrected the manuscript.

Chapter 6

This chapter is published in *Journal of Materials Chemistry C* **2017**, *5*, 7527-7534 under the title:

“Fluorination in thieno[3,4-c]pyrrole-4,6-dione copolymers leading to electron transport, high crystallinity and end-on alignment”

by **Tina Weller**, Marion Breunig, Christian J. Müller, Elliot Gann, Christopher R. McNeill and Mukundan Thelakkat.

I characterized the materials regarding their thermal, optical and electrochemical properties and studied the charge transport in OFET. Further, I prepared the samples for the GIWAXS experiments and wrote the corresponding parts of the manuscript.

Marion Breunig synthesized the TPD monomer **1**, the comonomer **2c** as well as the three polymers during her three- as well as six-week internships under my supervision.

Christian J. Müller provided the comonomers **2a** and **2b** and was involved in the scientific discussion.

Eliot Gann characterized the polymers using GIWAXS and wrote the GIWAXS section of the manuscript.

Christopher R. McNeill was involved in the scientific discussions and corrected the manuscript.

Mukundan Thelakkat supervised the project, was involved in the scientific discussion and corrected the manuscript.

Chapter 7

This chapter is prepared for submission under the title:

“Influence of fluorination and backbone extension in thieno[3,4-c]pyrrole-4,6-dione based copolymers carrying thiophene and terthiophene comonomers”

by **Tina Weller**, Christopher R. McNeill and Mukundan Thelakkat

I synthesized the monomers as well as polymers and characterized the materials regarding their thermal, optical and electrochemical properties. Further, I studied the charge transport in OFET and performed the GIWAXS experiments of the neat polymers during the beamtime of the group of Prof. McNeill at the Australian Synchrotron. I evaluated and analyzed the GIWAXS data and wrote the manuscript.

Christopher R. McNeill organized and supervised the beamtime, helped with the GIWAXS analysis and was involved in the scientific discussions.

Mukundan Thelakkat supervised the project, was involved in the scientific discussion and corrected the manuscript.

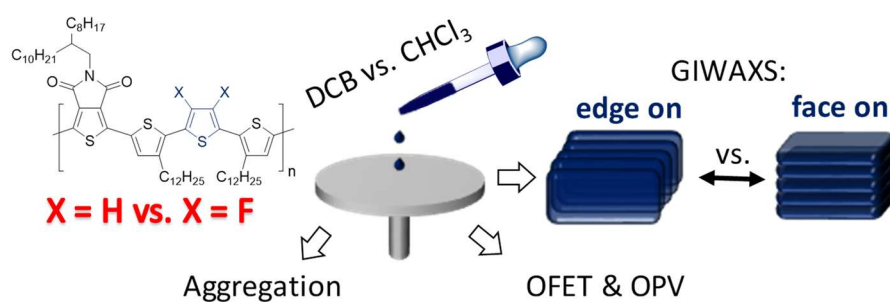
4 Influence of the edge-on or face-on alignment of thieno[3,4-c]pyrrole-4,6-dione based copolymer films achieved by processing on devices

Tina Weller,^a Kira Rundel,^b Adam Welford,^b Christopher R. McNeill^b and Mukundan Thelakkat^{a*}

^a Applied Functional Polymers, Macromolecular Chemistry I, University of Bayreuth, 95440 Bayreuth, Germany.

^b Department of Materials Science and Engineering, Monash University, Wellington Road, Clayton VIC, 3800, Australia.

* Corresponding author: mukundan.thelakkat@uni-bayreuth.de



Prepared for submission to *ACS Applied Materials and Interfaces*.

Abstract

We investigate the influence of solvent and thermal processing on the alignment of polymer chains in thin films of two thieno[3,4-c]pyrrole-4,6-dione (TPD) based copolymers. These two TPD-based copolymers, PTPDTTT and PTPDTTF₂T, were prepared via Stille polycondensation by copolymerizing the TPD monomer with either thiophene or difluorothiophene, respectively. DSC measurements showed that these materials are highly crystalline and the melting as well as crystallization temperatures increased upon fluorination. As a consequence, these polymers strongly aggregate in solution, which was studied by temperature dependent UV-Vis measurements in chloroform and dichlorobenzene. Grazing incidence wide-angle X-ray scattering measurements reveal that the degree of face-on or edge-on orientation of crystallites in thin films is found to be sensitive to fluorination, solvent, and thermal annealing. In general, fluorination, annealing and the use of dichlorobenzene promote edge-on packing while the use of chloroform promotes face-on packing in as-cast films. To study the influence of molecular alignment on device properties, organic field-effect transistors (OFETs) and organic solar cells have been prepared. The charge carrier mobilities in OFETs for both polymers are found to be improved by processing films from dichlorobenzene which favor edge-on alignment. In contrast, the solar cell performance of these materials is improved by processing from chloroform due to a more favorable morphology with the faster drying chloroform limiting phase separation in blends with PC₇₁BM. Both TPD polymers deliver a PCE of ~5.3% in combination with PC₇₁BM, with the fluorinated PTPDTTF₂T supporting a higher open-circuit voltage.

4.1 Introduction

Donor-acceptor (D-A) copolymers are widely used in applications such as organic photovoltaics (OPVs) and organic field effect transistors (OFETs)^[1] due to their attractive light harvesting and charge transporting properties. In order to improve the performance of these materials, several structural modifications are available. Besides adjusting the molecular weights of the polymers, the solubilizing side chains can be manipulated by modifying the branching point, length as well as position along the polymer backbone.^[2] Moreover, substituents can be introduced along the polymer backbone. Especially fluorine was proven to be an efficient substituent to improve the performance of polymers in optoelectronic devices.^[3-8] Fluorination can lower the material's energy levels while maintaining the band gap, resulting in an increased open-circuit voltage, when combined with fullerene as acceptor material in organic solar

cells.^[5,9–11] Additionally, the fluorine atoms induce a dipole along the C-F bond and, therefore, inter- and intramolecular interactions are promoted.^[12] Thus, planarization of the polymer backbone occurs via non-covalent interactions of fluorine with neighboring substituents.^[13,14] Higher backbone planarity as well as a closer solid-state packing can improve charge transport.^[15] Furthermore, fluorination can also improve electron transporting behavior due to the high electronegativity of fluorine.^[16] Fluorination of the donor unit or acceptor unit (or indeed both) in low bandgap (LBG) copolymers has been reported in the literature. Examples of fluorinated monomer units include benzotriazole,^[3] benzothiadiazole,^[9,17–19] quinoxaline,^[7] thieno[3,4-*b*]thiophene,^[20] isoindigo,^[21,22] phenyl,^[10,23–26] thiophene^[5,27–29] as well as bithiophene.^[4,6,8,11] Depending on the monomer unit, mono-, di- or tetra-fluorination is possible with the influence of the degree of fluorination studied in several reports.^[11,25] In particular the degree of fluorination was extensively studied in a D-A polymer consisting of bithiophene and benzothiadiazole, where fluorination of one or both moieties is possible. A power conversion efficiency (PCE) of 9.1% was achieved with monofluorinated benzothiadiazole and 3,3'-difluoro-2,2'-bithiophene.^[30]

Besides the structural modification of D-A copolymers, the device performance can be altered by the processing conditions, which can influence the alignment of crystallites with respect to the substrate surface. In general, the planar π -conjugated polymer backbones can orient either in an edge-on or face-on manner to the substrate and in very special cases end-on alignment is also possible.^[31,32] This thin film alignment considerably influences the performance in devices dependent on the device geometry. A face-on alignment is generally thought to favor bulk charge transport in solar cells, whereas an edge-on alignment is considered to favor interfacial lateral charge transport in OFETs.^[1] Even though many structural and physical properties of conjugated polymers can be theoretically predicted, it is usually very difficult to forecast the orientation behavior of semiconducting polymers. Therefore, processing is an important tool to optimize the alignment as desired in the device geometry. This was, for example, shown for thin films of poly(3-hexylthiophene) (P3HT).^[33,34] P3HT exhibits different aggregation behavior depending on solvent quality, with the alignment of crystallites in thin film also strongly influenced by processing conditions.^[1,35] As a consequence, charge transport can be altered by processing from different solvents^[33,36] with tuning of microstructure also possible through the use of solvent additives^[37] and the mixing of good and poor solvents.^[38] The pre-aggregation of polymer chains has also been shown to be beneficial for improving order and charge

transport.^[39,40] Recently, it was shown for difluorobenzothiadiazole-based polymers that face-on and edge-on alignment can be tuned by simply changing the processing solvent.^[41] The influence of processing solvent on device performance in fullerene based solar cells has also been discussed in the literature for P3HT^[42] as well as low band gap polymers.^[17,43,44]

In D-A copolymers containing thieno[3,4-c]pyrrole-4,6-dione (TPD) as the acceptor unit, only a few examples of fluorination are known.^[45,46] Li and coworkers copolymerized thiophene flanked TPD with difluoro-bithiophene or bithiophene, achieving an improved PCE upon fluorination.^[47] The number of thiophenes in the repeating unit also highly influences the performance of TPD copolymers.^[48] A maximum PCE of 7.7% was achieved with terthiophene as the comonomer, with the position of the solubilizing alkyl side chains on the thiophene units found to be crucial for performance.^[49] Due to the positive effect of fluorine substitution on device performance (as confirmed by many studies in the literature) and the attractive properties of TPD copolymers, we have chosen to study the effect of fluorination on the TPD-terthiophene copolymer, substituting the central thiophene with the corresponding difluorinated thiophene. These two polymers are compared regarding crystallinity and charge transport properties in OFETs and the performance is evaluated in terms of the nature of the chain alignment. Moreover, the influence of processing on thin film alignment, charge transport and solar cell performance is studied in detail. In this paper, we show that a desired alignment – such as edge-on for OFET application – can be achieved by varying the processing conditions. Thus, for the same copolymer PTPD₃TTT, a very high OFET hole mobility of $0.12 \text{ cm}^2\text{V}^{-1}\text{s}^{-1}$ was obtained by suppression of face-on alignment by processing from dichlorobenzene. The OPV performance is as well dependent on the casting solvent achieving a significant higher PCE by processing from chloroform. Here, the thin film alignment in PC₇₁BM blends is not determining rather the blend morphology, which is impacted by the casting solvent.

4.2 Experimental part

4.2.1 Materials and methods

All commercially available reagents were used without further purification unless otherwise noted. Reactions under microwave irradiation were performed in a Biotage Initiator Eight+ Microwave. Size exclusion chromatography (SEC) was carried out on an Agilent (Polymer Laboratories Ltd.) PL-SEC 220 high temperature chromatographic unit equipped with three linear mixed bed columns (PSS Polefin linear XL) and DP and RI detectors. Analysis was performed at 160 °C using 1,2,4-trichlorobenzene as the mobile phase. For sample preparation, the polymer (0.1 wt-%) was dissolved in the mobile phase solvent in an external oven and the solutions were run without filtration. The molecular weights of the samples were referenced to polystyrene standards ($M_w = 518\text{-}2,600,000 \text{ g mol}^{-1}$, $K = 12.100$ and $\text{Alpha} = 0.707$). Cyclic voltammetry was performed in thin films under moisture- and oxygen-free conditions using tetra-*n*-butylammonium hexafluorophosphate in acetonitrile with a concentration of 0.1 M as electrolyte solution. A three-electrode assembly connected to a potentiostat (model 263A, EG&G Princeton Applied Research) was used at a scan rate of 100 m V s^{-1} . Glass substrates coated with ITO ($10 \Omega \square^{-1}$) were used as working electrodes, onto which thin films from CHCl_3 solutions with a concentration of 5 mg mL^{-1} at 1500 rpm were deposited by spin coating. A platinum wire in the respective electrolyte solution and an Ag wire in an AgNO_3 solution in acetonitrile (0.1 M) were used as counter and reference electrode, respectively. Each measurement was calibrated by the internal standard ferrocene/ferrocenium. Absorption measurements were carried out on a JASCO V-670 spectrophotometer. Fluorescence spectroscopy was performed on a JASCO FP-8600 spectrofluorometer using the maximum of transition as excitation wavelength. The optical properties in solution were analyzed either in chloroform or dichlorobenzene (0.01 mg mL^{-1}) using quartz cuvettes with an internal diameter of 10 mm. For solid state measurements, thin films were spin coated on glass slides from chloroform solutions (5 mg mL^{-1}) at 1500 rpm. Thermogravimetric analysis (TGA) was performed on a Netzsch STA 449 F3 Jupiter at a heating rate of 10 K min^{-1} under nitrogen atmosphere. The temperature of decomposition $T_{5\%}$ was determined at 5% mass loss. Flash DSC measurements were conducted on a Mettler-Toledo Flash DSC 1 at scan rates between 50 and 1000 K min^{-1} under nitrogen. GIWAXS measurements were performed at the SAXS/WAXS beamline at the Australian Synchrotron.^[50] Samples were prepared by spin coating polymer films onto silicon

wafers (n-doped with Sb) from chloroform or pre-heated dichlorobenzene (DCB) solutions (15-20 mg mL⁻¹) at 1000-1500 rpm. Samples relevant to organic solar cells were prepared as described below. Films from DCB solutions were put under high vacuum overnight in order to remove residual solvent. 11 keV X-rays were used with 2D scattering patterns recorded on a Dectris Pilatus 1M detector. The sample to detector distance was calibrated using a silver behenate scattering standard. Scattering patterns were collected from incidence angles (α) between 0.02° and 0.35° with an X-ray exposure time of 3 s. Three separate 1 s exposures were taken with different lateral positions to fill in the gaps between the detector elements. These different exposures were combined in software. Data was analyzed using a modified version of NIKA 2D^[51] based in IgorPro. The organic thin film transistors with a bottom gate, bottom contact architecture were purchased from Fraunhofer IPMS (OFET Gen. 4). A heavily n-doped silicon wafer (doping at wafer surface: $n \sim 3 \times 10^{17} \text{ cm}^{-3}$) was used as the substrate and gate electrode. The gate electrode was separated from the source and drain electrodes by a silicon dioxide (thermal oxidation) dielectric (230 nm \pm 10nm). Source and drain electrodes were made from gold with a thickness of 30 nm with a layer of 10 nm ITO adhesion layer. One chip carried four groups with four identical transistors with a channel length of 2.5, 5, 10 and 20 μm , respectively, and a channel width of 10 mm. The substrates were rinsed with acetone and purified by ultrasonification in acetone and 2-propanol for 10 min each. After plasma treatment for 15 min at 50 °C, silanisation with octadecyltrichlorosilane in toluene (1 vol%) at 60 °C for 1h was conducted. The devices were rinsed with toluene and stored in 2-propanol before spin coating. Films were spin coated from chloroform or pre-heated DCB solutions (10 mg mL⁻¹) at 5000 rpm under ambient conditions and directly transferred into the glove box. Current-Voltage characteristics were measured under nitrogen atmosphere using an Agilent B1500 Semiconductor Parameter Analyzer. Annealing was performed at 100 °C and 250 °C for 15 min each under nitrogen atmosphere. The charge carrier mobility was calculated using equation (1), where I_{DS} is the drain-source current, V_G the gate voltage, L the channel length, W the channel width and C_i the capacitance. Therefore, the square root of the drain-source current $I_{DS}^{1/2}$ was plotted against the gate voltage V_G in the saturation regime and the slope of the resulting curve was determined to calculate the mobility.

$$\mu_{sat} = \left(\frac{\partial \sqrt{I_{DS}}}{\partial V_G} \right)^2 \cdot \frac{2L}{WC_i} \quad (1)$$

Inverted organic solar cells were fabricated with the following architecture: ITO/PEIE/Active Layer/MoO_x/Ag. ITO-coated glass substrates were first sequentially cleaned in acetone and 2-propanol for 10 minutes each before UV-ozone treatment for 10 minutes. Next, a 0.4% PEIE (polyethylenimine ethoxylated) in 2-methoxyethanol solution (Sigma Aldrich) was spin cast on to the substrates at 5000 rpm for 60 seconds. The subsequent films were dried at 120 °C for 15 minutes before being transferred into a nitrogen-filled glove box, where active layers were deposited. A 1:2 Donor:PC₇₁BM ratio was used for both PTPD_{TTT} and PTPD_{TF₂T} devices fabricated from chloroform and dichlorobenzene, each with 3% 1,8-Diiodooctane (DIO), with a solution concentration of 15 g/L. Substrates and solutions were both heated to 55 °C and 140 °C for chloroform and DCB solutions respectively, in order to avoid aggregation of the polymer in solution prior to spin casting. PTPD_{TF₂T} in dichlorobenzene was especially susceptible to this, accounting for the large standard deviation observed in solar cell parameters. Optimized active layers were then spin cast for 60 seconds at 3000 RPM for both PTPD_{TTT} and PTPD_{TF₂T} in dichlorobenzene and 1000 RPM in chloroform. These had thicknesses of 54 ± 6 nm (DCB) and 161 ± 5 nm (chloroform) for PTPD_{TTT}, and 84 ± 16 nm (DCB) and 138 ± 18 nm (chloroform) for PTPD_{TF₂T}. Following active layer deposition, substrates were transferred to an Angstrom Engineering Covap evaporator in order to deposit 12 nm of molybdenum oxide (0.3 Å s⁻¹) and 100 nm of silver (1.0 Å s⁻¹). Finally, edge clips were fitted to the substrates and they were encapsulated by epoxy and glass prior to being removed from the glove box for characterization. A Photo Emission Tech model SS550AAA solar simulator was used to simulate AM1.5G radiation with 100 mW cm⁻² irradiance. Intensity was calibrated using a silicon reference cell with a KG3 glass filter. *J-V* characteristics of devices were characterized using a Keithley 2635 source meter. External quantum efficiency (EQE) spectra were measured using a spot size less than the active area of the pixel in the device. This allows for a cross-check with the measured *J_{SC}* under the solar simulator, as it measures the EQE independently of the device active area. Prior to measurement, a Thorlabs FDS-100CAL photo-diode was used for calibration. An Oriel Cornerstone 130 monochromator was used to disperse light from a tungsten filament (Newport 250 W QTH).

4.2.2 Synthesis procedures

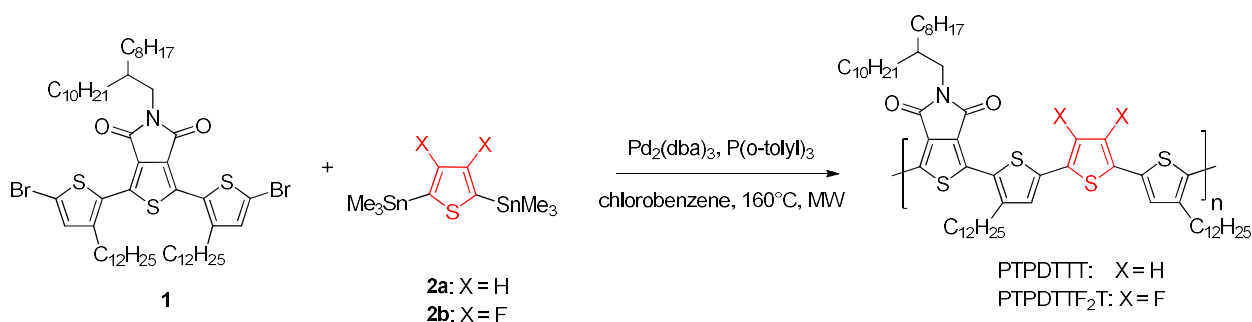
PTPDTTT: A microwave vial was loaded with the monomers 1,3-bis(5-bromo-3-dodecylthiophen-2-yl)-5-(2-octyldodecyl)-4*H*-thieno[3,4-*c*]pyrrol-4,6(5*H*)-dione **1** (199 mg, 0.183 mmol, 1 eq) and 2,5-bis(trimethylstannyl)thiophene **2a** (74.8 mg, 0.183 mmol, 1 eq). Tri(*o*-tolyl)phosphine (6.67 mg, 0.022 mmol, 0.12 eq). and chlorobenzene (61 mM) were added. After degassing by argon bubbling for 10 min, tris(dibenzylideneacetone)dipalladium(0) (5.01 mg, 5.48 μ mol, 0.03 eq) was added. The microwave vial was sealed and purged with argon once more. The polymerization was conducted at 160 °C for 1 h under microwave irradiation. After cooling to room temperature, 2-tributyltinthiophene was added to end-cap the polymers and the reaction mixture was stirred for 5 min at 160 °C. This end-capping step was subsequently repeated with 2-bromothiophene. The polymer solution was precipitated in methanol (300 mL) and filtered. Further purification was carried out by sequential Soxhlet extraction using methanol, acetone, *n*-hexane and dichloromethane. Finally, the polymer was collected with chloroform and the solution was concentrated under reduced pressure. Precipitation in methanol, filtration and drying in vacuum yielded the desired polymer (181 mg, 87%).

PTPDTTF₂T: A microwave vial was loaded with the monomers 1,3-bis(5-bromo-3-dodecylthiophen-2-yl)-5-(2-octyldodecyl)-4*H*-thieno[3,4-*c*]pyrrol-4,6(5*H*)-dione **1** (210 mg, 0.192 mmol, 1 eq) and 3,4-difluoro-2,5-bis(trimethylstannyl)thiophene **2b** (85.6 mg, 0.192 mmol, 1 eq). Tri(*o*-tolyl)phosphine (7.03 mg, 0.023 mmol, 0.12 eq) and chlorobenzene (38 mM) were added. After degassing by argon bubbling for 10 min, tris(dibenzylideneacetone)dipalladium(0) (5.28 mg, 5.77 μ mol, 0.03 eq) was added. The microwave vial was sealed and purged with argon once more. The polymerization was conducted at 160 °C for 1 h under microwave irradiation. After cooling to room temperature, 2-tributyltinthiophene was added to end-cap the polymers and the reaction mixture was stirred for 5 min at 160 °C. This end-capping step was subsequently repeated with 2-bromothiophene. The polymer solution was precipitated in methanol (300 mL) and filtered. Further purification was carried out by sequential Soxhlet extraction using methanol, acetone, *n*-hexane and dichloromethane. Finally, the polymer was collected with chloroform and the solution was concentrated under reduced pressure. Precipitation in methanol, filtration and drying in vacuum yielded the desired polymer (168 mg, 88%).

4.3 Results and discussion

4.3.1 Synthesis and characterization of copolymers

The synthesis of the thiophene flanked TPD monomer **1** starts from the dibromo functionalized TPD. In order to flank the TPD with two thiophenes carrying linear dodecyl alkyl chains in a Stille cross-coupling reaction, the substituted thiophene is first converted to the corresponding tin compound. The subsequent Stille reaction is followed by bromination yielding the TPD monomer **1** in high purity. Detailed synthetic procedures and analysis can be found in the Supporting Information. As comonomers, 2,5-bis(trimethylstannyl)thiophene as well as 3,4-difluoro-2,5-bis(trimethylstannyl)thiophene were used.^[15] The Stille polycondensation was carried out in chlorobenzene at 160 °C in a microwave reactor using tris(dibenzylideneacetone)dipalladium as a catalyst and tri(*o*-tolylphosphine) as a ligand (Scheme 4.1). After the polymerization, two end-capping steps using 2-bromothiophene followed by 2-tributyltinthiophene were conducted and the polymers were purified by Soxhlet extraction.



Scheme 4.1. Stille polymerization of the TPD monomer flanked with thiophene **1** with the respective thiophene monomers **2**, which are non-fluorinated as well as fluorinated.

Analysis of the molecular weight distribution was carried out at high temperatures in 1,2,4-trichlorobenzene with PS calibration. In Table 4.1, the results of the size exclusion chromatography (SEC) are summarized showing a number-averaged molecular weight (M_n) of 62 400 g mol⁻¹ for PTPDTTT. In contrast, the number-average molecular weight of the fluorinated polymer PTPDTF₂T is 27 500 g mol⁻¹. Fluorination leads to an increase of backbone planarity and, therefore, the solubility of the polymer is reduced, thus probably limiting the degree of polymerization in chlorobenzene. The dispersities (\mathcal{D}) of both polymers are in the range of 1.6 to 1.8 and the samples possess relatively high molecular weights. The SEC elugrams showing the molecular weight distributions can be found in the Supporting Information (Figure S 4.1).

Table 4.1. Molecular weights from SEC as well as thermal, optical and electrochemical properties of PTPDTTT and PTPDITTF₂T.

	M_n^a [kg mol ⁻¹]	M_w^a [kg mol ⁻¹]	\bar{D}	$T_{5\%}^b$ [°C]	T_m^c [°C]	T_c^c [°C]	ΔH_m^c [J g ⁻¹]	E_{opt}^d [eV]	IP^e [eV]
PTPDITTT	62.4	99.9	1.60	434	261	246	27	1.83	-5.54
PTPDITTF ₂ T	27.5	48.1	1.75	434	273	260	29	1.85	-5.85

^a Determined by SEC in 1,2,4-trichlorobenzene at 160 °C using PS calibration; ^b decomposition at 5% mass loss determined by TGA at 10 K min⁻¹ under N₂; ^c melting and crystallization temperature from DSC measurements at 10 K min⁻¹ under N₂; ^d optical gap determined by absorption edge in thin films; ^e ionization potential (IP) determined from cyclic voltammetry in thin films.

The thermal properties of these polymers were studied by TGA and DSC measurements. Both polymers, PTPDITTT and PTPDITTF₂T, show a decomposition ($T_{d5\%}$ measured at 5% mass loss) at around 434 °C (see Figure S 4.2). In DSC measurements, melting as well as crystallization could be clearly observed for both polymers at scan rates of 10 K min⁻¹. The second heating and cooling curves are summarized in Figure 4.1a. In Table 4.1 the melting as well as crystallization temperatures are given together with the melting enthalpies. The melting enthalpies for the two polymers are in the same range indicating a similar degree of crystallinity and the very high ΔH_m values observed for these polymers indicate that the degree of crystallinity is high. However, an exact degree of crystallinity can be calculated only after doing extensive WAXS studies. Fluorination increases the melting and crystallization temperatures indicating an increase in crystal thickness. In detail, the polymer PTPDITTT shows a melting temperature at 261 °C in contrast to the fluorinated polymer, which shows a higher melting temperature of 273 °C.

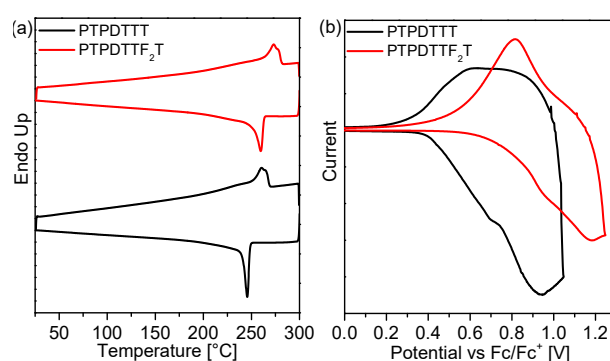


Figure 4.1. (a) Second heating and cooling curves from differential scanning calorimetry for PTPDITTT and PTPDITTF₂T measured at scan rates of 10 K min⁻¹ under nitrogen. (b) Cyclic voltammetry measurements in thin films of PTPDITTT and PTPDITTF₂T.

The electrochemical properties were determined by cyclic voltammetry measurements of thin films using a three-electrode assembly in acetonitrile. For both polymers, only the oxidation process could be observed, which is reversible as shown in Figure 4.1b. The calculation of the ionization potential was carried out from the onset of the oxidation potential using ferrocene as

an internal standard. Figure 4.1b clearly shows that the onset of the oxidation potential is shifted to higher potentials upon fluorination. The ionization potential yields a value of -5.54 eV for PTPDTTT and -5.85 eV for the fluorinated polymer. In summary, the ionization potential is lowered by fluorination by around 0.3 eV, which is expected to facilitate a higher open circuit voltage in solar cell devices. Since both polymers have similar optical gaps, a lowering of HOMO in the fluorinated copolymer should be accompanied by a similar lowering of LUMO, if the exciton binding energies in both are similar. Thus, this may also favor electron transport in PTPDTTF₂T.

4.3.2 Optical properties

The optical properties of both polymers were studied by UV-Vis and photoluminescence measurements in solution and in the solid state. To understand the aggregation behavior and the quality of aggregates as a function of temperature and nature of solvent, temperature dependent UV-Vis measurements were carried out in two different solvents, namely chloroform and dichlorobenzene. The temperature of the polymer solution was gradually increased in 5 °C steps for chloroform and 10 °C steps for dichlorobenzene starting from 20 °C and recording a UV-Vis spectrum at each temperature. In Figure 4.2, the UV-Vis spectra for the two polymers in the different solvents are given.

For PTPDTTT in chloroform, a broad and relatively featureless absorption band at 580 nm is observed at room temperature with a slight shoulder at 650 nm (Figure 4.2a), which can be attributed to a weakly aggregated species. By increasing the temperature of the solution, the intensity of the absorption band at 580 nm decreases while a new absorption band at 480 nm emerges. This absorption band originates from the absorption of non-aggregated polymer chains, with most of the solution being almost aggregate-free at 55 °C. Consequently, a clear isosbestic point at 515 nm is observed, which indicates that two species – aggregated and non-aggregated – can be interconverted and that only these two species exist. In dichlorobenzene, the vibronic bands of the aggregated species are more pronounced than in chloroform (Figure 4.2c). The aggregates are again completely converted to amorphous coil-like structures at 55 °C and the isosbestic point is found at 522 nm.

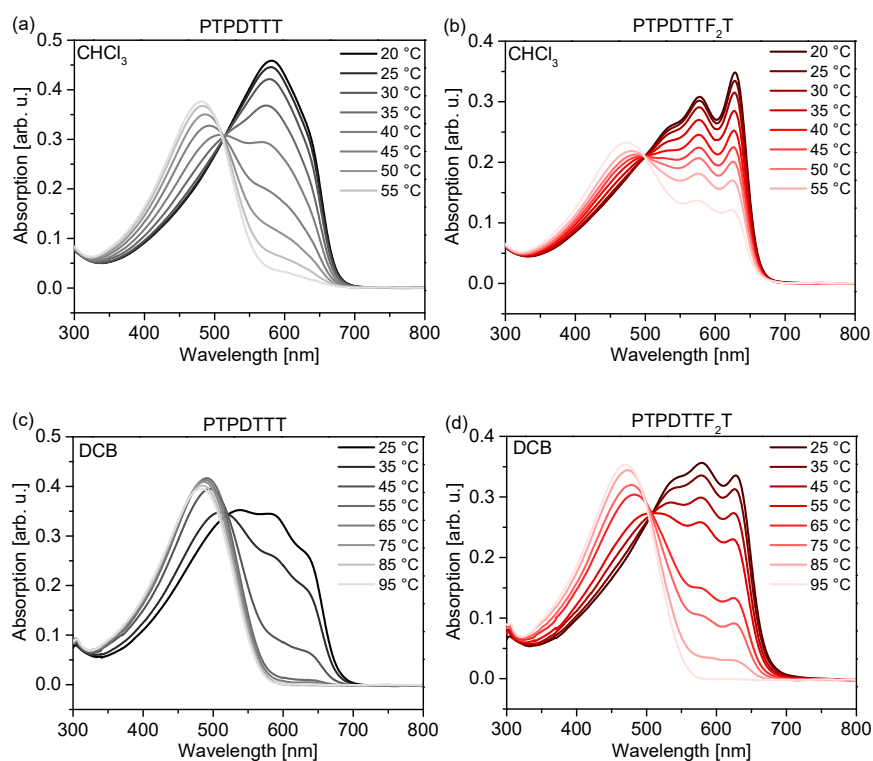


Figure 4.2. Temperature dependent UV-Vis spectroscopy in chloroform (a,b) and DCB (c,d) solution for PTPDTTT (a,c) and PTPDTTF₂T (b,d), respectively.

On the contrary, the fluorinated copolymer PTPDTTF₂T shows a stronger aggregation behavior reflected by the pronounced vibronic bands at 580 nm and 630 nm in both solvents at 25 °C. In chloroform, the aggregates cannot be completely deagglomerated at 55 °C (Figure 4.2b), but in DCB the aggregates are fully converted into the amorphous phase only at 95 °C (Figure 4.2d). The absorption band of the non-aggregated species appears at 475 nm. In comparison, the relative intensities of the 0-0 and 0-1 transitions considerably differ in the two different solvents indicating different nature or quality of aggregation.^[52,53] In detail, for the polymer PTPDTTF₂T the ratio I_{0-0}/I_{0-1} , which is an indicator of the quality and nature of aggregates, gives a value of 1.13 in chloroform and 0.94 in DCB indicating stronger aggregation in chloroform. The isosbestic point is observed at 500 nm in chloroform and at 508 nm in DCB. Due to the planarization of the backbone by incorporation of fluorine, the crystallinity and tendency towards aggregation is increased. Therefore, the aggregates cannot be completely dissolved in chloroform for the fluorinated polymer and higher temperatures are required to completely disassemble the aggregates in DCB. Both polymers show a perfect isosbestic point, which is blue shifted upon fluorination.

The UV-Vis and photoluminescence spectra recorded in thin films cast from chloroform are depicted in Figure 4.3. The corresponding spectra of thin films cast from DCB only slightly differs and can be found in the Supporting Information (Figure S 4.3). For as-cast films, both polymers show a similar absorption edge, which gives a value of ~ 1.8 eV for the optical gap. A main absorption peak is observed at 578 nm for both polymers. Whereas only a shoulder arises for PTPDTT at 622 nm, this peak is considerably more pronounced for the fluorinated polymer. The photoluminescence spectra display two peaks at 703 nm and 706 nm for both polymers. Here also the fluorinated polymer exhibits stronger aggregation features compared to the non-fluorinated one.

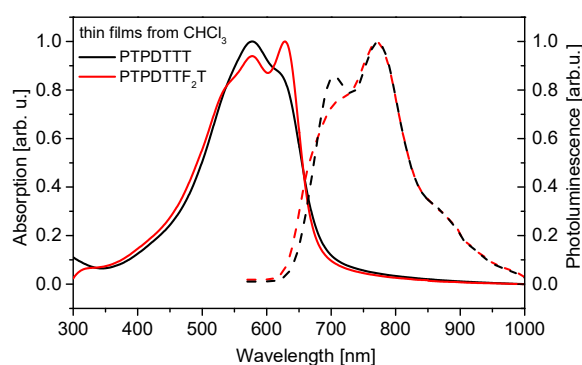


Figure 4.3. UV-Vis (solid lines) and photoluminescence (dashed lines) spectra of thin films cast from chloroform of PTPDTT (black) and PTPDTTF₂T (red).

In summary, fluorination improves crystallinity and, therefore, strongly influences the aggregation behavior in solution while keeping the optical gap in thin film essentially unaffected. However, the aggregation behavior cannot only be influenced by the molecular structure but also by the choice of solvent. The degree of pre-aggregation and the quality of aggregates depend strongly on the conditions of processing and the solvent used for solution casting. Therefore, we further investigated the influence of processing on structural alignment and device performance.

4.3.3 GIWAXS

The crystalline packing in the solid state was investigated in neat thin films with grazing incidence wide angle X-ray scattering (GIWAXS). Due to different aggregation behavior of the copolymers in chloroform and DCB solutions, films cast from these two solvents were studied as-cast and after annealing at 250 °C for 15 min. The corresponding two-dimensional scattering patterns, which were taken near the critical angle for maximum scattering intensity, are presented in

Figure 4.4a and b. One-dimensional scattering profiles along the out-of-plane (Q_z) and in-plane (Q_{xy}) directions are summarized in Figure 4.4c and d.

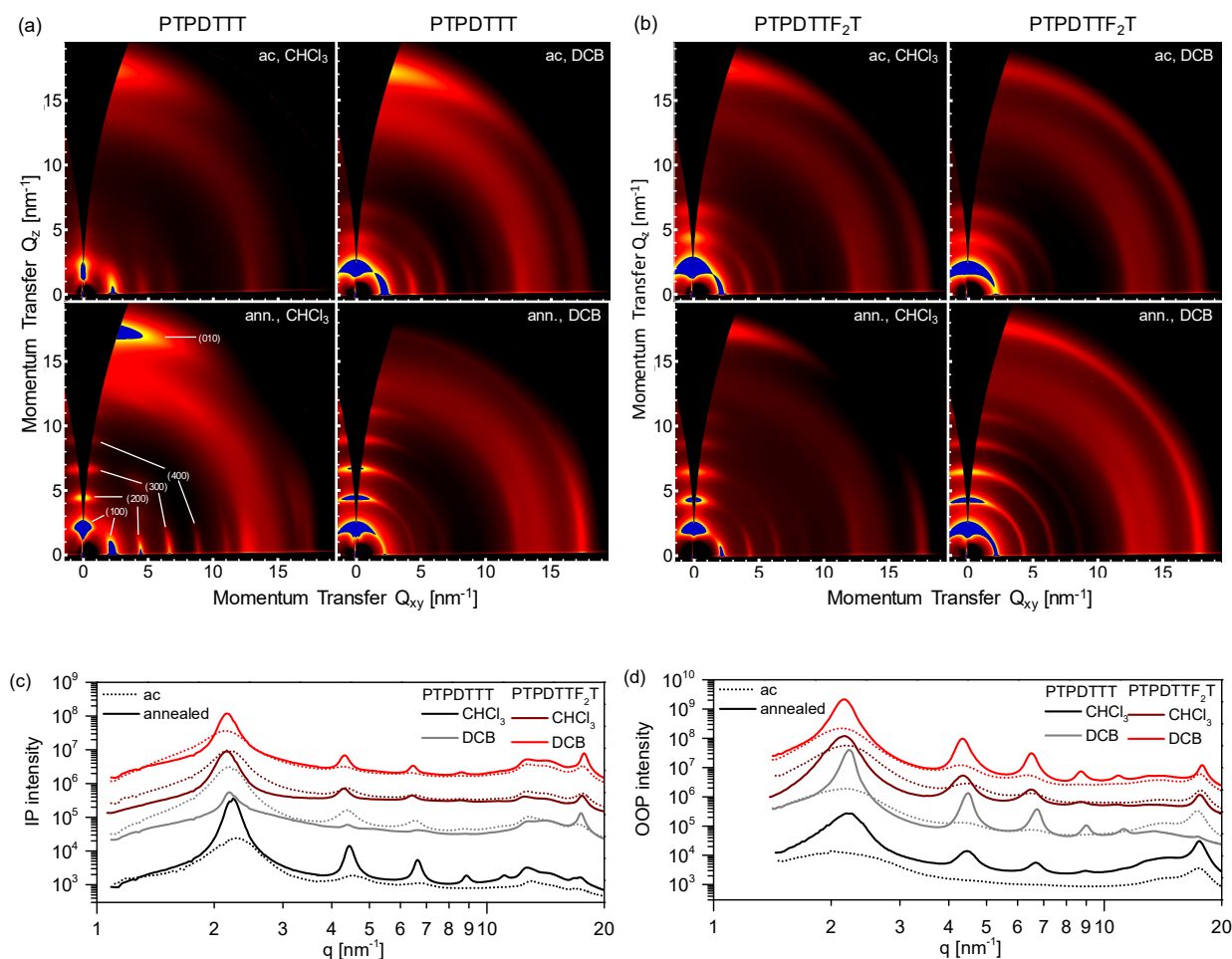


Figure 4.4. Two dimensional GIWAXS scattering patterns of PTPDTT (a) and PTPDTTF₂T (b) for as-cast (ac) and annealed (ann.) films cast from chloroform and DCB, respectively. Corresponding one-dimensional GIWAXS scattering profiles taken along the in-plane (c) and out-of-plane (d) directions are also shown.

Alkyl lamella stacking indexed as (k00) up to multiple orders and π - π stacking peaks indexed as (010) are clearly observed in all scattering patterns. Corresponding distances and coherence lengths are given in Table 4.2. All polymers show very high crystallinity with up to five orders of lamellar stacking, which are present in varying extents in the in-plane as well as out-of-plane direction, indicating that in general a mixture of edge-on and face-on crystallites exists. In order to quantify the degree of edge-on vs. face-on thin film alignment, the Herman's Orientation Parameter S ^[54] was calculated based on the polar angle-dependence of the (200) peak. A value for the S parameter of $S = 1$ indicates perfectly edge-on orientation, while a value of $S = -0.5$ corresponds to a perfectly face-on orientation. In Figure 4.5, S is plotted as a function of incidence angle. Whereas the top of the film is probed by angles below the critical angle, the

bulk of the film is probed by angles higher than the critical angle. For PTPDTTT, the as-cast films from both chloroform and DCB show a similar S parameter of around $S = -0.1$, indicating that no edge-on but face-on orientation is more dominant. The alkyl stacking as well as π - π stacking distances are considerably increased for as-cast films deposited from DCB compared to films deposited from chloroform. In contrast, the molecular stacking distances of the annealed films in both cases do not differ, resulting in an alkyl stacking distance of 2.82 nm and a π - π stacking distance of 0.36 nm. Upon annealing the diffraction peaks sharpen and multiple orders of the alkyl stacking peak become visible, caused by an increase in coherence length. Interestingly, the coherence lengths of the thin films cast from DCB are higher, indicating a higher degree of long-range order and better solid-state packing. Furthermore, the annealing of films cast from chloroform results in a more distinct face-on orientation, whereas the annealing of films from DCB results in an increased proportion of edge-on orientation. Similar results were obtained for the fluorinated polymer. However, the thin film alignment of the fluorinated polymer is not as much as of PTPDTTT affected by processing from different solvents. Due to the higher crystallinity of the fluorinated polymer, the reorganization of the polymer chains upon annealing is impeded. Comparison of the crystalline parameters shows that the alkyl stacking is increased by fluorination. Referenced to PTPDTTT, the π - π stacking distance is decreased due to planarization of the polymer backbone upon fluorination.

Table 4.2. Crystalline parameters analyzed from GIWAXS patterns.

		CHCl ₃				DCB			
		d_{alkyl}^a	ζ_{alkyl}^b	$d_{\pi-\pi}^c$	$\zeta_{\pi-\pi}^d$	d_{alkyl}^a	ζ_{alkyl}^b	$d_{\pi-\pi}^c$	$\zeta_{\pi-\pi}^d$
		[nm]	[nm]	[nm]	[nm]	[nm]	[nm]	[nm]	[nm]
PTPDTTT	as cast	2.75	18.7	0.348	3.21	2.86	24.8	0.363	4.40
	annealed	2.82	48.0	0.360	5.72	2.82	60.1	0.360	7.65
PTPDTF ₂ T	as cast	2.86	22.9	0.356	3.97	2.93	20.1	0.357	3.89
	annealed	2.91	43.8	0.357	5.69	2.90	51.1	0.353	7.40

^a Alkyl spacing; ^b alkyl spacing coherence length; ^c π - π stacking spacing; ^d π - π stacking coherence length.

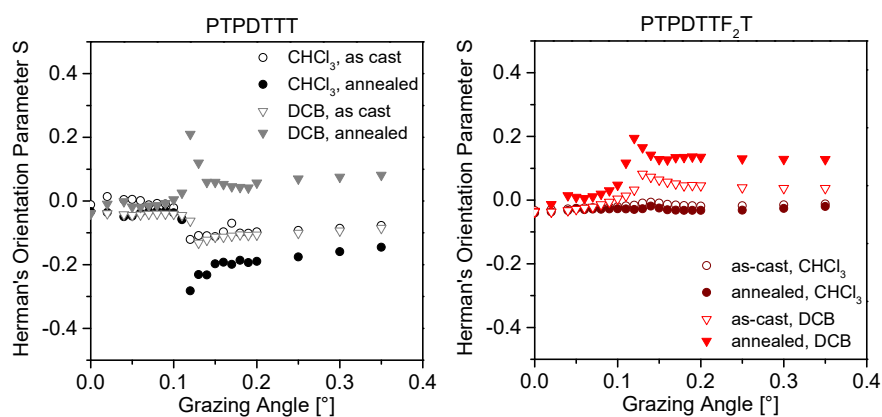


Figure 4.5. Herman's orientation parameter S vs. incident angle for (a) PTPDTTT and (b) PTPDTTF₂T.

In summary, processing in combination with thermal annealing has a strong impact on the crystallinity and thin film alignment, especially for PTPDTTT. Films processed from chloroform give a higher degree of face-on alignment, which is suppressed by casting the films from DCB. Due to the higher crystallinity of PTPDTTF₂T, this swapping of alignment effect is much less pronounced. From the GIWAXS results, it becomes clear that processing should influence the performance of these materials in OFET devices as well as organic solar cells, since a face-on alignment is expected to favor solar cell performance, whereas an edge-on alignment favors charge transport in an OFET device.

4.4 OFET

Organic field effect transistors using a bottom gate (n-doped Si), bottom contact configuration were fabricated for both polymers. The charge carrier mobilities were determined in both p-type and n-type regime by tuning the gate voltage. Within narrow channels parallel to the substrate, the charge transport is determined at the dielectric interface in thin films. Details regarding device preparation as well as the mobility determination can be found in the experimental section. Thin films were processed from both chloroform and DCB solutions. Additionally, the influence of annealing is investigated and thus charge carrier mobilities were determined in as-cast films and after annealing at 100 °C and 250 °C, the latter being a compromise between close to the high melting temperatures of the polymers and avoiding dewetting of the films. Annealing at 100 °C was performed in order to eliminate residual solvent from device processing. Furthermore, annealing at 250 °C was conducted to improve crystallization and, therefore, charge carrier mobility. All output and transfer characteristics of the two polymers processed

from chloroform and DCB before and after annealing are shown in the Supporting Information. The charge carrier mobilities are summarized in Table 4.3.

Table 4.3. Summary of hole and electron mobilities for PTPDTTT and PTPDTTF₂T processed from chloroform and DCB, respectively. Mobilities are reported for as-cast films and after annealing at 100 °C and 250 °C, respectively.

		p-type						n-type			
		as-cast		100 °C		250 °C		100 °C		250 °C	
		μ_h^a	V_T^b	μ_h^a	V_T^b	μ_h^a	V_T^b	μ_e^a	V_T^b	μ_e^a	V_T^b
		[cm ² V ⁻¹ s ⁻¹]	[V]	[cm ² V ⁻¹ s ⁻¹]	[V]	[cm ² V ⁻¹ s ⁻¹]	[V]	[cm ² V ⁻¹ s ⁻¹]	[V]	[cm ² V ⁻¹ s ⁻¹]	[V]
PTPDTTT	CHCl ₃	0.0082 ± 0.002	-5	0.015 ± 0.002	-6	0.078 ± 0.007	-13	-	-	-	-
	DCB	0.037 ± 0.003	-6	0.074 ± 0.005	-5	0.120 ± 0.015	-10	-	-	0.015 ± 0.005	31
PTPDTTF ₂ T	CHCl ₃	0.0035 ± 0.001	-24	0.014 ± 0.002	-13	0.039 ± 0.006	-13	0.002 ± 0.001	43	0.006 ± 0.002	48
	DCB	0.011 ± 0.002	-7	0.047 ± 0.004	-5	0.061 ± 0.011	-12	0.011 ± 0.004	30	0.032 ± 0.009	26

^a Hole (μ_h) and electron (μ_e) mobilities calculated from the saturation regime. ^b Threshold voltages (V_T) determined in the saturation regime. All values are averaged for a minimum of six devices.

In the as-cast films processed from chloroform (which favors face-on alignment for PTPDTTT and nor preference for PTPDTTF₂T) both polymers show exclusively p-type behavior with hole mobilities in the range of 10⁻³ cm² V⁻¹ s⁻¹, whereas the mobility of PTPDTTT slightly exceeds that of the fluorinated polymer. After annealing at 100 °C the hole mobilities are increased by one order of magnitude and are identical for both materials. Further annealing at 250 °C leads to an even higher hole mobility of 0.08 cm² V⁻¹ s⁻¹ for PTPDTTT. The hole mobility of the fluorinated polymer, PTPDTTF₂T, is slightly lower, reaching a value of 0.04 cm² V⁻¹ s⁻¹. Additionally, this polymer shows n-type behavior at high gate voltages after annealing at 100 °C as well as at 250 °C. Due to fluorination of the backbone, the electron affinity is increased, enabling n-type behavior. Additionally, the LUMO level is lowered by fluorination, which should enable injection of electrons from the gold electrodes. As discussed in the electrochemical characterization, PTPDTTF₂T is expected to have lower-lying LUMO values, which may facilitate electron injection at high voltages. As expected, the n-type behavior is only facilitated at gate voltages of 60 V.

Processing from DCB (where both polymers show a preference towards edge-on alignment) has a stronger impact on charge carrier mobilities, especially for the as-cast samples and after thermal annealing at 100 °C. All mobilities are improved up to one order of magnitude compared to processing from chloroform. After annealing at 250 °C, maximum hole mobilities of 0.12 cm² V⁻¹ s⁻¹ for PTPDTTT and of 0.061 cm² V⁻¹ s⁻¹ for PTPDTTF₂T are reached. Additionally, electron transport evolves even for PTPDTTT after annealing at 250 °C by processing from DCB.

As shown in the previous chapter, processing from DCB suppresses face-on alignment favoring more edge-on alignment, which is beneficial for lateral charge transport in OFET devices.

4.5 Organic solar cells

PTPDTTT and PTPDTTF₂T were blended with the electron acceptor PC₇₁BM to explore the potential application of these polymers in organic solar cells exploiting the advantages of alignment as a function of processing. The absorption profiles of PTPDTTT and PTPDTTF₂T blended with PC₇₁BM are shown in Figure 4.6a for thin films processed from chloroform and dichlorobenzene. The blends show good coverage of the solar spectrum, with the addition of PC₇₁BM extending the absorption profile below 400 nm. At lower wavelengths, the polymers exhibit similar absorption behavior that is solvent-dependent as opposed to substituent-dependent. In fact, the films spin cast from chloroform exhibit higher absorption across all wavelengths below 500 nm. Similar to the UV-Vis spectra of the neat films (Figure 4.3), the PTPDTTT:PC₇₁BM blend shows only a shoulder at ~620 nm while the PTPDTTF₂T:PC₇₁BM blend shows a more pronounced vibronic peak at this wavelength, irrespective of solvent, indicating its higher level of aggregation in solution compared to the PTPDTTT:PC₇₁BM blend. Additional absorption spectra of neat PC₇₁BM films cast from the two solvents as well as comparative spectra of polymers and blends can be found in the Supporting Information.

The solar cell performance of PTPDTTT has previously been reported,^[48,49] with high device efficiencies of over 7.7% achieved largely due to a fill factor (FF) of almost 80%, when PC₇₁BM was used as the acceptor. An open circuit voltage (V_{oc}) of ~0.8 V was also reported for PTPDTTT:PC₇₁BM blends. With blends based on PTPDTTF₂T it is expected to achieve a higher open circuit voltage. Solar cells based on PTPDTTT:PC₇₁BM and PTPDTTF₂T:PC₇₁BM blends in chloroform and dichlorobenzene were fabricated with a weight ratio of 1:1 (Figure 4.6b-c). The previous studies of PTPDTTT found that processing with the solvent additive 1,8-diiodooctane resulted in improved solar cell performance while annealing of the active layers did not. It was also found here that DIO improved solar cell performance with all blends processed with 3 vol.% DIO. When PTPDTTT:PC₇₁BM blends were spin cast from chloroform, a maximum PCE of 5.3% was achieved. This reduction in performance, compared to previously published results, is due to a lower FF (67 %) and short circuit current density (J_{sc}). Devices made from PTPDTTF₂T did indeed show an increase in V_{oc} over PTPDTTT, with V_{oc} increasing from 0.8 V to 0.9 V with fluorination, reflecting the lower HOMO level of PTPDTTF₂T. However, PTPDTTF₂T devices

showed a lower FF compared to the PTPDTT devices, with FF decreasing from 67% to 57.2%, which accounts for the overall PCE of 5.4% being comparable to that achieved for PTPDTT. Spin casting from dichlorobenzene lowered the performance of both polymers, with maximum PCEs of 3.4% and 2.4% achieved for PTPDTT and PTPDTTF₂T blends, respectively. The EQE spectra were integrated in order to estimate the potential J_{SC} and agree to within 15% of the values observed from measuring the J - V characteristics. Any discrepancies are likely to do with edge effects associated with the small active area of the cells (0.045 cm²).

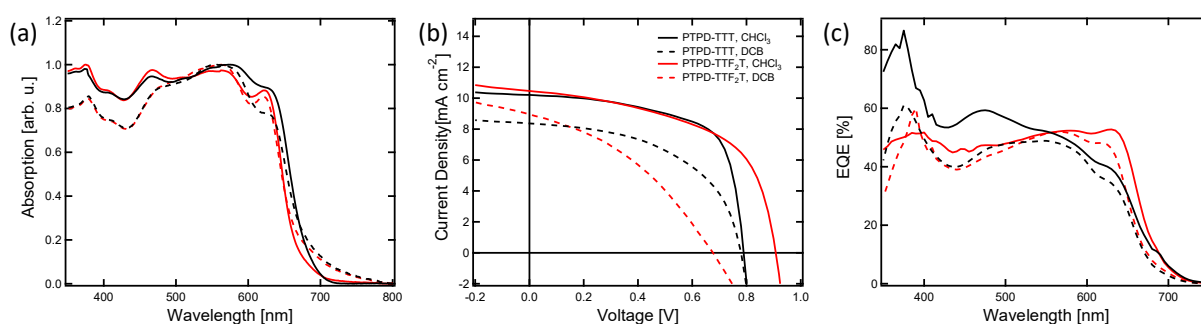


Figure 4.6. Current-voltage characteristics (a), external quantum efficiency (b), and UV-Vis absorption spectra of the polymer:fullerene blends (c).

Table 4.4. Solar cell performance for the two copolymers processed from chloroform and dichlorobenzene.

		J_{SC} [mA cm ⁻²]	V_{OC} [V]	FF [%]	PCE [%]	EQE J_{SC} [mA cm ⁻²]
PTPD-TTT	CHCl ₃	10.0 ± 0.3	0.80 ± 0.0	67.0 ± 2.3	5.3 ± 0.1	9.2
	DCB	8.4 ± 0.6	0.77 ± 0.0	53.0 ± 6.0	3.4 ± 0.7	7.6
PTPD-TTF ₂ T	CHCl ₃	10.4 ± 0.9	0.91 ± 0.0	57.2 ± 2.0	5.4 ± 0.3	8.9
	DCB	9.0 ± 0.8	0.73 ± 0.2	37.2 ± 0.5	2.4 ± 0.5	8.1

GIWAXS was used to further understand the effect of processing solvent on the morphology of PTPDTT and PTPDTTF₂T blends with PC₇₁BM (Figure 4.7). 1D line cuts are included in the Supporting Information. The systematic changes in polymer orientation with changes in processing and fluorination observed for neat films (Figure 4.4) are not reflected in the blends with both polymers only exhibiting weak ordering in blends processed from chloroform and DCB. The polymers in general also show a more edge-on orientation in blends, meaning that the potentially favorable face-on orientation of neat PTPDTT is not retained in blends. The blends processed from chloroform show additional sharp, relatively isotropic features which are attributed to PCBM crystallites.

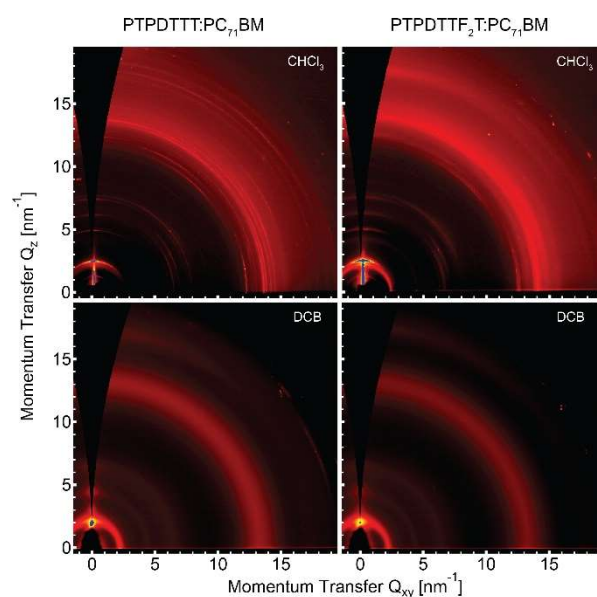


Figure 4.7. 2D GIWAXS images cast from chloroform (top) and dichlorobenzene (bottom) for PTPD(TTT):PC₇₁BM (left) and PTPD(TTF₂T):PC₇₁BM (right) blends.

Atomic force microscopy (AFM) was employed in order to further characterize the blend morphology for both polymers. The images in Figure S 4.16 clearly show the strong dependence of morphology on spin casting solvent. While films of both PTPD(TTT) and PTPD(TTF₂T) blends cast from chloroform appear to have similar distributions of well-mixed donor and acceptor domains, changing the casting solvent to dichlorobenzene drastically alters the films' morphology. For the PTPD(TTT):PC₇₁BM blend cast from DCB, the domains become larger as the morphology is coarsened, indicating less favorable conditions for exciton dissociation, as there are fewer donor/acceptor interfaces available. Interestingly, the PTPD(TTF₂T):PC₇₁BM film cast from DCB shows drastically different features compared to the other three films. The surface roughness is noticeably reduced, and the film surface appears to contain small aggregates of one phase surrounded by a more continuous second phase. Transmission electron microscopy (TEM) images (Figure 4.8) confirm that changing the casting solvent from chloroform to dichlorobenzene noticeably coarsens the morphology. Both PTPD(TTT) and PTPD(TTF₂T) blends cast from chloroform show a fibrillar morphology, with these fibers expanding in both length and width when the casting solvent is changed to dichlorobenzene. This coarsening of the morphology may be responsible for the reduced J_{SC} observed in devices, because a larger separation between donor and acceptor phases can reduce the likelihood of exciton dissociation and free carrier collection at the contacts. Between PTPD(TTT) and PTPD(TTF₂T), it appears the fluorinated polymer has a coarser morphology in combination with PC₇₁BM when cast from both

chloroform and dichlorobenzene, which can explain the lower J_{SC} and FF observed in these devices.

Overall, the casting solvent plays an important role in the device performance observed in both materials. Chloroform is the preferred solvent for high-performing solar cells due to its faster drying kinetics, limiting the coarser morphology formation observed in films cast from DCB. Fluorination was found to improve the V_{OC} by 0.1 V for devices cast from chloroform, however a reduction in both J_{SC} and FF, most likely caused by a coarser morphology, resulted in similar device efficiencies of 5.3% and 5.4% for PTPDTTT and PTPDTTF₂T respectively.

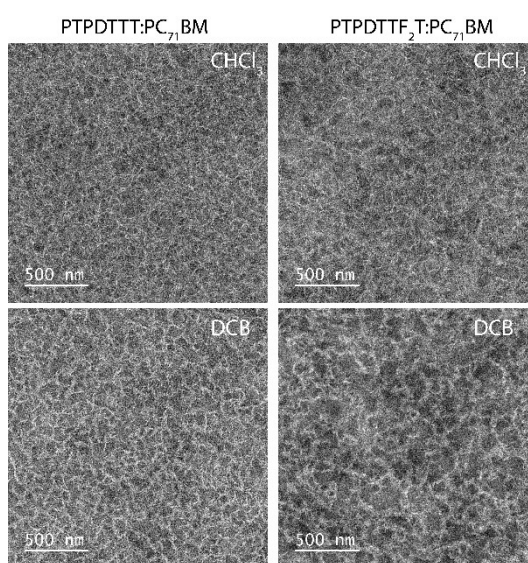


Figure 4.8. TEM images for blends spin cast from chloroform (top) and dichlorobenzene (bottom) for PTPDTTT (left) and PTPDTTF₂T (right).

4.6 Conclusion

We synthesized two highly crystalline copolymers based on thieno[3,4-c]pyrrole-4,6-dione, PTPDTTT and PTPDTTF₂T, with and without fluorination and showed that processing has a strong effect on thin film alignment and therefore on both OFET and OPV device performance. Upon fluorination, the melting as well as crystallization temperature is considerably increased, and the polymers show different solution dependent aggregation behavior, which impacted the processability for organic solar cells. The crystallinity of films cast from chloroform and DCB solutions were analyzed with GIWAXS measurements. Additionally, the influence of thermal annealing was also studied, which has a great impact on solid-state packing and, therefore, on charge carrier mobilities. PTPDTTT films processed from chloroform give predominately face-on orientation after thermal annealing, whereas processing from DCB suppresses the formation of

these face-on stacks resulting in higher hole mobilities in OFET devices. The hole mobility of the fluorinated polymer is slightly lower compared to the non-fluorinated polymer. However, the fluorinated polymer shows ambipolar charge transport behavior after thermal annealing, especially when processed from DCB, which again does not favor any face-on alignment. In inverted solar cells, higher power conversion efficiencies are achieved in combination with PC₇₁BM by processing from chloroform. Fluorination indeed leads to a higher open-circuit voltage due to the lowered ionization potential and compensates the loss in fill factor leading to similar PCE values of 5.3% and 5.4% for PTPDTTT and PTPDTTF₂T respectively.

4.7 Acknowledgements

We acknowledge financial support from Bavarian State Ministry for Education, Science and the Arts (Project: SolTech) and Deutsche Forschungsgemeinschaft (SFB 840). This work was performed in part at the SAXS/WAXS beamline at the Australian Synchrotron, part of ANSTO.

4.8 References

- [1] R. Hildner, A. Köhler, P. Müller-Buschbaum, F. Panzer, M. Thelakkat, *Adv. Energy Mater.* **2017**, *85*, 1700314.
- [2] T. Marszalek, M. Li, W. Pisula, *Chem. Commun.* **2016**, *52*, 10938.
- [3] S. C. Price, A. C. Stuart, L. Yang, H. Zhou, W. You, *J. Am. Chem. Soc.* **2011**, *133*, 4625.
- [4] J. W. Jo, J. W. Jung, H.-W. Wang, P. Kim, T. P. Russell, W. H. Jo, *Chem. Mater.* **2014**, *26*, 4214.
- [5] J. Wolf, F. Cruciani, A. El Labban, P. M. Beaujuge, *Chem. Mater.* **2015**, *27*, 4184.
- [6] J. W. Jung, J. W. Jo, C.-C. Chueh, F. Liu, W. H. Jo, T. P. Russell, A. K.-Y. Jen, *Adv. Mater.* **2015**, *27*, 3310.
- [7] S. Chen, Y. An, G. K. Dutta, Y. Kim, Z.-G. Zhang, Y. Li, C. Yang, *Adv. Funct. Mater.* **2016**, *27*, 1603564.
- [8] S. Zhang, Y. Qin, M. A. Uddin, B. Jang, W. Zhao, D. Liu, H. Y. Woo, J. Hou, *Macromolecules* **2016**, *49*, 2993.
- [9] Y. Zhang, J. Zou, C.-C. Cheuh, H.-L. Yip, A. K.-Y. Jen, *Macromolecules* **2012**, *45*, 5427.
- [10] J. Y. Lee, J. W. Jo, W. H. Jo, *Organic Electronics* **2015**, *20*, 125.
- [11] K. Kawashima, T. Fukuhara, Y. Suda, Y. Suzuki, T. Koganezawa, H. Yoshida, H. Ohkita, I. Osaka, K. Takimiya, *J. Am. Chem. Soc.* **2016**, *138*, 10265.

- [12] N. Leclerc, P. Chávez, O. A. Ibraikulov, T. Heiser, P. Lévêque, *Polymers* **2016**, *8*, 11.
- [13] N. E. Jackson, B. M. Savoie, K. L. Kohlstedt, M. La Olvera de Cruz, G. C. Schatz, L. X. Chen, M. A. Ratner, *J. Am. Chem. Soc.* **2013**, *135*, 10475.
- [14] T. Lei, X. Xia, J.-Y. Wang, C.-J. Liu, J. Pei, *J. Am. Chem. Soc.* **2014**, *136*, 2135.
- [15] C. J. Mueller, C. R. Singh, M. Fried, S. Huettner, M. Thelakkat, *Adv. Funct. Mater.* **2015**, *25*, 2725.
- [16] C. J. Mueller, C. R. Singh, M. Fried, S. Huettner, M. Thelakkat, *Adv. Funct. Mater.* **2015**, *25*, 2725.
- [17] J. R. Tumbleston, B. A. Collins, L. Yang, A. C. Stuart, E. Gann, W. Ma, W. You, H. Ade, *Nat. Photonics* **2014**, *8*, 385.
- [18] J. W. Jo, S. Bae, F. Liu, T. P. Russell, W. H. Jo, *Adv. Funct. Mater.* **2015**, *25*, 120.
- [19] A. Najari, P. Berrouard, C. Ottone, M. Boivin, Y. Zou, D. Gendron, W.-O. Caron, P. Legros, C. N. Allen, S. Sadki, M. Leclerc, *Macromolecules* **2012**, *45*, 1833.
- [20] Y.-J. Hwang, B. A. E. Courtright, A. S. Ferreira, S. H. Tolbert, S. A. Jenekhe, *Adv. Mater.* **2015**, *27*, 4578.
- [21] G. E. Park, S. Choi, J. Shin, M. J. Cho, D. H. Choi, *Organic Electronics* **2016**, *34*, 157.
- [22] Y. Yang, R. Wu, X. Wang, X. Xu, Z. Li, K. Li, Q. Peng, *Chem. Commun.* **2014**, *50*, 439.
- [23] A. Luzio, D. Fazzi, F. Nübling, R. Matsidik, A. Straub, H. Komber, E. Giussani, S. E. Watkins, M. Barbatti, W. Thiel, E. Gann, L. Thomsen, C. R. McNeill, M. Caironi, M. Sommer, *Chem. Mater.* **2014**, *26*, 6233.
- [24] C. J. Mueller, E. Gann, C. R. McNeill, M. Thelakkat, *J. Mater. Chem. C* **2015**, *3*, 8916.
- [25] J. H. Park, E. H. Jung, J. W. Jung, W. H. Jo, *Adv. Mater.* **2013**, *25*, 2583.
- [26] P. Sonar, J. Chang, Z. Shi, J. Wu, J. Li, *J. Mater. Chem. C* **2015**, *3*, 2080.
- [27] Z. Fei, M. Shahid, N. Yaacobi-Gross, S. Rossbauer, H. Zhong, S. E. Watkins, T. D. Anthopoulos, M. Heeney, *Chem. Commun.* **2012**, *48*, 11130.
- [28] Y. Gao, X. Zhang, H. Tian, J. Zhang, D. Yan, Y. Geng, F. Wang, *Adv. Mater.* **2015**, *27*, 6753.
- [29] K. Do, Q. Saleem, M. K. Ravva, F. Cruciani, Z. Kan, J. Wolf, M. R. Hansen, P. M. Beaujuge, J.-L. Brédas, *Adv. Mater.* **2016**, *28*, 8197.
- [30] J. W. Jo, J. W. Jung, E. H. Jung, H. Ahn, T. J. Shin, W. H. Jo, *Energy Environ. Sci.* **2015**, *8*, 2427.
- [31] C. J. Mueller, E. Gann, C. R. Singh, M. Thelakkat, C. R. McNeill, *Chem. Mater.* **2016**, *28*, 7088.

- [32] T. Weller, M. Breunig, C. J. Mueller, E. Gann, C. R. McNeill, M. Thelakkat, *J. Mater. Chem. C* **2017**, *5*, 7527.
- [33] J.-F. Chang, B. Sun, D. W. Breiby, M. M. Nielsen, T. I. Sölling, M. Giles, I. McCulloch, H. Sirringhaus, *Chem. Mater.* **2004**, *16*, 4772.
- [34] J. Balko, G. Portale, R. H. Lohwasser, M. Thelakkat, T. Thurn-Albrecht, *J. Mater. Res.* **2017**, *32*, 1957.
- [35] J. Clark, J.-F. Chang, F. C. Spano, R. H. Friend, C. Silva, *Appl. Phys. Lett.* **2009**, *94*, 163306.
- [36] K. Vakhshouri, B. H. Smith, E. P. Chan, C. Wang, A. Salleo, C. Wang, A. Hexemer, E. D. Gomez, *Macromolecules* **2016**, *49*, 7359.
- [37] H.-C. Liao, C.-C. Ho, C.-Y. Chang, M.-H. Jao, S. B. Darling, W.-F. Su, *Mater. Today* **2013**, *16*, 326.
- [38] M. Chang, D. Choi, B. Fu, E. Reichmanis, *ACS Nano* **2013**, *7*, 5402.
- [39] A. Luzio, L. Criante, V. D'Innocenzo, M. Caironi, *Sci. Rep.* **2013**, *3*, 3425.
- [40] N.-K. Kim, S.-Y. Jang, G. Pace, M. Caironi, W.-T. Park, D. Khim, J. Kim, D.-Y. Kim, Y.-Y. Noh, *Chem. Mater.* **2015**, *27*, 8345.
- [41] M. Li, C. An, T. Marszalek, M. Baumgarten, H. Yan, K. Müllen, W. Pisula, *Adv. Mater.* **2016**, *28*, 9430.
- [42] M. A. Ruderer, S. Guo, R. Meier, H.-Y. Chiang, V. Körstgens, J. Wiedersich, J. Perlich, S. V. Roth, P. Müller-Buschbaum, *Adv. Funct. Mater.* **2011**, *21*, 3382.
- [43] S. Guo, W. Wang, E. M. Herzig, A. Naumann, G. Tainter, J. Perlich, P. Müller-Buschbaum, *ACS Appl. Mater. Interfaces* **2017**, *9*, 3740.
- [44] Y. J. Kim, W. Jang, S. Ahn, C. E. Park, D. H. Wang, *Organic Electronics* **2016**, *34*, 42.
- [45] S. Liu, Z. Kan, S. Thomas, F. Cruciani, J.-L. Brédas, P. M. Beaujuge, *Angew. Chem. Int. Ed.* **2016**, *55*, 12996.
- [46] S. Liu, Z. Kan, S. Thomas, F. Cruciani, J.-L. Brédas, P. M. Beaujuge, *Angew. Chem. Int. Ed.* **2016**, *55*, 12996.
- [47] K. Wang, Z. Xu, B. Guo, X. Guo, M. Zhang, Y. Li, *RSC Adv.* **2016**, *6*, 63338.
- [48] N. Zhou, X. Guo, R. Ponce Ortiz, T. Harschneck, E. F. Manley, S. J. Lou, P. E. Hartnett, X. Yu, N. E. Horwitz, P. Mayorga Burrezo, T. J. Aldrich, J. T. López Navarrete, M. R. Wasielewski, L. X. Chen, R. P. H. Chang, A. Facchetti, T. J. Marks, *J. Am. Chem. Soc.* **2015**, *137*, 12565.

- [49] X. Guo, N. Zhou, S. J. Lou, J. Smith, D. B. Tice, J. W. Hennek, R. P. Ortiz, J. T. L. Navarrete, S. Li, J. Strzalka, L. X. Chen, R. P. H. Chang, A. Facchetti, T. J. Marks, *Nat. Photonics* **2013**, *7*, 825.
- [50] N. M. Kirby, S. T. Mudie, A. M. Hawley, D. J. Cookson, H. D. T. Mertens, N. Cowieson, V. Samardzic-Boban, *J. Appl. Crystallogr.* **2013**, *46*, 1670.
- [51] J. Ilavsky, *J. Appl. Crystallogr.* **2012**, *45*, 324.
- [52] J. Clark, C. Silva, R. H. Friend, F. C. Spano, *Phys. Rev. Lett.* **2007**, *98*, 206406.
- [53] J. Clark, J.-F. Chang, F. C. Spano, R. H. Friend, C. Silva, *Appl. Phys. Lett.* **2009**, *94*, 163306.
- [54] L. A. Perez, P. Zalar, L. Ying, K. Schmidt, M. F. Toney, T.-Q. Nguyen, G. C. Bazan, E. J. Kramer, *Macromolecules* **2014**, *47*, 1403.

Supporting Information

Influence of the edge-on or face-on alignment of thieno[3,4-*c*]pyrrole-4,6-dione based copolymer films achieved by processing on devices

Tina Weller,^a Kira Rundel,^b Adam Welford,^b Christopher R. McNeill^b and Mukundan Thelakkat^{a*}

^a Applied Functional Polymers, Macromolecular Chemistry I, University of Bayreuth, 95440 Bayreuth, Germany.

^b Department of Materials Science and Engineering, Monash University, Wellington Road, Clayton VIC, 3800, Australia.

* Corresponding author: mukundan.thelakkat@uni-bayreuth.de

Table of Contents

1	Monomer Syntheses.....	93
1.1	Materials and Methods.....	93
1.2	Synthesis of the TPD monomer	93
2	Polymer Characterization	95
2.1	Size exclusion chromatography	95
2.2	Thermogravimetric Analysis (TGA)	96
3	UV-Vis and fluorescence spectroscopy	96
4	OFET <i>I</i> - <i>V</i> curves.....	97
5	UV-Visible Absorption of solid-state neat and blend films.	100
6	1D GIWAXS for blend films	101
7	AFM	102
8	References	102

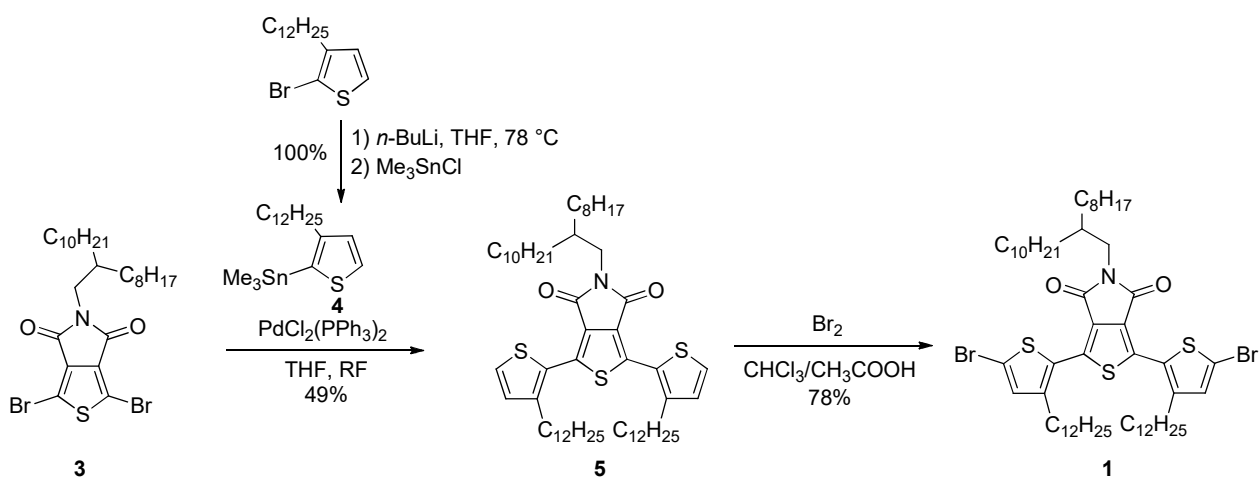
1 Monomer Syntheses

1.1 Materials and Methods

Water and air sensitive reactions were conducted in Schlenk apparatuses under argon, which were previously baked out in high vacuum. Commercially available solvents were purchased from Sigma Aldrich and Acros Organics in sealed bottles with mole sieve. ^1H - and ^{19}F -NMR spectra were recorded on a Bruker Avance spectrometer (300 MHz) with deuterated solvents purchased from Deutero. Chemical shifts are reported in ppm relative to the known value of residual solvent signal. Molecular weights were assessed either by electron ionization mass spectrometry performed on a Finnigan MAT 8500 spectrometer (70 eV) or by electrospray ionization mass spectrometry in high resolution (ESI/HRMS) performed on a Thermo Fisher Scientific Q Exactive Hybrid-Quadrupole-Orbitrap spectrometer.

1.2 Synthesis of the TPD monomer

The overall synthesis of the TPD monomer **1** is shown in Scheme S 4.1 and the synthetic procedures are adapted from literature.^[1,2] The synthesis of compound **3** can be found in the literature.^[3]



Scheme S 4.1. Synthesis of the TPD monomer **1**.

2-(trimethylstannyl)-3-dodecylthiophene **4**

A solution of 2-bromo-3-dodecylthiophene (2.50 g, 7.54 mmol, 1 eq) in 45 mL anhydrous tetrahydrofuran was cooled to -78 °C. Addition of a 2.5 M solution of *n*-butyl lithium in hexane (3.30 mL, 8.30 mmol, 1.1 eq) results in a yellow solution. After the solution was stirred for 1 h at -78 °C, trimethyltin chloride (2.00 g, 10.2 mmol, 1.35 eq) was added at -78 °C in one portion. The reaction mixture was further stirred for 30 min at -78 °C and allowed to warm to room temperature. After stirring for 1 h at room temperature water was added and the aqueous phase was extracted with diethyl ether twice. The combined organic phases were washed with water and saturated, aqueous solution of NaCl followed by drying over MgSO₄. Filtration and removal of the solvent by rotary evaporation yielded 2-(trimethylstannyl)-3-dodecylthiophene **4** (3.12 g, 7.51 mmol, 100%) as colorless liquid, which was used in the next step without further purification.

¹H-NMR (300 MHz, CDCl₃): δ = 7.53 (d, *J* = 4.7 Hz, 1H), 7.09 (d, *J* = 4.5 Hz, 1H), 2.55-2.66 (m, 2H), 1.57 (q, *J* = 7.7 Hz, 2H), 1.18-1.41 (m, 18H), 0.88 (t, *J* = 6.7 Hz, 3H), 0.37 ppm (s, 9H). EI-MS (70 eV): *m/z* 416 (M⁺).

1,3-Di(3-dodecylthien-2-yl)-5-(2-octyl-1-dodecyl)-4*H*-thieno[3,4-*c*]pyrrole-4,6(5*H*)-dione **5**

A solution of 1,3-dibromo-5-(2-octyl-1-dodecyl)-4*H*-thieno[3,4-*c*]pyrrol-4,6(5*H*)-dione **3** (1.42 g, 2.41 mmol, 1 eq) and 2-(trimethylstannyl)-3-dodecylthiophene **4** (3.00 g, 7.22 mmol, 3 eq) in 80 mL anhydrous tetrahydrofuran was degassed for 10 min. After addition of bis(triphenylphosphine)palladium(II) chloride (0.101 g, 0.144 mmol, 0.06 eq), the reaction mixture was stirred under reflux for 22 h. Addition of water was followed by extraction with dichloromethane for three times. The combined organic phases were washed with water and saturated, aqueous solution of NaCl, respectively. After drying over MgSO₄ and removal of the solvent by rotary evaporation, the raw product was purified by column chromatography (silica; *n*Hex:DCM 10:1-2:1) yielding 1,3-di(3-dodecylthien-2-yl)-5-(2-octyl-1-dodecyl)-4*H*-thieno[3,4-*c*]pyrrole-4,6(5*H*)-dione **5** (1.10 g, 1.18 mmol, 49%) as an orange solid.

¹H-NMR (300 MHz, CDCl₃): δ = 7.40 (d, *J* = 5.1 Hz, 2H), 7.01 (d, *J* = 5.3 Hz, 2H), 3.50 (d, *J* = 7.2 Hz, 2H), 2.79 (t, *J* = 7.8 Hz, 4H), 1.84 (bs, 1H), 1.64 (q, *J* = 7.5 Hz, 4H), 1.15-1.41 (m, 68H), 0.83-0.91 ppm (m, 12H). HRMS (ESI, positive): calc. for C₅₈H₉₅NO₂S₃ (M+H)⁺: 934.6598, found: 934.6589.

1,3-Di(5-bromo-3-dodecylthien-2-yl)-5-(2-octyl-1-dodecyl)-4H-thieno[3,4-c]pyrrole-4,6(5H)-dione **1**

A mixture of 50 mL chloroform and 10 mL acetic acid was added to 1,3-di(3-dodecylthien-2-yl)-5-(2-octyl-1-dodecyl)-4H-thieno[3,4-c]pyrrole-4,6(5H)-dione **5** (1.04 g, 1.11 mmol, 1 eq) and purged with argon. After the addition of bromine (0.115 mL, 2.23 mmol, 2 eq), the reaction mixture was stirred for 2.5 h at room temperature. Water was added, and the reaction mixture was extracted with chloroform. The combined organic phases were washed with saturated, aqueous solution of NaCl and dried over MgSO₄. After removal of the solvent by rotary evaporation, the raw product was purified by column chromatography (silica; *n*Hex:DCM 20:1-5:1) yielding 1,3-di(5-bromo-3-dodecylthien-2-yl)-5-(2-octyl-1-dodecyl)-4H-thieno[3,4-c]pyrrole-4,6(5H)-dione **1** (0.95 g, 0.87 mmol, 78%) as a yellow solid.

¹H-NMR (300 MHz, CDCl₃): δ = 6.97 (s, 2H), 3.49 (d, *J* = 7.4 Hz, 2H), 2.73 (t, *J* = 7.8 Hz, 4H), 1.83 (bs, 1H) 1.62 (q, *J* = 7.1 Hz, 4H), 1.18-1.37 (m, 68H), 0.83-0.91 ppm (m, 12H). HRMS (ESI, positive): calc. for C₅₈H₉₄Br₂NO₂S₃ (M+H)⁺: 1092.4788, found: 1092.4782.

2 Polymer Characterization

2.1 Size exclusion chromatography

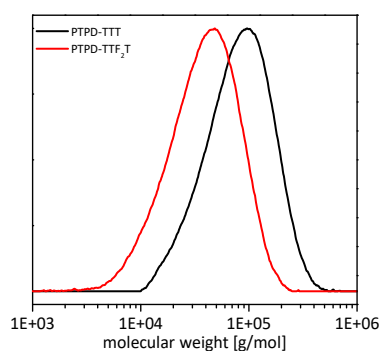


Figure S 4.1. Size exclusion chromatography of PTPDs in 1,2,4-trichlorobenzene at 160 °C using PS calibration.

2.2 Thermogravimetric Analysis (TGA)

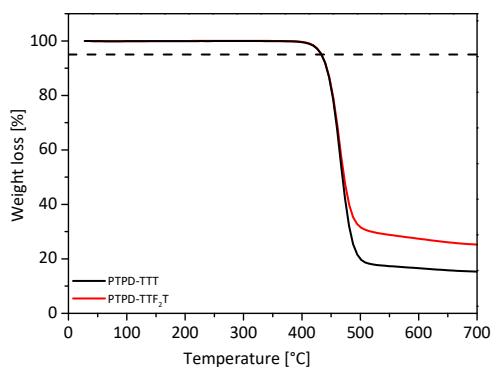


Figure S 4.2. Thermogravimetric analysis of the PTPDs with the decomposition onset ($T_{5\%}$).

3 UV-Vis and fluorescence spectroscopy

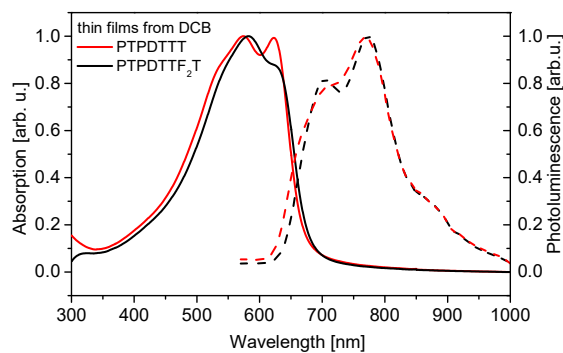


Figure S 4.3. UV-Vis (solid lines) and photoluminescence (dashed lines) spectra of thin films from DCB of PTPD-TTT (black) and PTPD-TTF₂T (red).

4 OFET I-V curves

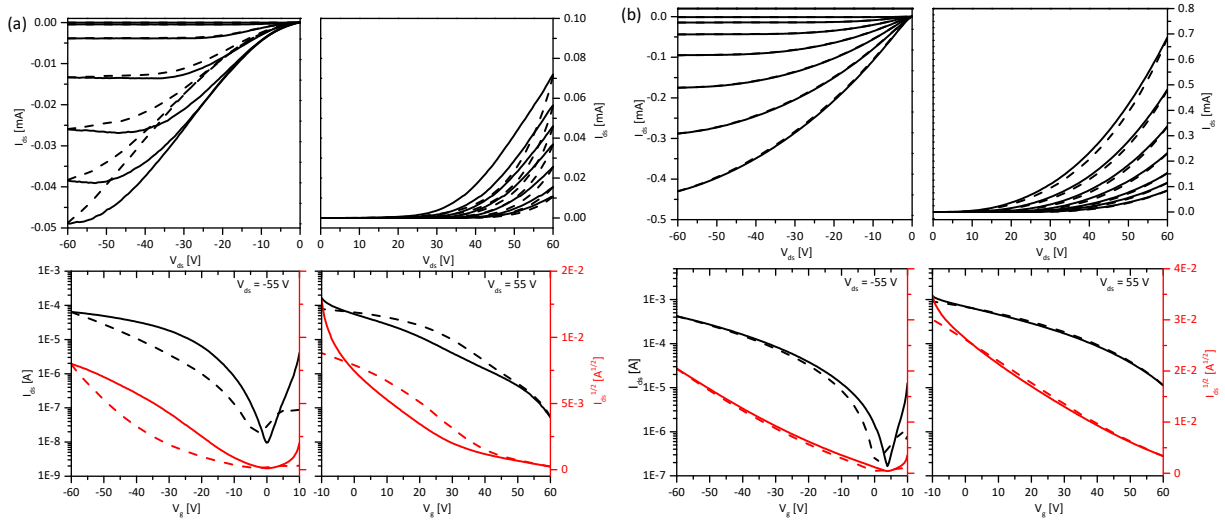


Figure S 4.4. OFET output (top) and transfer (bottom) characteristics: p-channel operation (left) and n-channel operation (right) of PTPDTT in the as-cast state processed from chloroform (a) and DCB (b). Solid lines represent forward scans and dashed lines reversed scans.

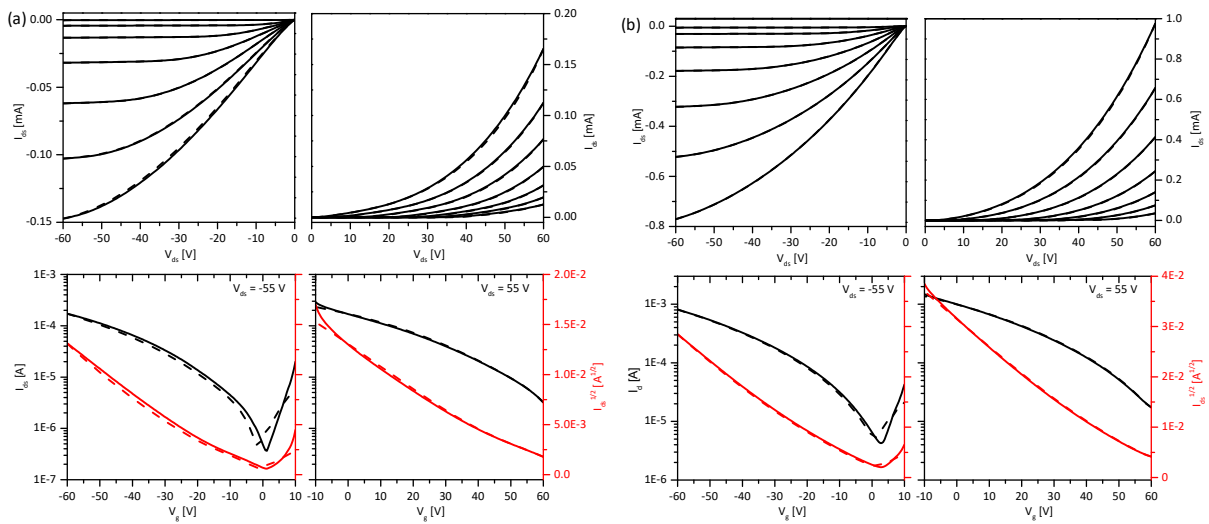


Figure S 4.5. OFET output (top) and transfer (bottom) characteristics: p-channel operation (left) and n-channel operation (right) of PTPDTT after thermal annealing at 100 °C processed from chloroform (a) and DCB (b). Solid lines represent forward scans and dashed lines reversed scans.

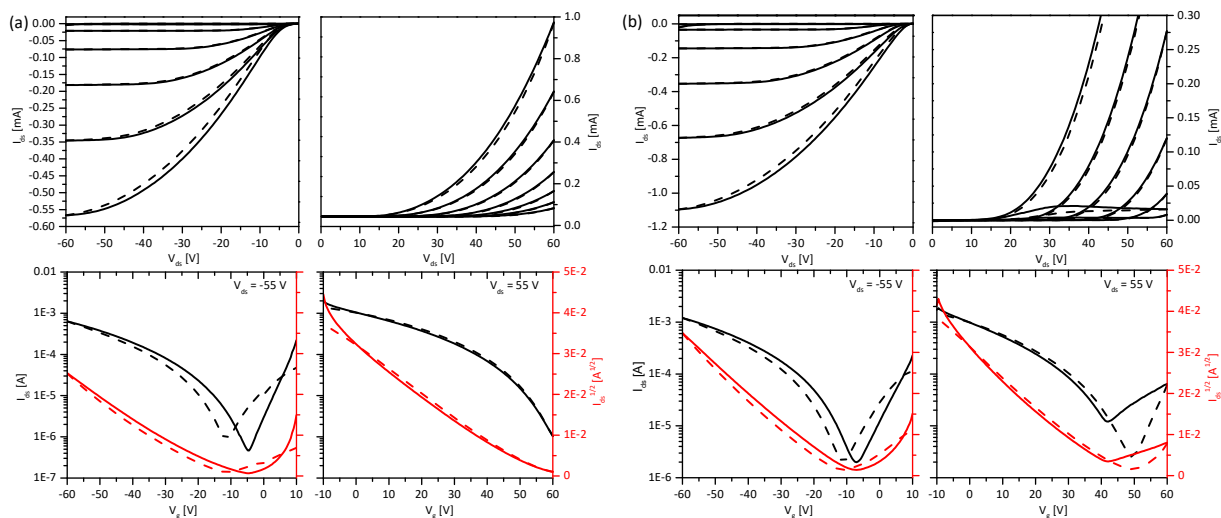


Figure S 4.6. OFET output (top) and transfer (bottom) characteristics: p-channel operation (left) and n-channel operation (right) of PTPDTT after thermal annealing at 250 °C processed from chloroform (a) and DCB (b). Solid lines represent forward scans and dashed lines reversed scans.

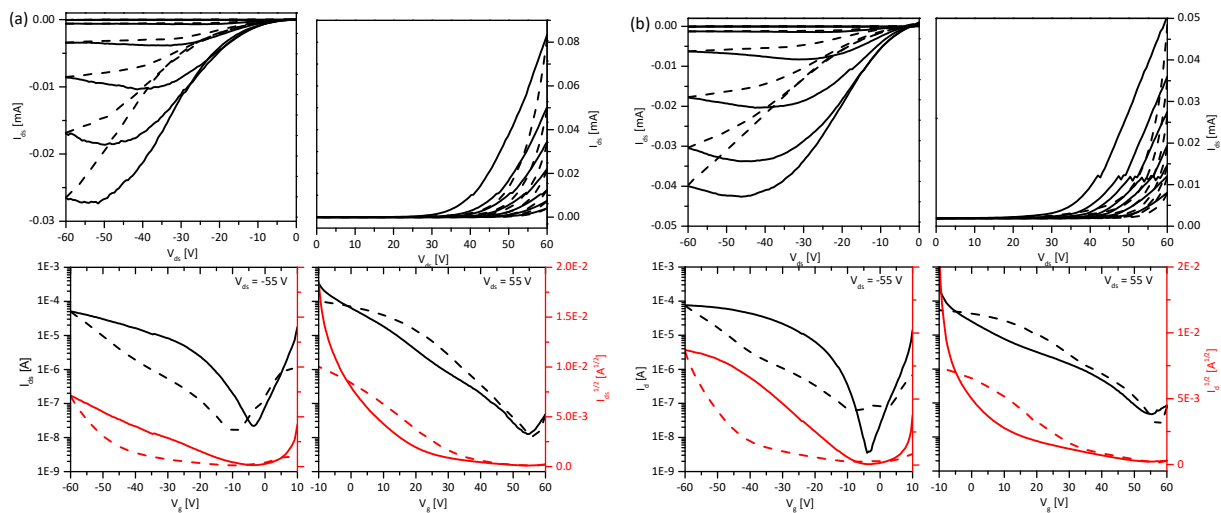


Figure S 4.7. OFET output (top) and transfer (bottom) characteristics: p-channel operation (left) and n-channel operation (right) of PTPDTF₂T in the as-cast state processed from chloroform (a) and DCB (b). Solid lines represent forward scans and dashed lines reversed scans.

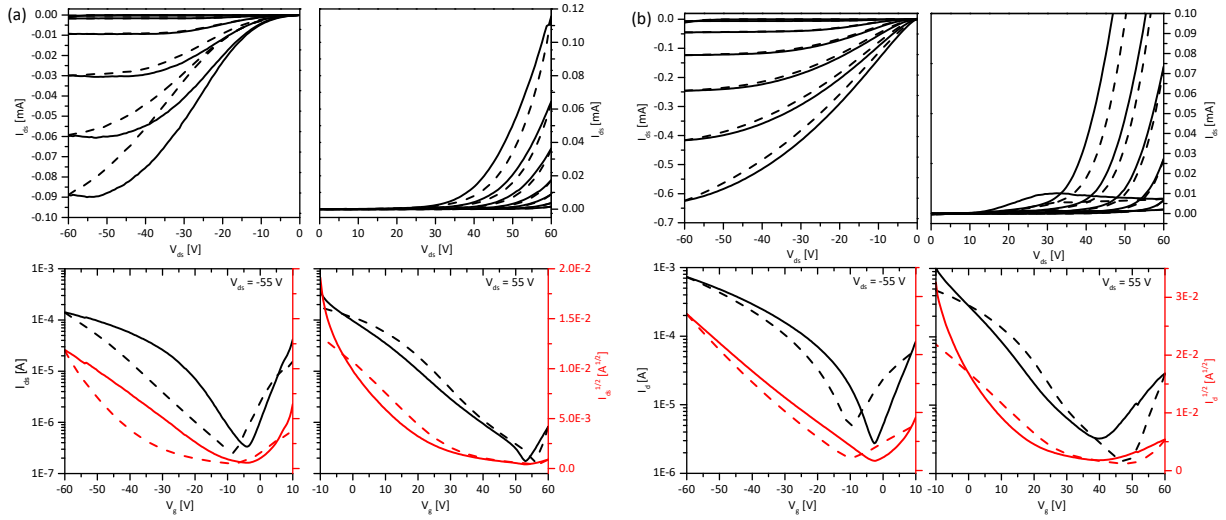


Figure S 4.8. OFET output (top) and transfer (bottom) characteristics: p-channel operation (left) and n-channel operation (right) of PTPDTTF₂T after thermal annealing at 100 °C processed from chloroform (a) and DCB (b). Solid lines represent forward scans and dashed lines reversed scans.

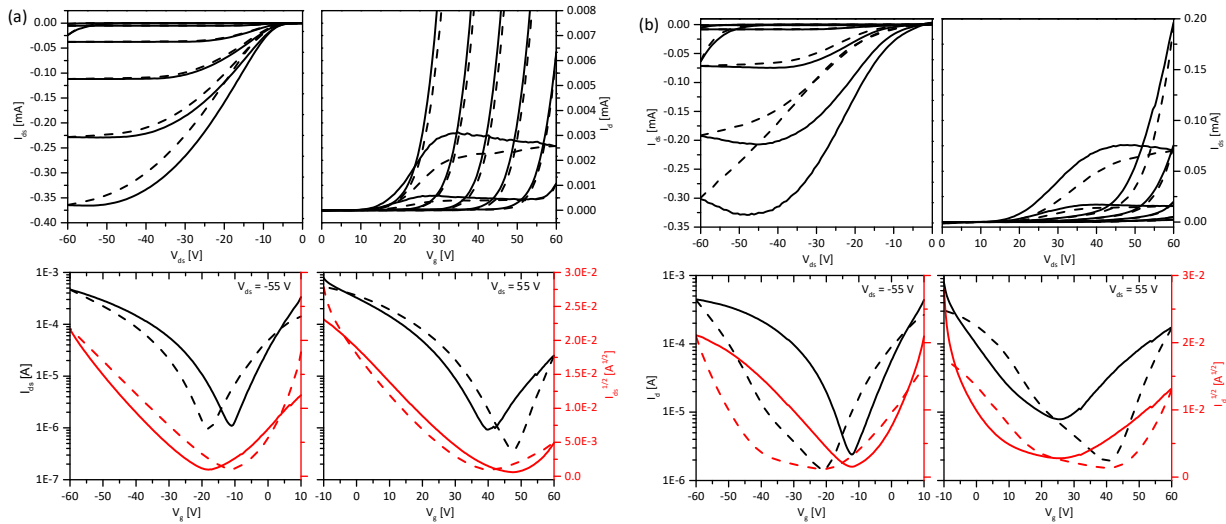


Figure S 4.9. OFET output (top) and transfer (bottom) characteristics: p-channel operation (left) and n-channel operation (right) of PTPDTTF₂T after thermal annealing at 250 °C processed from chloroform (a) and DCB (b). Solid lines represent forward scans and dashed lines reversed scans.

5 UV-Visible Absorption of solid-state neat and blend films.

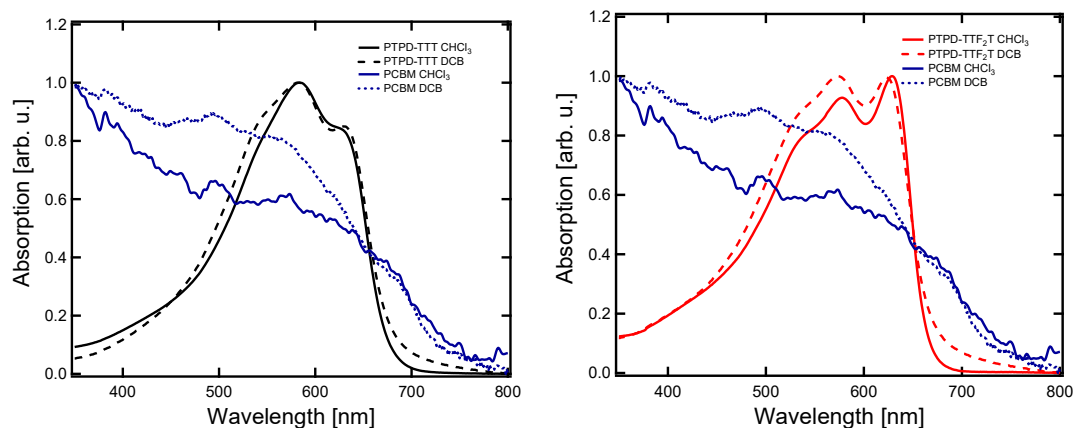


Figure S 4.10. UV-Visible absorption profiles for neat PTPDTT (left) and PTPDTTF₂T (right) films cast from dichlorobenzene (dashed lines) and chloroform (solid lines). Absorption of PC₇₁BM cast from both solvents are also shown.

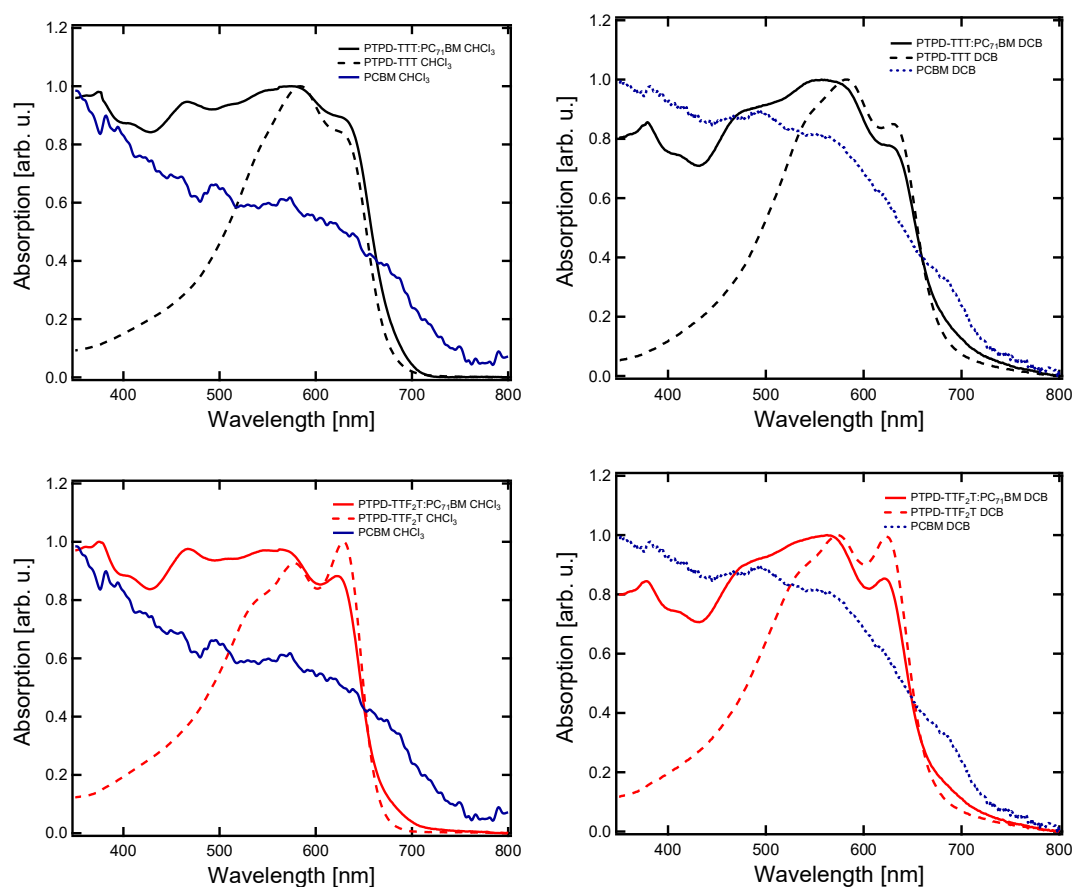


Figure S 4.11. Solid-state UV-Visible absorption profiles for PTPDTT (top) and PTPDTTF₂T (bottom) of neat (dashed lines) and blend (solid lines) films cast from chloroform (left) and dichlorobenzene (right). Neat films of PC₇₁BM are also shown.

6 1D GIWAXS for blend films

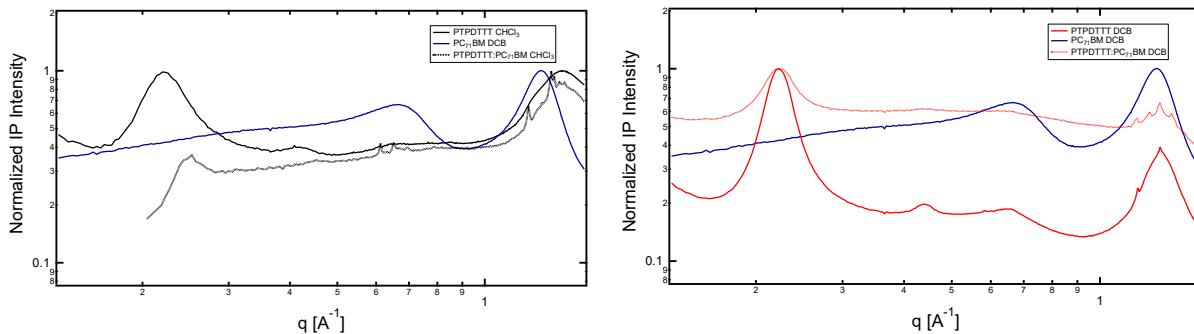


Figure S 4.12. Normalized in plane 1D GIWAXS line profiles for neat and blend films cast from chloroform (top) and dichlorobenzene (bottom) for PTPDTT.

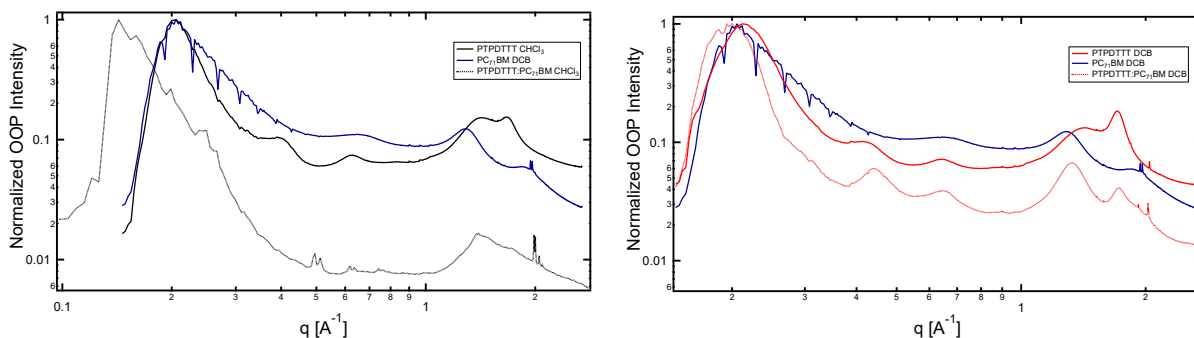


Figure S 4.13. Normalized out of plane 1D GIWAXS line profiles for neat and blend films cast from chloroform (top) and dichlorobenzene (bottom) for PTPDTT.

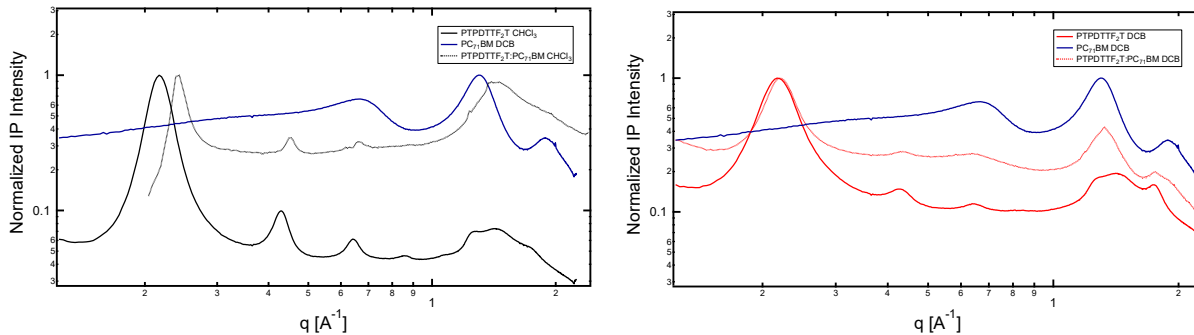


Figure S 4.14. Normalized in plane 1D GIWAXS line profiles for neat and blend films cast from chloroform (top) and dichlorobenzene (bottom) for PTPDTTF₂T.

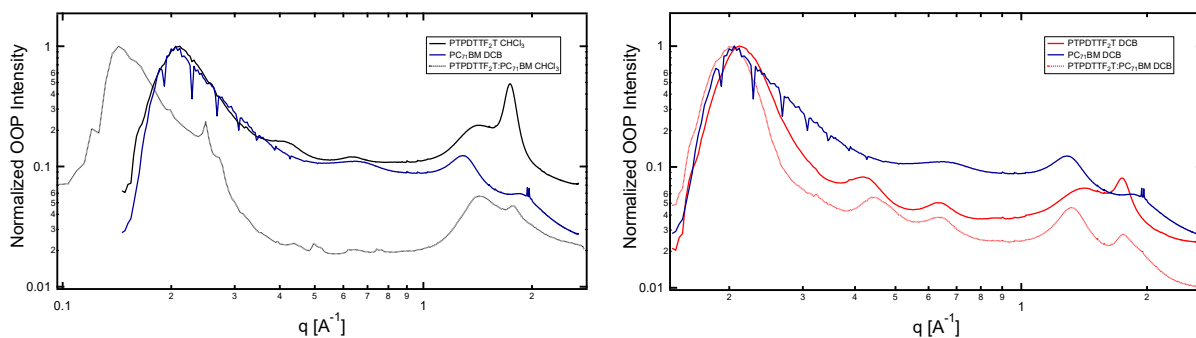


Figure S 4.15. Normalized out of plane 1D GIWAXS line profiles for neat and blend films cast from chloroform (top) and dichlorobenzene (bottom) for PTPDTTF₂T.

7 AFM

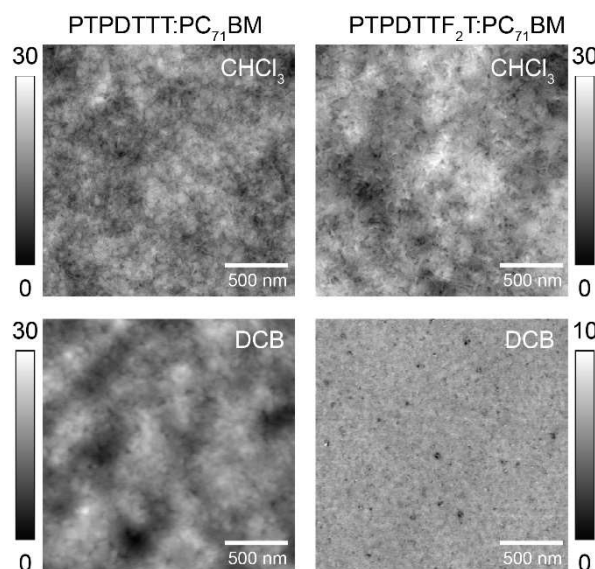


Figure S 4.16. AFM images for blends spin cast from chloroform (top) and dichlorobenzene (bottom) for PTPDTT (left) and PTPDTTF₂T (right).

8 References

- [1] A. Najari, P. Berrouard, C. Ottone, M. Boivin, Y. Zou, D. Gendron, W.-O. Caron, P. Legros, C. N. Allen, S. Sadki, M. Leclerc, *Macromolecules* **2012**, *45*, 1833.
- [2] X. Guo, N. Zhou, S. J. Lou, J. Smith, D. B. Tice, J. W. Hennek, R. P. Ortiz, J. T. L. Navarrete, S. Li, J. Strzalka, L. X. Chen, R. P. H. Chang, A. Facchetti, T. J. Marks, *Nat. Photonics* **2013**, *7*, 825.
- [3] T. Weller, M. Breunig, C. J. Mueller, E. Gann, C. R. McNeill, M. Thelakkat, *J. Mater. Chem. C* **2017**, *5*, 7527.

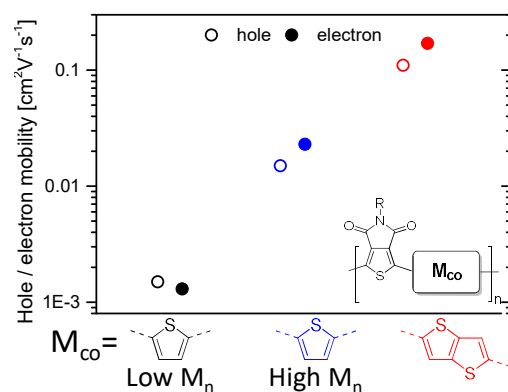
5 Highly efficient and balanced charge transport in thieno[3,4-*c*]pyrrole-4,6-dione copolymers: Dramatic influence of thieno[3,2-*b*]thiophene comonomer on alignment and charge transport

Tina Weller,^a Kira Rundel,^b Gert Krauss,^a Christopher R. McNeill^b and Mukundan Thelakkat^{a*}

^a Applied Functional Polymers, Macromolecular Chemistry I, University of Bayreuth, 95440 Bayreuth, Germany.

^b Department of Materials Science and Engineering, Monash University, Wellington Road, Clayton VIC, 3800, Australia.

* Corresponding author: mukundan.thelakkat@uni-bayreuth.de



Published in *Journal of Physical Chemistry C*, **2018**, 122, 7565-7574

Reproduced with permission from <https://pubs.acs.org/doi/abs/10.1021/acs.jpcc.7b11984>.

Copyright 2018 American Chemical Society.

Abstract

The design, synthesis, characterization, and application of a novel series of copolymers based on the electron deficient thieno[3,4-*c*]pyrrole-4,6-dione building block, copolymerized with either thieno[3,2-*b*]thiophene (PTPDTT) or thiophene (PTPDT), are reported. High molecular weights were obtained for PTPDTT via Stille polycondensation. For the PTPDTs, different molecular weights were achieved by varying the polymerization conditions. The increase in molecular weight (PTPDT-2) favors face-on alignment and increases the charge carrier mobility. Grazing-incidence wide-angle X-ray scattering measurements reveal higher crystallinity for PTPDTT with up to 5 orders of lamellar stacking compared to PTPDTs. All polymers show ambipolar charge transport with highly balanced hole and electron mobilities in organic field effect transistors (OFETs), which improve considerably upon thermal annealing. A shift of comonomer from simple thiophene in PTPDT-2 to planar and electron-dense thienothiophene in PTPDTT drastically changes the alignment from face-on to edge-on fashion. Consequently, the charge carrier mobility increases considerably by 1 order of magnitude in PTPDTT, reaching excellent charge carrier mobilities for both holes ($0.11 \text{ cm}^2 \text{ V}^{-1} \text{ s}^{-1}$) and electrons ($0.17 \text{ cm}^2 \text{ V}^{-1} \text{ s}^{-1}$). PTPDTT was tested as a donor material in combination with PC₇₁BM as well as an acceptor material along with a donor polymer. As a donor material, a power conversion efficiency of 4.3% was reached in combination with PC₇₁BM.

5.1 Introduction

Conjugated polymers designed according to the donor-acceptor concept show predominately p-type and comparatively rare n-type behavior in solution processed organic field effect transistors (OFETs). The ability to transport both charge carriers (holes and electrons) in one material is interesting for the application in complementary-like logic circuits^[1,2] and light-emitting field-effect transistors.^[3,4] Therefore, the charge carrier mobilities of these ambipolar materials need to be high and balanced. In most semiconducting polymers, the hole mobility exceeds the electron mobility, even though there is no theoretical support for this. The experimentally observed difference may arise from the fact that electrons are more likely trapped in defect sites within the energy bandgap.^[5] Additionally, the device performance is considerably influenced by the alignment of polymer chains, which can orient either in an edge-on, face-on,^[6] or end-on manner.^[7] The thin film morphology based on molecular packing can be controlled by the chemical structure, which is, for example, demonstrated in conjugated polymers based on

naphthodithiophenediimide.^[8] Here, the use of thieno[3,2-*b*]thiophene as a comonomer results in edge-on orientation and high electron mobilities in OFETs, whereas polymers with thiophene orient face-on, which is beneficial for the performance in polymer blend organic solar cells. As the electron-deficient building block, we chose thieno[3,4-*c*]pyrrole-4,6-dione (TPD) because of its strong electron-deficient character and simple synthetic accessibility. Its symmetric and coplanar structure favors inter- and intrachain interactions in the corresponding copolymers. Additionally, Rivaton et al. have shown that polymers with this moiety exhibit high stability under ultraviolet (UV) irradiation, which is crucial for long-term application.^[9] TPD-based copolymers have emerged as attractive donor materials for solar cell devices exceeding power conversion efficiencies of 9%.^[10,11] Whereas the performance of these materials in organic solar cells is superior, the OFET mobilities are limited. By incorporating fused ring aromatic moieties, the polymer coplanarity can be extended facilitating intermolecular packing, and thus, charge carrier transport can be improved. Besides cyclopentanedithiophene^[12] and naphthodithiophene,^[13] thienothiophene was proven to be a good building block for high charge carrier mobilities.^[14-16] TPD copolymers containing thienothiophene show high performance as a donor material in organic solar cells and in p-type OFETs. In detail, a solar cell efficiency^[10] of 9.21% in combination with a fullerene-based acceptor and an OFET hole mobility^[17] of $1.29 \text{ cm}^2 \text{ V}^{-1} \text{ s}^{-1}$ was achieved, which are both the highest values for TPD copolymers reported to date. Because of the high electron withdrawing properties of the TPD unit, electron transport can also be facilitated in TPD copolymers.^[18-21] However, only a few examples are reported to date using TPD copolymers as acceptor materials in all-polymer solar cells.^[22,23] Ambipolar charge transport was shown for TPD copolymers carrying thiophene^[24,25] and for bithienopyrroledione-based copolymers^[26] in OFET devices. In the latter, an electron mobility of $1.02 \text{ cm}^2 \text{ V}^{-1} \text{ s}^{-1}$ and a hole mobility of $0.33 \text{ cm}^2 \text{ V}^{-1} \text{ s}^{-1}$ were shown.

In this report, we address the following questions: (1) Is it possible to get appreciably high electron mobility as well as hole mobility in TPD copolymers? (2) Can the use of thienothiophene as the comonomer (instead of thiophene) in a simplified structure also result in high electron transport? (3) Is there any dependence of charge transport on molecular weight or the nature of comonomer used? To address the above questions, we copolymerized TPD with thienothiophene. A comparison of this polymer, PTPDTT, with two copolymers carrying thiophene as comonomers (PTPDT-1 and -2) with different molecular weights is carried out. All polymers show ambipolar transistor behavior with balanced hole and electron mobilities. The

highest OFET-mobilities, both for holes and electrons, are reached in PTPD TT with TT as the comonomer, and the results are correlated with the thin film microstructure analyzed by grazing-incidence wide-angle X-ray scattering (GIWAXS).

5.2 Experimental Section

5.2.1 Materials and Methods

Commercially available reagents were used as received unless otherwise noted. For reactions under microwave irradiation, a Biotage Initiator Eight+ Microwave was used. Size exclusion chromatography (SEC) was conducted on an Agilent (Polymer Laboratories Ltd.) PL-SEC 220 high temperature chromatographic unit equipped with differential pressure and refractive index detectors and three linear mixed bed columns (PSS POLEFIN linear XL). SEC analysis was performed at 160 °C using 1,2,4-trichlorobenzene as the mobile phase. For sample preparation, the polymer (0.1 wt %) was dissolved in the mobile phase solvent in an external oven and the solutions were run without filtration. The molecular weights of the samples were referenced to polystyrene standards ($M_w = 518\text{--}2\,600\,000\text{ g mol}^{-1}$, $K = 12.100$, and $\alpha = 0.707$). Cyclic voltammetric measurements were carried out in thin films under moisture- and oxygen-free conditions using a three-electrode assembly connected to a potentiostat (model 263A, EG&G Princeton Applied Research) at a scanning rate of 100 mV s^{-1} . A solution of tetra-*n*-butylammonium hexafluorophosphate in acetonitrile with a concentration of 0.1 M was used as the electrolyte solution. As working electrode glass substrates coated with indium tin oxide (ITO) ($10\ \Omega/\square$) were used, on which thin films from CHCl_3 solutions with a concentration of 5 mg mL^{-1} were spin-coated at 1500 rpm. A platinum wire in the respective electrolyte solution and Ag/AgNO₃ in acetonitrile (0.1 M) were used as counter and reference electrodes, respectively. Each measurement was calibrated by the internal standard ferrocene/ferrocenium. UV-vis spectra were recorded on a JASCO V-670 spectrophotometer. The wavelength corresponding to the absorption peak was used as the excitation wavelength in photoluminescence measurements, which were performed on a JASCO FP-8600 spectrofluorometer. Analysis of the optical properties was conducted either in chloroform solutions (0.01 mg mL^{-1}) using quartz cuvettes with an internal diameter of 10 mm or in thin films spin-coated on glass slides from chloroform solutions (5 mg mL^{-1}) at 1500 rpm. The thermogravimetric analysis (TGA) was performed on a Netzsch STA 449 F3 Jupiter at a scanning rate of 10 K min^{-1} under a nitrogen atmosphere. The temperature of decomposition $T_{5\%}$ was determined at 5% mass loss. For Flash

differential scanning calorimetry (DSC) measurements, a Mettler-Toledo Flash DSC 1 at scanning rates between 50 and 1000 K min⁻¹ under nitrogen was used. GIWAXS measurements were performed at the SAXS/WAXS beamline at the Australian Synchrotron.^[27] All samples were prepared by spin-coating polymer films onto silicon wafers (n-doped with Sb) from chloroform solutions (15–20 mg mL⁻¹) at 1000–1500 rpm apart from samples relevant to organic solar cells which were prepared following optimized device conditions [15 mg mL⁻¹ in chlorobenzene with 2% 1,8-diiodooctane (DIO) as the solvent additive, spin-coated at 3000 rpm]. X-rays (11 keV) were used with 2D scattering patterns recorded on a Dectris Pilatus 1 M detector. The sample to detector distance was calibrated using a silver behenate scattering standard. Scattering patterns were collected from incidence angles (α) between 0.02° and 0.35° with an X-ray exposure time of 3 s. Three separate 1 s exposures were taken with different lateral positions to fill in the gaps between the detector elements. These different exposures were combined in software. Data were analyzed using a modified version of Nika 2D^[28] based in Igor Pro. The organic thin film transistor substrates with a bottom-gate bottom-contact architecture were purchased from Fraunhofer IPMS (OFET Gen. 4). A heavily n-doped silicon wafer (doping at the wafer surface: $n \approx 3 \times 10^{17} \text{cm}^{-3}$) was used as the substrate and gate electrode. As the dielectric, a thermally grown silicon dioxide (standard 90/230 nm) was used to separate the gate electrode from the gold source and drain electrodes which were 30 nm thick with an underlying 10 nm ITO adhesion layer. Transistors with channel lengths of 10 and 20 μm and a channel width of 10 mm were used. The substrates were first rinsed with acetone followed by cleaning in acetone and 2-propanol in an ultrasonic bath for 10 min each. After treatment for 15 min at 50 °C in an ozone oven, the substrates were immersed in a solution of octadecyltrichlorosilane in toluene (1 vol %) at 60 °C for 1 h. Subsequently, the devices were rinsed with toluene and 2-propanol and stored in 2-propanol until spin-coating. Films were prepared by spin-coating from chloroform solutions (10 mg mL⁻¹) at 5000 rpm under ambient conditions. For the measurements of the current–voltage characteristics, the substrates were directly transferred into the glovebox. An Agilent B1500 semiconductor parameter analyzer was used for the analysis of the as-cast and annealed films. Annealing was performed under a nitrogen atmosphere at 100 and 250 °C for 15 min, respectively. The charge carrier mobilities were evaluated in the saturation regime using eq 1, where I_{DS} is the drain–source current, V_G the gate voltage, L the channel length, W the channel width, and C_i the capacitance. For the mobility calculation, the slope in the $I_{DS}^{1/2}$ versus V_G plots was determined in the saturation regime.

$$\mu_{sat} = \left(\frac{\partial \sqrt{I_{DS}}}{\partial V_G} \right)^2 \cdot \frac{2L}{WC_i} \quad (1)$$

Inverted solar cells were fabricated as follows. ITO-patterned glass substrates were sequentially cleaned in acetone and 2-propanol for 10 min each, followed by 10 min of UV-ozone treatment. Immediately after, the substrates were spin-coated with a 0.4% PEIE (polyethylenimine ethoxylated) in 2-methoxyethanol solution (Sigma-Aldrich) at 5000 rpm. The films were subsequently dried at 120 °C for 20 min before being transferred to an inert nitrogen-filled glovebox. Active layers (solutions heated at 70 °C for a minimum of 12 h prior to deposition, 15 mg mL⁻¹ concentration with a D/A wt ratio of 1:1.5) were then deposited at an optimized 3000 rpm, for 60 s and transferred to an Angstrom Engineering Covap evaporator where 12 nm of molybdenum oxide (0.3 Å s⁻¹) and 100 nm Ag (1.0 Å s⁻¹) were evaporated sequentially under no more than 9 × 10⁻⁷ Torr. Following this, the devices were fitted with edge clips and encapsulated by epoxy and glass. Simulated AM1.5 G radiation with 100 mW cm⁻² irradiance was provided by a Photo Emission Tech model SS50AAA solar simulator with a silicon reference cell with a KG3 glass filter used to calibrate the intensity. A Keithley 2635 source meter was used to characterize the *J-V* characteristics of devices. External quantum efficiency (EQE) spectra were subsequently measured using a spot size less than the active area of the pixel in the device. This ensures that the EQE measurement is independent of the device active area, enabling a cross-check with the measured *J_{sc}* under the solar simulator. For testing PTPDTT as the acceptor, we used PBDTTT-EFT (also called PCE-10) as the donor polymer, which was purchased from 1-Material with *M_n* = 25 kDa, *D* = 3.6. An Oriel Cornerstone 130 monochromator was used to disperse light from a tungsten filament (Newport 250 W QTH). Prior to measurement, this system was calibrated using a Thorlabs FDS-100CAL photodiode placed at the exact location devices occupy during measurements. A Cary 300 UV-vis Spectrophotometer was used to measure the solid-state absorption spectra for all films between 350 and 800 nm sited in the organic solar cells part of the Supporting Information.

5.2.2 Synthesis and Procedures

PTPDT-1: A microwave vial was loaded with the monomers 1,3-dibromo-5-(2-octyldodecyl)-4*H*-thieno[3,4-*c*]pyrrole-4,6(5*H*)-dione 1a (262 mg, 0.442 mmol, 1 equiv) and 2,5-bis(trimethylstannyl)thiophene 2 (181 mg, 0.442 mmol, 1 equiv). Tri(*o*-tolyl)phosphine (16.2 mg, 0.053 mmol, 0.12 equiv) was added followed by 5 mL chlorobenzene. After degassing by argon

bubbling for 10 min, tris(dibenzylideneacetone)dipalladium(0) (12.2 mg, 0.013 mmol, 0.03 equiv) was added. The microwave vial was sealed and purged with argon once more. The polymerization reaction was conducted at 160 °C for 1 h under microwave irradiation. After cooling to room temperature, 2-(tributylstannyl)thiophene was added to end-cap the polymer chains and the reaction mixture was stirred for 5 min at 160 °C. The end-capping step was, subsequently, repeated with 2-bromothiophene for 10 min. The polymer solution was precipitated in methanol (300 mL) and filtered. Further purification was carried out by sequential Soxhlet extraction using methanol and acetone. Finally, the polymer was collected by chloroform extraction and the solution was concentrated under reduced pressure. Precipitation in methanol, filtration, and drying in vacuum yielded the desired polymer (217 mg, 81%). ¹H nuclear magnetic resonance (NMR) (300 MHz, CDCl₃, δ): 6.42–8.54 (2H), 3.12–4.08 (2H), 0.47–2.50 (39H).

PTPDT-2: A Schlenk tube was loaded with the monomers 1,3-dibromo-5-(2-octyldodecyl)-4*H*-thieno[3,4-*c*]pyrrole-4,6(5*H*)-dione 1a (293 mg, 0.495 mmol, 1 equiv) and 2,5-bis(trimethylstannyl)thiophene 2 (203 mg, 0.495 mmol, 1 equiv). Tri(*o*-tolyl)phosphine (18.1 mg, 0.053 mmol, 0.12 equiv) was added followed by 16.5 mL tetrahydrofuran. After degassing by argon bubbling for 10 min, tris(dibenzylideneacetone)dipalladium(0) (13.6 mg, 0.015 mmol, 0.03 equiv) was added. The Schlenk tube was sealed and purged with argon once more. The polymerization reaction was conducted at 70 °C for 40 h. After cooling to room temperature, 2-(tributylstannyl)thiophene was added to end-cap the polymer chains and the reaction mixture was stirred for 2 h at 70 °C. The end-capping step was, subsequently, repeated with 2-bromothiophene under the same reaction conditions. The polymer solution was precipitated in methanol (300 mL) and filtered. Further purification was carried out by sequential Soxhlet extraction using methanol, acetone, and 2-butanone. Finally, the polymer was collected by chloroform extraction and the solution was concentrated under reduced pressure. Precipitation in methanol, filtration, and drying in vacuum yielded the desired polymer (216 mg, 80%). ¹H NMR (300 MHz, CDCl₃, δ): 7.36–9.15 (1H), 6.25–7.21 (1H), 3.11–4.47 (2H), 0.44–2.22 (49H).

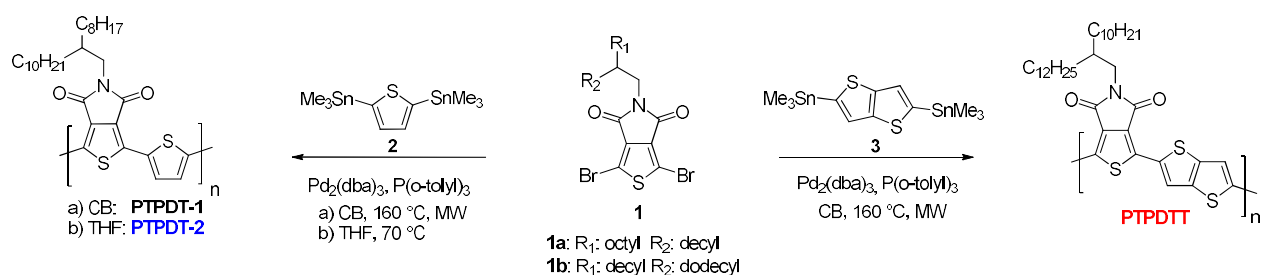
PTPDTT: A microwave vial was loaded with the monomers 1,3-dibromo-5-(2-decyltetradecyl)-4*H*-thieno[3,4-*c*]pyrrole-4,6(5*H*)-dione 1b (243 mg, 0.375 mmol, 1 equiv) and 2,5-bis(trimethylstannyl)thieno[3,2-*b*]thiophene 3 (175 mg, 0.375 mmol, 1 equiv). Tri(*o*-tolyl)phosphine (13.5 mg, 0.044 mmol, 0.12 equiv) was added followed by 4.8 mL

chlorobenzene. After degassing by argon bubbling for 10 min, tris(dibenzylideneacetone)dipalladium(0) (10.2 mg, 0.011 mmol, 0.03 equiv) was added. The microwave vial was sealed and purged with argon once more. The polymerization reaction was conducted at 160 °C for 1 h under microwave irradiation. After cooling to room temperature, 2-(tributylstannyl)thiophene was added to end-cap the polymer chains and the reaction mixture was stirred for 5 min at 160 °C. The end-capping step was, subsequently, repeated with 2-bromothiophene for 10 min. The polymer solution was precipitated in methanol (300 mL) and filtered. Further purification was carried out by sequential Soxhlet extraction using methanol, acetone, *n*-hexane, and dichloromethane. Finally, the polymer was collected by chloroform extraction and the solution was concentrated under reduced pressure. Precipitation in methanol, filtration, and drying in vacuum yielded the desired polymer (210 mg, 86%). ¹H NMR (300 MHz, CDCl₃, δ): 7.35–9.17 (2H), 3.09–4.47 (2H), 0.43–2.19 (49H).

5.3 Results and Discussion

5.3.1 Synthesis

The syntheses of the dibromo-TPD monomers with solubilizing octyldodecyl and decyltetradecyl side chains were carried out according to literature reported procedures.^[7] To polymerize the dibromo-TPD with thiophene and thienothiophene as comonomers, Stille polycondensation was utilized (Scheme 5.1). The stannylated thiophene was freshly recrystallized prior to polymerization, and the details of the synthesis of the stannylated thienothiophene are given in the Supporting Information. Stille polymerization of TPD carrying octyldodecyl side chains with thiophene was carried out with tris(dibenzylideneacetone)dipalladium(0) as a catalyst and tri(*o*-tolylphosphine) as a ligand in chlorobenzene at 160 °C in a microwave reactor. After a reaction time of 1 h, the polymer chains were end-capped with thiophene and purified by Soxhlet extraction.



Scheme 5.1. Synthesis of TPD containing polymers via Stille polymerization.

Analysis of the polymer PTPDT-1 by high-temperature SEC in 1,2,4-trichlorobenzene results in a number-average molecular weight (M_n) of 5610 g/mol (PS calibration). Similar molecular weights were reported for TPD copolymers carrying thiophene as the comonomer.^[25] In general, the relative molecular weights obtained for semicrystalline polymers with PS calibration need to be cautiously interpreted in terms of the real molecular weights. Interestingly, the dispersity is very low (1.07), which is not expected for a polycondensation even after Soxhlet extraction. To increase the degree of polymerization, the solvent was changed to tetrahydrofuran and the polymerization was conducted for 40 h at 70 °C under conventional heating. End-capping and purification were performed as described above. By changing the solvent to tetrahydrofuran, a higher number-average molecular weight of 9420 g mol⁻¹ is achieved. The molecular weight distribution of the polymer PTPDT-2 is slightly broadened resulting in a dispersity of 1.36, which is still low for polycondensates. Polymerization of TPD with thienothiophene was conducted in chlorobenzene as described initially. The TPD monomer with the octyldodecyl side chain could not maintain solubility, and only insoluble product was afforded. Therefore, we decorated the TPD monomer with the longer solubilizing decyltetradecyl side chain, and the polymerization with this TPD monomer resulted in a soluble material. High number-average molecular weights of 27 960 g mol⁻¹ with a dispersity of 3.67 were achieved for the polymer PTPDTT. All molecular weights and dispersities of the three polymers are summarized in Table 5.1, and the SEC data can be found in the Supporting Information (Figure S 5.4-6). Additionally, the polymers were analyzed by ¹H NMR spectroscopy, and the spectra are depicted in the Supporting Information (Figure S 5.1-3). In summary, polymerization of TPD with thiophene and thienothiophene was carried out under identical reaction conditions to obtain soluble polymers with different molecular weights. A higher degree of polymerization could be achieved for PTPDT by changing the solvent from chlorobenzene to tetrahydrofuran.

Table 5.1. SEC data and thermal and electrochemical properties of the TPD containing copolymers.

polymer	M_n^a [g mol ⁻¹]	M_w^a [g mol ⁻¹]	\mathcal{D}	$T_{d5\%}^b$ [°C]	T_m^c [°C]	$T_c^{1000\text{ K/min }c}$ [°C]	$T_c^{400\text{ K/min }c}$ [°C]	E_{opt}^d [eV]	IP ^e [eV]	EA ^e [eV]	E_{fund}^f [eV]
PTPDT-1	5610	5820	1.07	429	~420	373	385	1.71	-6.08	-3.64	2.44
PTPDT-2	9420	12 800	1.36	427	~400	374	380	1.72	-5.93	-3.53	2.40
PTPDTT	27 960	102 640	3.67	412				1.77	-5.95	-3.68	2.27

^a Determined by SEC in 1,2,4-trichlorobenzene at 160 °C using PS calibration. ^b Decomposition at 5% mass loss determined by TGA at 10 K min⁻¹ under N₂. ^c Melt and crystallization temperature from Flash DSC measurements at 1000 K min⁻¹ under N₂. ^d Optical gap determined by absorption edge in thin films. ^e Ionization potential (IP) and electron affinity (EA) determined from cyclic voltammetry in thin films. ^f Fundamental gap calculated by IP-EA.

The thermal properties of the polymers PTPDT-1, PTPDT-2, and PTPDTT were analyzed by TGA and Flash DSC. All values for the thermal properties are summarized in Table 5.1. The copolymers show a high decomposition temperature of above 400 °C (at 5% mass loss) revealing high thermal stability (Figure S 5.7). With Flash DSC measurements, the melting as well as crystallization processes near the decomposition temperature can be detected. Only the PTPDT copolymers with thiophene as comonomers show melting as well as crystallization in Flash DSC measurements, and the DSC plots for scanning rates at 400 and 1000 K min⁻¹ are shown in Figure 5.1a. The complete Flash DSC spectra for all samples at the different scanning rates are given in the Supporting Information (Figure S 5.8). In the first heating cycle with a scanning rate of 50 K min⁻¹, a clear melting temperature at 421 °C is observed for PTPDT-1, whereas in the following cycles the melting is only hardly detectable. The polymer PTPDT-2 shows a relatively lower melting temperature at around 400 °C. Herein, the polymer PTPDT-2 with a higher molecular weight accompanied by a higher dispersity results in a diminished melting temperature. Crystallization is detectable for both polymers only at high scanning rates and occurs at similar values of around 370 and 380 °C depending on the scanning rate. The polymer PTPDTT shows no thermal transitions up to 500 °C, indicating very high crystallinity because of the more rigid building block, thienothiophene.

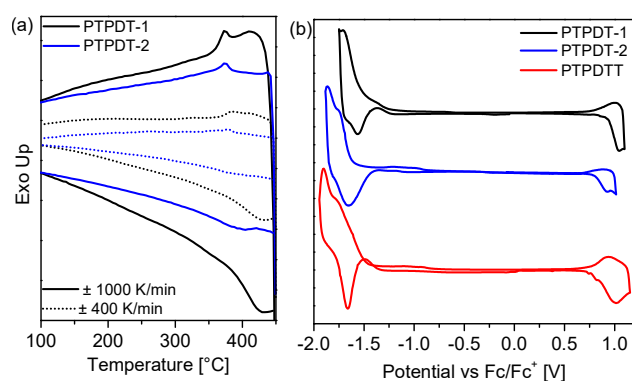


Figure 5.1. (a) Flash DSC measurements for PTPDT-1 and -2 at scanning rates of 400 K min⁻¹ (dotted line) and 1000 K min⁻¹ (solid line). (b) Cyclic voltammetry measurements of PTPDT-1, -2 and PTPDTT in thin films.

5.3.2 Optical and Electrochemical Properties

In Figure 5.2, the absorption spectra measured in solution and thin films are depicted. The absorption spectra of the polymers PTPDT-1 and PTPDT-2 show completely different intensities for the vibronic peaks, even though the molecular structures are identical. This is an indication of different degrees of aggregation and the quality of aggregates for the different molecular weights. For PTPDT-1, the main absorption peak in solution is located at 463 nm accompanied

by two shoulders at higher wavelengths (556 and 614 nm). In contrast, the polymer PTPDT-2 shows two absorption peaks at 570 and 618 nm. These two absorption peaks are located at similar positions as the two absorption shoulders of PTPDT-1 indicating a stronger aggregation behavior for PTPDT-2 in solution. For the polymer PTPDTT, the absorption spectrum features two peaks at 597 and 648 nm. The relative intensities of the vibronic peaks (ratio of I_{0-0} to I_{0-1}) give a measure for the quality and nature of aggregates, which can be a combination of H- and J-aggregates as studied by Spano and others.^[29-31] In conjugated polymers, the formation of H-aggregates favored by interchain interactions competes with the formation of J-aggregates favored by intrachain interactions. In the solid state, the absorption peaks of both PTPDT-1 and PTPDT-2 converge toward same values, indicating that the nature of aggregation in both is the same and the difference of absorption in solution is just caused by the difference in the solubility leading to difference in aggregation. Additionally, the 0-0 vibronic peak is intensified for PTPDT-2 as well as PTPDTT, indicating a stronger aggregation. Furthermore, the absorption edge is shifted to longer wavelengths for all three polymers in thin films as shown in Figure 5.2b. Especially for PTPDT-1, the shoulder at 617 nm becomes more prominent as a result of stronger aggregation. All polymers have a similar absorption edge at around 700 nm. The optical gap determined by the absorption edge in the solid state is 1.71 eV for PTPDT-1 as well as PTPDT-2 and 1.77 eV for PTPDTT. The qualitative photoluminescence spectra after excitation at the absorption peak maximum in solution and thin films can be found in the Supporting Information (Figure S 5.9-10). The electrochemical properties were investigated in cyclic voltammetry measurements in thin films using a three-electrode assembly. ITO coated with the polymer was used as the working electrode, and the measurements were conducted in acetonitrile. During the measurement, the polymers do not dissolve out of the electrode. The cyclic voltammograms are shown in Figure 5.1b. For all three polymers, reversible oxidation and reduction processes can be observed. The approximate EA, as well as the IP, is calculated from the onset of the respective potential waves by taking into account the solvent effects^[32] and are summarized in Table 5.1. These values are only an approximate estimate of the energy levels of thin films in polar solvents and should not be considered as absolute values. In comparison to PTPDT-1, the energy levels of PTPDT-2 are slightly lower accompanied by a slightly smaller fundamental gap. For PTPDTT, the fundamental gap is even smaller, whereas the IP is slightly increased. In comparison to the PTPDTs, PTPDTT shows a larger optical gap contrary to its smaller

fundamental gap, which may be attributed to a comparatively smaller exciton binding energy of PTPDTT.^[33]

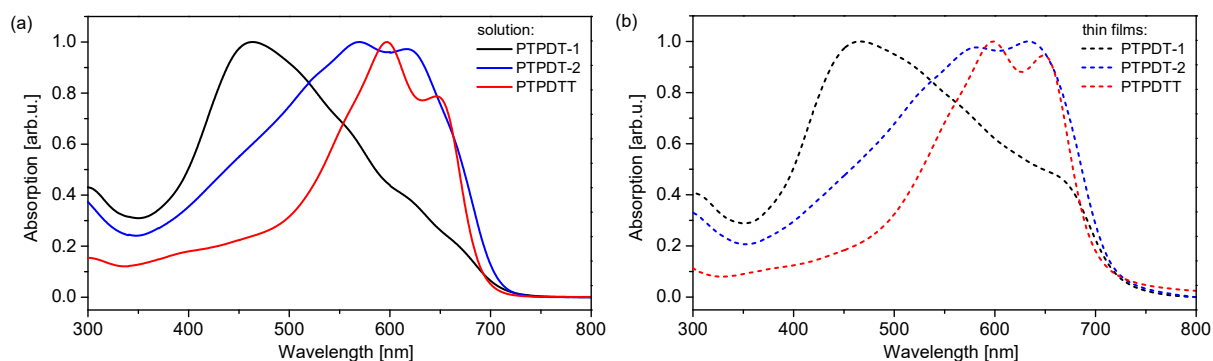


Figure 5.2. UV-Vis absorption spectra of PTPDT-1, -2 and PTPDTT in chloroform solution (a) and thin films (b)

5.3.3 Structural Analysis by GIWAXS

To investigate the crystalline packing in solid state, thin films of the three polymers were examined with GIWAXS. Measurements of the as-cast films and annealed films (250 °C for 15 min) have been performed, and the corresponding two-dimensional scattering patterns are presented in Figure 5.3a. These patterns were taken near the critical angle (0.11°–0.14°), with the images shown corresponding to the angle with maximum scattering intensity. One-dimensional scattering profiles along the out-of-plane (Q_z) and in-plane (Q_{xy}) directions of all three polymers (as-cast as well as annealed samples) are summarized in Figure 5.3c.

All polymers show alkyl lamella stacking indexed as (k00) up to multiple orders and π - π stacking peaks indexed as (010). The alkyl and π - π stacking distances together with their respective coherence lengths are summarized in Table 5.2. In the as-cast as well as annealed films, PTPDT-1 shows little or no preferential orientation of polymer chains with respect to the surface. After annealing, a backbone stacking peak, indexed as (001), is observed at Q values of $\sim 3.5 \text{ nm}^{-1}$ ($d_{\text{backbone}} = 1.81 \text{ nm}$; $\zeta_{\text{backbone}} = 19.1 \text{ nm}$). This (001) peak also shows a high degree of anisotropy indicating that polymer backbones in this sample are not all lying flat, likely to be related to the low molecular weight (and hence small contour length) of this sample. In contrast to the full rotational disorder of crystallites in polymer PTPDT-1, polymer PTPDT-2 shows crystallites with a strong orientational preference, even in the as-cast samples. The lamellar stacking peaks of PTPDT-2 are predominately observed in-plane, indicating a preferential face-on orientation with respect to the substrate. The corresponding π - π stacking peaks are located out-of-plane at $\sim 17.5 \text{ nm}^{-1}$.

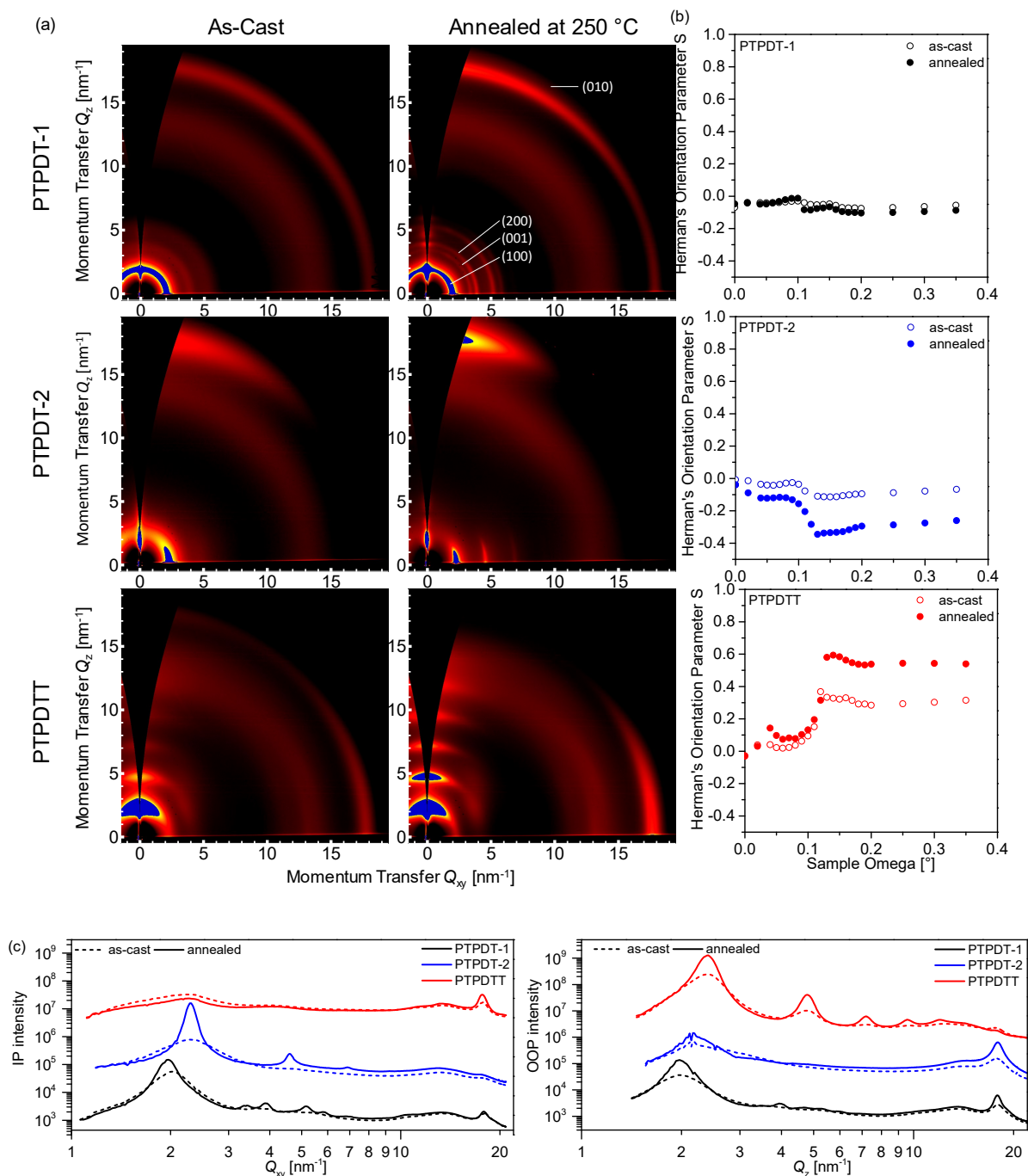


Figure 5.3. (a) 2D GIWAXS patterns of as-cast (left) and annealed films (right), (b) Herman's orientation parameter S vs. incident angle and (c) 1D scattering profiles taken along in-plane (left) and out-of-plane (right) direction.

Besides the more oriented microstructure of PTPDT-2 films in comparison to PTPDT-1 films, the alkyl spacing distance of PTPDT-2 is decreased from ~ 3.2 to ~ 2.8 nm. In PTPDT-2 film, the polymer chains are rather weakly ordered in the as-cast sample showing only the first order of lamellar stacking. With annealing, the crystallites grow in size and become more ordered evidenced by up to 3 orders of lamellar stacking and a more defined π - π stacking peak. Additionally, the lamellar stacking peaks are intensified and sharpened leading to a 6-fold

increase in coherence length, whereas the coherence length of the π - π stacking is doubled. We use Herman's orientation parameter, S , to quantify the degree of edge-on versus face-on thin film alignment.^[6] Perfectly edge-on oriented chains correspond to $S = 1$, whereas $S = 0.5$ indicates a perfectly face-on orientation. In Figure 5.3b, S is plotted as a function of incidence angle. Angles below the critical angle of around 0.13° probe the top 5–10 nm of the film, whereas angles above the critical angle probe the bulk of the film (film thickness: 90–130 nm).

Calculation of the S parameter for PTPDT-2 gives a value of $S = -0.09$ (no preferential orientation) for the as-cast film and $S = -0.3$ for the annealed film, indicating a predominately face-on orientation after annealing. By substituting the thiophene unit in PTPDT with the fused thienothiophene unit to form PTPDTT, the thin-film crystallinity and molecular orientation is considerably altered. In particular, thin films of PTPDTT show 4 orders of lamellar stacking in the as-cast sample and even 5 orders after thermal annealing. Moreover, strong lamellar stacking peaks are observed in the out-of-plane direction and the π - π stacking peaks are observed in the in-plane direction, indicating edge-on orientation of the polymer chains. S parameters calculated for PTPDTT films results in values of $S = 0.3$ for the as-cast film and $S = 0.6$ for the annealed film. Interestingly, a tighter alkyl spacing of 2.6 nm is observed for PTPDTT despite the increased length of alkyl chains, indicating a different side chain packing geometry, facilitated by the longer length of the thienothiophene unit. Additionally, the π - π stacking distance is slightly decreased, indicating a tighter molecular packing. Annealed PTPDTT films also show the largest π - π stacking coherence length. The edge-on orientation of PTPDTT chains may be expected to favor charge transport in an OFET, while the face-on orientation in PTPDT-2 may be expected to promote vertical charge transport in bulk. A similar change in alignment on switching from thiophene to thienothiophene comonomer was also observed in copolymers based on naphthodithiophenediimide.^[8] However, the alignment behavior of thin films of semicrystalline polymers on a substrate is a net result of structural features as well as processing conditions and influence of solvents used for film casting. Therefore, it is usually difficult to give an explanation for the observed orientation just based on one of the above parameters.

Table 5.2. Crystalline parameters analyzed from GIWAXS patterns.

polymer	film state	d_{alkyl}^a	ζ_{alkyl}^b	$d_{\pi-\pi}^c$	$\zeta_{\pi-\pi}^d$
		[nm]	[nm]	[nm]	[nm]
PTPDT-1	as-cast	3.27	18.5	0.356	4.48
	annealed	3.19	36.6	0.351	7.01
PTPDT-2	as-cast	2.79	8.48	0.359	2.77
	annealed	2.78	57.2	0.357	5.32
PTPDTT	as-cast	2.63	23.3	0.354	5.38
	annealed	2.63	40.5	0.355	8.21

^a Alkyl spacing. ^b Alkyl spacing coherence length. ^c π - π stacking spacing. ^d π - π stacking coherence length.

5.3.4 Charge Transport in OFETs

The charge carrier mobilities were determined in OFETs with a bottom-gate, bottom-contact architecture. Within narrow channels, the lateral charge transport in thin films is measured at the dielectric interface. In the Experimental Section, the device preparation as well as the evaluation of the charge carrier mobilities is described. Measurements were performed under the nitrogen atmosphere in the as-cast films as well as after annealing at 100 and 250 °C, respectively. The annealing at 100 °C was separately performed as there was concern that the films may dewet with annealing at higher temperatures. Annealing experiments were conducted for 15 min under nitrogen. All three polymers show ambipolar charge transport. Figure 5.4 depicts exemplary output and transfer characteristics for PTPDTT after annealing at 250 °C. All other OFET characteristics are given in the Supporting Information (Figure S 5.11–16). The hole and electron mobilities of the as-cast and annealed films are summarized in Table 5.3.

Table 5.3. OFET hole and electron mobilities and corresponding threshold voltages in the as-cast state as well as after annealing at 100 and 250 °C, respectively.^a

Polymer	p-type			n-type		
	as-cast	100 °C	250 °C	as-cast	100 °C	250 °C
	μ_h^b [cm ² V ⁻¹ s ⁻¹]	μ_h^b [cm ² V ⁻¹ s ⁻¹]	μ_h^b [cm ² V ⁻¹ s ⁻¹]	μ_e^b [cm ² V ⁻¹ s ⁻¹]	μ_e^b [cm ² V ⁻¹ s ⁻¹]	μ_e^b [cm ² V ⁻¹ s ⁻¹]
PTPDT-1	(3.4 ± 1.1) x 10 ⁻⁶	(1.7 ± 1.4) x 10 ⁻⁵	(1.5 ± 0.1) x 10 ⁻³	(3.5 ± 1.1) x 10 ⁻⁶	(1.4 ± 0.2) x 10 ⁻⁵	(1.3 ± 0.2) x 10 ⁻³
PTPDT-2	(6.0 ± 1.4) x 10 ⁻⁴	(1.1 ± 0.3) x 10 ⁻³	(1.5 ± 0.3) x 10 ⁻²	(5.6 ± 0.8) x 10 ⁻⁴	(1.2 ± 0.2) x 10 ⁻³	(2.3 ± 0.5) x 10 ⁻²
PTPDTT	(5.9 ± 2.7) x 10 ⁻³	(1.8 ± 0.6) x 10 ⁻²	0.11 ± 0.02	-	(8.7 ± 2.1) x 10 ⁻²	0.17 ± 0.05

^a Annealing was performed for 15 min under the nitrogen atmosphere in a glovebox. ^b Hole (μ_h) and electron (μ_e) mobilities calculated from the saturation regime. All values are averaged for a minimum of six devices.

In Figure 5.5, both the hole and electron mobility values are illustrated graphically. The polymers PTPDT-1 and PTPDT-2 show very balanced mobilities, where neither hole nor electron transport dominates. These balanced mobilities indicate highly pure domains, where electron trapping is diminished. For polymer PTPDT-1, the hole and electron mobility are in the range of $10^{-6} \text{ cm}^2 \text{ V}^{-1} \text{ s}^{-1}$ in the as-cast films. After annealing at 100°C , the charge carrier mobilities are improved by 1 order of magnitude and further annealing at 250°C even results in a further improvement of 2 orders of magnitude. A hole and electron mobility of about $1.5 \times 10^{-3} \text{ cm}^2 \text{ V}^{-1} \text{ s}^{-1}$ was finally reached. The increase of the molecular weight in polymer PTPDT-1 has a strong impact on the charge carrier mobilities. In the as-cast films and after annealing at 100°C , both the hole and electron mobility is improved by 2 orders of magnitude in comparison to PTPDT-1. After annealing at 250°C , a hole mobility of $1.5 \times 10^{-2} \text{ cm}^2 \text{ V}^{-1} \text{ s}^{-1}$ and an electron mobility of $2.3 \times 10^{-2} \text{ cm}^2 \text{ V}^{-1} \text{ s}^{-1}$ could be achieved. As described in the previous GIWAXS part, the polymer PTPDT-2 shows face-on alignment, which may not additionally support the lateral charge transport. However, the higher crystallinity seems to improve the OFET mobility, which is a sum of both intra- and interchain transport. Annealing at 250°C increases crystallinity for all the three polymers, and therefore, charge transport within all the three polymers is enhanced. In comparison, the GIWAXS measurements for PTPDT-1 show no preferential order of the polymer chains to the substrate resulting in lower charge carrier mobilities.

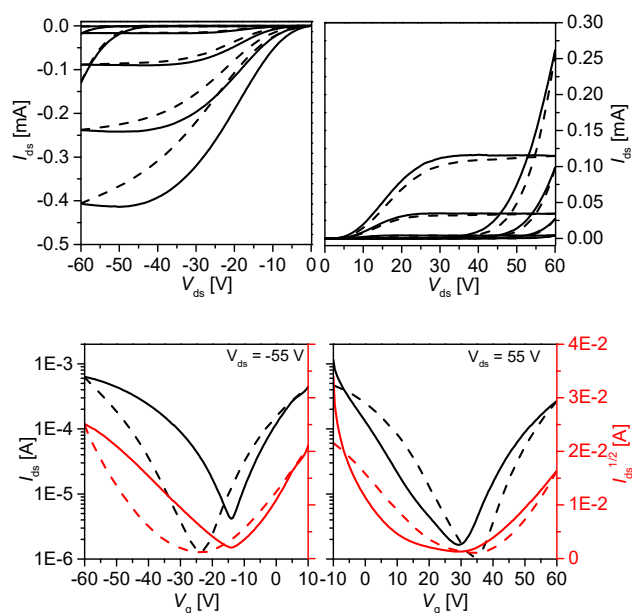


Figure 5.4. OFET output (top) and transfer (bottom) characteristics of PTPDTT; p- and n-channel operation after annealing at 250°C . Solid lines represent forward scans and dashed lines reversed scans.

In contrast to the two PTPDT polymers, polymer PTPDTT shows higher crystallinity and edge-on alignment resulting in even higher charge carrier mobilities. Even though only hole mobilities of $5.9 \times 10^{-3} \text{ cm}^2 \text{ V}^{-1} \text{ s}^{-1}$ are observed in the as-cast films, ambipolar charge transport evolves after annealing at $100 \text{ }^\circ\text{C}$, resulting in a high hole mobility of $1.8 \times 10^{-2} \text{ cm}^2 \text{ V}^{-1} \text{ s}^{-1}$ and an electron mobility of $8.7 \times 10^{-2} \text{ cm}^2 \text{ V}^{-1} \text{ s}^{-1}$. Further annealing at $250 \text{ }^\circ\text{C}$ give excellent and matching mobilities, with a hole mobility of $0.11 \text{ cm}^2 \text{ V}^{-1} \text{ s}^{-1}$ and an electron mobility of $0.17 \text{ cm}^2 \text{ V}^{-1} \text{ s}^{-1}$. Whereas both polymers PTPDT-1 and PTPDT-2 show a negligible hysteresis, PTPDTT shows a significant hysteresis in forward/backward scan. Interestingly, the hysteresis is more pronounced in the p-channel operation. This electron mobility is among the highest mobilities for TPD copolymers reported to date. By extensive device engineering and optimization, the values might be pushed to even higher values.

In summary, all three polymers show ambipolar charge transport with highly balanced hole and electron mobilities after thermal annealing. By increasing the molecular weight in PTPDT polymers, the mobilities can be considerably increased mainly because of the higher crystallinity and better structural order of PTPDT-2. By changing the comonomer to thienothiophene, the preferential face-on alignment of PTPDT-2 is changed to edge-on alignment, leading to a further increase of OFET charge carrier mobilities.

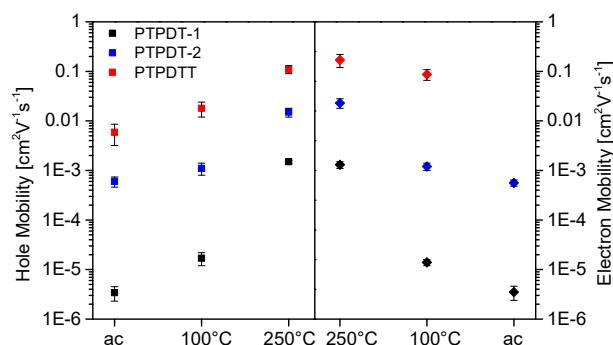


Figure 5.5. Summary chart of hole and electron mobilities for PTPDT-1, -2 and PTPDTT.

5.3.5 Solar Cell Performance.

Solar cells using PTPDT is already reported in the literature with very low performance giving a power conversion efficiency (PCE) = 0.35%.^[24] Because of the low performance reported in the literature, these solar cells were not again prepared and characterized here. To demonstrate the potential applications of PTPDTT, inverted solar cells were fabricated using the following architecture: ITO/PEIE/active layer/MoO_x/Ag. PTPDTT was used as a donor with PC₇₁BM as the

acceptor, and PTPDTT was also trialed as an acceptor material paired with the polymer PBDTTT–EFT as the donor. Despite exhibiting high V_{OC} values when used as an acceptor with PBDTTT–EFT, see Figure S 5.17, devices showed very poor performance, so photovoltaic work focused on PTPDTT as a donor in conjunction with PC₇₁BM. The normalized UV–vis solid-state absorption spectra of films of neat PTPDTT, neat PC₇₁BM, and their blend are shown in Figure S 5.19. PTPDTT exhibits a series of well-defined vibronic peaks which are retained after blending with PC₇₁BM. While PTPDTT shows strong absorption in the visible regime between 500 and 700 nm, its spectrum is not broad enough to cover higher energy wavelengths below 500 nm. An extension of the absorption profile into this regime is observed when the polymer is blended with PC₇₁BM, where the film continues to absorb strongly below 500 nm. Although OFET devices fabricated from PTPDTT showed improved performance with annealing, in solar cells, annealing the active layer at either 100 or 250 °C resulted in systematic lowering of the V_{OC} and J_{SC} , see Figure S 5.18a. However, the fill factor was improved with annealing, indicating a possible enhancement of charge extraction due to increased levels of crystallinity within the active layer, as was discussed previously. Conversely, annealing can coarsen the morphology resulting in reduced exciton dissociation yield, resulting in the lower J_{SC} observed in annealed devices. Thus, while annealing increases cell FF because of improved crystallinity and charge collection, the overall solar cell efficiency decreases likely due to the morphology becoming too coarse. The use of different solvents and solvent additives can be used instead to optimize morphology. Three different solvents with different drying kinetics were chosen: chloroform, chlorobenzene, and dichlorobenzene (Figure S 5.18b). Despite producing devices with the highest OFET mobilities, chloroform did not result in the best performing solar cells. Instead, chlorobenzene produced the highest PCE in devices, shown in Figure 5.6. Additionally, the inclusion of the solvent additive, DIO - which has previously been shown to improve solar cell efficiency by altering the morphology of blend films by suppressing the growth of large domains^[34] - results in further improvement in cell efficiency. Figure 5.6 shows the effect of fabricating solar cells with varying concentrations of DIO in the casting solution, showing that up to 2% DIO, the additive systematically improves the J_{SC} dramatically. This is indicative of more efficient free-carrier generation in the active layer as a result of morphology modification by the DIO. After careful device optimization, a maximum PCE of 4.3% was achieved with a 1:1.5 ratio of PTPDTT:PC₇₁BM deposited from chlorobenzene, using 2% DIO as a solvent additive. The solution concentration was optimized to 15 mg mL⁻¹ with a film thickness of approximately 85 nm. It was also found

that a thin layer of PEIE polymer alone (rather than in conjunction with a ZnO layer) resulted in the best solar cell performance. Details of the device fabrication and characterization can be found in the Experimental Section. Figure 5.6 shows the J - V characteristics and EQE of devices as a function of DIO concentration. DIO (2%) resulted in the most efficient devices, significantly increasing the J_{sc} from 6.1 to 8.4 mA cm^{-2} ; however, the V_{oc} was found to systematically decrease with increasing DIO concentration.

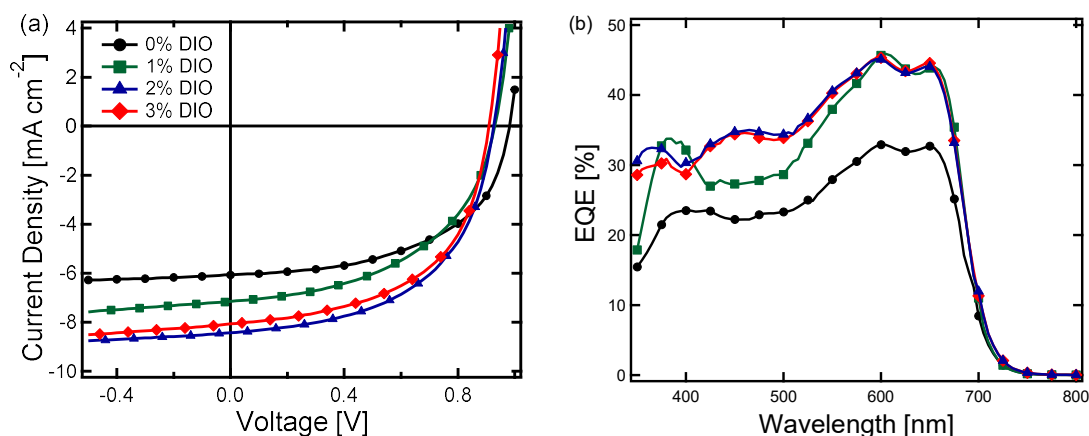


Figure 5.6. J - V characteristics (a) and EQE spectra (b) for PTPD TT:PC₇₁BM devices with various concentrations of DIO as solvent additive. 2% DIO was found to be the optimum for device efficiency.

The EQE spectra show similar trends, with the devices using 2% DIO resulting in the broadest EQE spectra, suggesting that DIO helps to improve light harvesting from the PC₇₁BM phase. Slightly higher J_{sc} values are obtained under the solar simulator compared to the value predicted by integrating the EQE spectra, which is likely to be due to edge effects in the small active area devices. A summary of the J - V characteristics at the different DIO concentrations is given in Table 5.4.

Table 5.4. J - V characteristics for at least three devices in dependence of the DIO concentration.

DIO concentration [%]	J_{sc} [mA cm^{-2}]	V_{oc} [V]	FF [%]	PCE [%]	EQE J_{sc} [mA cm^{-2}]
0	6.1 ± 0.3	0.98 ± 0.02	56.7 ± 0.5	3.3 ± 0.1	5.3 ± 0.1
1	7.8 ± 0.1	0.93 ± 0.01	53.4 ± 1.0	3.0 ± 0.1	7.2 ± 0.4
2	8.4 ± 0.1	0.92 ± 0.01	54.7 ± 0.9	4.3 ± 0.1	7.6 ± 0.1
3	8.1 ± 0.2	0.91 ± 0.01	55.0 ± 1.0	4.0 ± 0.1	7.5 ± 0.2

GIWAXS measurements have been performed to examine the microstructure of PTPD TT:PC₇₁BM blends. Figure S 5.20 shows the GIWAXS patterns for neat PTPD TT, neat PC₇₁BM, and a 1:1.5 blend prepared with 2% DIO concentration, cast from chlorobenzene solutions. Interestingly,

the neat film cast from chlorobenzene shows a slightly higher (100) spacing (2.76 nm) compared to the neat film from chloroform (2.63 nm, Figure 5.3), likely due to the different casting solvent and possibly also the different film thickness. Because of the difference in boiling point for chloroform and chlorobenzene (along with the additional 2% DIO), the film drying time and thus the drying kinetics are significantly impacted by the casting solvent. The higher (100) spacing observed in films cast from chlorobenzene and 2% DIO could be a result of slower film drying. The GIWAXS pattern of the blend shows scattering features from both PTPDTT and PC₇₁BM, indicating that donor and acceptor materials separately crystallize/aggregate. Compared to the neat film, PTPDTT is less crystalline in the blend with PC₇₁BM with a significant portion of crystallites oriented face-on to the substrate, which is expected to be beneficial for vertical charge transport as required in a solar cell device. As was discussed previously, the distribution and size of donor and acceptor domains in the blend are responsible for efficient free carrier generation and extraction in a solar cell. The GIWAXS data, as well as results presented in Figure 5.6, indicate that the addition of DIO in the solvent optimizes the morphology to produce a film with smaller donor-rich and acceptor-rich phases, resulting in higher solar cell performance.

5.4 Conclusion

We report a novel donor–acceptor copolymer based on thieno[3,4-*c*]pyrrole-4,6-dione and thienothiophene, which was synthesized via Stille polycondensation with high molecular weights. To compare the influence of the very rigid aromatic moiety thienothiophene with thiophene, TPD was additionally copolymerized with thiophene to get two different samples of copolymers with different molecular weights. Annealing has a very pronounced effect on the nature and degree of crystallization of all copolymers. Especially, thin films of PTPDTT show 4 orders of lamellar stacking in the as-cast sample and even 5 orders after thermal annealing. Ambipolar charge transport with highly balanced hole and electron mobilities is observed for all polymers, whereas the highest mobilities were obtained for PTPDTT after thermal annealing at 250 °C. The high charge carrier mobilities agree with the very high crystallinity and edge-on alignment observed in GIWAXS measurements. Polymer PTPDT with low molecular weights shows no preferential order in thin films and, therefore, exhibited the lowest charge carrier mobilities. Charge transport could be improved in PTPDT by increasing the molecular weight, resulting in enhanced structural ordering. Because of the high mobilities of PTPDTT, this material

was applied either as a donor material in combination with PC₇₁BM acceptor or as an acceptor in organic solar cells. The PTPD_{TT}/PC₇₁BM device delivered a PCE of 4.3%.

5.5 Acknowledgements

We acknowledge finance support from Bavarian State Ministry for Education, Science and the Arts under the SolTech project and German Research Council (DFG) under SFB840. This work was performed in part at the SAXS/WAXS beamline at the Australian Synchrotron, part of ANSTO.

5.6 References

- [1] Chen, Z.; Lemke, H.; Albert-Seifried, S.; Caironi, M.; Nielsen, M. M.; Heeney, M.; Zhang, W.; McCulloch, I.; Sirringhaus, H. High Mobility Ambipolar Charge Transport in Polyselenophene Conjugated Polymers. *Adv. Mater.* **2010**, *22*, 2371–2375.
- [2] Baeg, K.-J.; Caironi, M.; Noh, Y.-Y. Toward Printed Integrated Circuits Based on Unipolar or Ambipolar Polymer Semiconductors. *Adv. Mater.* **2013**, *25*, 4210–4244.
- [3] Zhang, C.; Chen, P.; Hu, W. Organic Light-Emitting Transistors: Materials, Device Configurations, and Operations. *Small* **2016**, *12*, 1252–1294.
- [4] Gwinner, M. C.; Kabra, D.; Roberts, M.; Brenner, T. J. K.; Wallikewitz, B. H.; McNeill, C. R.; Friend, R. H.; Sirringhaus, H. Highly Efficient Single-Layer Polymer Ambipolar Light-Emitting Field-Effect Transistors. *Adv. Mater.* **2012**, *24*, 2728–2734.
- [5] Nicolai, H. T.; Kuik, M.; Wetzelaer, G. A. H.; Boer, B. de; Campbell, C.; Risko, C.; Bredas, J. L.; Blom, P. W. M. Unification of Trap-Limited Electron Transport in Semiconducting Polymers. *Nat. Mater.* **2012**, *11*, 882–887.
- [6] Mueller, C. J.; Gann, E.; Singh, C. R.; Thelakkat, M.; McNeill, C. R. Control of Molecular Orientation in Polydiketopyrrolopyrrole Copolymers via Diffusive Noncovalent Interactions. *Chem. Mater.* **2016**, *28*, 7088–7097.
- [7] Weller, T.; Breunig, M.; Mueller, C. J.; Gann, E.; McNeill, C. R.; Thelakkat, M. Fluorination in Thieno[3,4-c]pyrrole-4,6-dione Copolymers Leading to Electron Transport, High Crystallinity and End-On Alignment. *J. Mater. Chem. C* **2017**, *5*, 7527–7534.
- [8] Nakano, K.; Nakano, M.; Xiao, B.; Zhou, E.; Suzuki, K.; Osaka, I.; Takimiya, K.; Tajima, K. Naphthodithiophene Diimide-Based Copolymers: Ambipolar Semiconductors in Field-Effect Transistors and Electron Acceptors with Near-Infrared Response in Polymer Blend Solar Cells. *Macromolecules* **2016**, *49*, 1752–1760.

- [9] Tournebize, A.; Gardette, J.-L.; Taviot-Guého, C.; Bégué, D.; Arnaud, M. A.; Dagron-Lartigau, C.; Medlej, H.; Hiorns, R. C.; Beaupré, S.; Leclerc, M. *et al.* Is There a Photostable Conjugated Polymer for Efficient Solar Cells? *Polym. Degrad. Stab.* **2015**, *112*, 175–184.
- [10] Kim, J.-H.; Park, J. B.; Jung, I. H.; Grimsdale, A. C.; Yoon, S. C.; Yang, H.; Hwang, D.-H. Well-Controlled Thieno[3,4-c]pyrrole-4,6-(5H)-dione Based Conjugated Polymers for High Performance Organic Photovoltaic Cells with the Power Conversion Efficiency Exceeding 9%. *Energy Environ. Sci.* **2015**, *8*, 2352–2356.
- [11] Qiao, X.; Chen, W.; Wu, Q.; Zhang, S.; Wu, H.; Liu, Z.; Yang, R.; Li, H. Bithienopyrroledione vs. Thienopyrroledione Based Copolymers: Dramatic Increase of Power Conversion Efficiency in Bulk Heterojunction Solar Cells. *Chem. Commun.* **2017**, *53*, 3543–3546.
- [12] Hong, Y.-R.; Ng, J. Y.; Wong, H. K.; Moh, L. C.; Yip, Y. J.; Chen, Z.-K.; Norsten, T. B. Synthesis and Characterization of a Series of Low-Bandgap Copolymers Based on Cyclopenta[2,1-b:3,4-b']dithiophene and Thienopyrroledione for Photovoltaic Applications. *Solar Energy Materials and Solar Cells* **2012**, *102*, 58–65.
- [13] Shi, S.; Jiang, P.; Yu, S.; Wang, L.; Wang, X.; Wang, M.; Wang, H.; Li, Y.; Li, X. Efficient Polymer Solar Cells Based on a Broad Bandgap D–A Copolymer of “Zigzag” Naphthodithiophene and Thieno[3,4-c]pyrrole-4,6-dione. *J. Mater. Chem. A* **2013**, *1*, 1540–1543.
- [14] Fei, Z.; Pattanasattayavong, P.; Han, Y.; Schroeder, B. C.; Yan, F.; Kline, R. J.; Anthopoulos, T. D.; Heeney, M. Influence of Side-Chain Regiochemistry on the Transistor Performance of High-mobility, All-Donor Polymers. *J. Am. Chem. Soc.* **2014**, *136*, 15154–15157.
- [15] Cai, P.; Chen, Z.; Zhang, L.; Chen, J.; Cao, Y. An Extended π -Conjugated Area of Electron-Donating Units in D–A Structured Polymers towards high-mobility field-effect transistors and highly efficient polymer solar cells. *J. Mater. Chem. C* **2017**, *5*, 2786–2793.
- [16] Sun, B.; Hong, W.; Aziz, H.; Li, Y. A Pyridine-Flanked Diketopyrrolopyrrole (DPP)-Based Donor–Acceptor Polymer Showing High Mobility in Ambipolar and n-Channel Organic Thin Film Transistors. *Polym. Chem.* **2015**, *6*, 938–945.
- [17] Wu, Q.; Wang, M.; Qiao, X.; Xiong, Y.; Huang, Y.; Gao, X.; Li, H. Thieno[3,4-c]pyrrole-4,6-dione Containing Copolymers for High Performance Field-Effect Transistors. *Macromolecules* **2013**, *46*, 3887–3894.
- [18] Wang, Z. A.; Kuwabara, J.; Ichige, A.; Yasuda, T.; Kanbara, T. Synthesis of n-Type Semiconducting Polymer Consisting of Benzodipyrrolidone and Thieno-[3,4-c]-pyrrole-4,6-dione via C-H Direct Arylation. *Synth. Met.* **2016**, *222*, 383–387.

- [19] Wang, W.; Yan, S.; Lv, W.; Zhao, Y.; Sun, M.; Zhou, M.; Ling, Q. New n-Type Copolymers Based on Pentafluorobenzene-Substituted Thieno [3,4-c] Pyrrole-4,6-dione for All-Polymer Solar Cells. *Journal of Macromolecular Science, Part A* **2015**, *52*, 892–900.
- [20] Kim, G.; Han, A.-R.; Lee, H. R.; Lee, J.; Oh, J. H.; Yang, C. Acceptor-Acceptor Type Isoindigo-Based Copolymers for High-Performance n-Channel Field-Effect Transistors. *Chem. Commun.* **2014**, *50*, 2180–2183.
- [21] Grenier, F.; Berrouard, P.; Pouliot, J.-R.; Tseng, H.-R.; Heeger, A. J.; Leclerc, M. Synthesis of New n-Type Isoindigo Copolymers. *Polym. Chem.* **2013**, *4*, 1836–1841.
- [22] Liu, S.; Song, X.; Thomas, S.; Kan, Z.; Cruciani, F.; Laquai, F.; Bredas, J.-L.; Beaujuge, P. M. Thieno[3,4-c]Pyrrole-4,6-Dione-Based Polymer Acceptors for High Open-Circuit Voltage All-Polymer Solar Cells. *Adv. Energy Mater.* **2017**, *376*, 1602574.
- [23] Liu, S.; Kan, Z.; Thomas, S.; Cruciani, F.; Brédas, J.-L.; Beaujuge, P. M. Thieno[3,4-c]pyrrole-4,6-dione-3,4-difluorothiophene Polymer Acceptors for Efficient All-Polymer Bulk Heterojunction Solar Cells. *Angew. Chem. Int. Ed.* **2016**, *55*, 12996–13000.
- [24] Zhou, N.; Guo, X.; Ponce Ortiz, R.; Harschneck, T.; Manley, E. F.; Lou, S. J.; Hartnett, P. E.; Yu, X.; Horwitz, N. E.; Mayorga Burrezo, P. *et al.* Marked Consequences of Systematic Oligothiophene Catenation in Thieno[3,4-c]pyrrole-4,6-dione and Bithiopheneimide Photovoltaic Copolymers. *J. Am. Chem. Soc.* **2015**, *137*, 12565–12579.
- [25] Guo, X.; Ortiz, R. P.; Zheng, Y.; Kim, M.-G.; Zhang, S.; Hu, Y.; Lu, G.; Facchetti, A.; Marks, T. J. Thieno[3,4-c]pyrrole-4,6-dione-Based Polymer Semiconductors: Toward High-Performance, Air-Stable Organic Thin-Film Transistors. *J. Am. Chem. Soc.* **2011**, *133*, 13685–13697.
- [26] Qiao, X.; Wu, Q.; Wu, H.; Zhang, J.; Li, H. Bithienopyrroledione-Based Copolymers, Versatile Semiconductors for Balanced Ambipolar Thin-Film Transistors and Organic Solar Cells with Voc > 1 V. *Adv. Funct. Mater.* **2017**, *27*, 1604286.
- [27] Kirby, N. M.; Mudie, S. T.; Hawley, A. M.; Cookson, D. J.; Mertens, H. D. T.; Cowieson, N.; Samardzic-Boban, V. A Low-Background-Intensity Focusing Small-Angle X-Ray Scattering Undulator Beamline. *J Appl Crystallogr* **2013**, *46*, 1670–1680.
- [28] Ilavsky, J. Nika: Software for Two-Dimensional Data Reduction. *J Appl Crystallogr* **2012**, *45*, 324–328.

- [29] Hildner, R.; Köhler, A.; Müller-Buschbaum, P.; Panzer, F.; Thelakkat, M. π -Conjugated Donor Polymers: Structure Formation and Morphology in Solution, Bulk and Photovoltaic Blends. *Adv. Energy Mater.* **2017**, *85*, 1700314.
- [30] Panzer, F.; Bässler, H.; Lohwasser, R.; Thelakkat, M.; Köhler, A. The Impact of Polydispersity and Molecular Weight on the Order–Disorder Transition in Poly(3-hexylthiophene). *J. Phys. Chem. Lett.* **2014**, *5*, 2742–2747.
- [31] Spano, F. C.; Clark, J.; Silva, C.; Friend, R. H. Determining Exciton Coherence from the Photoluminescence Spectral Line Shape in Poly(3-Hexylthiophene) Thin Films. *J. Chem. Phys.* **2009**, *130*, 74904.
- [32] Gräf, K.; Rahim, M. A.; Das, S.; Thelakkat, M. Complementary Co-Sensitization of an Aggregating Squaraine Dye in Solid-State Dye-Sensitized Solar Cells. *Dyes and Pigments* **2013**, *99*, 1101–1106.
- [33] Bredas, J.-L. Mind the Gap! *Mater. Horiz.* **2014**, *1*, 17–19.
- [34] Liang, Y.; Xu, Z.; Xia, J.; Tsai, S.-T.; Wu, Y.; Li, G.; Ray, C.; Yu, L. For the Bright Future-Bulk Heterojunction Polymer Solar Cells with Power Conversion Efficiency of 7.4%. *Adv. Mater.* **2010**, *22*, E135-138.

Supporting Information

Highly efficient and balanced charge transport in thieno[3,4- c]pyrrole-4,6-dione copolymers: Dramatic influence of thieno[3,2- b]thiophene comonomer on alignment and charge transport

Tina Weller,^a Kira Rundel,^b Gert Krauss,^a Christopher R. McNeill^b and Mukundan Thelakkat^{a*}

^a Applied Functional Polymers, Macromolecular Chemistry I, University of Bayreuth, 95440 Bayreuth, Germany.

^b Department of Materials Science and Engineering, Monash University, Wellington Road, Clayton VIC, 3800, Australia.

* Corresponding author: mukundan.thelakkat@uni-bayreuth.de

Table of Contents

1	Monomer Syntheses.....	129
1.1	Materials and Methods.....	129
1.2	Synthesis of TT monomer	129
2	Polymer Characterization	132
2.1	Polymer NMR spectra	132
2.2	Polymer SEC	134
3	Thermal Properties	135
3.1	Thermogravimetric analysis.....	135
3.2	Flash Differential Scanning Calorimetry (DSC).....	135
4	UV-vis and fluorescence spectroscopy.....	136
5	Additional OFET <i>I-V</i> curves	137
6	Organic Solar Cells	140
7	References	141

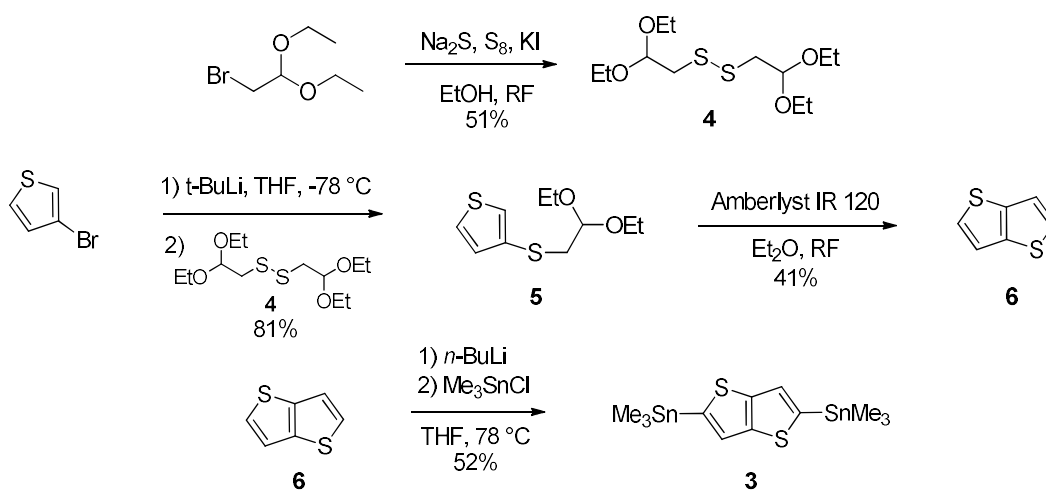
1 Monomer Syntheses

1.1 Materials and Methods

Water and air sensitive reactions were conducted in Schlenk apparatuses under argon, which were previously baked out in high vacuum. Commercially available solvents were purchased from Sigma Aldrich and Acros Organics in sealed bottles with mole sieve. ^1H and ^{19}F NMR spectra were recorded on a Bruker Avance spectrometer (300 MHz) with deuterated solvents purchased from Deutero. Chemical shifts are reported in ppm relative to the known value of residual solvent signal. Molecular weights were assessed by the electron ionization mass spectrometry performed on a Finnigan MAT 8500 spectrometer (70 eV) at the Department of Chemistry of University Bayreuth.

1.2 Synthesis of TT monomer

The overall synthesis of the TT monomer is shown in Scheme S 5.1 and the synthetic procedure are adapted from literature.^[1,2]



Scheme S 5.1. Synthesis of the TT monomer.

1,2-Bis(2,2-diethoxyethyl)disulfide **4**

A mixture of 2-bromo-1,1-diethoxyethane (95.0 mL, 632 mmol, 1 eq), sodium sulfide (121 g, 505 mmol, 0.8 eq), sulfur (20.3 g, 632 mmol, 1 eq) and potassium iodide (5.24 g, 31.6 mmol, 0.05 eq) in 500 mL ethanol was stirred under reflux for 12 h. After removal of the main part of ethanol by distillation, the residual suspension was filtered and rinsed with ethyl acetate for several times. The combined filtrates were washed with water and a saturated, aqueous solution of NaCl

followed by drying over MgSO_4 . Filtration and removal of the solvent by rotary evaporation results in a black oil, which contains beside the product the mono- and trisulfide analogs. Analysis by GC gives a composition of 72% product, 15% monosulfide and 13% trisulfide. The crude product was purified by vacuum distillation ($\theta_{\text{steam}} = 110\text{-}115\text{ }^\circ\text{C}$, $p = 1.5\text{-}3.2 \times 10^{-3}$ mbar) yielding 1,2-bis(2,2-diethoxyethyl)disulfide 4 (38.5 g, 129 mmol, 51%) in 90% purity as a brown oil.

^1H NMR (300 MHz, CDCl_3): $\delta = 4.71$ (t, $J = 5.6$ Hz, 2H), 3.50-3.73 (m, 8H), 2.96 (d, $J = 5.7$ Hz, 4H), 1.22 (t, $J = 7.1$ Hz, 15H) ppm. EI-MS (70 eV): m/z 298 (M^+).

3-(2,2-Diethoxyethylsulfanyl)thiophene 5

A solution of 3-bromothiophene (7.17 mL, 77.0 mmol, 1 eq) in 500 mL dry diethyl ether was cooled down to $-78\text{ }^\circ\text{C}$ followed by the dropwise addition of a 1.7 M solution of tert-butyl lithium in hexane (90.0 mL, 153 mmol, 2 eq). After the solution was stirred at $-78\text{ }^\circ\text{C}$ for 30 min, bis(2,2-diethoxyethyl)disulfide 4 (22.8 g, 77.0 mmol, 1 eq) were added dropwise within 15 min. The turbid mixture was allowed to warm to room temperature and was stirred overnight. Water (200 mL) was added and the layers were separated. The organic phase was washed with a 1 M solution of NaOH (3 x 50 mL) and a saturated, aqueous solution of NaCl (3 x 50 mL), respectively. After drying over MgSO_4 and filtration, the solvent was removed under reduced pressure. The crude product was purified by distillation in vacuo ($\theta_{\text{steam}} = 80\text{-}85\text{ }^\circ\text{C}$, $p = 10^{-1}$ mbar) yielding 3-(2,2-diethoxyethylsulfanyl)thiophene 5 (10.4 g, 44.8 mmol, 81%) as a yellow oil.

^1H NMR (300 MHz, CDCl_3): $\delta = 7.31$ (dd, $J = 5.1, 3.0$ Hz, 1H), 7.20 (dd, $J = 3.2, 1.3$ Hz, 1H), 7.06 (dd, $J = 4.9, 1.3$ Hz, 1H), 4.62 (t, $J = 5.6$ Hz, 1H), 3.49-3.74 (m, 4H), 3.05 (d, $J = 5.7$ Hz, 2H), 1.20 ppm (t, $J = 7.1$ Hz, 6H) ppm. EI-MS (70 eV): m/z 232 (M^+).

Thieno[3,2-*b*]thiophene 6

A mixture of 3-(2,2-diethoxyethylsulfanyl)thiophene 5 (9.30 g, 40.0 mmol, 1 eq) in 200 mL diethyl ether and 9.40 g Amberlyst® IR 120 was refluxed for 4 h. The solution was decanted and the resin beads were suspended in another portion of diethyl ether (50 mL). This procedure was repeated three times to extract the residual product from the resin. After removal of the solvent by rotary evaporation, the crude oil was purified by column chromatography (silica; *n*-Hex) yielding thieno[3,2-*b*]thiophene 6 (3.57 g, 25.5 mmol, 41 %) as white crystals.

^1H NMR (300 MHz, CDCl_3): $\delta = 7.40$ ($J = 5.1$ Hz, 2H), 7.28 ($J = 5.1$ Hz, 2H) ppm. EI-MS (70 eV): m/z 140 (M^+).

2,5-Bis(trimethylstannyl)thieno[3,2-*b*]thiophene 3

A solution of thieno[3,2-*b*]thiophene 6 (1.50 g, 10.7 mmol, 1 eq) in 90 mL dry THF was cooled to -78 °C and a 1.6 M solution of *n*-butyl lithium in hexane (13.4 mL, 21.4 mmol, 3 eq) was added dropwise. After stirring for 10 min at -78 °C, the reaction mixture was allowed to warm to room temperature and was further stirred for 3 h at room temperature. The reaction mixture was again cooled to -78 °C and chlorotrimethylstannane (4.26 g, 21.4 mmol, 2 eq) was added in one portion. Further stirring for 10 min at -78 °C was followed by removal of the cooling bath and the reaction mixture was stirred overnight at room temperature. Water (150 mL) was added and the aqueous phase was extracted with diethyl ether (3 x 100 mL). The combined organic phases were washed with a saturated, aqueous solution of NaCl and dried over MgSO_4 . After filtration, the solvent was concentrated under reduced pressure until precipitation occurs. The crystals were filtered, washed with cold ethanol and dried in vacuo yielding 2,5-bis(trimethylstannyl)thieno[3,2-*b*]thiophene 3 (2.59 g, 5.56 mmol, 52%) as white crystals.

^1H NMR (300 MHz, $\text{THF-}d_8$): $\delta = 7.28$ (s, 2H), 0.36 (s, 18H) ppm. EI-MS (70 eV): m/z 466 (M^+).

2 Polymer Characterization

2.1 Polymer NMR spectra

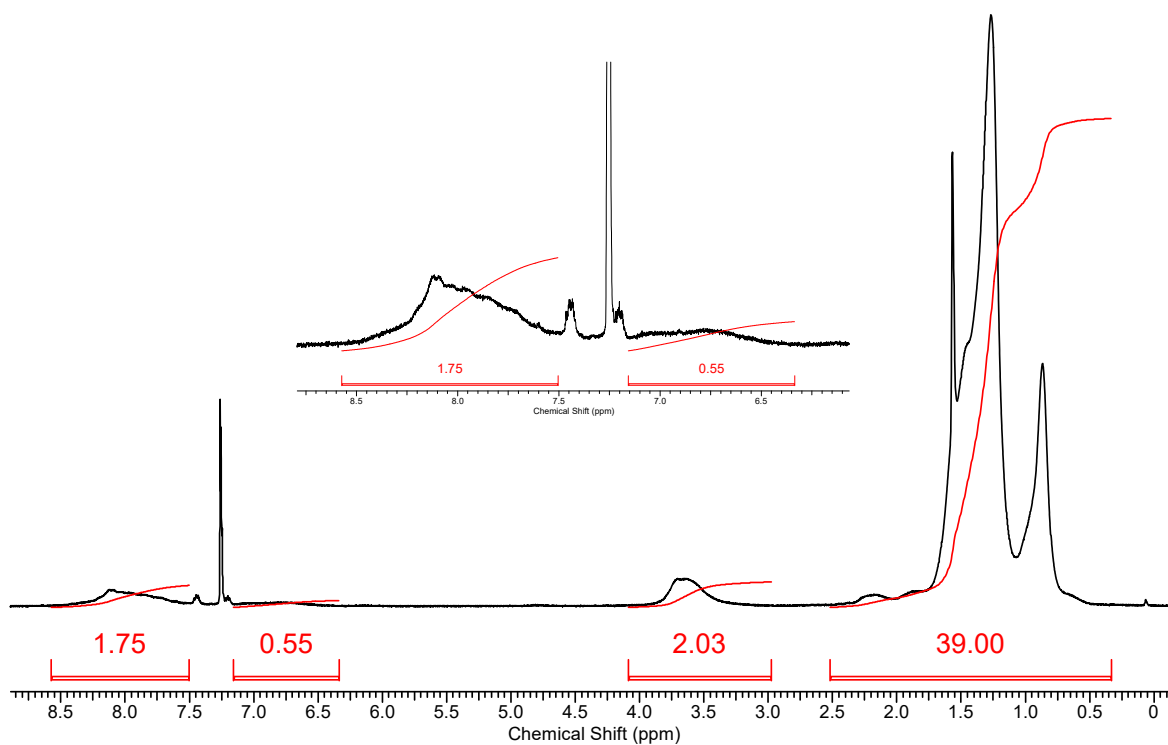


Figure S 5.1. $^1\text{H-NMR}$ spectrum of PTPDT-1 in CDCl_3 .

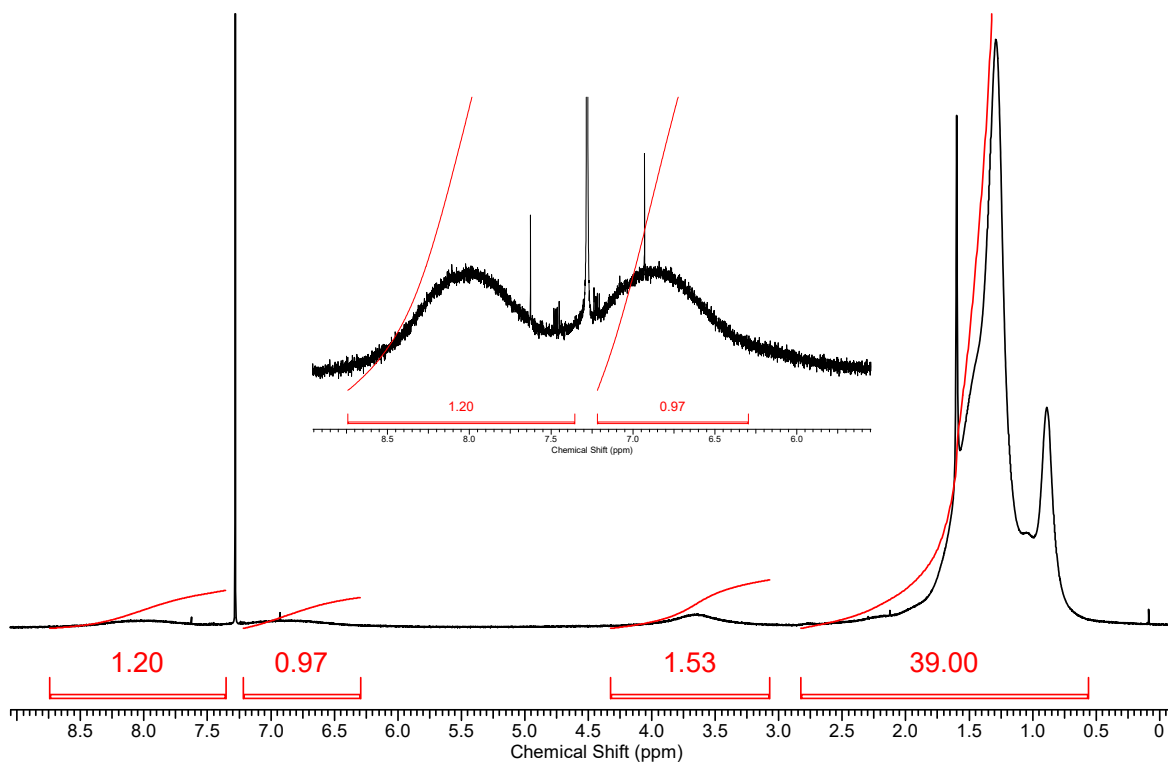


Figure S 5.2. $^1\text{H-NMR}$ spectrum of PTPDT-2 in CDCl_3 .

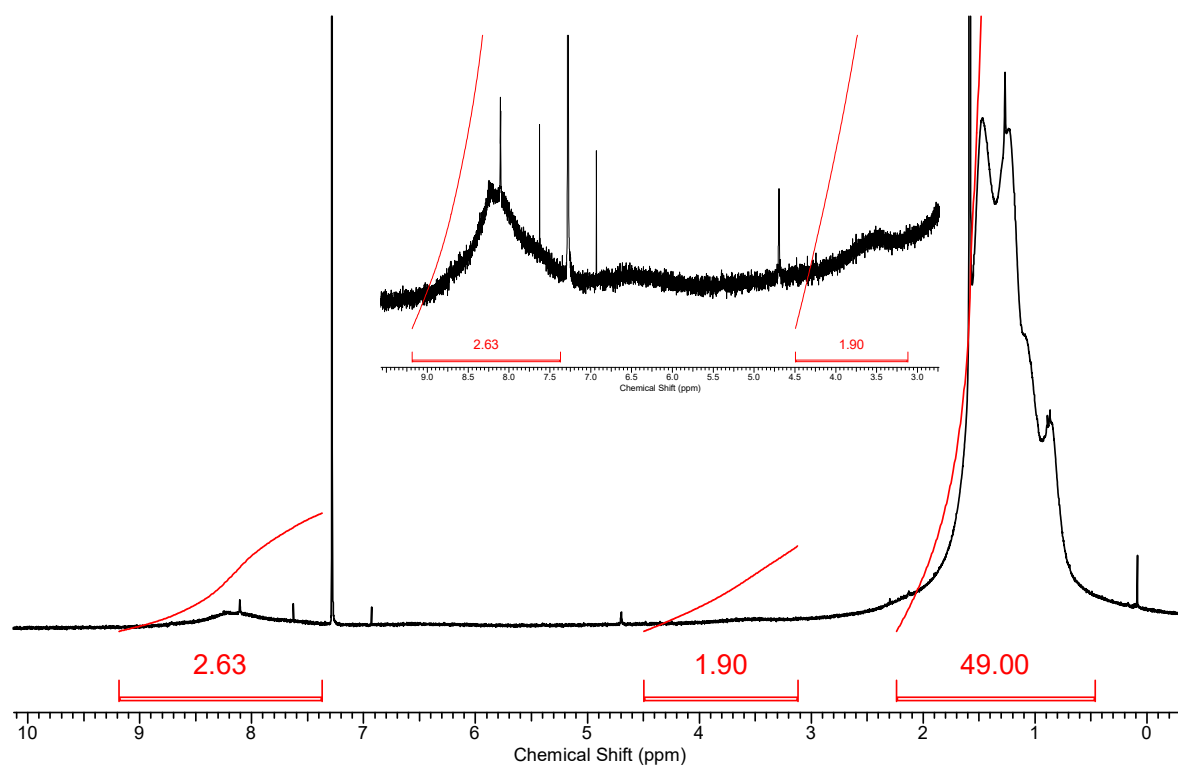


Figure S 5.3. $^1\text{H-NMR}$ spectrum of PTPDTT in CDCl_3 .

2.2 Polymer SEC

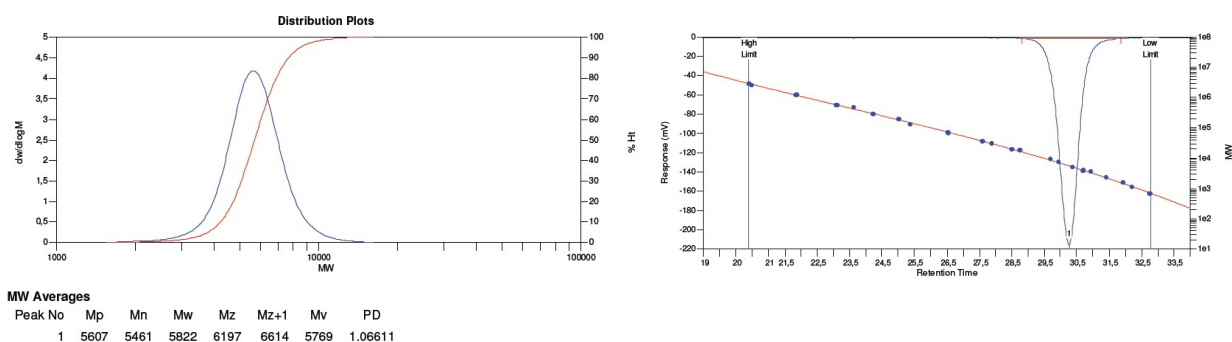


Figure S 5.4. High temperature size exclusion chromatography of PTPDT-1 in 1,2,4-trichlorobenzene at 160 °C with PS calibration

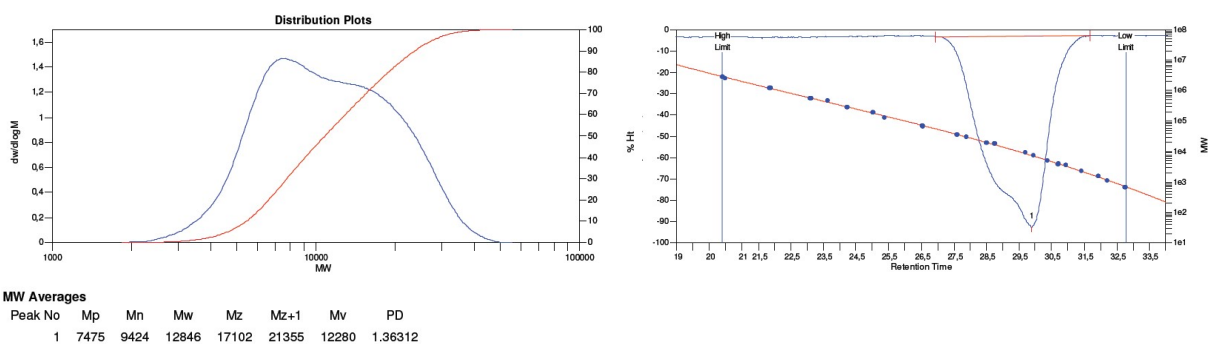


Figure S 5.5. High temperature size exclusion chromatography of PTPDT-2 in 1,2,4-trichlorobenzene at 160 °C with PS calibration.

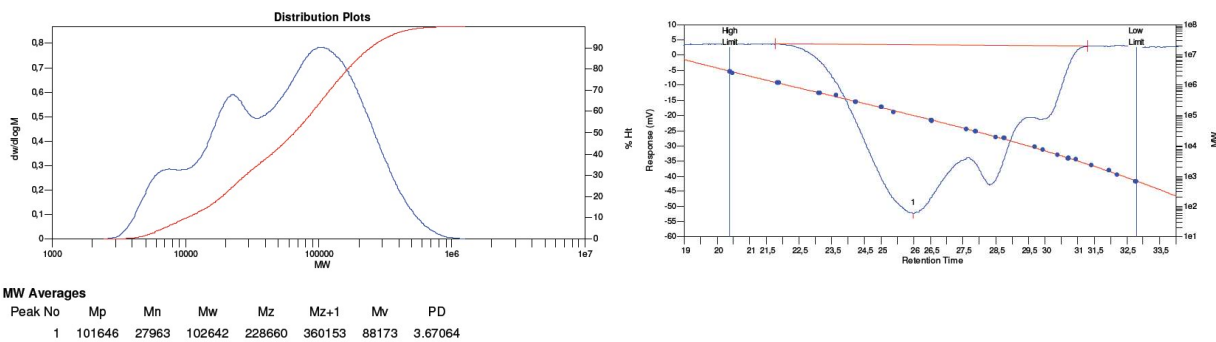


Figure S 5.6. High temperature size exclusion chromatography of PTPDTT in 1,2,4-trichlorobenzene at 160 °C with PS calibration.

3 Thermal Properties

3.1 Thermogravimetric analysis

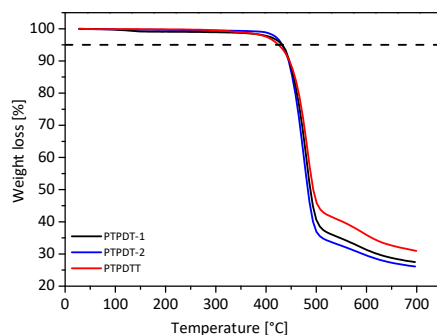


Figure S 5.7. Thermogravimetric analysis of the PTPDs with the decomposition onset ($T_{5\%}$).

3.2 Flash Differential Scanning Calorimetry (DSC)

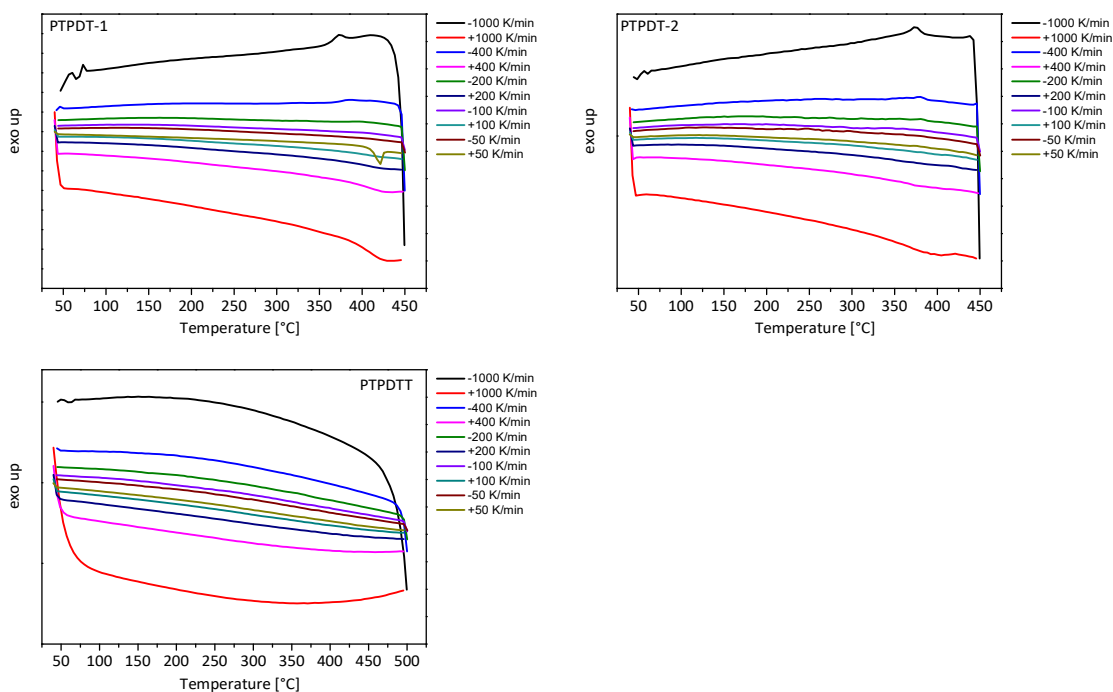


Figure S 5.8. Flash DSC analysis of the PTPDs with scanning rates from 50-1000 $K\ min^{-1}$.

4 UV-Vis and fluorescence spectroscopy

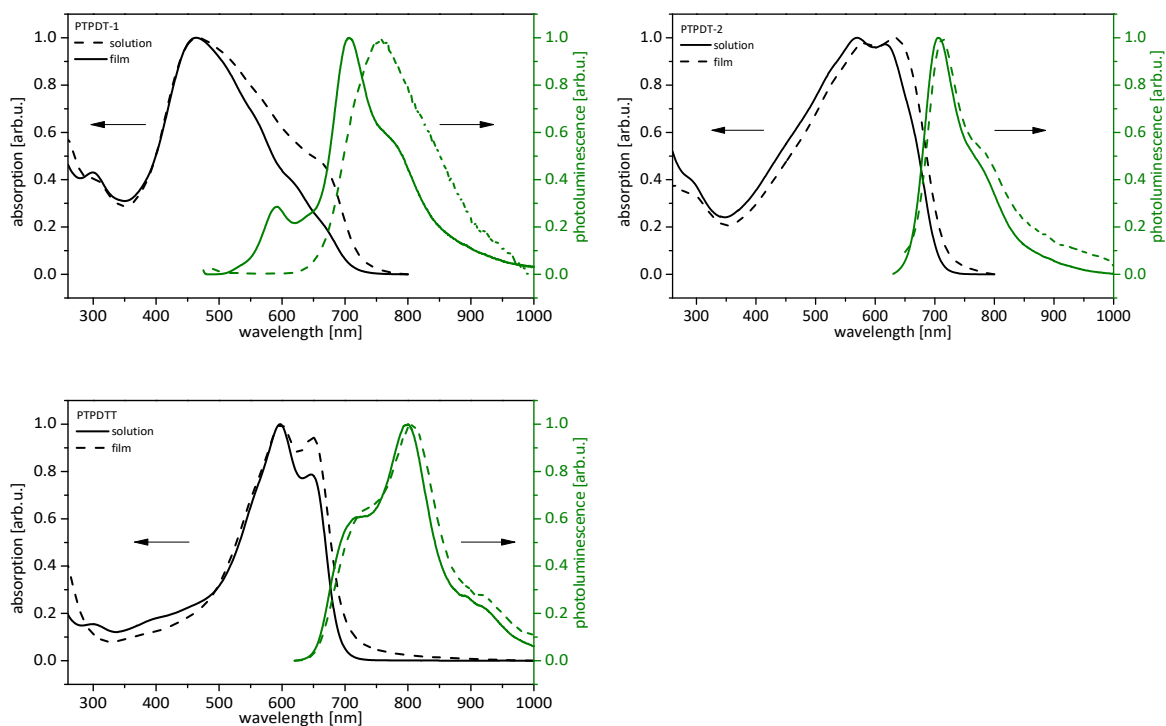


Figure S 5.9. UV-Vis and photoluminescence spectra in chloroform solution (0.01 mg mL^{-1}) and thin films for each PTPD.

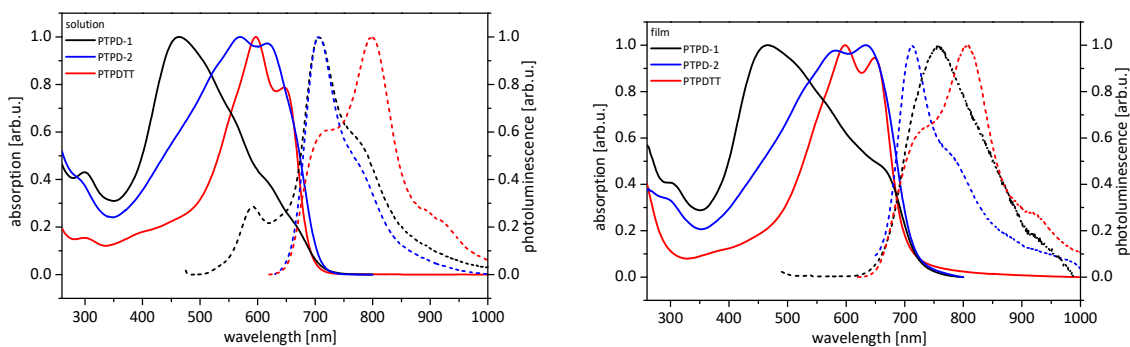


Figure S 5.10. Comparison of UV-Vis and photoluminescence spectra in chloroform solution (0.01 mg mL^{-1}) and thin films.

5 Additional OFET I - V curves

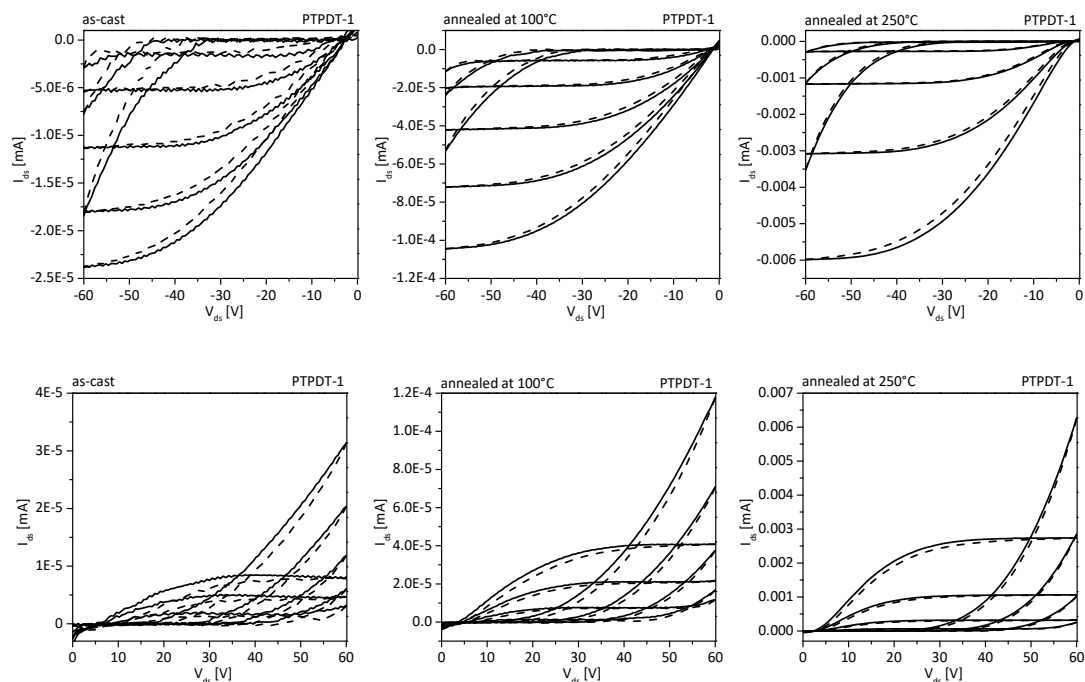


Figure S 5.11. OFET output characteristics: p -channel operation (top) and n -channel operation (bottom) of PTPDT-1 in as-cast films (left), annealed films at 100 °C (middle) and 250 °C (right). Solid lines represent forward scans and dashed lines reversed scans.

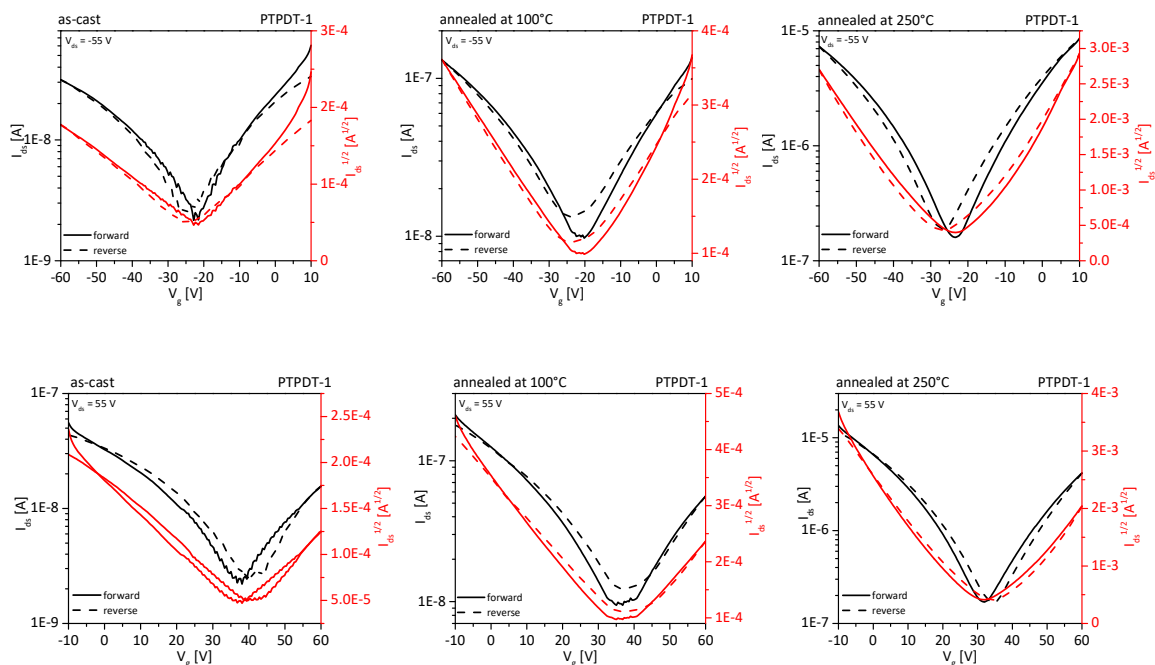


Figure S 5.12. OFET transfer characteristics: p -channel operation (top) and n -channel operation (bottom) of PTPDT-1 in as-cast films (left), annealed films at 100 °C (middle) and 250 °C (right). Solid lines represent forward scans and dashed lines reversed scans.

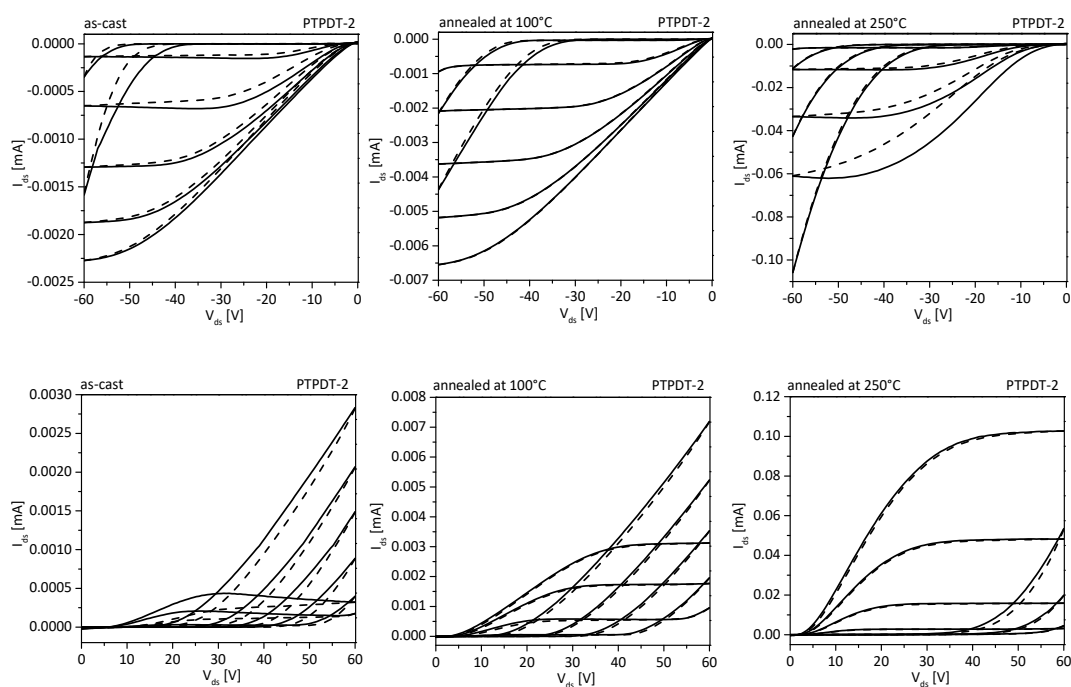


Figure S 5.13. OFET output characteristics: p-channel operation (top) and n-channel operation (bottom) of PTPDT-2 in as-cast films (left), annealed films at 100 °C (middle) and 250 °C (right). Solid lines represent forward scans and dashed lines reversed scans.

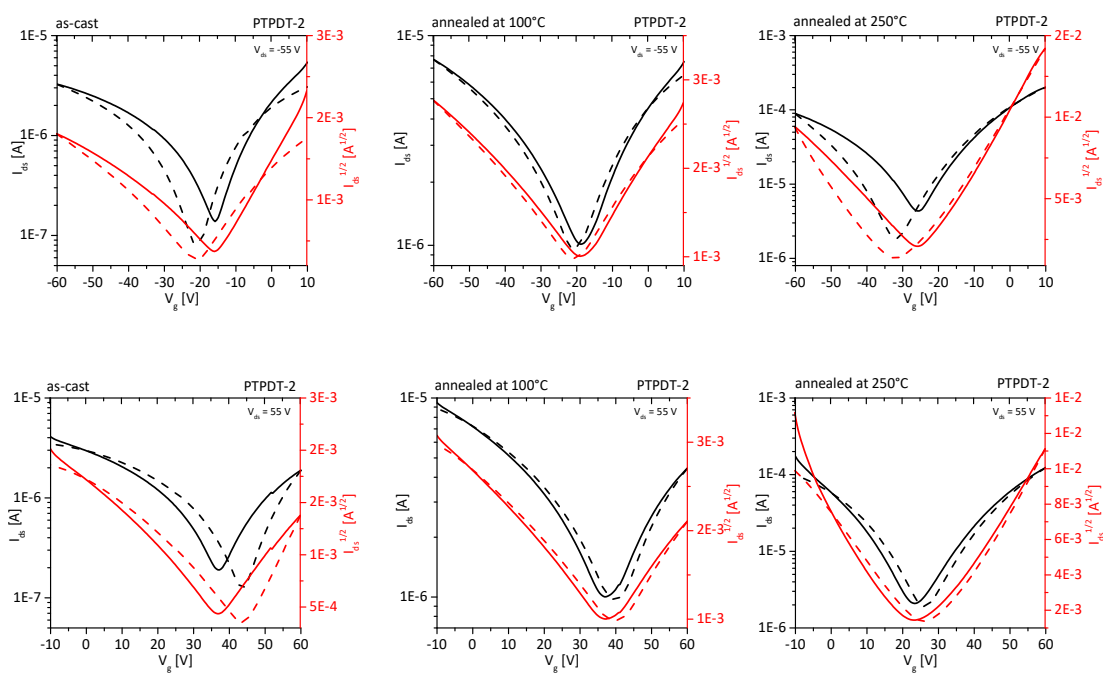


Figure S 5.14. OFET transfer characteristics: p-channel operation (top) and n-channel operation (bottom) of PTPDT-2 in as-cast films (left), annealed films at 100 °C (middle) and 250 °C (right). Solid lines represent forward scans and dashed lines reversed scans.

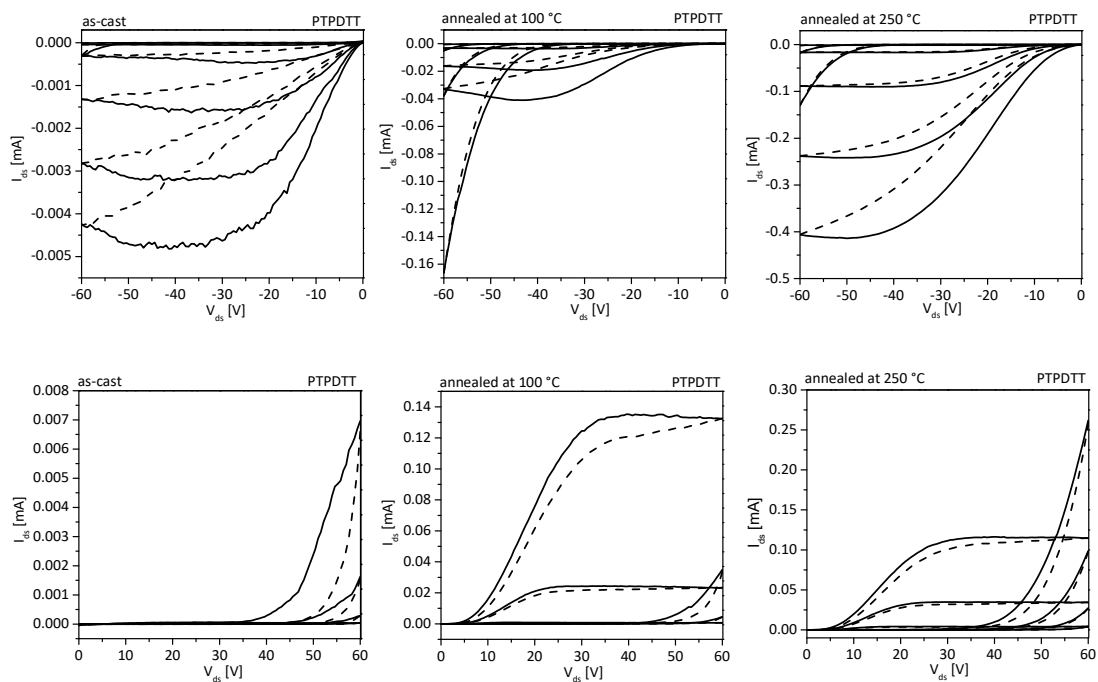


Figure S 5.15. OFET output characteristics: p-channel operation (top) and n-channel operation (bottom) of PTPDTT in as-cast films (left), annealed films at 100 °C (middle) and 250 °C (right). Solid lines represent forward scans and dashed lines reversed scans.

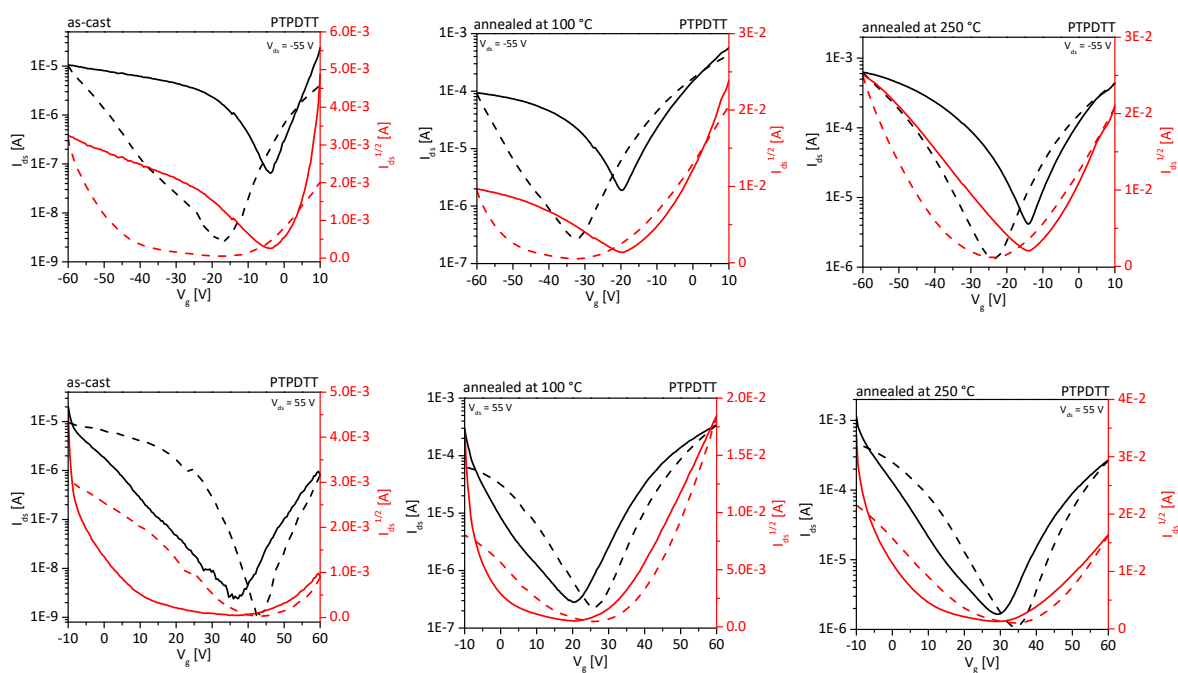
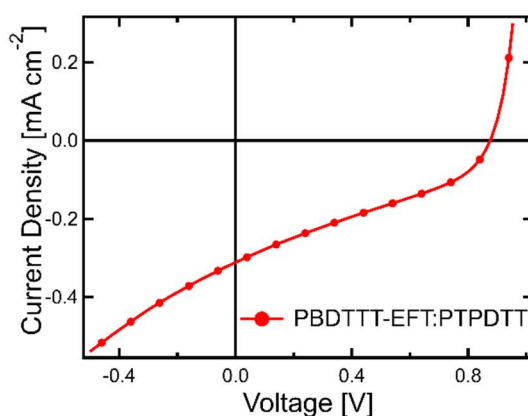
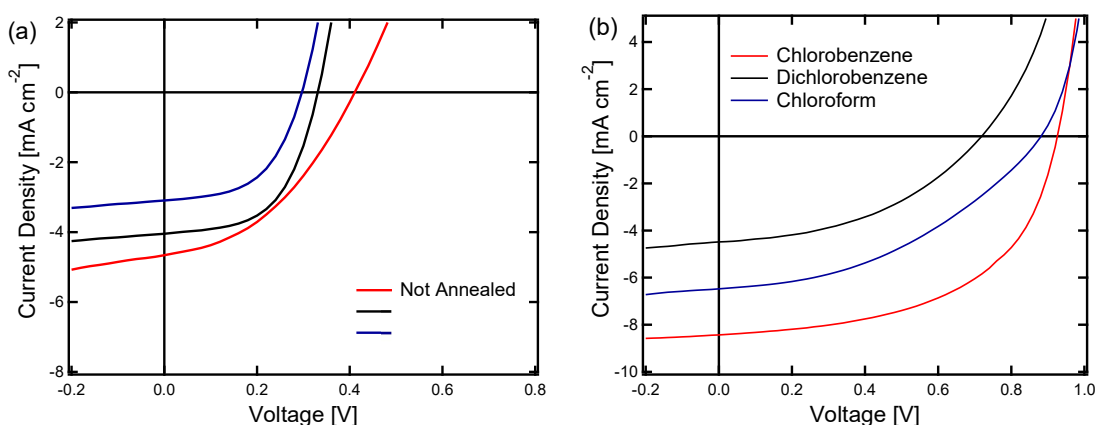


Figure S 5.16. OFET transfer characteristics: p-channel operation (top) and n-channel operation (bottom) of PTPDTT in as-cast films (left), annealed films at 100 °C (middle) and 250 °C (right). Solid lines represent forward scans and dashed lines reversed scans.

Table S 5.1. Threshold voltages V_T in the as cast state as well as after annealing at 100 °C and 250 °C, respectively. Annealing was performed for 15 min under nitrogen atmosphere in a glovebox.

Polymer	p-type			n-type		
	ac	100 °C	250 °C	ac	100 °C	250 °C
	V_T (V)	V_T (V)	V_T (V)	V_T (V)	V_T (V)	V_T (V)
PTPDT-1	-10	-10	-23	27	29	35
PTPDT-2	-5	1	-12	27	23	30
PTPDTT	-16	-26	-19	-	35	32

6 Organic Solar Cells

**Figure S 5.17.** J-V curve for devices utilizing PTPDPT as an acceptor with the donor polymer PBDTTT-EFT.**Figure S 5.18.** Unoptimized J-V curves for PTPDPT:PC₇₁BM devices which investigate optimum annealing conditions (processed from CB) (a) and solvent (with 2% DIO) (b). Devices in (a) show lower V_{oc} values due to an unoptimized donor:acceptor ratio.

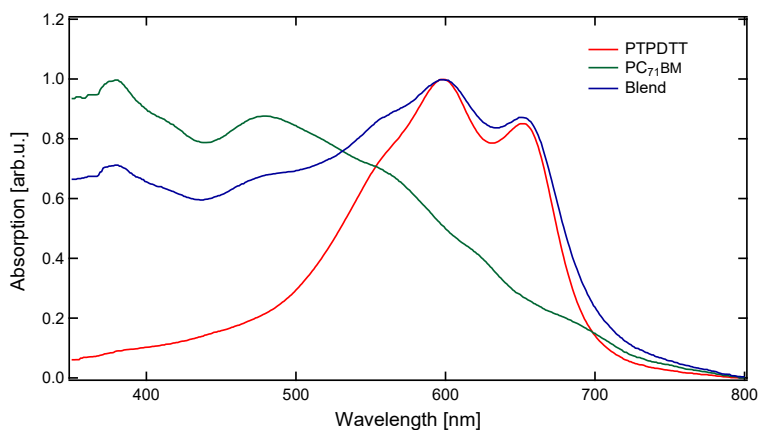


Figure S 5.19. Normalized absorbance for PTPDTT (red), PC₇₁BM (green) and 1:1.5 PTPDTT:PC₇₁BM blend films (black). Films were cast from solutions in chlorobenzene without DIO as DIO is transparent at visible wavelengths.

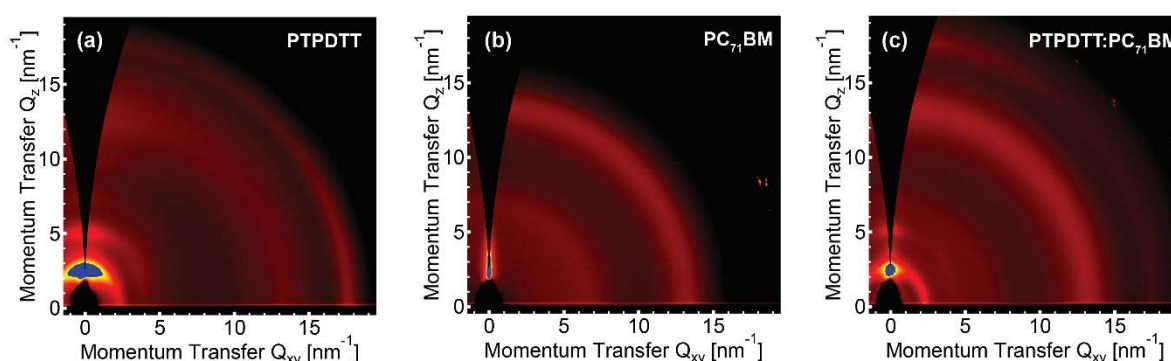


Figure S 5.20. 2D GIWAXS images for PTPDTT (a), PC₇₁BM (b), and a 1:1.5 PTPDTT: PC₇₁BM blend with 2% DIO.

Table S 5.2. Crystalline parameters analyzed from GIWAXS patterns for films processed using optimized solar cell conditions.

Polymer	Alkyl spacing (IP) (nm)	π - π spacing (IP) (nm)	Alkyl spacing (OOP) (nm)	π - π spacing (OOP) (nm)
PTPDTT – solar cells	2.76	0.356	2.77	0.359
PTPDTT – transistors	2.63	0.354	2.63	0.354
PTPDTT:PC ₇₁ BM blend	2.71	0.358	2.90	0.356

The discrepancy in alkyl stacking distance for PTPDTT is attributed to spin casting from different solvents (chloroform and chlorobenzene).

7 References

- [1] Chongjun, J.; Kirner, Hans, Jürg; Zhou, M.; Weitz, T.; Mishra, A. K. Heteroacene Compounds for Organic Electronics. PCT/IB2013/060391, Nov 25, **2013**.
- [2] Henssler, J. T.; Matzger, A. J. Facile and Scalable Synthesis of the Fused-Ring Heterocycles Thieno[3,2-b]thiophene and Thieno[3,2-b]furan. *Org. Lett.* **2009**, *11*, 3144–3147.

6 Fluorination in thieno[3,4-c]pyrrole-4,6-dione copolymers leading to electron transport, high crystallinity and end-on alignment

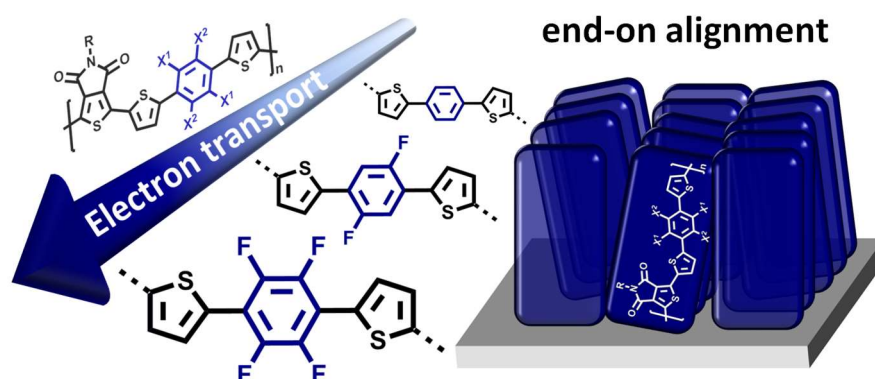
Tina Weller,^a Marion Breunig,^a Christian J. Müller,^a Elliot Gann^c, Christopher R. McNeill^b and Mukundan Thelakkat^{a*}

^a Applied Functional Polymers, Macromolecular Chemistry I, University of Bayreuth, 95440 Bayreuth, Germany.

^b Department of Materials Science and Engineering, Monash University, Wellington Road, Clayton VIC, 3800, Australia.

^c Materials Measurement Laboratory, National Institute of Standards and Technology, 100 Bureau Dr, Gaithersburg, MD 20899, USA.

* Corresponding author: mukundan.thelakkat@uni-bayreuth.de



Published in *Journal of Material Chemistry C*, **2017**, *5*, 7527-7534

Reproduced with permission of *The Royal Society of Chemistry*

Abstract

A series of copolymers based on thieno[3,4-*c*]pyrrole-4,6-dione and thiophene-phenylthiophene with varying degrees of fluorination on the phenyl unit was synthesized by Stille polycondensation. The influence of the degree of fluorination on the optical, thermal and electrochemical properties of these polymers is systematically studied. Additionally, the charge transport in organic field effect transistors (OFETs) as well as the thin film alignment are investigated. After thermal annealing the non-fluorinated as well as difluorinated polymers show ambipolar charge transport in OFETs. In contrast, tetrafluorination results in exclusively n-type behavior with an electron mobility of $3.7 \times 10^{-4} \text{ cm}^2 \text{ V}^{-1} \text{ s}^{-1}$. GIWAXS measurements of as-cast and annealed films reveal a very interesting structural alignment in thin films. All polymers show the rarely observed “end-on” orientation, where the polymer chains stand on the substrate. This may be explained by the low molecular weights of these polymers in relation to the film thickness. Fluorination does not influence the microstructural properties, only the propensity of crystallization is increased.

6.1 Introduction

In the past, research in the field of polymeric semiconductors has mainly focused on hole-conducting materials synthesized according to the alternating donor–acceptor concept. Recently, there is increasing interest in electron-conducting materials, also as an alternative for fullerene derivatives for applications. In particular naphthalene diimide (NDI) containing copolymers have attracted appreciable attention and have been successfully applied in all-polymer solar cells with efficiencies exceeding 8%.^[1] Moreover, it has been repeatedly shown that in all-polymer solar cells, the alignment of polymer chains with their planar π -faces of their backbone, either in an edge-on or face-on manner, considerably affects the device performance.^[2,3] Thieno[3,4-*c*]pyrrole-4,6-dione (TPD) is an interesting electron-deficient building block unit due to its high planarity and easy synthetic accessibility.^[4,5] Additionally, copolymers incorporating this acceptor unit show high long-term thermal stability, which is also an important and desirable property for application in optoelectronic devices.^[6] In general, the TPD moiety has been incorporated as an electron withdrawing unit into classical low bandgap copolymers to obtain donor materials,^[7–10] which achieved efficiencies of over 9% in combination with fullerenes in organic solar cells.^[11] Also, some of these materials exhibit very high hole mobilities of up to $1.3 \text{ cm}^2 \text{ V}^{-1} \text{ s}^{-1}$ in OFET devices.^[12] Regarding electron transport, only

a few examples have been published to date to the best of our knowledge.^[13–16] The highest mobility for unipolar n-type transport was reported for copolymers consisting of TPD and isoindigo resulting in a field-effect mobility of $0.01 \text{ cm}^2 \text{ V}^{-1} \text{ s}^{-1}$.^[15] Marks et al. showed ambipolar charge transport in TPD containing copolymers with thiophene as the comonomer, where the n-type field effect mobility even exceeds the corresponding hole mobility.^[17] Very recently, TPD containing copolymers were applied as acceptor polymers in polymer/polymer blend solar cells with appreciable performance.^[18,19] As a comonomer, we selected thiophene-phenyl-thiophene (TPT), which is a rigid building block leading to highly crystalline materials.^[20,21] Intrachain nonbonding interactions such as H–S or H–F can improve the planarity and therefore, the crystallinity and stacking behavior. This is the case for di- and tetrasubstitution of the phenyl protons with small and strongly electronegative fluorine atoms. Crystal structures of the difluorinated small molecules gave evidence that the structure is locked by H–F interactions^[21] contrary to some reports where S–F interactions were claimed.^[22] In particular, Ratner et al. showed that the contribution of S–F interactions is nearly zero as determined by theoretical calculations.^[23] Besides the influence of fluorination on the crystalline structure, it is also a powerful tool to improve the electron affinity resulting in higher electron transport and in some cases ambipolar charge transport. In the literature, several reports have been published, which show this concept, mainly based on diketopyrrolopyrrole (DPP)^[24–28] and naphthalene diimide (NDI)^[29,30] copolymers. In this contribution, we report a series of TPD containing copolymers with different degrees of fluorination of the TPT unit. The synthesis and detailed structural characterization of the copolymers containing TPD and different TPT units are described. To guarantee sufficient solubility, the TPD unit was decorated with a branched octyldodecyl substituent. The comonomer TPT was di- and tetrafluorinated (TPF₂T and TPF₄T) in order to gradually increase the degree of fluorination. The systematic study of the influence of fluorination on the properties regarding structure formation and OFET mobilities are given here. In particular, we were interested to elucidate the influence of fluorination on crystallinity and consequently on charge transport. Very surprisingly, the GIWAXS studies show the end-on alignment of polymer chains, which is usually rare in the case of conjugated polymers without any reactive grafting of the chain onto a substrate.

6.2 Experimental part

6.2.1 Materials and methods

All commercially available reagents were used as received unless otherwise noted. Reactions under microwave irradiation were conducted in a Biotage Initiator Eight + Microwave. Size exclusion chromatography (SEC) was carried out on an Agilent (Polymer Laboratories Ltd) PL-SEC 220 high temperature chromatographic unit equipped with three linear mixed bed columns (PSS Polefin linear XL) and DP and RI detectors. Analysis was performed at 160 °C using 1,2,4-trichlorobenzene as the eluent. The samples were prepared by dissolving the polymer (0.1 wt%) in the solvent in an external oven and the solutions were injected and eluted without filtration. The molecular weights of the samples were referenced to polystyrene standards ($M_w = 518\text{--}600\,000\text{ g mol}^{-1}$, $K = 12.100$ and $\text{Alpha} = 0.707$). Cyclic voltammetric measurements were carried out in thin films under moisture- and oxygen-free conditions using a three-electrode assembly connected to a potentiostat (model 263A, EG&G Princeton Applied Research) at a scanning rate of 100 mV s^{-1} . As an electrolyte solution tetra-*n*-butylammonium hexafluorophosphate in acetonitrile with a concentration of 0.1 M was used. Glass substrates coated with ITO ($10\ \Omega\ \square^{-1}$) were used as working electrodes, on which thin films from CHCl_3 solutions with a concentration of 5 mg mL^{-1} were spin coated at 1500 rpm. A platinum wire in the respective electrolyte solution and Ag/AgNO_3 in acetonitrile (0.1 M) were used as the counter and reference electrode, respectively. Each measurement was calibrated by the internal standard ferrocene/ferrocenium. UV/Vis spectra were recorded on a JASCO V-670 spectrophotometer. Fluorescence spectroscopy was performed on a JASCO FP-8600 spectrofluorometer using the wavelength maximum of transition for absorption as the excitation wavelength. The optical properties were analyzed either in chloroform solutions (0.01 mg mL^{-1}) using quartz cuvettes with an internal diameter of 10 mm or in thin films spin coated on glass slides from chloroform solutions (5 mg mL^{-1}) at 1500 rpm. For thermogravimetric analysis (TGA) a Netzsch STA 449 F3 Jupiter was used at a scanning rate of 10 K min^{-1} under a nitrogen atmosphere. The temperature of decomposition, $T_{5\%}$, was determined at 5% mass loss. Flash DSC measurements were conducted on a Mettler-Toledo Flash DSC 1 at scanning rates between 50 and 1000 K min^{-1} under nitrogen. The organic thin film transistor substrates with a bottom gate, bottom contact architecture were purchased from Fraunhofer IPMS (OFET Gen. 4). As the substrate and gate electrode a heavily n-doped silicon wafer (doping at the wafer surface: $n \sim 3 \times 10^{17}\text{ cm}^{-3}$) was used. The gate electrode is separated

from the source and drain electrodes by thermal silicon dioxide (Standard 90/230 nm) as a dielectric. Source and drain electrodes are made from gold with a thickness of 30 nm adhered to the dielectric by a layer of 10 nm ITO. One chip carries four groups with four identical transistors with a channel length of 2.5, 5, 10 and 20 mm, respectively, and a channel width of 10 mm. The substrates were rinsed with acetone and purified by ultrasonification in acetone and 2-propanol for 10 min each. After plasma treatment for 15 min at 50 °C, silanisation with octadecyltrichlorosilane in toluene (1 vol%) at 60 °C for 1 h was conducted. The devices were rinsed with toluene and stored in 2-propanol until spin coating. Films were spin coated from chloroform solutions (10 mg mL⁻¹) at 5000 rpm under ambient conditions and directly transferred into the glove box. Current-voltage characteristics were measured under a nitrogen atmosphere using an Agilent B1500 Semiconductor Parameter Analyzer. Annealing was performed at 250 °C for 15 min under a nitrogen atmosphere. The charge carrier mobility was calculated using eqn (1), where I_{DS} is the drain–source current, V_G the gate voltage, L the channel length, W the channel width and C_i the capacitance. Therefore, the square root of the drain-source current $I_{DS}^{1/2}$ was plotted against the gate voltage V_g in the saturation regime and the slope of the resulting curve was determined to calculate the mobility.

$$\mu_{sat} = \left(\frac{\partial \sqrt{I_{DS}}}{\partial V_G} \right)^2 \cdot \frac{2L}{WC_i} \quad (1)$$

6.2.2 Synthesis procedures

General procedure for the Stille polycondensation.

A microwave vial was loaded with the monomers 1,3-dibromo-5-(2-octyldecyl)-4*H*-thieno[3,4-*c*]pyrrol-4,6(5*H*)-dione **1** (1 eq.) and the different TPTs **2** (1 eq.), and tri(*o*-tolyl)phosphine (0.12 eq.) and chlorobenzene were added. After degassing by argon bubbling for 10 min, tris(dibenzylideneacetone)dipalladium(0) (0.03 eq.) was added. The microwave vial was sealed and purged with argon once more. The polymerization reaction was conducted at 180 °C for 1 h under microwave irradiation. After cooling to room temperature, 2-tributyltinthiophene was added to end-cap the polymers and the reaction mixture was stirred for 5 min at 180 °C. The end-capping step was, subsequently, repeated with 2-bromothiophene for 10 min. The polymer solution was precipitated in methanol (300 mL) and filtered. Further purification was carried out by sequential Soxhlet extraction using methanol, acetone and hexane. Finally, the polymer was

collected by chloroform extraction and the solution was concentrated under reduced pressure. Precipitation in methanol, filtration and drying in a vacuum yielded the desired polymer.

P(TPD-TPT). Following the general procedure, a solution of 1,3-dibromo-5-(2-octyldodecyl)-4*H*-thieno[3,4-*c*]pyrrol-4,6(5*H*)-dione **1** (183 mg, 0.309 mmol, 1 eq.), 1,4-bis(5-(trimethylstannyl)-thiophen-2-yl)benzene (176 mg, 0.309 mmol, 1 eq.) **2a**, tri(*o*-tolyl)phosphine (11.3 mg, 0.037 mmol, 0.12 eq.) and tris(dibenzylideneacetone)dipalladium(0) (8.50 mg, 9.27 μ mol, 0.03 eq.) in 4 mL chlorobenzene was stirred for 1 h at 180 °C yielding P(TPD-TPT) (120 mg, 55%) as a black solid. ^1H NMR (300 MHz, CDCl_3): δ = 5.06-8.28 (8H), 2.90-3.88 (2H), 0.31-2.16 (39H) ppm.

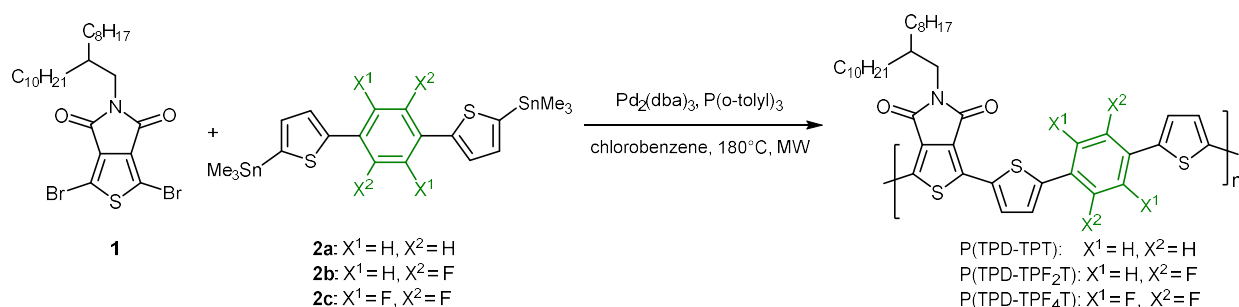
P(TPD-TPF₂T). Following the general procedure, a solution of 1,3-dibromo-5-(2-octyldodecyl)-4*H*-thieno[3,4-*c*]pyrrol-4,6(5*H*)-dione **1** (183 mg, 0.309 mmol, 1 eq.), (5,5'-(2,5-difluoro-1,4-phenylene)bis(thiophene-5,2-diyl))bis(trimethylstannane) **2b** (187 mg, 0.309 mmol, 1 eq.), tri(*o*-tolyl)phosphine (11.3 mg, 0.037 mmol, 0.12 eq.) and tris(dibenzylideneacetone)dipalladium(0) (8.50 mg, 9.27 μ mol, 0.03 eq.) in 4 mL chlorobenzene was stirred for 1 h at 180 °C yielding P(TPD-TPF₂T) (100 mg, 44%) as a black solid. ^1H NMR (300 MHz, CDCl_3): δ = 5.06-8.63 (6H), 2.90-3.94 (2H), 0.50-2.37 (39H) ppm. ^{19}F NMR (300 MHz, CDCl_3): δ = - (114-120) ppm.

P(TPD-TPF₄T). Following the general procedure, a solution of 1,3-dibromo-5-(2-octyldodecyl)-4*H*-thieno[3,4-*c*]pyrrol-4,6(5*H*)-dione **1** (139 mg, 0.234 mmol, 1 eq.), (5,5'-(perfluoro-1,4-phenylene)bis(thiophene-5,2-diyl))bis(trimethylstannane) **2c** (150 mg, 0.234 mmol, 1 eq.), tri(*o*-tolyl)phosphine (8.57 mg, 0.028 mmol, 0.12 eq.) and tris(dibenzylideneacetone)dipalladium(0) (6.45 mg, 7.03 μ mol, 0.03 eq.) in 3 mL chlorobenzene was stirred for 1 h at 180 °C yielding P(TPD-TPF₄T) (145 mg, 80%) as a black solid. ^1H NMR (300 MHz, CDCl_3): δ = 5.10-8.29 (4H), 2.93-3.96 (2H), 0.53-2.44 (39H) ppm. ^{19}F NMR (300 MHz, CDCl_3): δ = - (135-142) ppm.

6.3 Results and discussion

6.3.1 Synthesis

The dibromo TPD monomer carrying octyldodecyl solubilizing side chains was synthesized following the procedures described in the literature.^[31] These long, asymmetric branched side chains were chosen to maintain the solubility of the polymer due to the less soluble TPT comonomer. Detailed synthesis procedures of all monomers can be found in the ESI.† The syntheses of the stannylated TPT comonomers have already been reported by our group.^[25] The dibrominated phenyl derivatives are coupled with thiophene in a Stille reaction followed by bromination and stannylation. For the stannylated TPF₄T monomer with a tetrafluorinated phenyl unit, we chose an alternative synthetic procedure. The tetrafluorinated phenyl group was flanked with thiophene by direct heteroarylation starting from the corresponding brominated compound as reported in the literature.^[32] With palladium acetate as a catalyst and potassium pivalate as base in dimethylacetamide, precursor TPF₄T was synthesized in 47% yield. Direct arylation is a powerful tool to combine aromatic units without the need for additional functionalization of one of the coupling compounds with, for example, boronic acid ester or tin compounds. This compound was directly stannylated using *n*-butyl lithium and trimethyltin chloride without prior bromination achieving the stannylated monomer in high purity following a literature described procedure.^[33] Stille polycondensation was applied to polymerize the TPD monomer with the three different TPT monomers carrying different numbers of fluorine atoms (Scheme 6.1).



Scheme 6.1. Synthesis of TPD containing polymers via Stille polymerization in a microwave reactor.

The polymerization was conducted with tris(dibenzylideneacetone)dipalladium(0) as a catalyst and tri(*o*-tolylphosphine) as a ligand in chlorobenzene for one hour at 180 °C under microwave irradiation. After polymerization, the polymer chains were end-capped using thiophene and were purified by Soxhlet extraction. All the three polymers are well soluble in common organic

solvents such as chloroform and toluene. Size exclusion chromatography was conducted in trichlorobenzene at 160 °C due to the strong aggregation of polymer chains at room temperature, especially with increasing degree of fluorination (Figure 6.1). The molecular weights (PS calibration) as well as the dispersities are summarized in Table 6.1. In general, the relative molecular weights obtained for semicrystalline polymers with PS calibration need to be cautiously interpreted in terms of the real molecular weights. However, a comparison among the three polymers provides some indications. With the degree of fluorination, the number-average molecular weights (M_n) increase from 7.90 kg mol⁻¹ for P(TPD-TPT) to 11.0 kg mol⁻¹ for P(TPD-TPF₂T) and to 13.6 kg mol⁻¹ for P(TPD-TPF₄T). These relative molecular weights (from SEC) do not constitute very high molecular weights. However, for a comparison of the influence of structural changes on crystallinity, orientation and charge transport, these are sufficient, since we have eliminated the influence of end-groups by end-capping. The dispersities for all three polymers are in the range of 1.1–1.3. Even after taking into account the fact that the polymers were purified by Soxhlet extraction, these dispersities are very low for polycondensates. Additionally, the polymers were analyzed by ¹H- and ¹⁹F-NMR and the spectra are depicted in the ESI.† In the ¹⁹F-NMR spectra, the peaks arising from the fluorine can be assigned.

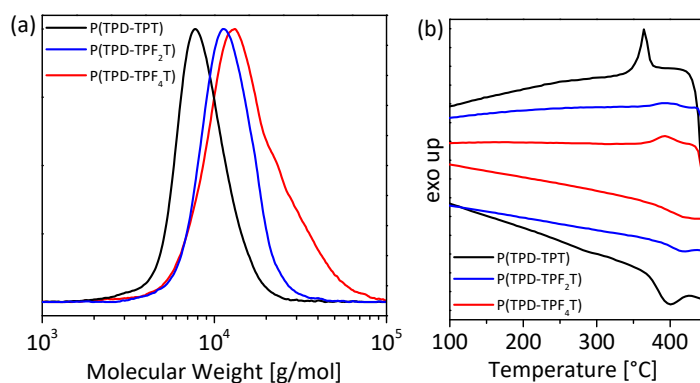


Figure 6.1. (a) SEC measurements in trichlorobenzene at 160 °C calibrated with PS standards. (b) Flash DSC traces with a scanning rate of 1000 K min⁻¹.

All the three polymers show high thermal stability as shown in TGA measurements. The decomposition temperatures at 5% mass loss are in the range of 435 to 442 °C (Table 6.1). The crystallization behavior was investigated with Flash DSC measurements, where the melting and crystallization near the decomposition can be studied due to high scanning rates in the range from 50 to 1000 K min⁻¹. In Figure 6.1b, the region of interest is shown for a scanning rate of 1000 K min⁻¹ and the corresponding melting and crystallization temperatures are summarized in Table 6.1. The complete spectra with all scanning rates are shown in the ESI† (see Figure S 6.2).

The polymer P(TPD-TPT) shows a clear melting as well as a crystallization peak at 400 °C and 364 °C, respectively. For the fluorinated polymers, melting and crystallization are not so pronounced as is the case for the non-fluorinated sample. Due to the fluorination, the adhesion of the polymers to the sample chip in Flash DCS is reduced making the exact thermal measurement difficult. The melting and crystallization temperatures for the di- and tetra-fluorinated polymers are very similar and in the range of 420 °C and 390 °C, respectively. By fluorination, the melting as well as the crystallization temperature is shifted to higher values due to the stronger intermolecular interactions in fluorinated polymers. However, the degree of fluorination does not influence the melting and crystallization temperatures.

Table 6.1. SEC, absorption, electrochemical and thermal properties of the TPD containing polymers.

	M_n^a	M_w^a	\bar{D}	$T_{5\%}^b$	T_m^c	T_c^c	Absorbance peaks [nm] ^d		E_{opt}^e	IP ^f	EA ^f
	[kg/mol]	[kg/mol]		[°C]	[°C]	[°C]	Solution	Film	[eV]	[eV]	[eV]
P(TPD-TPT)	7.85	8.87	1.13	441	400	364	452	475	1.97	-5.46	-3.56
P(TPD-TPF ₂ T)	12.5	12.5	1.14	435	417	394	435	460	1.92	-5.75	-3.64
P(TPD-TPF ₄ T)	13.6	17.6	1.28	442	420	393	427	453	1.95	-6.03	-3.90

^a Determined by SEC in 1,2,4-trichlorobenzene at 160 °C using PS calibration; ^b decomposition at 5% mass loss determined by TGA at 10 K min⁻¹ under N₂. ^c Melt and crystallization temperature from Flash DSC measurements at 1000 K min⁻¹ under N₂. ^d Maximum absorption peaks from a CHCl₃ solution and in thin films. ^e Optical gap determined by the absorption edge in thin films. ^f Ionization potential (IP) and electron affinity (EA) determined from cyclic voltammetry in thin films.

6.3.2 Optical properties

In order to study the influence of fluorination on the optical properties, UV/Vis as well as fluorescence measurements were performed in solution and in the solid state. The spectra are shown in Figure 6.2 and the absorption peaks in solution and thin films as well as the optical gap obtained from the absorption edge of thin film spectra are summarized in Table 6.1. In solution, all the three polymers feature a single broad absorption band, which is slightly blue shifted upon fluorination due to the electron withdrawing properties of the fluorine atoms. Besides this broad absorption band centered at around 420–450 nm, a shoulder at around 550 nm is visible, which arises from an aggregated character of chains in solution. In the solid state, the absorption is red-shifted as compared to their solution spectra due to aggregation; the corresponding spectra can be found in the ESI† (see Figure 6.3). Additionally, the shoulder of aggregated species becomes more prominent. The optical gap was calculated from the absorption edge in thin films resulting in similar values of just below 2 eV for all polymers. In conclusion, fluorination has almost no effect on the optical gap. Excitation at the absorption maximum results in three emission peaks in solution. The intensity of the photoluminescence decreases possibly caused

by the stronger aggregation of the fluorine containing polymers in solution. Moreover, the relative intensities of the vibronic peaks change drastically upon fluorination, which gives a measure for the quality and nature of aggregates.^[34] In comparison, the photoluminescence in thin films shift to red and show only the two main emission peaks, whereas the third one becomes weak.

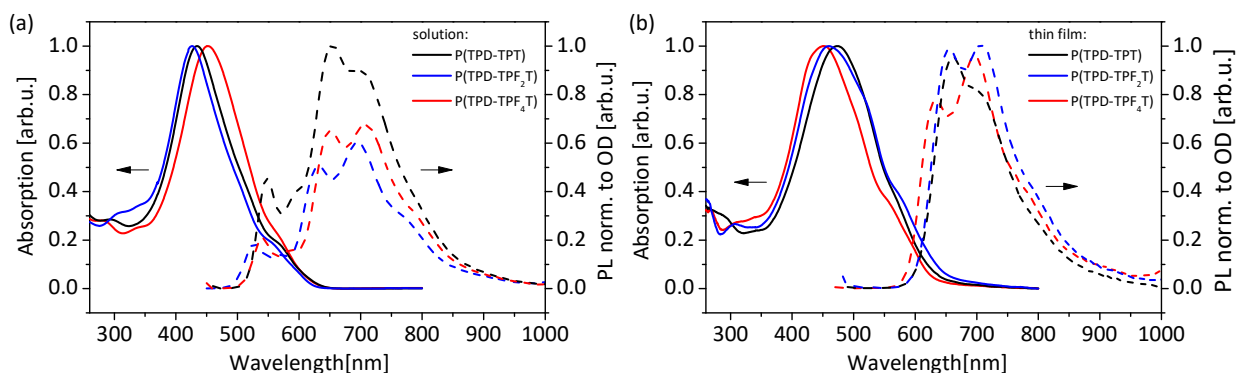


Figure 6.2. Comparison of absorption and fluorescence measurements of the three TPD containing polymers in (a) CHCl_3 solution and (b) thin films.

6.3.3 Electrochemical properties

As fluorination is known to have a significant effect on the energy levels of conjugated polymers, the electrochemical properties of thin films of the polymers were analyzed by cyclic voltammetry measurements. A three-electrode setup with ITO as a working electrode in acetonitrile was used. The cyclic voltammograms are shown in Figure 6.3a. A reversible oxidation peak is observed for all the three polymers. Upon fluorination, the oxidation waves are shifted to higher voltages and therefore, the polymers become less oxidizable due to the decreased electron density along the polymer backbone. Additionally, the reduction potential is affected by fluorination and is shifted to lower voltages. In comparison to the oxidation, the reduction seems to be irreversible under our conditions of measurements. The ionization potentials and electron affinities were calculated from the onset of the reduction and oxidation waves, respectively. These values are only an approximate estimate of the energy levels of thin films in polar solvents and should not be considered as absolute values. In Table 6.1 the results are summarized and the energy levels are graphically illustrated in Figure 6.3b. Difluorination results in the lowering of the IP by 0.3 eV, whereas the EA is almost not affected. By tetrafluorination the IP and EA are further lowered by 0.3 eV, respectively. The lowering of energy levels upon fluorination agrees with similar studies reported in the literature for other low band-gap polymers.^[24,35,36] The band-gap determined by cyclic voltammetry is increased by fluorination and remains constant for di- and tetra-fluorinated

polymers while both energy levels are lowered. Cyclic voltammetry measurements clearly show that the fluorination has a strong impact on the energy levels, which are gradually lowered upon fluorination.

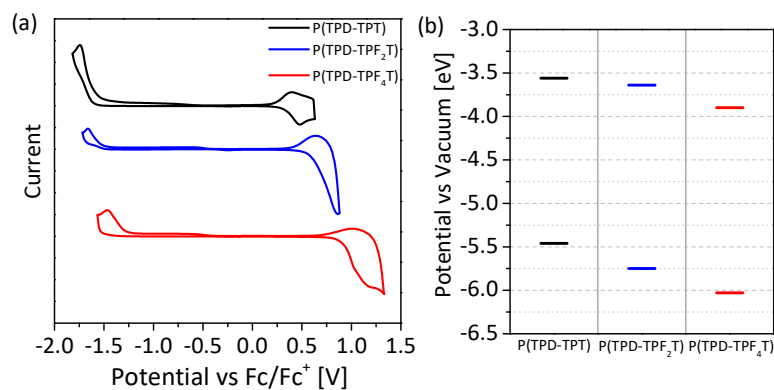


Figure 6.3. (a) Cyclic voltammetry measurements in thin films and (b) energy levels calculated from the onset of oxidation and reduction potential.

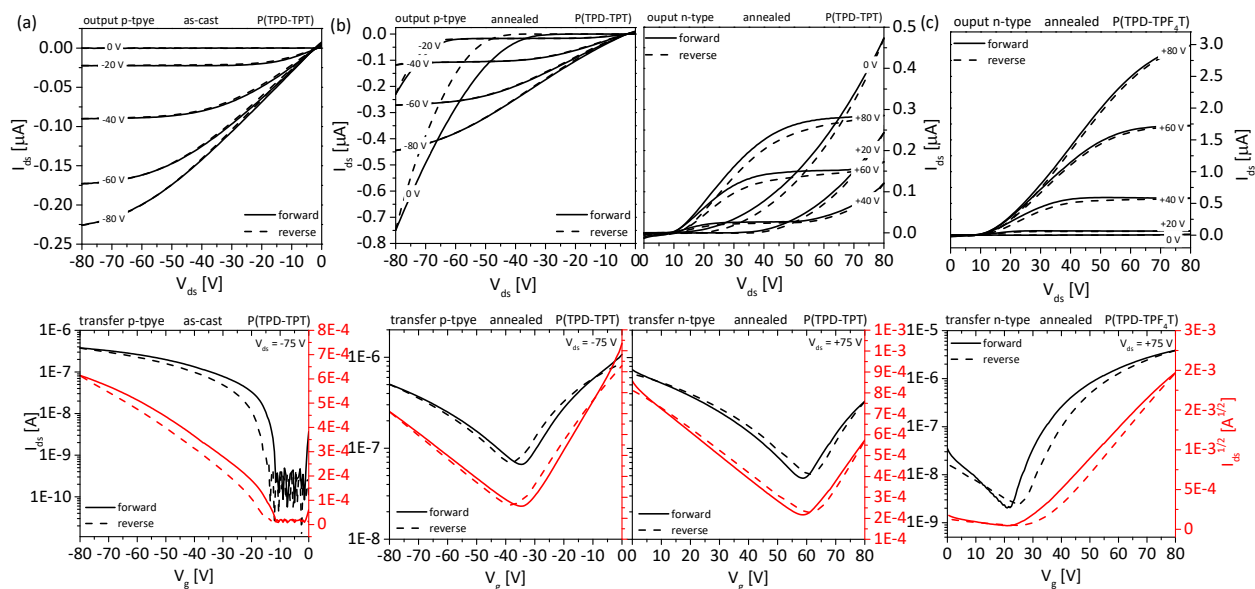
6.3.4 OFETs

The charge carrier mobilities of the polymers were measured using OFETs with a bottom gate, bottom contact architecture. Here, the charge transport occurs in the plane of the thin film at the dielectric interface. Procedures for the device preparation as well as the mobility determination can be found in the Experimental part. Measurements were performed on both as-cast films and films annealed at 250 °C for 15 min under nitrogen. In Table 6.2, the average values for hole and electron mobilities of a minimum of six devices are summarized. The output and transfer characteristics of the as-cast and annealed P(TPD-TPT) films are depicted in Figure 6.4. In the case of the as-cast film, exclusively p-channel behavior (Figure 6.4a) is observed, whereas the material shows ambipolar character after annealing (Figure 6.4b). The hole mobility reaches a value of $0.4 \times 10^{-4} \text{ cm}^2 \text{ V}^{-1} \text{ s}^{-1}$ and the electron mobility $1.1 \times 10^{-4} \text{ cm}^2 \text{ V}^{-1} \text{ s}^{-1}$. Herein, the hole mobility is improved by one order of magnitude after annealing. Interestingly, the polarity of the charge carriers is ambipolar even without fluorination. The same observation was made for the difluorinated polymer P(TPD-TPF₂T) but having slightly higher hole and electron mobilities. The corresponding characteristics can be found in the ESI.[†] No clear transistor behavior was observed for the tetrafluorinated polymer in the as-cast state. After annealing, exclusively n-channel behavior (Figure 6.4c) was observed with an electron mobility of $3.7 \times 10^{-4} \text{ cm}^2 \text{ V}^{-1} \text{ s}^{-1}$, which is in the same range as the difluorinated polymer. The observed high threshold voltage (see Table S 6.1 in the ESI[†]) can be ascribed to electron trapping at the dielectric/polymer interface.

Table 6.2. OFET hole and electron mobilities for as-cast films and after thermal annealing at 250 °C for 15 min under nitrogen.

	As-cast	Annealed	
	μ_h^a [$\text{cm}^2 \text{V}^{-1} \text{s}^{-1}$]	μ_h^a [$\text{cm}^2 \text{V}^{-1} \text{s}^{-1}$]	μ_e^a [$\text{cm}^2 \text{V}^{-1} \text{s}^{-1}$]
P(TPD-TPT)	$(2.5 \pm 0.8) \times 10^{-5}$	$(0.4 \pm 0.8) \times 10^{-4}$	$(1.1 \pm 0.1) \times 10^{-4}$
P(TPD-TPF ₂ T)	$(5.0 \pm 1.9) \times 10^{-5}$	$(1.1 \pm 0.5) \times 10^{-4}$	$(3.4 \pm 1.5) \times 10^{-4}$
P(TPD-TPF ₄ T)	-	-	$(3.7 \pm 1.6) \times 10^{-4}$

^a Hole (μ_h) and electron (μ_e) mobilities calculated from the saturation regime. All values are averaged for a minimum of six devices.


Figure 6.4. Representative OFET output (top) and transfer (bottom) characteristics. Solid lines represent forward scans and dashed line reversed scans. (a) p-channel operation of P(TPD-TPT) as-cast and (b) p- and n-channel operation of P(TPD-TPT) after annealing at 250 °C. (c) n-channel operation of P(TPD-TPF₄T) after annealing at 250 °C.

These measurements give a good insight into the nature of charge carrier polarity but can be of course shifted to higher values by extensive device optimisation, which is not the main question of this work. After annealing, the non-fluorinated as well as the difluorinated polymer shows ambipolar character, whereas by fluorination the hole as well as the electron mobility are increased. In contrast, tetrafluorination generates exclusively n-type behavior with comparable electron mobilities as for the difluorinated polymers.

6.3.5 Structural analysis - GIWAXS

In order to understand the influence of structural order and alignment in this series of copolymers, grazing incidence wide-angle X-ray scattering (GIWAXS) was performed at the SAXS/WAXS beamline at the Australian Synchrotron.^[37] 11 keV electrons were used with scattering patterns recorded on a Dectris Pilatus 1M detector, following the procedures detailed elsewhere.^[38] Figure 6.5 presents the two-dimensional scattering patterns of the as-cast and annealed films. The images presented in Figure 6.5 were taken close to the critical angle ($\sim 0.12^\circ$)

which was identified as the angle of incidence that gave the maximum scattering intensity. One-dimensional in-plane and out-of-plane scattering profiles are also provided in Figure 6.6. All polymers exhibit multiple orders of alkyl stacking, indexed as (k00), even in the as-cast films indicating a high propensity of these polymers to crystallise. The alkyl stacking scattering intensity is mainly observed along Q_z for the polymers indicating a predominantly “edge-on” stacking of crystallites. Prominent π -stacking peaks, indexed as (010), are observed in-plane consistent with this molecular orientation. Alkyl stacking scattering intensity is also observed from crystallites at other azimuthal angles indicating the presence of crystallites with orientation other than edge-on. A backbone stacking peak, indexed as (001), is also seen at a Q value of $\sim 3.2 \text{ nm}^{-1}$. Curiously this backbone stacking peak is observed out-of-plane (along Q_z , just below the second order alkyl stacking peak) as well as along Q_{xy} . Generally, for conjugated polymers the backbone is thought to lie flat in the plane of the film which is likely to be the case for thin films where the film thickness is smaller than the contour length of the polymer. Here, however, a significant (001) peak intensity is observed out-of-plane indicating the “end-on” orientation of some polymer chains. This unusual observation is thought to be due to the relatively low molecular weight of these polymers and the relatively large film thickness of these films (around 120 nm) relative to the contour length. The series of alkyl stacking peaks along Q_z and the presence of a backbone stacking peak along Q_z indicates separate populations of polymer chains with distinct orientation. The lamellar stacking peak associated with end-on oriented chains is expected to be found along Q_{xy} suggesting that the in-plane (100) peak is associated with end-on oriented chains rather than face-on oriented crystallites. Such an assignment is consistent with the fact that only a very weak π -stacking peak is observed out-of-plane. For both edge-on and end-on oriented chains the π -stacking peak is expected to be found along Q_{xy} . Despite having different degrees of fluorination, the polymers all possess similar crystallographic parameters (see Figure S 6.8 in the ESI†). A π - π stacking distance of $0.38 \pm 0.01 \text{ nm}$ is observed for all polymers with there being more variation with annealing than from polymer to polymer (the effect of annealing of the π - π stacking however is not systematic). Fluorination does seem to lead to a tighter alkyl stacking distance, decreasing from 3.4 nm to 3.3 nm going from P(TPD-TPT) to P(TPD-TPF₄T), although a slight increase is observed for P(TPD-TPF₂T) ($\sim 3.45 \text{ nm}$). Judging by the increase in scattering intensity of the alkyl stacking peaks, there appears to be an increase in the degree of crystallinity with fluorination, particularly in the as-cast films. This would suggest that while fluorination has not affected the molecular packing of the polymers, it

has increased the propensity of chains to crystallise during solution deposition. Relating the microstructural data to the OFET data, the similar charge carrier mobilities achieved for the different polymers can be seen as being consistent with the similar microstructural properties. The fact that hole conduction was not observed in the case of P(TPD-TPF₄T) is then likely due to difficulties in injecting holes into the deep HOMO of this polymer.

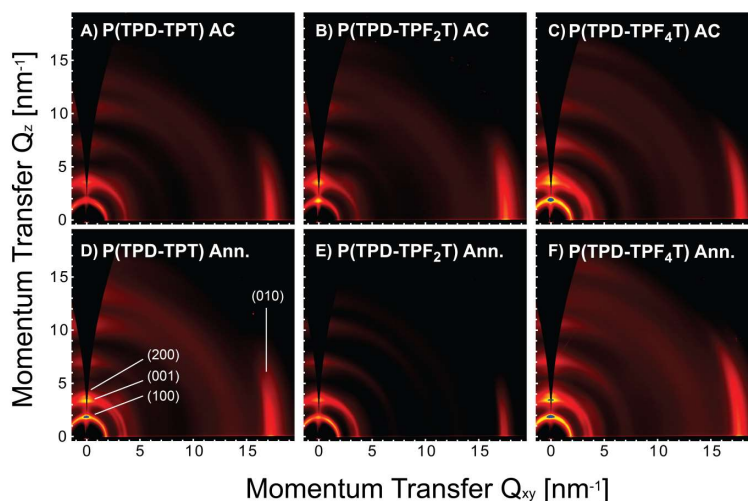


Figure 6.5. Two-dimensional GIWAXS patterns of P(TPD-TPT) (a and d), P(TPD-TPF₂T) (b and e) and P(TPD-TPF₄T) (c and f). (a–c) show as-cast films while (d–f) show films annealed at 250 °C.

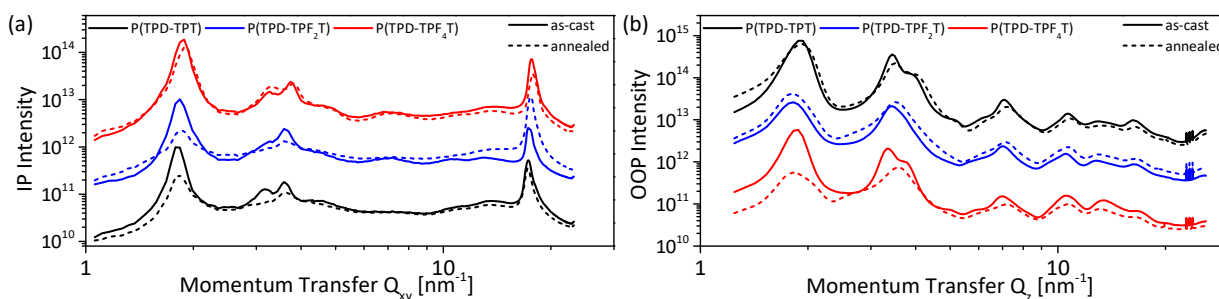


Figure 6.6. One-dimensional GIWAXS scattering profiles of P(TPD-TPT), P(TPD-TPF₂T) and P(TPD-TPF₄T) taken along the in-plane (a) and out-of-plane (b) directions.

6.4 Conclusion

We have demonstrated that fluorination is a powerful tool to generate exclusively n-type behavior in thieno[3,4-c]pyrrole-4,6-dione based polymers. For this, thieno[3,4-c]pyrrole-4,6-dione was successfully copolymerized with thiophene-phenyl-thiophene moieties with different degrees of fluorination. Whereas the optical properties are almost not affected by fluorination, the energy levels, both IP and EA, are lowered. In GIWAXS measurements the thin film alignment of these polymers surprisingly shows end-on alignment, which is rarely observed in conjugated polymers without any reactive grafting of the chains to the substrate. This may be explained by

the relatively low molecular weights and therefore, small contour length of these polymers in comparison to the film thickness.

6.5 Acknowledgements

We acknowledge finance support from Bavarian State Ministry for Education, Science and the Arts under the SolTech project. T. W. acknowledges the Elite Network Bavaria Macromolecular Science programme at the University of Bayreuth. This research was undertaken in part at the SAXS/WAXS beamline at the Australian Synchrotron, Victoria, Australia. C.R.M. acknowledges support from the Australian Research Council (DP130102616).

6.6 References

- [1] L. Gao, Z.-G. Zhang, L. Xue, J. Min, J. Zhang, Z. Wei, Y. Li, *Adv. Mater.* **2016**, *28*, 1884.
- [2] K. Zhou, R. Zhang, J. Liu, M. Li, X. Yu, R. Xing, Y. Han, *ACS Appl. Mater. Interfaces* **2015**, *7*, 25352.
- [3] J. W. Jo, J. W. Jung, H. Ahn, M. J. Ko, A. K.-Y. Jen, H. J. Son, *Adv. Energy Mater.* **2017**, *7*, 1601365.
- [4] J. Warnan, C. Cabanetos, A. El Labban, M. R. Hansen, C. Tassone, M. F. Toney, P. M. Beaujuge, *Adv. Mater.* **2014**, *26*, 4357.
- [5] N. Zhou, X. Guo, R. Ponce Ortiz, T. Harschneck, E. F. Manley, S. J. Lou, P. E. Hartnett, X. Yu, N. E. Horwitz, P. Mayorga Burrezo, T. J. Aldrich, J. T. López Navarrete, M. R. Wasielewski, L. X. Chen, R. P. H. Chang, A. Facchetti, T. J. Marks, *J. Am. Chem. Soc.* **2015**, *137*, 12565.
- [6] A. Tournebize, J.-L. Gardette, C. Taviot-Guého, D. Bégué, M. A. Arnaud, C. Dagron-Lartigau, H. Medlej, R. C. Hiorns, S. Beaupré, M. Leclerc, A. Rivaton, *Polym. Degrad. Stab.* **2015**, *112*, 175.
- [7] Y. Zhang, S. K. Hau, H.-L. Yip, Y. Sun, O. Acton, A. K.-Y. Jen, *Chem. Mater.* **2010**, *22*, 2696.
- [8] Y. Zou, A. Najari, P. Berrouard, S. Beaupré, B. R. Aïch, Y. Tao, M. Leclerc, *J. Am. Chem. Soc.* **2010**, *132*, 5330.
- [9] Z. Li, S.-W. Tsang, X. Du, L. Scoles, G. Robertson, Y. Zhang, F. Toll, Y. Tao, J. Lu, J. Ding, *Adv. Funct. Mater.* **2011**, *21*, 3331.
- [10] M.-C. Yuan, M.-Y. Chiu, S.-P. Liu, C.-M. Chen, K.-H. Wei, *Macromolecules* **2010**, *43*, 6936.
- [11] J.-H. Kim, J. B. Park, I. H. Jung, A. C. Grimsdale, S. C. Yoon, H. Yang, D.-H. Hwang, *Energy Environ. Sci.* **2015**, *8*, 2352.

- [12] Q. Wu, M. Wang, X. Qiao, Y. Xiong, Y. Huang, X. Gao, H. Li, *Macromolecules* **2013**, *46*, 3887.
- [13] Z. A. Wang, J. Kuwabara, A. Ichige, T. Yasuda, T. Kanbara, *Synth. Met.* **2016**, *222*, 383.
- [14] W. Wang, S. Yan, W. Lv, Y. Zhao, M. Sun, M. Zhou, Q. Ling, *Journal of Macromolecular Science, Part A* **2015**, *52*, 892.
- [15] G. Kim, A.-R. Han, H. R. Lee, J. Lee, J. H. Oh, C. Yang, *Chem. Commun.* **2014**, *50*, 2180.
- [16] F. Grenier, P. Berrouard, J.-R. Pouliot, H.-R. Tseng, A. J. Heeger, M. Leclerc, *Polym. Chem.* **2013**, *4*, 1836.
- [17] X. Guo, R. P. Ortiz, Y. Zheng, M.-G. Kim, S. Zhang, Y. Hu, G. Lu, A. Facchetti, T. J. Marks, *J. Am. Chem. Soc.* **2011**, *133*, 13685.
- [18] S. Liu, X. Song, S. Thomas, Z. Kan, F. Cruciani, F. Laquai, J.-L. Bredas, P. M. Beaujuge, *Adv. Energy Mater.* **2017**, *376*, 1602574.
- [19] S. Liu, Z. Kan, S. Thomas, F. Cruciani, J.-L. Brédas, P. M. Beaujuge, *Angew. Chem. Int. Ed.* **2016**, *55*, 12996.
- [20] D. J. Crouch, P. J. Skabara, M. Heeney, I. McCulloch, S. J. Coles, M. B. Hursthouse, *Chem. Commun.* **2005**.
- [21] D. J. Crouch, P. J. Skabara, J. E. Lohr, J. J. W. McDouall, M. Heeney, I. McCulloch, D. Sparrowe, M. Shkunov, S. J. Coles, P. N. Horton, M. B. Hursthouse, *Chem. Mater.* **2005**, *17*, 6567.
- [22] H. G. Kim, B. Kang, H. Ko, J. Lee, J. Shin, K. Cho, *Chem. Mater.* **2015**, *27*, 829.
- [23] N. E. Jackson, B. M. Savoie, K. L. Kohlstedt, M. La Olvera de Cruz, G. C. Schatz, L. X. Chen, M. A. Ratner, *J. Am. Chem. Soc.* **2013**, *135*, 10475.
- [24] J. H. Park, E. H. Jung, J. W. Jung, W. H. Jo, *Adv. Mater.* **2013**, *25*, 2583.
- [25] C. J. Mueller, E. Gann, C. R. McNeill, M. Thelakkat, *J. Mater. Chem. C* **2015**, *3*, 8916.
- [26] C. J. Mueller, C. R. Singh, M. Fried, S. Huettner, M. Thelakkat, *Adv. Funct. Mater.* **2015**, *25*, 2725.
- [27] J. Y. Lee, J. W. Jo, W. H. Jo, *Org. Electron.* **2015**, *20*, 125.
- [28] P. Sonar, J. Chang, Z. Shi, J. Wu, J. Li, *J. Mater. Chem. C* **2015**, *3*, 2080.
- [29] A. Luzio, D. Fazzi, F. Nübling, R. Matsidik, A. Straub, H. Komber, E. Giussani, S. E. Watkins, M. Barbatti, W. Thiel, E. Gann, L. Thomsen, C. R. McNeill, M. Caironi, M. Sommer, *Chem. Mater.* **2014**, *26*, 6233.

- [30] X. Li, X. Liu, P. Sun, Y. Feng, H. Shan, X. Wu, J. Xu, C. Huang, Z.-K. Chen, Z.-X. Xu, *RSC Adv* **2017**, *7*, 17076.
- [31] A. Najari, S. Beaupré, P. Berrouard, Y. Zou, J.-R. Pouliot, C. Lepage-Pérusse, M. Leclerc, *Adv. Funct. Mater.* **2011**, *21*, 718.
- [32] R. Matsidik, J. Martin, S. Schmidt, J. Obermayer, F. Lombeck, F. Nübling, H. Komber, D. Fazzi, M. Sommer, *J. Org. Chem.* **2015**, *80*, 980.
- [33] N. J. Findlay, J. Bruckbauer, A. R. Inigo, B. Breig, S. Arumugam, D. J. Wallis, R. W. Martin, P. J. Skabara, *Adv. Mater.* **2014**, *26*, 7290.
- [34] F. C. Spano, J. Clark, C. Silva, R. H. Friend, *J. Chem. Phys.* **2009**, *130*, 74904.
- [35] K. Kawashima, T. Fukuhara, Y. Suda, Y. Suzuki, T. Koganezawa, H. Yoshida, H. Ohkita, I. Osaka, K. Takimiya, *J. Am. Chem. Soc.* **2016**, *138*, 10265.
- [36] Z. Li, J. Lu, S.-C. Tse, J. Zhou, X. Du, Y. Tao, J. Ding, *J. Mater. Chem.* **2011**, *21*, 3226.
- [37] N. M. Kirby, S. T. Mudie, A. M. Hawley, D. J. Cookson, H. D. T. Mertens, N. Cowieson, V. Samardzic-Boban, *J Appl Crystallogr* **2013**, *46*, 1670.
- [38] T. T. Do, K. Rundel, Q. Gu, E. Gann, S. Manzhos, K. Feron, J. Bell, C. R. McNeill, P. Sonar, *New J. Chem.* **2017**, *41*, 2899.

Supporting Information

Fluorination in thieno[3,4-*c*]pyrrole-4,6-idone copolymers leading to electron transport, high crystallinity and end-on alignment

Tina Weller,^a Marion Breunig,^a Christian J. Müller,^a Elliot Gann^c, Christopher R. McNeill^b and Mukundan Thelakkat^{a*}

^a Applied Functional Polymers, Macromolecular Chemistry I, University of Bayreuth, 95440 Bayreuth, Germany.

^b Department of Materials Science and Engineering, Monash University, Wellington Road, Clayton VIC, 3800, Australia.

^c Materials Measurement Laboratory, National Institute of Standards and Technology, 100 Bureau Dr, Gaithersburg, MD 20899, USA.

* Corresponding author: mukundan.thelakkat@uni-bayreuth.de

Table of Contents

1	Monomer Syntheses.....	163
1.1	Materials and Methods.....	163
1.2	Synthesis of the TPD monomer	163
1.3	Synthesis of the TPF ₄ T monomer.....	166
1.4	Polymer NMR spectra	167
2	Thermal Properties	170
2.1	Thermogravimetric Analysis (TGA)	170
2.2	Flash-Differential Scanning Calorimetry (DSC)	170
3	UV-Vis and fluorescence spectroscopy	171
4	OFET <i>I</i> - <i>V</i> curves	171
5	GIWAXS data.....	173
6	References	174

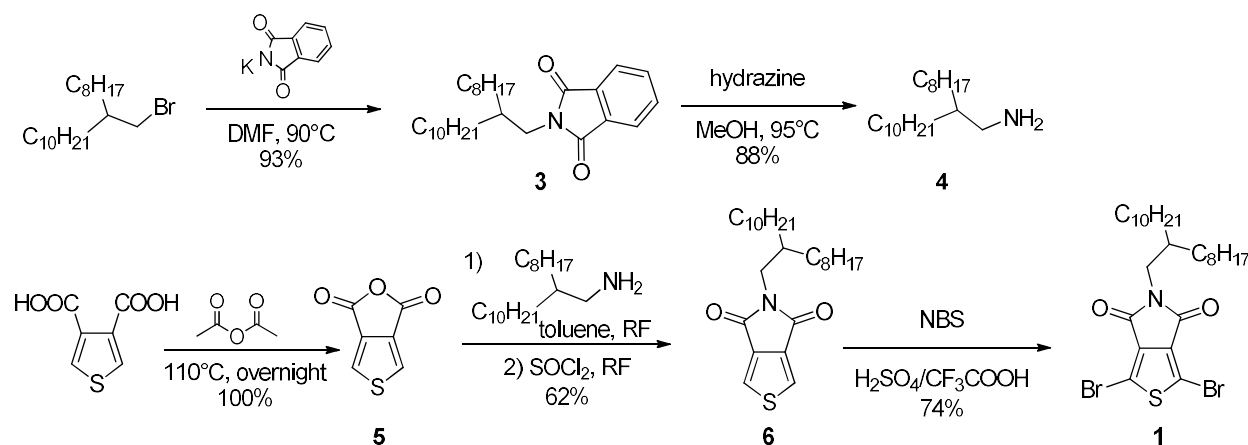
8 Monomer Syntheses

8.1 Materials and Methods

Water and air sensitive reactions were conducted in Schlenk apparatuses under argon, which were previously baked out in high vacuum. Commercially available solvents were purchased from Sigma Aldrich and Acros Organics in sealed bottles with mole sieve. ^1H - and ^{19}F -NMR spectra were recorded on a Bruker Avance spectrometer (300 MHz) with deuterated solvents purchased from Deutero. Chemical shifts are reported in ppm relative to the known value of residual solvent signal. Molecular weights were assessed by the electron ionization mass spectrometry performed on a Finnigan MAT 8500 spectrometer (70 eV) at the Department of Chemistry of University Bayreuth. 9-(Bromomethyl)nonadecane was synthesized as reported in the literature.^[1]

8.2 Synthesis of the TPD monomer

The overall synthesis of the TPD monomer is shown in Scheme S 6.1 and the synthetic procedures are adapted from literature.^[2,3]



Scheme S 6.1. Synthesis of the TPD monomer.

***N*-(2-Octyldodecyl)-phthalimide 3**

To a solution of 9-(bromomethyl)nonadecane (20.0 g, 55.3 mmol, 1 eq) in 60 mL anhydrous dimethylformamide potassium phthalimide (11.3 g, 60.9 mmol, 1.1 eq) was added. After stirring for 18 h at 90 °C, the mixture was cooled to room temperature followed by the addition of 100 mL water. The aqueous phase was extracted with dichloromethane (3 x 50 mL) and the combined organic phases were washed with aqueous solution of KOH (0.2 M) followed by water and saturated aqueous solution of NH₄Cl (each 200 mL). After drying over MgSO₄ and filtration, the solvent was removed under reduced pressure. The crude oil was purified by flash column chromatography (silica; Hex:DCM 1:1) yielding *N*-(2-octyldodecyl)-phthalimide **3** (21.9 g, 51.2 mmol, 93%) as a colorless liquid.

¹H-NMR (300 MHz, CDCl₃): δ = 7.79-7.91 (m, 2H), 7.63-7.78 (m, 2H), 3.56 (d, *J* = 7.3 Hz, 2H), 1.78-1.96 (m, 1H), 1.14-1.39 (m, 32 H), 0.79-0.94 ppm (m, 6H). EI-MS (70 eV): *m/z* 427 (M⁺).

2-Octyl-1-dodecylamine 4

To a solution of *N*-(2-octyldodecyl)-phthalimide **3** (21.9 g, 51.2 mmol, 1 eq) in 200 mL methanol were added hydrazine (4.80 mL, 154 mmol, 3 eq). The reaction mixture was stirred for 5 h at 95 °C until fully conversion was detected by TLC. After cooling to room temperature the solvent was reduced using rotary evaporation. Addition of 250 mL aqueous solution of KOH (10 wt%) was followed by extraction with DCM (3 x 200 mL). The combined organic layers were washed with saturated, aqueous solution of NaCl (300 mL) and dried over MgSO₄. After filtration the solvent was removed under reduced pressure and dried in high vacuum yielding 2-octyl-1-dodecylamine **4** (13.4 g, 45.0 mmol, 88%) as a colorless liquid.

¹H NMR (300 MHz, CDCl₃): δ = 2.64 (d, *J* = 5.5 Hz, 2H), 2.38 (br, 2H), 1.13-1.46 (m, 33 H), 0.78-0.94 ppm (m, 6H). EI-MS (70 eV): *m/z* 297 (M⁺).

Thieno[3,4-*c*]furan-1,3-dione 5

Thiophene-3,4-dicarboxylic acid (25.0 g, 145 mmol) was dissolved in 250 mL acetic anhydride and stirred at 110 °C overnight. After cooling to room temperature the solvent was removed under reduced pressure yielding thieno[3,4-*c*]furan-1,3-dione **5** (22.4 g, 145 mmol, 100%) as a light brown solid.

¹H NMR (300 MHz, CHCl₃): δ = 8.09 ppm (s, 2H). EI-MS (70 eV): *m/z* 155 (M+H)⁺.

5-(2-Octyl-1-dodecyl)-4*H*-thieno[3,4-*c*]pyrrol-4,6(5*H*)-dione 6

A solution of octyl-1-dodecylamine **4** (13.4 g, 45.0 mmol, 1.5 eq) and thieno[3,4-*c*]furan-1,3-dione **3** (4.60 g, 30.0 mmol, 1.0 eq) in 200 mL toluene was stirred for 24 h under reflux. After cooling to room temperature the solvent was removed under reduced pressure followed by the addition of 200 mL thionylchloride. The solution was stirred for 3 h at 75 °C and the thionylchloride was subsequently removed in high vacuum. Purification was carried out with column chromatography (silica; Hex:DCM 2:1) yielding 5-(2-octyl-1-dodecyl)-4*H*-thieno[3,4-*c*]pyrrol-4,6(5*H*)-dione **6** (9.60 g, 22.2 mmol, 74%) as a yellow solid.

¹H NMR (300 MHz, CDCl₃): δ = 7.80 (s, 2H), 3.50 (d, *J* = 7.3 Hz, 2H), 1.75- 1.91 (m, 1H), 1.15-1.43 (m, 32H), 0.80-0.93 ppm (m, 6H). EI-MS (70 eV): *m/z* 591 (M⁺).

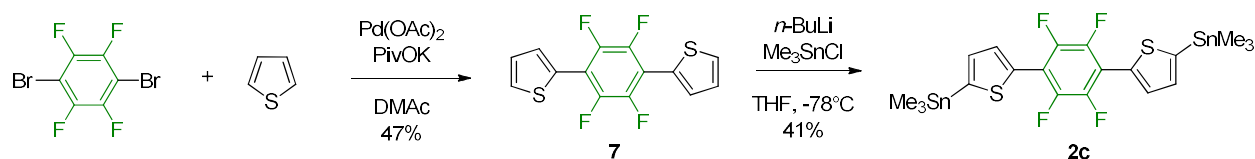
1,3-Dibromo-5-(2-octyl-1-dodecyl)-4*H*-thieno[3,4-*c*]pyrrol-4,6(5*H*)-dione 1

In a mixture of 25 mL sulfuric acid and 75 mL trifluoroacetic acid 5-(2-octyl-1-dodecyl)-4*H*-thieno[3,4-*c*]pyrrol-4,6(5*H*)-dione **6** (6.00 g, 13.8 mmol, 1 eq) was dissolved and cooled to 0 °C. After addition of *N*-bromosuccinimide (7.40 g, 41.5 mmol, 3 eq) in portions the cooling bath was removed and the solution was stirred overnight at room temperature. The solution was added dropwise to ice water resulting in a yellow suspension, which was extracted with DCM (3 x 100 mL). The combined organic layers were dried over MgSO₄, filtered and the solvent was removed under reduced pressure. Purification was carried out with column chromatography (silica; gradient: Hex:DCM 4:1 - 2:1) yielding 1,3-dibromo-5-(2-octyl-1-dodecyl)-4*H*-thieno[3,4-*c*]pyrrol-4,6(5*H*)-dione **1** (5.1 g, 8.59 mmol, 62%) as a light yellow solid.

¹H NMR (300 MHz, CDCl₃): δ = 3.47 (d, *J* = 7.3 Hz, 2H), 1.74-1.87 (m, 1 H), 1.25 (s, 29 H), 0.82-0.93 ppm (m, 5 H). EI-MS (70 eV): *m/z* 647 (M⁺).

8.3 Synthesis of the TPF₄T monomer

Synthetic procedure are adapted from literature.^[4,5]



Scheme 5.6.2. Synthesis of the TPF₄T monomer.

2,2'-(Perfluoro-1,4-phenylene)dithiophene 7

A solution of 1,4-dibromo-2,3,5,6-tetrafluorobenzene (2.00 g, 6.50 mmol, 1.0 eq), thiophene (7.70 mL, 97.0 mmol, 15 eq) and potassium pivalate (2.28 g, 16.2 mmol, 2.5 eq) in 34 mL anhydrous dimethylacetamide was degassed for 10 min followed by addition of palladium(II)acetate (73.0 mg, 0.325 mmol, 0.05 eq). After stirring for 3 days at 80 °C, the solution was cooled to room temperature. The solvent was removed under reduced pressure. Purification was carried out by column chromatography (silica; Hex) yielding 2,2'-(perfluoro-1,4-phenylene)dithiophene 7 (1.0 g, 3.2 mmol, 49%) as a colorless solid.

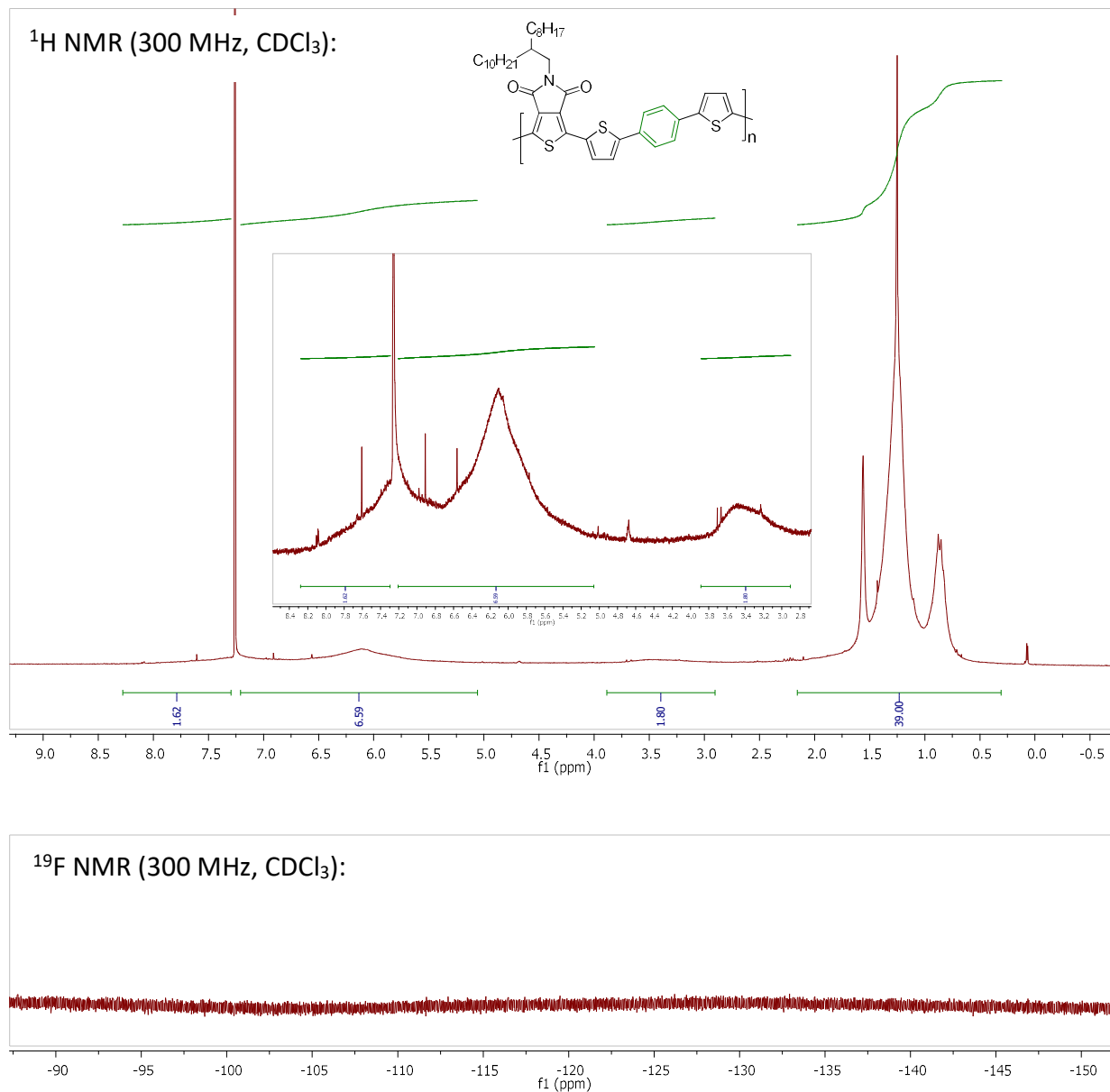
¹H NMR (300 MHz, CDCl₃): δ = 7.68 (d, J = 4.0 Hz, 2H), 7.57 (dd, J = 5.3, 1.1 Hz, 2H), 7.21 ppm (dd, J = 4.7, 4.1 Hz, 2H). EI-MS (70 eV): m/z 314 (M^+).

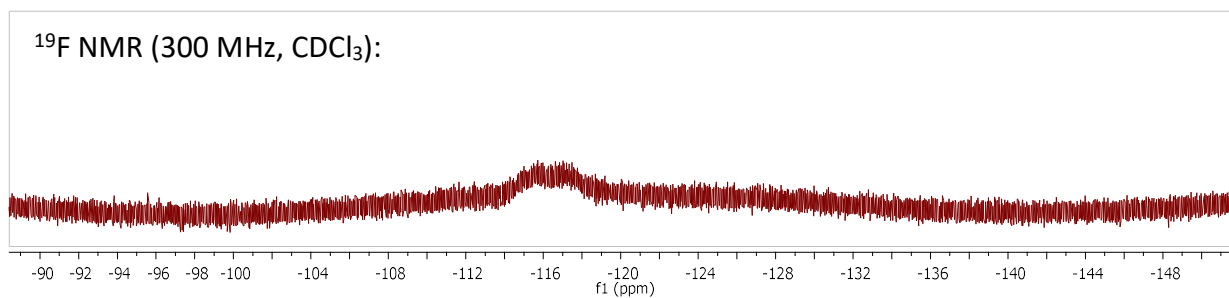
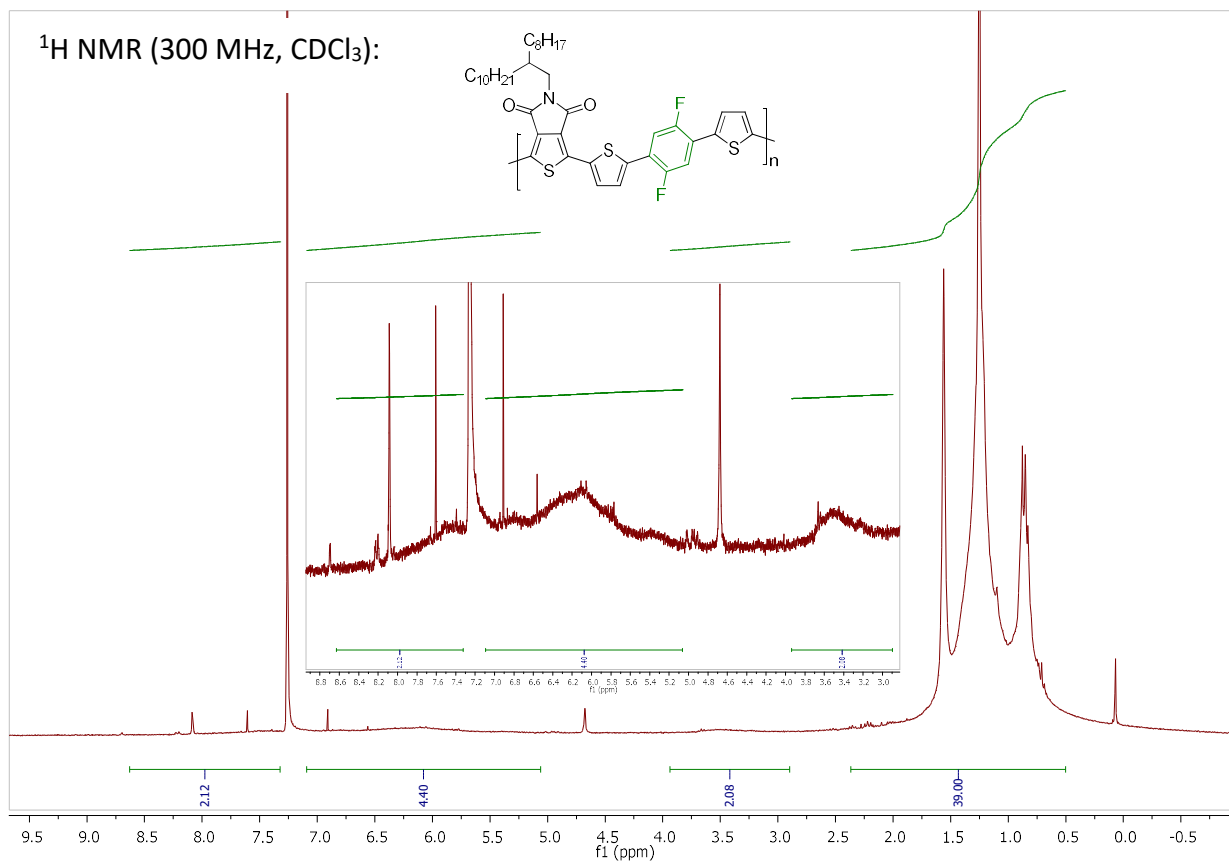
(5,5'-(Perfluoro-1,4-phenylene)bis(thiophene-5,2-diyl))bis(trimethylstannane) 2c

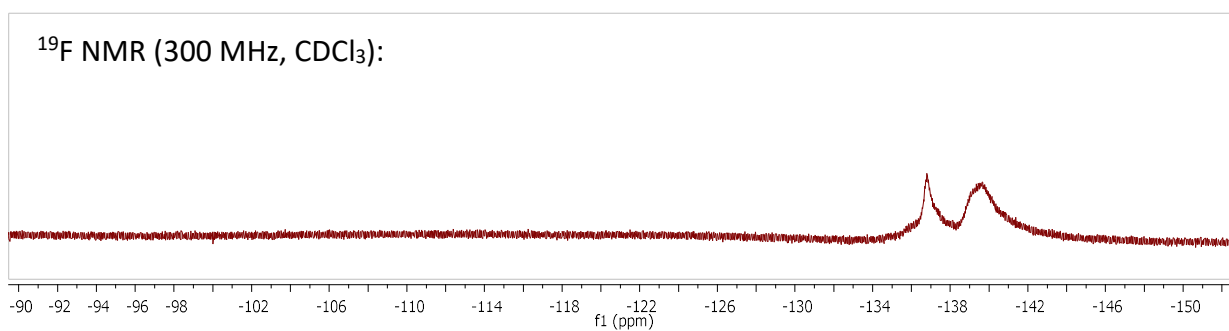
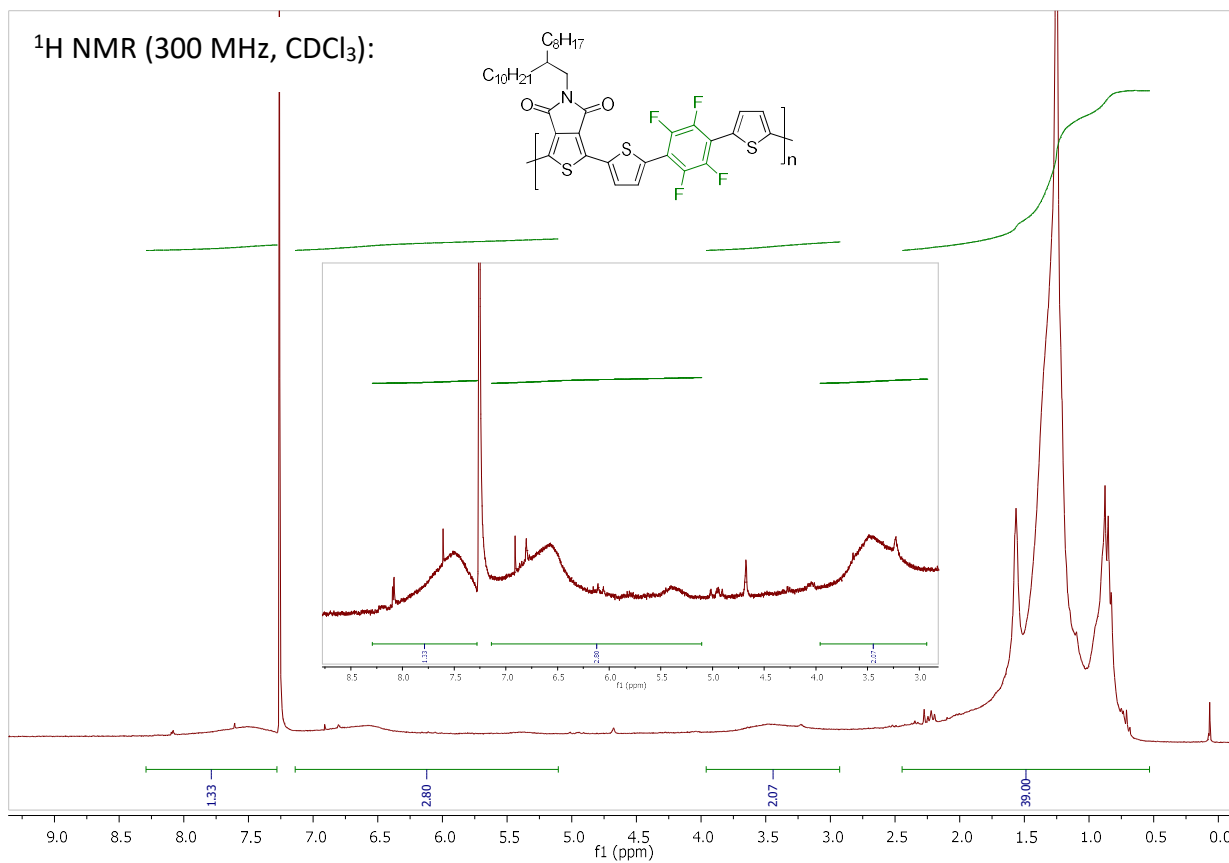
A solution of 2,2'-(perfluoro-1,4-phenylene)dithiophene 7 (0.60 g, 1.9 mmol, 1 eq) in 60 mL anhydrous THF was cooled to -78 °C followed by the addition of a 2.5 M solution of *n*-butyl lithium in hexane (1.6 mL, 4.0 mmol, 2.1 eq). The reaction mixture was stirred for 1 h at -78 °C and trimethyltinchloride (0.80 g, 4.0 mmol, 2.1 eq) was added. After stirring for 1 h at -78 °C, the reaction mixture was allowed to warm to room temperature and stirred overnight. Water (50 mL) was added and the aqueous layer was extracted with DCM (3 x 50 mL). The combined organic layers were washed with water and saturated, aqueous solution of NaCl (each 150 mL). After drying over MgSO₄ and filtration, the solvent was removed under reduced pressure. The crude product was purified by recrystallization from ethanol yielding (5,5'-(perfluoro-1,4-phenylene)bis(thiophene-5,2-diyl))bis(trimethylstannane) 2c (0.50 mg, 0.78 mmol, 41%) as a colorless solid.

^1H NMR (300 MHz, CDCl_3): $\delta = 7.76$ (d, $J = 3.6$ Hz, 2H), 7.28 (d, $J = 3.6$ Hz, 3H), 0.43 ppm (s, 16H).
EI-MS (70 eV): m/z 640 (M^+).

8.4 Polymer NMR spectra







9 Thermal Properties

9.1 Thermogravimetric Analysis (TGA)

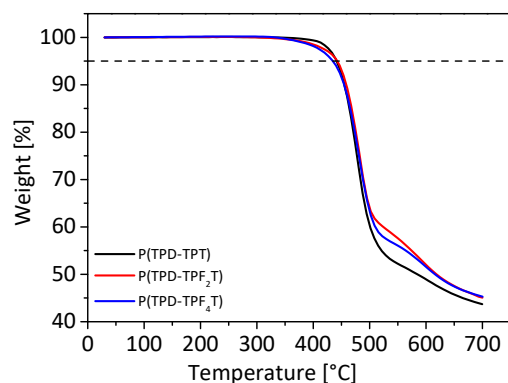


Figure S 6.1. Thermogravimetric analysis of the PTPDs with the decomposition onset (T5%).

9.2 Flash-Differential Scanning Calorimetry (DSC)

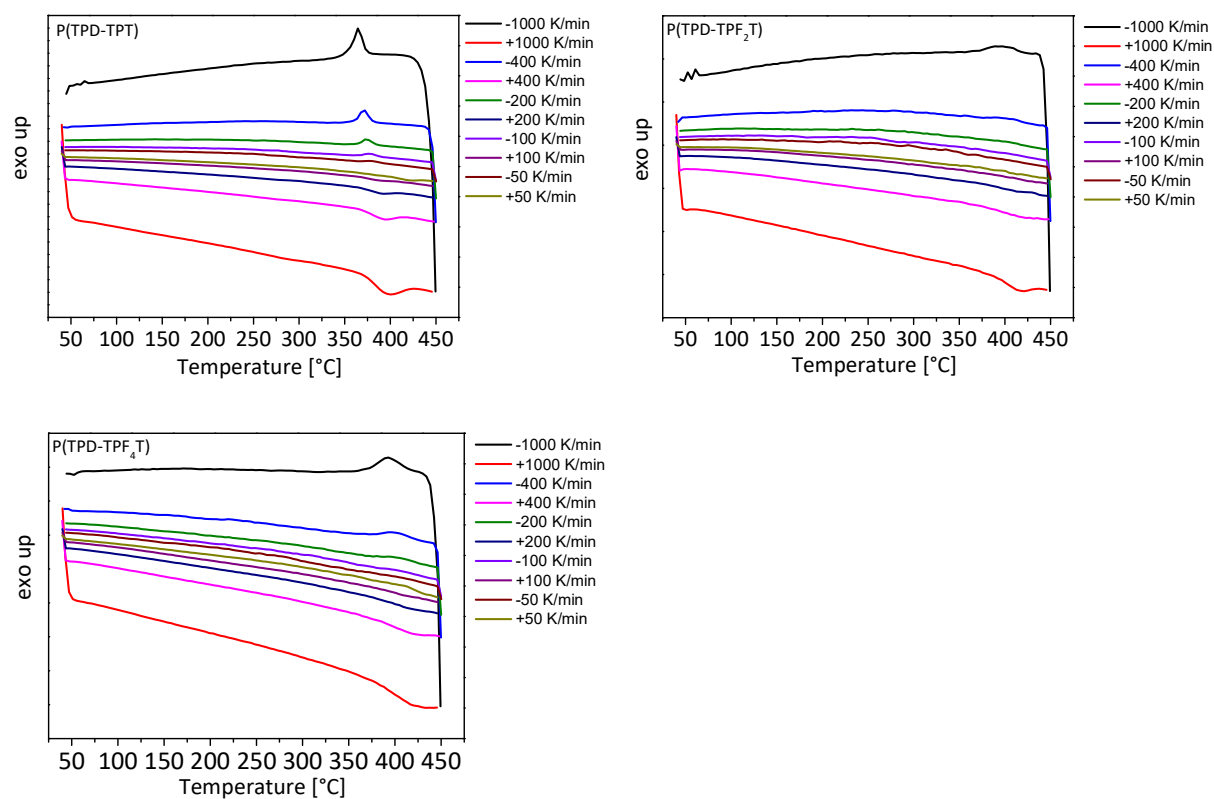


Figure S 6.2. Flash-DSC analysis of the PTPDs with scanning rates from 50-1000 K/min.

10 UV-Vis and fluorescence spectroscopy

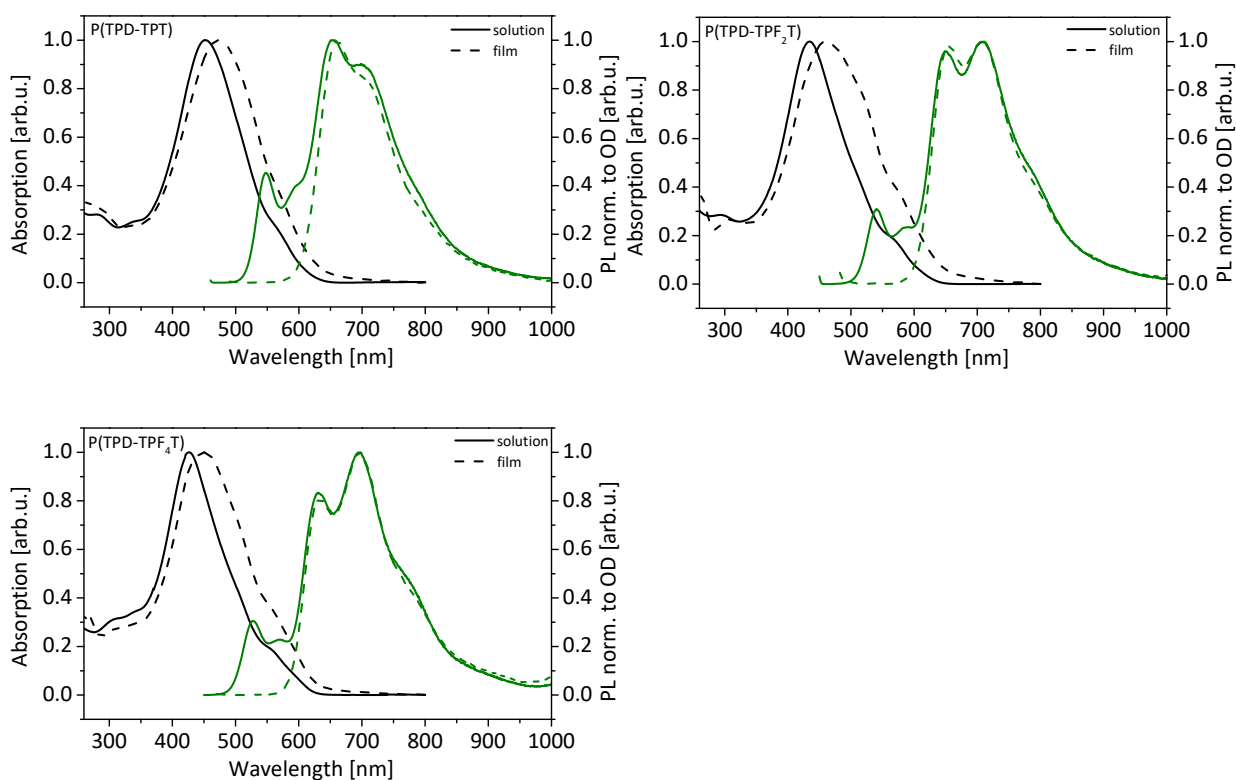


Figure S 6.3. UV-Vis and photoluminescence spectra in solution and thin films for each PTPD.

11 OFET *I*-*V* curves

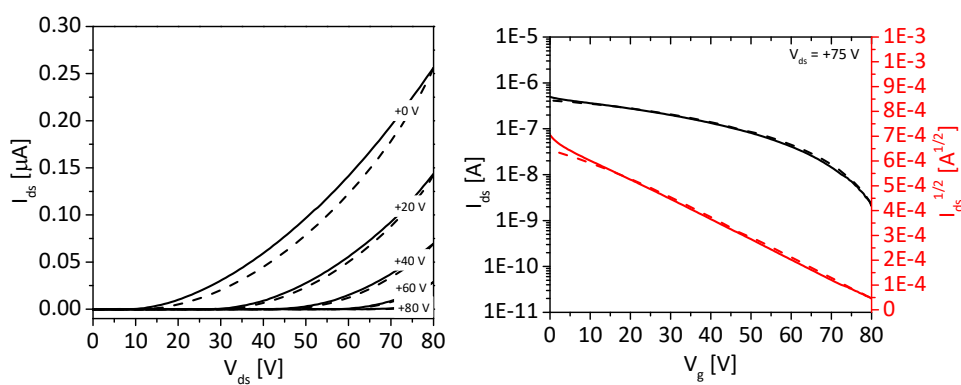


Figure S 6.4. OFET output (left) and transfer (right) characteristics: n-channel operation of P(TPD-TPT) in the as cast state. Solid lines represent forward scans and dashed lines reversed scans.

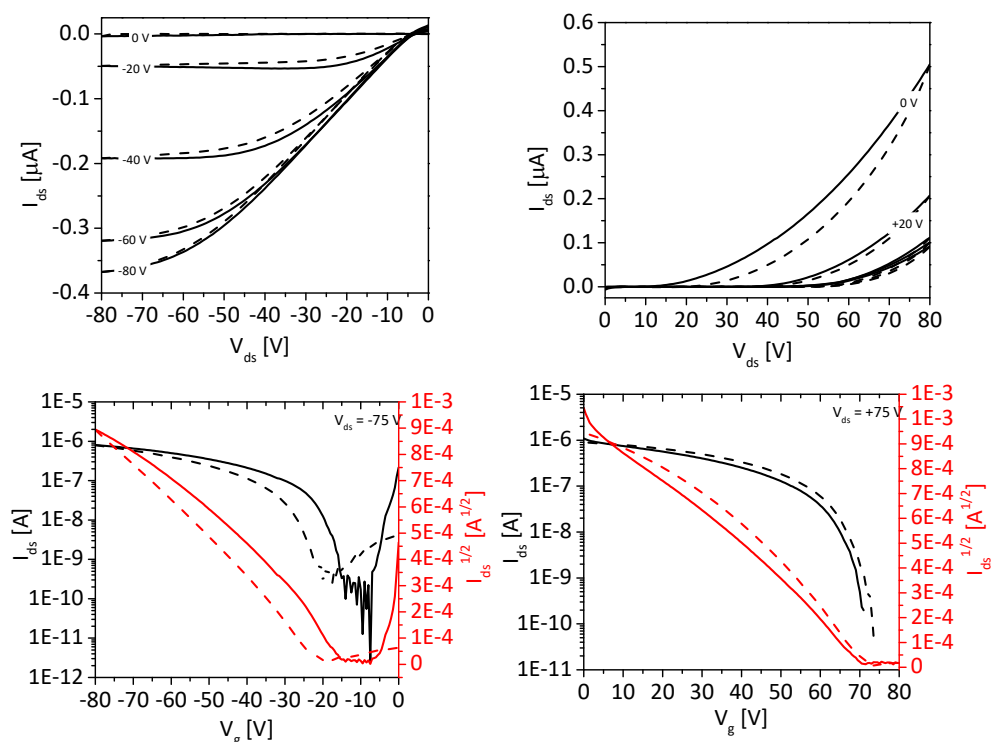


Figure S 6.5. OFET output (top) and transfer (bottom) characteristics: p-channel operation (left) and n-channel operation (right) of P(TPD-TPF₂T) in the as cast state. Solid lines represent forward scans and dashed lines reversed scans.

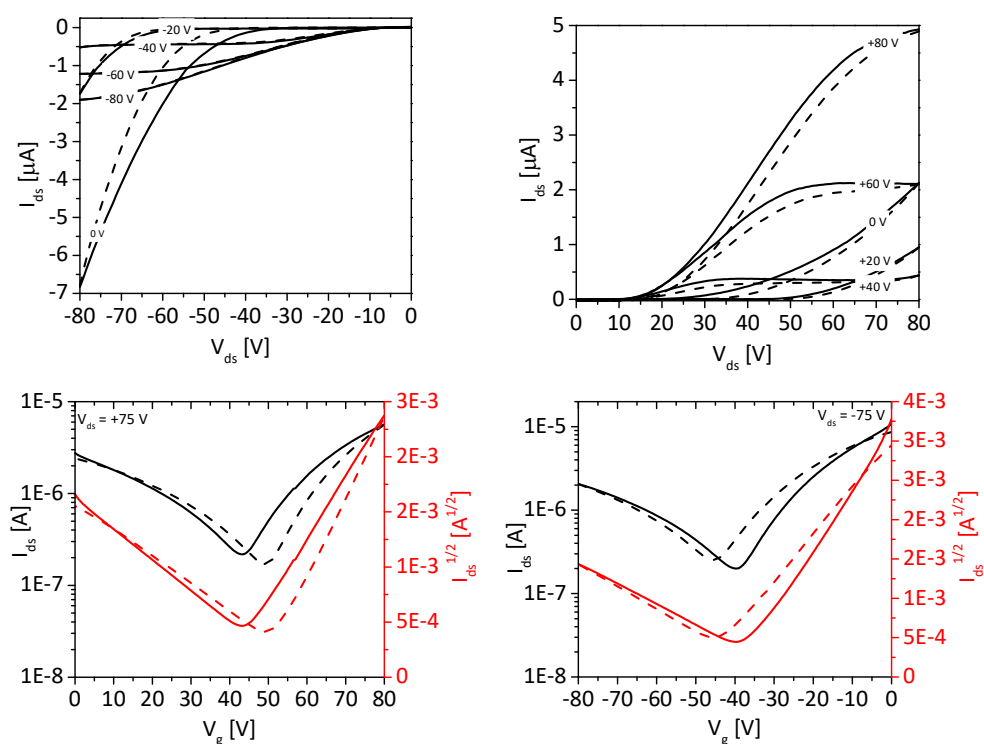


Figure S 6.6. OFET output (top) and transfer (bottom) characteristics: p-channel operation (left) and n-channel operation (right) of P(TPD-TPF₂T) after thermal annealing. Solid lines represent forward scans and dashed lines reversed scans.

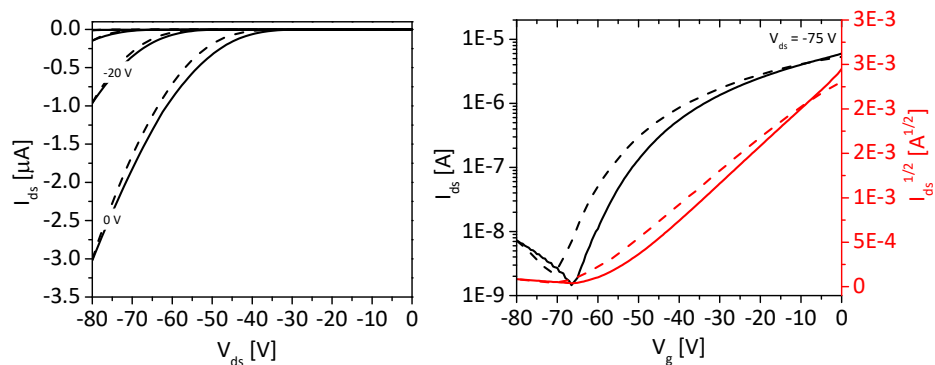


Figure S 6.7. OFET output (left) and transfer (right) characteristics: p-channel operation of P(TPD-TPF₄T) after thermal annealing. Solid lines represent forward scans and dashed lines reversed scans.

Table S 6.1. OFET hole and electron mobilities as well as corresponding threshold voltage for as-cast films and after thermal annealing at 250 °C for 15 min under nitrogen.

	as-cast		annealed			
	μ_h^a [cm ² V ⁻¹ s ⁻¹]	V_T [V]	μ_h^a [cm ² V ⁻¹ s ⁻¹]	V_T [V]	μ_e [cm ² V ⁻¹ s ⁻¹]	V_T [V]
P(TPD-TPT)	$(2.5 \pm 0.8) \times 10^{-5}$	4	$(0.4 \pm 0.1) \times 10^{-4}$	-14.0	$(1.1 \pm 0.1) \times 10^{-4}$	49.8
P(TPD-TPF ₂ T)	$(5.0 \pm 1.9) \times 10^{-5}$	8	$(1.1 \pm 0.5) \times 10^{-4}$	-30.3	$(3.4 \pm 1.5) \times 10^{-4}$	43.5
P(TPD-TPF ₄ T)	-	-	-	-	$(3.7 \pm 1.6) \times 10^{-4}$	28.3

12 GIWAXS data

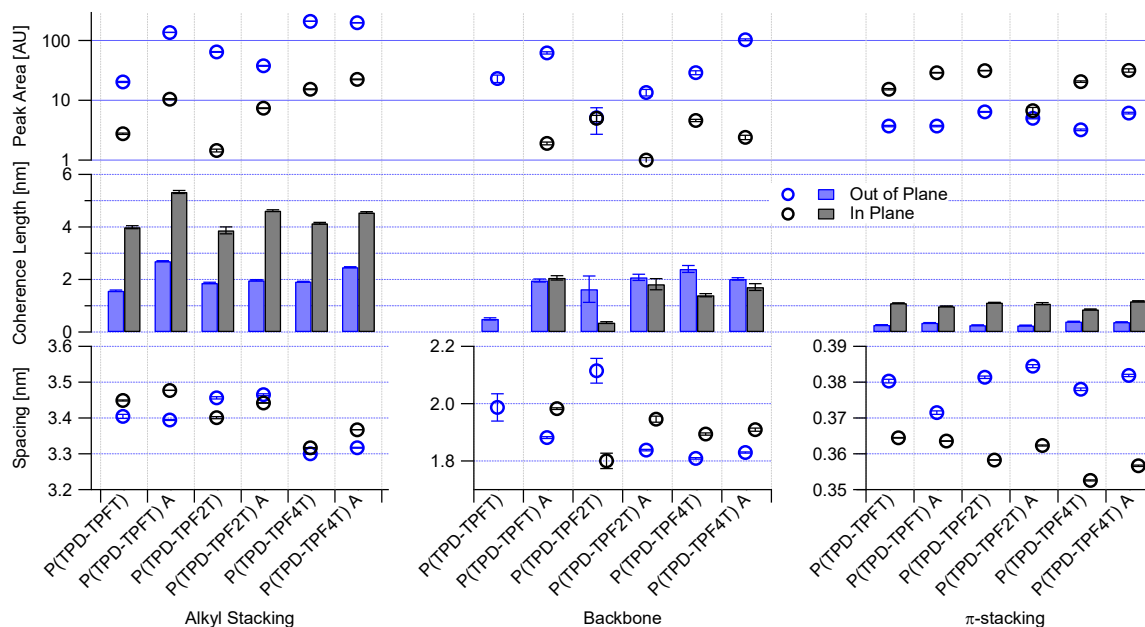


Figure S 6.8. Graphical summary of peak fitting analysis of the out-of-plane and in-plane scattering profiles.

13 References

- [1] H. Li, S. S. Babu, S. T. Turner, D. Neher, M. J. Hollamby, T. Seki, S. Yagai, Y. Deguchi, H. Möhwald and T. Nakanishi, *J. Mater. Chem. C* **2013**, *1*, 1943.
- [2] X. Guo and M. D. Watson, *Org. Lett.* **2008**, *10*, 5333.
- [3] A. Najari, S. Beaupré, P. Berrouard, Y. Zou, J. R. Pouliot, C. Lepage-Pérusse and M. Leclerc, *Adv. Funct. Mater.* **2011**, *21*, 718.
- [4] R. Matsidik, J. Martin, S. Schmidt, J. Obermayer, F. Lombeck, F. Nübling, H. Komber, D. Fazzi and M. Sommer, *J. Org. Chem.* **2015**, *80*, 980.
- [5] N. J. Findlay, J. Bruckbauer, A. R. Inigo, B. Breig, S. Arumugam, D. J. Wallis, R. W. Martin and P. J. Skabara, *Adv. Mater.* **2014**, *26*, 7290.

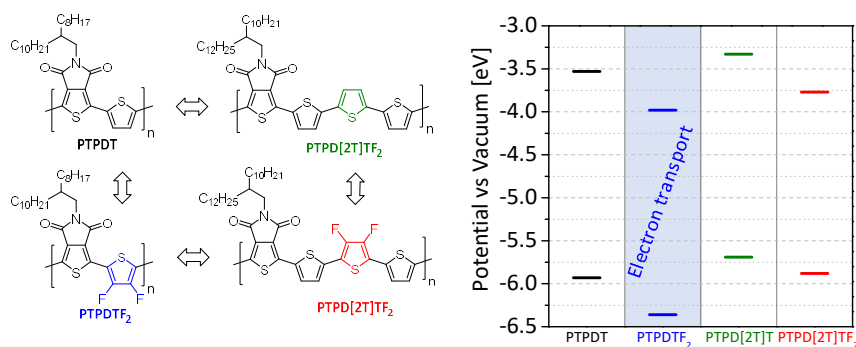
7 Influence of fluorination and backbone extension in thieno[3,4-c]pyrrole-4,6-dione based copolymers carrying thiophene and terthiophene comonomers

Tina Weller,^a Christopher R. McNeill^b and Mukundan Thelakkat^{a*}

^a Applied Functional Polymers, Macromolecular Chemistry I, University of Bayreuth, 95440 Bayreuth, Germany.

^b Department of Materials Science and Engineering, Monash University, Wellington Road, Clayton VIC, 3800, Australia.

* Corresponding author: mukundan.thelakkat@uni-bayreuth.de



Manuscript prepared for submission.

Abstract

Four copolymers based on thieno[3,4-*c*]pyrrole-4,6-dione (TPD) and thiophene derivatives as monomers were synthesized and the influence of the extension of the backbone from thiophene to terthiophene and fluorination in each were studied. First, in a Stille polycondensation, TPD was copolymerized with thiophene and difluorothiophene, respectively. Additionally, a TPD monomer flanked with thiophene was applied in the polycondensation to obtain terthiophene as donor units in order to study the influence of the extended repeating unit. Besides the systematic study of the optical, thermal and electrochemical properties, the thin film alignment was investigated in dependence of the annealing temperature. The charge transport properties were studied in organic field effect transistors (OFETs). For the TPD copolymer with difluorothiophene (PTPDTF₂), exclusively n-channel operation was achieved with an electron mobility in the range of $10^{-3} \text{ cm}^2 \text{ V}^{-1} \text{ s}^{-1}$. In contrast, the corresponding non-fluorinated polymer as well as the two polymers with extended repeating unit showed ambipolar channel operation. Here, the electron transport could be improved by fluorination and a similar OFET electron mobility as that for PTPDTF₂ was reached.

7.1 Introduction

The design of conjugated polymers for optoelectronic applications is based on the donor-acceptor copolymer concept generating predominantly p-type behavior. In order to replace fullerene and its derivatives with alternative acceptor materials, polymers showing electron transport are required. For this purpose, especially polymers based on naphthalene diimide (NDI) are in the focus, which showed a power conversion efficiency of 8.3% in all-polymer solar cells.^[1] Recently, a slightly higher PCE of 8.6% was reached with a naphthodiperylenetetraimide based polymer acceptor.^[2] For the design of polymer acceptors, highly electron-deficient acceptor units are a prerequisite. Besides NDI and PDI based acceptor units, thieno[3,4-*c*]pyrrole-4,6-dione (TPD) is an interesting moiety due to its strong electron withdrawing character and high photostability.^[3] Furthermore, TPD is easily synthetic accessible and high inter- and intrachain interactions are favored by its symmetric and coplanar structure. Copolymers based on TPD are mainly applied as donor materials in organic solar cells achieving efficiencies of 9.2% in combination with fullerene.^[4] Using alternative small molecule acceptors, the benchmark of 10% efficiency was reached recently.^[5] Moreover, in organic field effect transistors a highest hole mobility of $1.3 \text{ cm}^2 \text{ V}^{-1} \text{ s}^{-1}$ was obtained.^[6] Ambipolar charge transport

was observed using thiophene as comonomer showing rather low charge carrier mobilities though.^[7] In contrast, bithienopyrroledione based copolymers show ambipolar charge transport with an electron mobility of $1.02 \text{ cm}^2 \text{ V}^{-1} \text{ s}^{-1}$ and a hole mobility of $0.33 \text{ cm}^2 \text{ V}^{-1} \text{ s}^{-1}$.^[8] Only a few examples of copolymers showing unipolar n-channel operation are reported^[9–11] and the highest electron mobility achieved with TPD copolymers (in combination with isoindigo) was only $10^{-2} \text{ cm}^2 \text{ V}^{-1} \text{ s}^{-1}$.^[12] Beaujuge and coworkers first applied TPD containing polymers as acceptor materials in all-polymer solar cells with appreciable performance.^[13,14] In order to achieve electron transport, the electron affinity along the polymer backbone needs to be increased, e.g. by the incorporation of fluorine. In general, there are examples for this strategy in different kinds of donor-acceptor copolymers. For example, in isoindigo based copolymers, the polarity of charge transport could be tuned from unipolar p-type to ambipolar to unipolar n-type by fluorination of one or both comonomers.^[15] Similarly, ambipolar charge transport was achieved by fluorination of DPP copolymers, whereas the non-fluorinated copolymers showed exclusively p-channel operation.^[16–18] Additionally, fluorination improved especially the electron mobility in DPP copolymers showing ambipolar charge transport properties.^[19] In our previous study, we showed that tetrafluorination of the phenyl unit in copolymers based on TPD and 1,4-di(2-thienyl)benzene leads to exclusively n-channel operation.^[11] Besides influencing the polarity of charge transport, also the efficiency of charge transport can be improved through fluorination due to planarization of the polymer backbone by non-covalent interactions. For example, fluorination improved charge transport of n-type polymers based on NDI leading to an increased performance of the corresponding organic solar cells.^[20,21] To summarize, this fluorination method was reported in the literature for different polymer donors.^[22–30]

In this report, we incorporated difluorothiophene in TPD based copolymers and studied the influence of fluorination by comparing with the non-fluorinated copolymers. For this, we synthesized a series of four polymers based on two monomers, TPD and TPD flanked on both sides with thiophene units. Each TPD monomer was thus copolymerized with thiophene and difluorothiophene in a Stille polycondensation reaction. The fluorinated and non-fluorinated polymers are comparatively studied regarding their optical, thermal and electrochemical properties as well as charge transport properties in OFET. Additionally, the influence of the extended conjugation via terthiophene on the above properties was also investigated.

7.2 Experimental part

7.2.1 Materials and methods

All commercially available reagents were used as received unless otherwise noted. For reactions under microwave irradiation a Biotage Initiator Eight+ Microwave was used. Size exclusion chromatography (SEC) was carried out on an Agilent (Polymer Laboratories Ltd) PL-SEC 220 high temperature chromatographic unit equipped with three linear mixed bed columns (PSS Polefin linear XL) and DP and RI detectors. Analysis was performed at 160 °C using 1,2,4-trichlorobenzene as the eluent. The samples were prepared by dissolving the polymer (0.1 wt%) in the solvent in an external oven and the solutions were injected and eluted without filtration. Molecular weights were referenced to polystyrene standards ($M_w = 518\text{--}2\,600\,000\text{ g mol}^{-1}$, $K = 12.100$ and $\text{Alpha} = 0.707$). Cyclic voltammetric measurements were carried out in thin films under moisture- and oxygen-free conditions using a three-electrode assembly connected to a potentiostat (model 263A, EG&G Princeton Applied Research) at a scanning rate of 100 mV s^{-1} . A solution of tetra-*n*-butylammonium hexafluorophosphate in acetonitrile with a concentration of 0.1 M was used as electrolyte. Glass substrates coated with ITO ($10\ \Omega\ \square^{-1}$) were used as working electrodes, on which thin films were spin coated at 1500 rpm from CHCl_3 solutions with a concentration of 5 mg mL^{-1} . A platinum wire in the respective electrolyte solution and Ag/AgNO₃ in acetonitrile (0.1 M) were used as the counter and reference electrode, respectively. Each measurement was calibrated by the internal standard ferrocene/ferrocenium. UV-Vis spectra were recorded on a JASCO V-670 spectrophotometer. Fluorescence spectroscopy was performed on a JASCO FP-8600 spectrofluorometer using the wavelength maximum of transition for absorption as the excitation wavelength. Analysis of the optical properties was conducted either in chloroform solutions (0.01 mg mL^{-1}) using quartz cuvettes with an internal diameter of 10 mm or in thin films spin coated on glass slides from chloroform solutions (5 mg mL^{-1}) at 1500 rpm. For thermogravimetric analysis (TGA) a Netzsch STA 449 F3 Jupiter was used at a scanning rate of 10 K min^{-1} under a nitrogen atmosphere. The temperature of decomposition, $T_{5\%}$, was determined at 5% weight loss. Flash DSC measurements were conducted on a Mettler-Toledo Flash DSC 1 at scanning rates between 50 and 1000 K min^{-1} under nitrogen. GIWAXS measurements were performed at the SAXS/WAXS beamline at the Australian Synchrotron.^[31] All samples were prepared by spin coating polymer films onto silicon wafers (n-doped with antimony) from chloroform solutions ($15\text{--}20\text{ mg mL}^{-1}$) at 1000-1500 rpm. 11 keV X-rays were

used with 2D scattering patterns recorded on a Dectris Pilatus 1M detector. The sample to detector distance was calibrated using a silver behenate scattering standard. Scattering patterns were collected from incidence angles (α) between 0.02° and 0.35° with an X-ray exposure time of 3 s. Three separate 1 s exposures were taken with different lateral positions to fill in the gaps between the detector elements. These different exposures were combined in the software. The obtained data was processed and analyzed using a modified version of NIKA 2D^[32] based in IgorPro. For organic thin film transistor measurements, substrates with a bottom gate, bottom contact architecture were purchased from Fraunhofer IPMS (OFET Gen. 4). As the substrate and gate electrode a heavily n-doped silicon wafer (doping at the wafer surface: $n \approx 3 \times 10^{17} \text{ cm}^{-3}$) was used. The gate electrode is separated from the source and drain electrodes by a dielectric, which consists of thermally grown silicon dioxide (Standard 90/230 nm). Source and drain electrodes are made from gold with a thickness of 30 nm adhered to the dielectric by a layer of 10 nm ITO. One chip carries four groups with four identical transistors with a channel length of 2.5, 5, 10 and 20 μm , respectively, and a channel width of 10 μm . The substrates were first rinsed with acetone followed by ultrasonification in acetone and 2-propanol for 10 min each. After plasma treatment for 15 min at 50°C , silanisation with octadecyltrichlorosilane in toluene (1 vol%) at 60°C for 1 h was conducted. The devices were rinsed with toluene and stored in 2-propanol until spin coating. Films were spin coated from chloroform solutions (10 mg mL^{-1}) at 5000 rpm under ambient conditions and directly transferred into the glove box. Current-voltage characteristics were measured under nitrogen atmosphere using an Agilent B1500 Semiconductor Parameter Analyzer. Annealing was performed under nitrogen at 100°C and 250°C for 15 min, respectively. The charge carrier mobilities were calculated in the saturation regime using eqn (1), where I_{DS} is the drain–source current, V_G the gate voltage, L the channel length, W the channel width and C_i the capacitance. Therefore, the slope in the $I_{DS}^{1/2}$ vs V_g plot was determined and used for the calculation of the charge carrier mobilities.

$$\mu_{sat} = \left(\frac{\partial \sqrt{I_{DS}}}{\partial V_G} \right)^2 \cdot \frac{2L}{WC_i} \quad (1)$$

7.2.2 Synthesis procedures

General procedure for the Stille polycondensation: A microwave vial was loaded with the TPD monomer **1** or **2** (1 eq.) and the different thiophene monomers **3a** or **3b** (1 eq.). Tri(*o*-tolyl)phosphine (0.12 eq.) and chlorobenzene were added. After degassing by argon bubbling for 10 min, tris(dibenzylideneacetone)dipalladium(0) (0.03 eq.) was added. The microwave vial was sealed and purged with argon once more. The polymerization reaction was conducted at 160 °C for 1 h under microwave irradiation. After cooling to room temperature, 2-(tributylstannyl)thiophene was added to end-cap the polymers and the reaction mixture was stirred for 5 min at 160 °C. The end-capping step was subsequently repeated with 2-bromothiophene for 10 min. The polymer solution was precipitated in methanol (300 mL) and filtered. Further purification was carried out by sequential Soxhlet extraction. Finally, the polymer was collected by extraction with chloroform and the solution was concentrated under reduced pressure. Precipitation in methanol, filtration and drying in a vacuum yielded the respective polymer.

PTPDT: A Schlenk tube was loaded with the monomers 1,3-dibromo-5-(2-octyldodecyl)-4*H*-thieno[3,4-*c*]pyrrol-4,6(5*H*)-dione **1a** (293 mg, 0.495 mmol, 1 eq) and 2,5-bis(trimethylstannyl)thiophene **2** (203 mg, 0.495 mmol, 1 eq.). Tri(*o*-tolyl)phosphine (18.1 mg, 0.053 mmol, 0.12 eq.) was added followed by 16.5 mL tetrahydrofuran. After degassing by argon bubbling for 10 min, tris(dibenzylideneacetone)dipalladium(0) (13.6 mg, 0.015 mmol, 0.03 eq.) was added. The Schlenk tube was sealed and purged with argon once more. The polymerization reaction was conducted at 70 °C for 40 h. After cooling to room temperature, 2-(tributylstannyl)thiophene was added to end-cap the polymer chains and the reaction mixture was stirred for 2 h at 70 °C. The end-capping step was subsequently repeated with 2-bromothiophene under the same reaction conditions. The polymer solution was precipitated in methanol (300 mL) and filtered. Further purification was carried out by sequential Soxhlet extraction using methanol, acetone and butan-2-one. Finally, the polymer was collected by extraction with chloroform and the solution was concentrated under reduced pressure. Precipitation in methanol, filtration and drying in vacuum yielded the desired polymer (216 mg, 80%). ¹H NMR (300 MHz, CDCl₃): δ = 7.36-9.15 (1H), 6.25-7.21 (1H), 3.11-4.47 (2H), 0.44-2.22 (49H) ppm.

PTPDTF₂: Following the general procedure, a solution of 1,3-dibromo-5-(2-octyldodecyl)-4*H*-thieno[3,4-*c*]pyrrol-4,6(5*H*)-dione **1** (221 mg, 0.374 mmol, 1 eq.), 3,4-difluoro-2,5-bis(trimethylstannyl)thiophene **3b** (167 mg, 0.374 mmol, 1 eq.), tri(*o*-tolyl)phosphine 13.6 mg, 0.045 mmol, 0.12 eq.) and tris(dibenzylideneacetone)dipalladium(0) (10.3 mg, 11.2 μmol, 0.03 eq.) in 5 mL chlorobenzene was stirred for 1 h at 160 °C. Soxhlet extraction was carried out using methanol, acetone and butan-2-one yielding PTPDTF₂ (203 mg, 94%) as a black solid. ¹H NMR (300 MHz, CDCl₃): δ = 3.07-4.59 (2H), 0.28-3.04 (39H) ppm. ¹⁹F NMR (300 MHz, CDCl₃): δ = - (121-130) ppm.

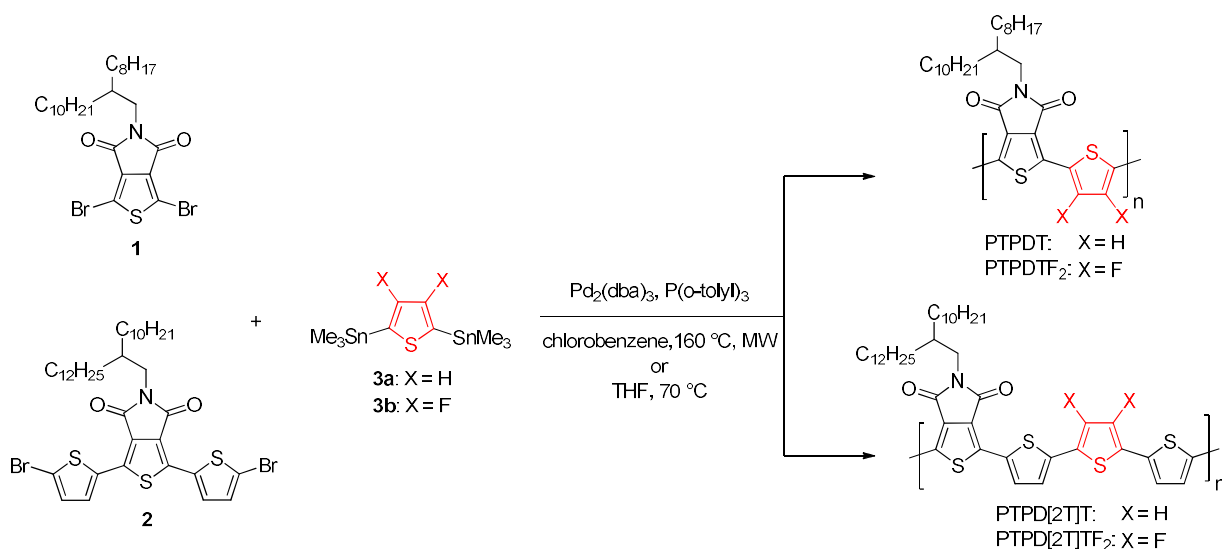
PTPD[2T]T: Following the general procedure, a solution of 1,3-di(5-bromothien-2-yl)-5-(2-decyl-1-tetradecyl)-4*H*-thieno[3,4-*c*]pyrrole-4,6(5*H*)-dione **2** (246 mg, 0.303 mmol, 1 eq.), 2,5-bis(trimethylstannyl)thiophene **3a** (124 mg, 0.303 mmol, 1 eq.), tri(*o*-tolyl)phosphine (11.1 mg, 0.036 mmol, 0.12 eq.) and tris(dibenzylideneacetone)dipalladium(0) (8.34 mg, 9.10 μmol, 0.03 eq.) in 4.7 mL chlorobenzene was stirred for 1 h at 160 °C. Soxhlet extraction was carried out using methanol, acetone, butan-2-one and hexane yielding PTPD[2T]T (217 mg, 94%) as a black solid. ¹H NMR (300 MHz, CDCl₃): δ = 7.35-8.35 (2H), 5.20-7.05 (4H), 2.93-3.98 (2H), 0.44-2.49 (47H) ppm.

PTPD[2T]TF₂: Following the general procedure, a solution of 1,3-di(5-bromothien-2-yl)-5-(2-decyl-1-tetradecyl)-4*H*-thieno[3,4-*c*]pyrrole-4,6(5*H*)-dione **2** (223 mg, 0.274 mmol, 1 eq.), 3,4-difluoro-2,5-bis(trimethylstannyl)thiophene **3b** (122 mg, 0.274 mmol, 1 eq.), tri(*o*-tolyl)phosphine (10.0 mg, 0.033 mmol, 0.12 eq.) and tris(dibenzylideneacetone)dipalladium(0) (7.54 mg, 8.23 μmol, 0.03 eq.) in 4.2 mL chlorobenzene was stirred for 1 h at 160 °C. Soxhlet extraction was carried out using methanol, acetone and butan-2-one yielding PTPD[2T]TF₂ (211 mg, 96%) as a black solid. ¹H NMR (300 MHz, CDCl₃): δ = 7.30-8.50 (2H), 5.43-6.87 (2H), 2.73-4.03 (2H), 0.29-2.64 (47H) ppm. ¹⁹F NMR (300 MHz, CDCl₃): δ = - (126-134) ppm.

7.3 Results and discussion

7.3.1 Synthesis

The synthesis of the dibromo functionalized TPD monomer **1** carrying octyldodecyl side chains is reported elsewhere.^[11] Following these reported procedures, the corresponding TPD carrying decyltetradecyl side chains was synthesized, which was then flanked with thiophene on both sides in a Stille reaction. Subsequent bromination gave the extended TPD monomer **2** and all the synthetic procedures can be found in the Supporting Information. The longer solubilizing side chains for the TPD monomer **2** were chosen to maintain solubility of the resulting polymers comprising of a repeating unit with extended conjugation. As shown in Scheme 7.1, both TPD monomers **1** and **2** were copolymerized with trimethyl stannate functionalized thiophene and difluorinated thiophene, resulting in four different polymers. The synthesis of 3,4-difluoro-2,5-bis(trimethylstannyl)-thiophene has already been reported in our group.^[18] Stille polymerization was carried out with tris(dibenzylideneacetone)dipalladium(0) as a catalyst and tri(*o*-tolylphosphine) as a ligand in chlorobenzene for one hour at 160 °C under microwave irradiation. Two end-capping steps were conducted using 2-(tributylstannyl)thiophene followed by bromothiophene. The final polymers were purified by Soxhlet extraction and were analyzed with high temperature size exclusion chromatography in trichlorobenzene at 160 °C. Under these polymerization conditions only low molecular weights are obtained for the polymer PTPDT. As shown in our previous study, a higher degree of polymerization could be facilitated with tetrahydrofuran as solvent.^[33]



Scheme 7.1. Synthesis of TPD containing polymers PTPDT, PTPDTF₂, PTPD[2T]T, PTPD[2T]TF₂ using Stille polycondensation.

In Table 7.1, the molecular weights (PS calibration) as well as the dispersities are summarized and the chromatograms can be found in the Supporting Information. Copolymerization of TPD with thiophene in THF results in a number average molecular weight of 9.40 kg mol⁻¹ with a dispersity of 1.4 for PTPDT. In contrast, the corresponding fluorinated polymer PTPDTF₂ exhibits a higher number average molecular weight of 20.9 kg mol⁻¹ with a dispersity of 1.97. The copolymers with extended thiophene backbone show a number average molecular weight of 11.0 kg mol⁻¹ for the non-fluorinated (PTPD[2T]T) and 15.4 kg mol⁻¹ for the fluorinated polymer (PTPD[2T]TF₂) with dispersities of 1.8 for both polymers. In conclusion, higher molecular weights were achieved for the polycondensation reactions with the fluorinated monomer.

Table 7.1. SEC, absorption, electrochemical and thermal properties of the TPD containing polymers.

	M_n^a [kg mol ⁻¹]	M_w^a [kg mol ⁻¹]	\mathcal{D}	$T_{5\%}^b$ [°C]	T_m^c [°C]	T_c^c [°C]	E_{opt}^d [eV]	IP ^e [eV]	EA ^e [eV]	E_{fund} [eV]
PTPDT	9.40	17.1	1.4	427	400	374	1.72	-5.93	-3.53	2.40
PTPDTF ₂	20.9	61.7	2.0	430	445	421	1.90	-6.36	-3.98	2.38
PTPD[2T]T	11.0	19.4	1.8	423	410	378	1.76	-5.69	-3.33	2.36
PTPD[2T]TF ₂	15.4	27.0	1.8	426	440	410	1.80	-5.88	-3.77	2.11

^a Determined by SEC in 1,2,4-trichlorobenzene at 160 °C using PS calibration; ^b decomposition at 5% mass loss determined by TGA at 10 K min⁻¹ under N₂. ^c Melt and crystallization temperature from Flash DSC measurements at 1000 K min⁻¹ under N₂. ^d Optical gap determined by the absorption edge in thin films. ^e Ionization potential (IP) and electron affinity (EA) determined from cyclic voltammetry in thin films.

The thermal stability of the polymers was determined with TGA and the decomposition temperatures at 5% mass loss are summarized in Table 7.1. All polymers show high thermal stability with decomposition temperatures in the range of 420-430 °C. Due to the high scanning rates of 50 to 1000 K min⁻¹ in Flash DSC, the melting and crystallization near the decomposition can be investigated. Therefore, flash DSC measurements were performed in order to study the crystallization behavior of this series of copolymers. For all polymers, a melting as well as crystallization temperature could be detected and the values at a scanning rate of 1000 K min⁻¹ are summarized in Table 7.1. The DSC traces at a scanning rate of 1000 K min⁻¹ are shown in Figure 7.1a and the complete DSC spectra at all scanning rates can be found in the Supporting Information. Polymer PTPDT shows a melting temperature at 400 °C and a crystallization temperature at 374 °C. By fluorination, the melting as well as crystallization temperature is increased to 445 °C and 421 °C, respectively. The same trend is observed for the polymers with extended backbone and the melting as well as crystallization temperatures are in a similar region. In conclusion, the incorporation of two additional thiophenes into the polymer backbone has a negligible effect on the thermal properties. By fluorination, the melting as well as crystallization temperature are increased for both polymers, probably due to larger crystals

resulting from increased planarization of the polymer backbone in both PTPDTF₂ and PTPD[2T]TF₂.

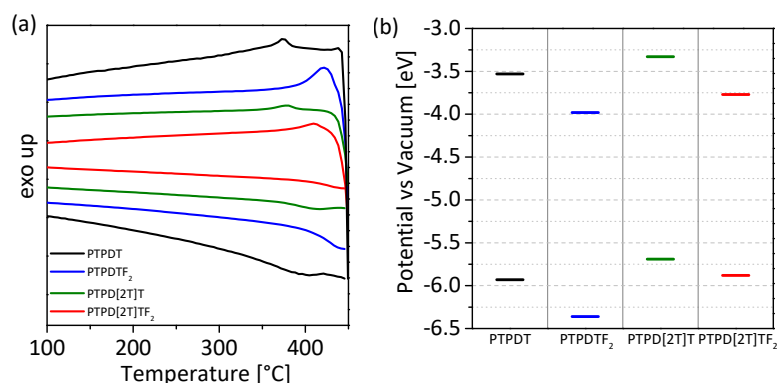


Figure 7.1. (a) Flash DSC measurements of PTPDT, PTPDTF₂, PTPD[2T]T and PTPD[2T]TF₂ at a scanning rate of 1000 K min⁻¹. (b) Energy levels determined from cyclic voltammetry measurements in thin films.

7.3.2 Optical and electrochemical properties

The optical properties of all the polymers were determined using UV-Vis measurements in solutions as well as thin films and the spectra are shown in Figure 7.2. PTPDT shows two absorption bands at 570 nm and 620 nm with similar intensities in solution. In thin films, both absorption bands are red-shifted by 10 nm. Fluorination has a strong impact on the absorption properties. The overall absorption region is narrowed, and one main absorption band arises at 550 nm accompanied by a shoulder at 590 nm. In thin films, this shoulder becomes more prominent and the absorption edge is red-shifted due to aggregation. The optical gap was calculated from the absorption edge in thin films and the results are summarized in Table 7.1. By fluorination of PTPDT the optical gap is increased from 1.72 eV to 1.90 eV in PTPDTF₂ due to the decreased donor strength of the fluorinated thiophene unit. Extension of the repeating unit with thiophene in PTPD[2T]T and PTPD[2T]TF₂ results in a main absorption peak at 500 nm in solution, which is blue-shifted in comparison to the PTPDT and PTPDTF₂ copolymers. In thin films, this absorption peak is red-shifted by 20 nm and the shoulder at 665 nm becomes again more prominent due to aggregation. The optical gap is slightly increased to 1.76 eV in PTPD[2T]T in comparison to polymer PTPDT (1.72 eV). Here, the main absorption features are maintained by fluorination and the overall absorption spectrum of PTPD[2T]TF₂ is blue-shifted by around 50 nm due to the electron withdrawing properties of fluorine. Additionally, the photoluminescence is measured after excitation at the absorption peak maximum in solution as well as thin films and the corresponding spectra can be found in the Supporting Information.

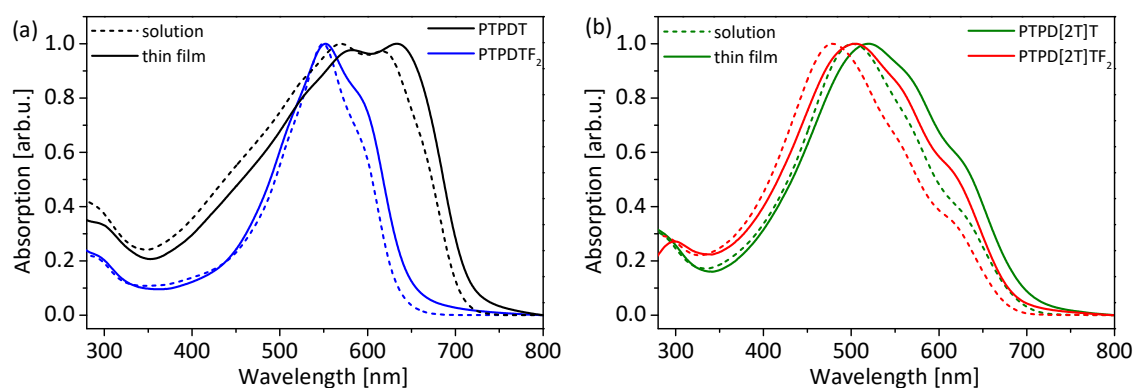


Figure 7.2. UV-Vis measurements in solutions (dashed line) and thin films (solid line) of polymers (a) PTPDT and PTPDFT₂ and (b) PTPD[2T]T and PTPD[2T]TF₂.

Cyclic voltammetry was performed in thin films using a three-electrode assembly in order to determine the redox energy levels. All cyclic voltammograms are given in the Supporting Information. The electron affinity (EA) and ionization potentials (IP) are calculated from the onsets of the reduction and oxidation waves, respectively. For the calculation, the solvent effects are considered^[34] and the values should not be taken as absolute values, but rather as an approximate estimation. In Figure 7.1b, the energy levels are graphically illustrated, and the corresponding values are given in Table 7.1. Both non-fluorinated polymers PTPDT and PTPD[2T]T show reversible oxidation as well as reduction processes. In contrast, the fluorinated polymers PTPDFT₂ and PTPD[2T]TF₂ show only a reversible oxidation and an irreversible reduction. By extension of the repeating unit with two thiophenes the energy levels are considerably affected. For PTPD[2T]T, the EA as well as IP are increased both by around 0.2 eV in comparison with PTPDT, and for PTPD[2T]TF₂ the EA is increased by 0.2 eV and the IP by 0.5 eV in comparison to PTPDFT₂. In comparison to TPD, TPD flanked with thiophene on both sides has a weaker acceptor strength resulting in a destabilization of the energy levels. By fluorination, the EA as well as IP are lowered by 0.2-0.4 eV for both fluorinated polymers PTPDFT₂ and PTPD[2T]TF₂ due to decreased electron density along the polymer backbone caused by the electron withdrawing fluorine substituents. In contrast to the optical gap, the fundamental gap is smaller for the respective fluorinated polymers than for the non-fluorinated polymers, which may be attributed to a comparatively smaller exciton binding energy.^[35]

7.3.3 GIWAXS

The crystalline packing of the neat polymers in thin films was analyzed with Grazing Incidence Wide Angle X-ray Scattering (GIWAXS). Additionally, the influence of annealing at 250 °C on the solid-state packing was studied and the corresponding two-dimensional scattering patterns of the as-cast and annealed films are depicted in Figure 7.3a and b. These scattering patterns were taken near the critical angle, where the scattering intensity is maximal.

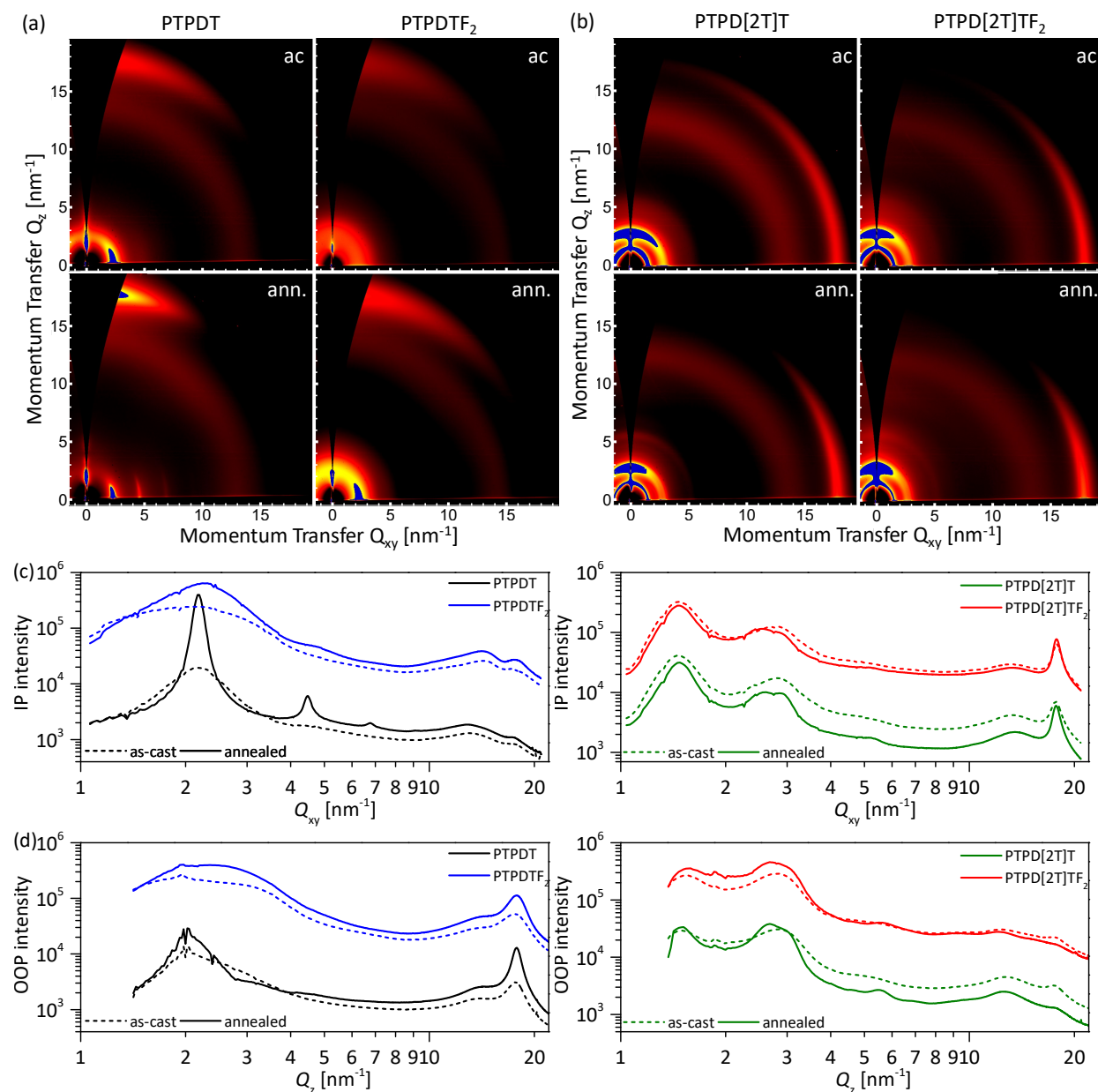


Figure 7.3. 2D GIWAXS pattern of as-cast (top: ac) and annealed films (bottom: ann.) for (a) polymer PTPDT and PTPDTF₂ and (b) polymer PTPD[2T]T and PTPD[2T]TF₂. 1D scattering profiles taken along (c) in-plane and (d) out-of-plane direction for all the polymers, for both as-cast and annealed conditions.

In Figure 7.3c and d, the one-dimensional lineouts along Q_{xy} (in-plane) as well as Q_z (out-of-plane) direction are shown for the as-cast and annealed films. From the lineouts, the stacking distances and coherence lengths are extracted, which are summarized in Table 7.2. Polymer PTPDT shows an alkyl stacking peak in the in-plane direction and a corresponding π - π stacking peak in the out-of-plane direction in the as-cast film. Thus, the polymer chains orient predominantly face-on with the planar π -systems lying flat on the substrate. After annealing, this face-on orientation is maintained and up to three orders of alkyl stacking is prominent. Moreover, the scattering peaks are more pronounced and sharpened resulting in considerably higher coherence lengths after thermal annealing. The fluorinated polymer PTPDTF₂ shows predominantly face-on orientation as well. However, the crystallinity seems to be reduced because only the first order of lamellar stacking is present before and after annealing. In comparison, the alkyl stacking distance of PTPDTF₂ is increased in the as-cast film by 0.2 nm upon fluorination, whereas both polymers PTPDT and PTPDTF₂ show an alkyl spacing of 2.8 nm after annealing. The π - π stacking distance of PTPDTF₂ is notably decreased by fluorination due to the planarization of the polymer backbone, which promote a closer staking. Both coherence lengths of the alkyl and π - π stacking are decreased for the fluorinated polymer PTPDTF₂ indicating a lower long-range order and an inferior solid-state packing.

The polymers with extended repeating unit show two sets of the (100) peak, which is indicative for the coexistence of two polymorphs. At Q values of 1.5 nm^{-1} , the scattering intensity is constant over all polar angles, whereas the peak at 2.8 nm^{-1} is predominately present along the z -direction. This suggests one isotropic polymorph and an edge-on oriented polymorph, which is supported by the corresponding π - π stacking peak observed in-plane. For both sets of scattering peaks, even the second order of alkyl stacking is slightly visible after thermal annealing. The edge-on stacks have a small alkyl stacking distance of around 2.2 nm and a small coherence length of below 10 nm. This small alkyl stacking distance in comparison to the polymers PTPDT and PTPDTF₂ can be explained by the longer spacing of two TPD moieties enabling a closer stacking. In contrast, the isotropic polymorph does not show a dense solid-state packing ($d = 4.3 \text{ nm}$). However, the coherence length is doubled in comparison to the edge-on oriented polymorph. Thermal annealing has almost no effect on the solid-state packing, only the coherence lengths for alkyl and π - π stacking are slightly increased. By fluorination, the π - π stacking is slightly influenced resulting in a smaller distance due to planarization and an increased coherence length.

Table 7.2. Crystalline parameters.

Polymer	Film State	d_{alkyl}^a [nm]	ζ_{alkyl}^b [nm]	$d_{\pi-\pi}^c$ [nm]	$\zeta_{\pi-\pi}^d$ [nm]
PTPDT	as-cast	2.79	8.48	0.359	2.77
	annealed	2.78	57.2	0.357	5.32
PTPDTF ₂	as-cast	2.99	3.41	0.356	2.18
	annealed	2.80	5.58	0.352	3.22
PTPD[2T]T	as-cast	4.29/2.19	15.9/8.29	0.355	4.58
	annealed	4.26/2.27	20.7/9.23	0.354	5.98
PTPD[2T]TF ₂	as-cast	4.25/2.22	16.9/8.02	0.352	5.70
	annealed	4.26/2.27	19.1/7.20	0.353	6.49

^a Alkyl spacing; ^b alkyl spacing coherence length; ^c π - π stacking spacing; ^d π - π stacking coherence length.

In conclusion, polymer PTPDT and PTPDTF₂ both show predominantly face-on orientation, but the crystallinity is considerably decreased upon fluorination. However, a closer π - π stacking is observed upon fluorination. In contrast, an isotropic and edge-on oriented polymorph coexist for the polymers with extended backbone. Here, fluorination has almost no effect on the solid-state packing and crystalline parameters.

7.3.4 OFETs

The charge carrier mobilities were determined in organic field effect transistors using a bottom gate bottom contact configuration. Devices were analyzed as-cast and after annealing at first 100 °C followed by 250 °C for 15 min each under inert atmosphere. All output and transfer characteristics can be found in the Supporting Information. The charge carrier mobilities were calculated in the saturation regime and the results are summarized in Table 7.3. Additionally, the results are graphically illustrated in Figure 7.4. The corresponding threshold voltages can be found in the Supporting Information. Thermal annealing has a strong effect on the charge carrier mobilities, which is most pronounced for PTPDT. This material shows highly balanced ambipolar charge transport with hole and electron mobilities of $6 \times 10^{-4} \text{ cm}^2 \text{ V}^{-1} \text{ s}^{-1}$ for as-cast films. Annealing at 100 °C and further at 250 °C improves the charge carrier mobilities by one order of magnitude each. A hole as well as electron mobility of $2 \times 10^{-2} \text{ cm}^2 \text{ V}^{-1} \text{ s}^{-1}$ is reached in the annealed films. By fluorination, exclusively electron transport is generated, which can be explained due to the more difficult hole injection into the deep lying HOMO energy level of PTPDTF₂. In comparison, the electron mobilities in the as-cast film and after annealing at 100 °C for both polymers lie in the same range. Further annealing at 250 °C has a negligible impact on the electron mobility of the fluorinated polymer. In comparison to the non-fluorinated polymer,

the electron mobility of PTPDFT₂ is one order of magnitude lower after thermal annealing at 250 °C, which can be explained by the lower crystallinity of polymer PTPDFT₂ as shown in the GIWAXS analysis. Due to the less favorable face-on orientation for OFET, the electron transport in a diode configuration might be even more efficient for these polymers.

Both polymers with extended repeating unit, PTPD[2T]T and PTPD[2T]TF₂ show ambipolar charge transport properties after thermal annealing. For polymer PTPD[2T]T, the electron mobility only evolves after annealing at 100 °C and is not affected by further annealing at 250 °C. The hole mobilities, however, are not influenced by annealing at 100 °C but further annealing at 250 °C results in an increased mobility by one order of magnitude. For the fluorinated polymer PTPD[2T]TF₂, the same trend is observed for the hole mobilities, whereas the absolute values are slightly higher compared to the corresponding non-fluorinated polymer. Electron transport is even observed in the as-cast film and annealing the films at 100 °C has a negligible effect on charge carrier mobility. By annealing at 250 °C, the electron mobility is increased by one order of magnitude reaching a value of $2 \times 10^{-3} \text{ cm}^2 \text{ V}^{-1} \text{ s}^{-1}$ for PTPD[2T]TF₂, which is one order of magnitude higher than for the corresponding non-fluorinated polymer. Thus, in the extended conjugated systems, by fluorination, especially the electron transport is improved, which cannot be explained by the GIWAXS measurements, where both polymers show a similar thin film alignment. Therefore, this might be largely owing to the increased electron affinity caused by fluorination, which results in a more stabilized radical anion.

Table 7.3. OFET hole and electron mobilities for as-cast films and after thermal annealing at 100 °C as well as 250 °C for 15 min under nitrogen.

	μ_h^a [$\text{cm}^2 \text{ V}^{-1} \text{ s}^{-1}$]			μ_e^b [$\text{cm}^2 \text{ V}^{-1} \text{ s}^{-1}$]		
	as-cast	100 °C	250 °C	as-cast	100 °C	250 °C
PTPDT	$(6.0 \pm 1.4) \times 10^{-4}$	$(1.1 \pm 0.3) \times 10^{-3}$	$(1.5 \pm 0.3) \times 10^{-2}$	$(5.6 \pm 0.8) \times 10^{-4}$	$(1.2 \pm 0.2) \times 10^{-3}$	$(2.3 \pm 0.5) \times 10^{-2}$
PTPDFT ₂	-	-	-	$(2.1 \pm 0.3) \times 10^{-4}$	$(0.6 \pm 0.2) \times 10^{-3}$	$(1.1 \pm 0.2) \times 10^{-3}$
PTPD[2T]T	$(0.9 \pm 0.4) \times 10^{-5}$	$(1.5 \pm 0.8) \times 10^{-5}$	$(0.8 \pm 0.4) \times 10^{-4}$	-	$(2.1 \pm 0.5) \times 10^{-4}$	$(3.3 \pm 1.2) \times 10^{-4}$
PTPD[2T]TF ₂	$(3.6 \pm 1.0) \times 10^{-5}$	$(6.2 \pm 2.4) \times 10^{-5}$	$(4.0 \pm 0.8) \times 10^{-4}$	$(1.4 \pm 0.2) \times 10^{-4}$	$(4.8 \pm 1.1) \times 10^{-4}$	$(2.0 \pm 1.7) \times 10^{-3}$

^a Hole (μ_h) and ^b electron (μ_e) mobilities calculated from the saturation regime. All values are averaged for a minimum of six devices.

In summary, exclusively n-channel operation in OFET could be achieved for the fluorinated polymer PTPDFT₂. All other polymers showed ambipolar charge transport due to the higher lying HOMO levels making hole injection accessible. Polymer PTPDT showed the best performance for electron transport after annealing the films at 250 °C in OFET devices. Here, the electron mobility

is similar to the fluorinated polymer in the as-cast state as well as after thermal annealing at 100 °C, but it exceeds after annealing at 250 °C. For the polymers with extended backbone, the charge carrier mobilities, especially the electron transport could be improved upon fluorination reaching a similar value as for the polymer PTPDTF₂.

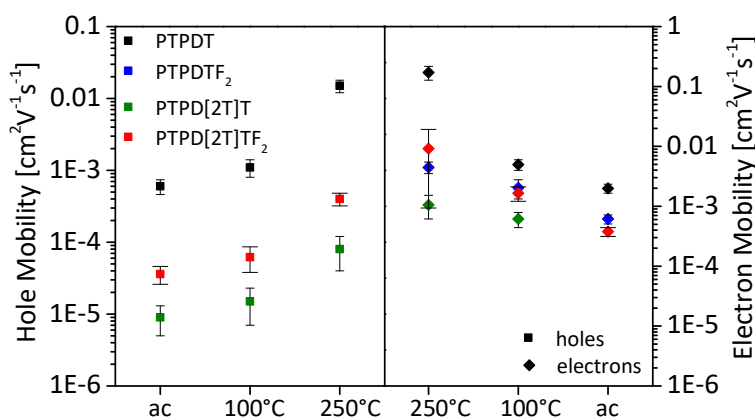


Figure 7.4. Summary chart of the OFET results for both hole and electron mobilities in as-cast and annealed films at different temperatures of all the polymers.

7.4 Conclusion

We incorporated difluorothiophene in the polymer backbone of different thieno[3,4-c]pyrrole-4,6-dione based copolymers in order to study the influence of fluorination in comparison to the non-fluorinated polymers. First, the copolymerization of TPD with a fluorinated thiophene was carried out, which yielded PTPDTF₂ and for comparison a non-fluorinated thiophene resulting in PTPDT. Further, a TPD monomer flanked with thiophene was synthesized and used in the Stille polycondensation to obtain polymers with extended conjugation, PTPD[2T]T and PTPD[2T]TF₂. Here, the influence of the extended backbone is studied with respect to structure formation, charge transport and alignment. All polymers are crystalline and show thermal transitions at very high temperatures in Flash DSC measurements, whereas the melting as well as crystallization temperatures are further shifted to higher temperatures by fluorination. Due to the electron withdrawing character of fluorine, the optical gap is enlarged and the energy levels, IP as well as EA, are lowered by fluorination. Moreover, the energy levels of the polymers with extended backbone are increased. In organic field effect transistors, exclusively n-channel operation could be achieved for polymer PTPDTF₂, whereas all other polymers show ambipolar charge transport properties. The highest electron mobility of 0.02 cm² V⁻¹ s⁻¹ was observed for PTPDT for electron transport after annealing the films at 250 °C and this is one order of magnitude higher than for

all the other polymers. On comparison of PTPDT and PTPDTF₂ in GIWAXS measurements, both polymers show predominantly face-on orientation, but only one order of alkyl stacking is observed for PTPDTF₂ in comparison to PTPDT showing three orders of alkyl stacking. Therefore, fluorination leads to a less crystalline material in this structure motive and a lower electron mobility. Nevertheless, more efficient charge transport would be expected in a diode configuration making PTPDTF₂ an interesting acceptor material for all-polymer solar cells. For the polymers with extended backbone, fluorination improves charge transport and especially the electron mobility is positively affected.

7.5 Acknowledgements

We acknowledge financial support from Bavarian State Ministry for Education, Science and the Arts under the SolTech project and Deutsche Forschungsgemeinschaft (SFB 840). This work was performed in part at the SAXS/WAXS beamline at the Australian Synchrotron, part of ANSTO.

7.6 References

- [1] L. Gao, Z.-G. Zhang, L. Xue, J. Min, J. Zhang, Z. Wei, Y. Li, *Adv. Mater.* **2016**, *28*, 1884.
- [2] Y. Guo, Y. Li, O. Awartani, H. Han, J. Zhao, H. Ade, H. Yan, D. Zhao, *Adv. Mater.* **2017**, *29*.
- [3] A. Tournebize, J.-L. Gardette, C. Taviot-Guého, D. Bégué, M. A. Arnaud, C. Dagron-Lartigau, H. Medlej, R. C. Hiorns, S. Beaupré, M. Leclerc, A. Rivaton, *Polym. Degrad. Stab.* **2015**, *112*, 175.
- [4] J.-H. Kim, J. B. Park, I. H. Jung, A. C. Grimsdale, S. C. Yoon, H. Yang, D.-H. Hwang, *Energy Environ. Sci.* **2015**, *8*, 2352.
- [5] F. Lin, W. Huang, H. Sun, J. Xin, H. Zeng, T. Yang, M. Li, X. Zhang, W. Ma, Y. Liang, *Chem. Mater.* **2017**, *29*, 5636.
- [6] Q. Wu, M. Wang, X. Qiao, Y. Xiong, Y. Huang, X. Gao, H. Li, *Macromolecules* **2013**, *46*, 3887.
- [7] X. Guo, R. P. Ortiz, Y. Zheng, M.-G. Kim, S. Zhang, Y. Hu, G. Lu, A. Facchetti, T. J. Marks, *J. Am. Chem. Soc.* **2011**, *133*, 13685.
- [8] X. Qiao, Q. Wu, H. Wu, J. Zhang, H. Li, *Adv. Funct. Mater.* **2017**, *27*, 1604286.
- [9] W. Wang, S. Yan, W. Lv, Y. Zhao, M. Sun, M. Zhou, Q. Ling, *Journal of Macromolecular Science, Part A* **2015**, *52*, 892.
- [10] Z. A. Wang, J. Kuwabara, A. Ichige, T. Yasuda, T. Kanbara, *Synth. Met.* **2016**, *222*, 383.

- [11] T. Weller, M. Breunig, C. J. Mueller, E. Gann, C. R. McNeill, M. Thelakkat, *J. Mater. Chem. C* **2017**, *5*, 7527.
- [12] G. Kim, A.-R. Han, H. R. Lee, J. Lee, J. H. Oh, C. Yang, *Chem. Commun.* **2014**, *50*, 2180.
- [13] S. Liu, Z. Kan, S. Thomas, F. Cruciani, J.-L. Brédas, P. M. Beaujuge, *Angew. Chem. Int. Ed.* **2016**, *55*, 12996.
- [14] S. Liu, X. Song, S. Thomas, Z. Kan, F. Cruciani, F. Laquai, J.-L. Bredas, P. M. Beaujuge, *Adv. Energy Mater.* **2017**, *376*, 1602574.
- [15] Y. Gao, Y. Deng, H. Tian, J. Zhang, D. Yan, Y. Geng, F. Wang, *Adv. Mater.* **2017**, *29*.
- [16] Y. Gao, X. Zhang, H. Tian, J. Zhang, D. Yan, Y. Geng, F. Wang, *Adv. Mater.* **2015**, *27*, 6753.
- [17] P. Homyak, Y. Liu, F. Liu, T. P. Russel, E. B. Coughlin, *Macromolecules* **2015**, *48*, 6978.
- [18] C. J. Mueller, C. R. Singh, M. Fried, S. Huettner, M. Thelakkat, *Adv. Funct. Mater.* **2015**, *25*, 2725.
- [19] J. H. Park, E. H. Jung, J. W. Jung, W. H. Jo, *Adv. Mater.* **2013**, *25*, 2583.
- [20] J. W. Jung, J. W. Jo, C.-C. Chueh, F. Liu, W. H. Jo, T. P. Russell, A. K.-Y. Jen, *Adv. Mater.* **2015**, *27*, 3310.
- [21] X. Li, X. Liu, P. Sun, Y. Feng, H. Shan, X. Wu, J. Xu, C. Huang, Z.-K. Chen, Z.-X. Xu, *RSC Adv* **2017**, *7*, 17076.
- [22] Z. Fei, M. Shahid, N. Yaacobi-Gross, S. Rossbauer, H. Zhong, S. E. Watkins, T. D. Anthopoulos, M. Heeney, *Chem. Commun.* **2012**, *48*, 11130.
- [23] J. W. Jo, S. Bae, F. Liu, T. P. Russell, W. H. Jo, *Adv. Funct. Mater.* **2015**, *25*, 120.
- [24] J. W. Jo, J. W. Jung, E. H. Jung, H. Ahn, T. J. Shin, W. H. Jo, *Energy Environ. Sci.* **2015**, *8*, 2427.
- [25] J. W. Jo, J. W. Jung, H.-W. Wang, P. Kim, T. P. Russell, W. H. Jo, *Chem. Mater.* **2014**, *26*, 4214.
- [26] K. Kawashima, T. Fukuhara, Y. Suda, Y. Suzuki, T. Koganezawa, H. Yoshida, H. Ohkita, I. Osaka, K. Takimiya, *J. Am. Chem. Soc.* **2016**, *138*, 10265.
- [27] G. E. Park, S. Choi, J. Shin, M. J. Cho, D. H. Choi, *Organic Electronics* **2016**, *34*, 157.
- [28] K. Wang, Z. Xu, B. Guo, X. Guo, M. Zhang, Y. Li, *RSC Adv* **2016**, *6*, 63338.
- [29] J. Wolf, F. Cruciani, A. El Labban, P. M. Beaujuge, *Chem. Mater.* **2015**, *27*, 4184.
- [30] S. Zhang, Y. Qin, M. A. Uddin, B. Jang, W. Zhao, D. Liu, H. Y. Woo, J. Hou, *Macromolecules* **2016**, *49*, 2993.

- [31] N. M. Kirby, S. T. Mudie, A. M. Hawley, D. J. Cookson, H. D. T. Mertens, N. Cowieson, V. Samardzic-Boban, *J Appl Crystallogr* **2013**, *46*, 1670.
- [32] J. Ilavsky, *J Appl Crystallogr* **2012**, *45*, 324.
- [33] T. Weller, K. Rundel, G. Krauss, C. R. McNeill, M. Thelakkat, *J. Phys. Chem. C* **2018**, *122*, 7565.
- [34] K. Gräf, M. A. Rahim, S. Das, M. Thelakkat, *Dyes and Pigments* **2013**, *99*, 1101.
- [35] J.-L. Bredas, *Mater. Horiz.* **2014**, *1*, 17.

Supporting Information

Influence of fluorination and backbone extension in thieno[3,4-c]pyrrole-4,6-dione based copolymers carrying thiophene and terthiophene comonomers

Tina Weller,^a Christopher R. McNeill^b and Mukundan Thelakkat^{a*}

^a Applied Functional Polymers, Macromolecular Chemistry I, University of Bayreuth, 95440 Bayreuth, Germany.

^b Department of Materials Science and Engineering, Monash University, Wellington Road, Clayton VIC, 3800, Australia.

* Corresponding author: mukundan.thelakkat@uni-bayreuth.de

Table of Contents

1	Monomer syntheses	197
1.1	Materials and methods	197
1.2	Synthesis of the TPD monomer	197
2	Polymer characterization.....	199
2.1	Polymer NMR spectra	199
2.2	Polymer SEC	201
3	Thermal properties	202
3.1	Thermogravimetric analysis.....	202
3.2	Flash differential scanning calorimetry.....	202
4	Cyclic voltammetry	203
5	UV-Vis and fluorescence spectroscopy	204
6	OFET I-V curves	205
7	References	209

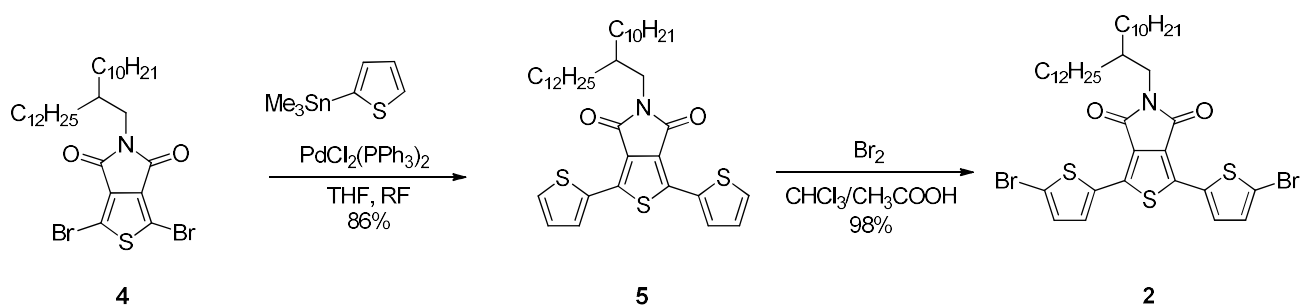
1 Monomer syntheses

1.1 Materials and methods

Water and air sensitive reactions were conducted in Schlenk apparatuses under argon, which were previously baked out in high vacuum. Commercially available solvents were purchased from Sigma Aldrich and Acros Organics in sealed bottles with mole sieve. ^1H and ^{19}F NMR spectra were recorded on a Bruker Avance spectrometer (300 MHz) with deuterated solvents purchased from Deutero. Chemical shifts are reported in ppm relative to the known value of residual solvent signal.

1.2 Synthesis of the TPD monomer

The overall synthesis of the TPD monomer **2** is shown in Scheme S 7.1 and the synthetic procedures are adapted from literature.^[1,2] The synthesis of compound **4** can be found in the literature.^[3]



Scheme S 7.1. Synthesis of the TPD monomer.

1,3-Di(thien-2-yl)-5-(2-decyl-1-tetradecyl)-4H-thieno[3,4-c]pyrrole-4,6(5H)-dione **5**

A solution of 1,3-dibromo-5-(2-decyl-1-tetradecyl)-4H-thieno[3,4-c]pyrrole-4,6(5H)-dione **4** (2.31 g, 3.57 mmol, 1 eq) and 2-(tributylstannyl)thiophene (3.40 mL, 10.7 mmol, 3 eq) in 70 mL anhydrous tetrahydrofuran was degassed for 10 min. After addition of bis(triphenylphosphine)palladium(II) chloride (0.150 g, 0.214 mmol, 0.06 eq), the reaction mixture was stirred under reflux for 22 h. Addition of an aqueous solution of KF (3.5 wt.%, 100 mL) was followed by extraction with dichloromethane for three times. The combined organic phases were washed with a saturated, aqueous solution of NaCl. After drying over MgSO_4 and removal of the solvent by rotary evaporation, the raw product was purified by column chromatography (silica; *n*Hex:DCM 5:1-1:1) yielding 1,3-di(thien-2-yl)-5-(2-decyl-1-tetradecyl)-4H-thieno[3,4-c]pyrrole-4,6(5H)-dione **5** (2.01 g, 3.07 mmol, 86%) as a yellow solid.

$^1\text{H-NMR}$ (300 MHz, CDCl_3): δ = 8.03 (dd, J = 3.8 Hz, 1.1 Hz, 2H), 7.43 Hz (dd, J = 5.1, 1.1 Hz, 2H), 7.13 Hz (dd, J = 5.1, 3.8 Hz, 2H), 3.55 (d, J = 7.3 Hz, 2H), 1.89 (bs, 1H), 1.15-1.38 (m, 40H), 0.87 ppm (tt, J = 6.8 Hz, 6H).

1,3-Di(5-bromothien-2-yl)-5-(2-decyl-1-tetradecyl)-4*H*-thieno[3,4-*c*]pyrrole-4,6(5*H*)-dione 2

A mixture of 40 mL chloroform and 40 mL acetic acid was added to 1,3-di(thien-2-yl)-5-(2-decyl-1-tetradecyl)-4*H*-thieno[3,4-*c*]pyrrole-4,6(5*H*)-dione **5** (2.00 g, 3.06 mmol, 1 eq) and cooled to 0 °C. After the addition of *N*-bromosuccinimide (1.37 g, 7.70 mmol, 2.5 eq), the cooling bath was removed, and the reaction mixture was stirred overnight at room temperature. Water was added, and the reaction mixture was extracted with chloroform twice. The combined organic phases were washed with water and dried over MgSO_4 . After removal of the solvent by rotary evaporation, the raw product was purified by column chromatography (silica; *n*Hex:DCM 5:1-3:1) yielding 1,3-di(5-bromothien-2-yl)-5-(2-decyl-1-tetradecyl)-4*H*-thieno[3,4-*c*]pyrrole-4,6(5*H*)-dione **2** (2.29 g, 3.00 mmol, 98%) as a yellow solid.

$^1\text{H-NMR}$ (300 MHz, CDCl_3): δ = 7.66 (d, J = 4.0 Hz, 2H), 7.08 Hz (d, J = 4.0 Hz, 2H), 3.53 (d, J = 7.5 Hz, 2H), 1.86 (bs, 1H), 1.11-1.43 (m, 40H), 0.87 ppm (tt, J = 6.8 Hz, 6H).

2 Polymer characterization

2.1 Polymer NMR spectra

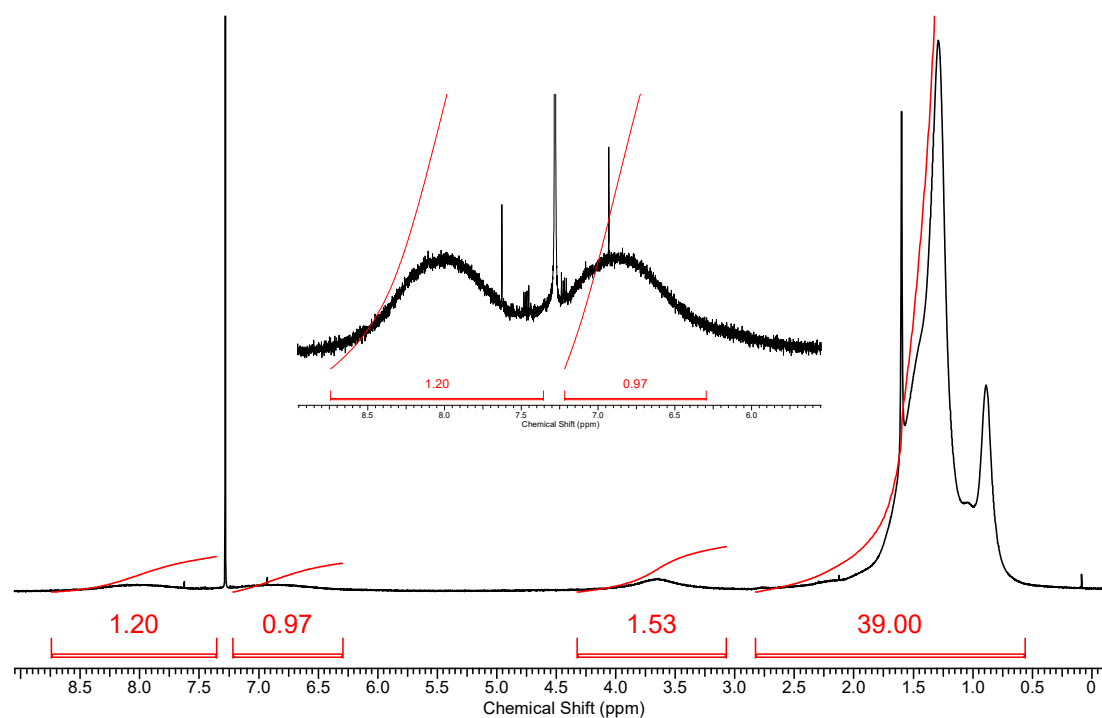


Figure S 7.1. $^1\text{H-NMR}$ spectrum of polymer PTPDT in CDCl_3 .

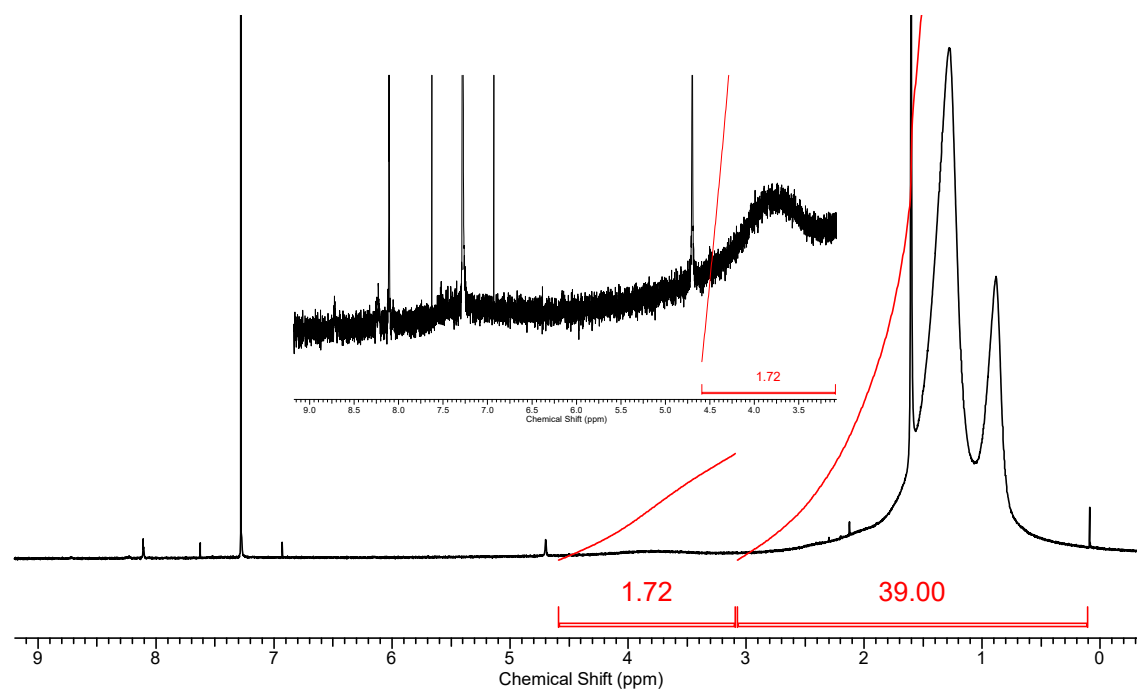


Figure S 7.2. $^1\text{H-NMR}$ of polymer PTPDTF₂ in CDCl_3 .

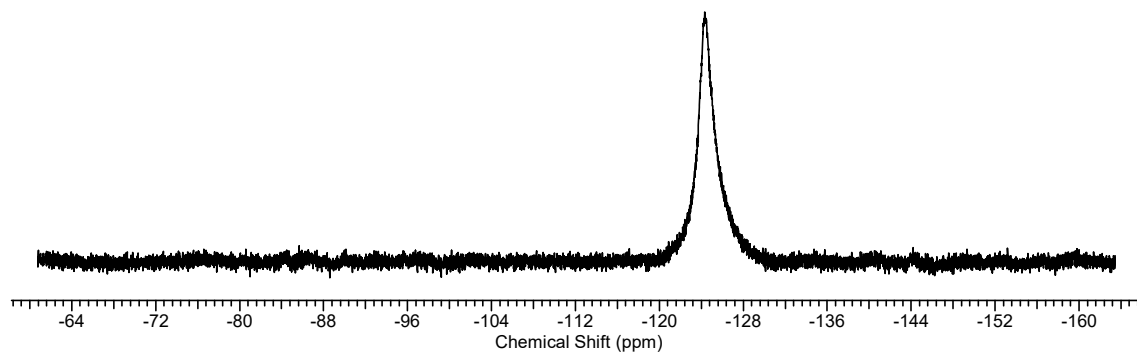


Figure S 7.3. ^{19}F -NMR spectra of polymer PTPD TF_2 in CDCl_3 .

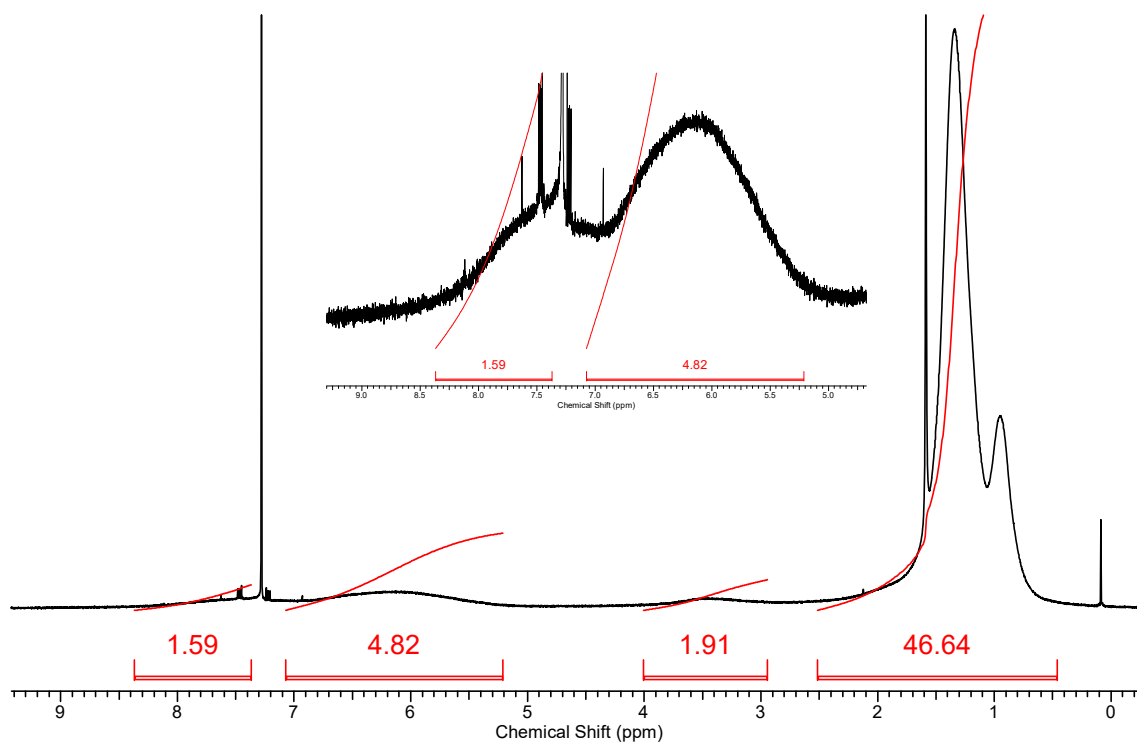


Figure S 7.4. ^1H -NMR spectrum of polymer PTPD[2T]T in CDCl_3 .

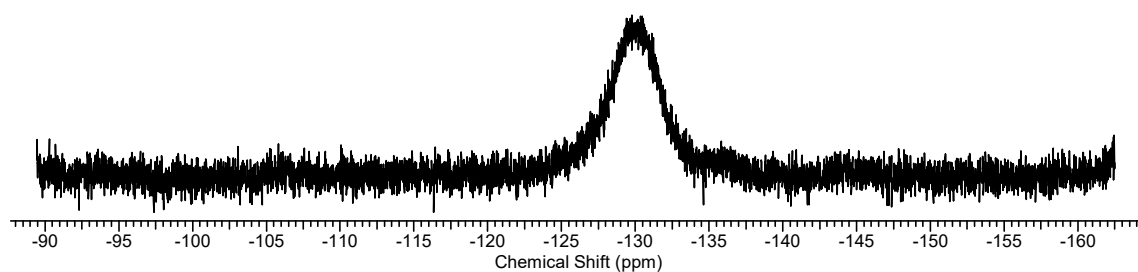


Figure S 7.5. ^{19}F -NMR spectrum of polymer PTPD[2T] TF_2 in CDCl_3 .

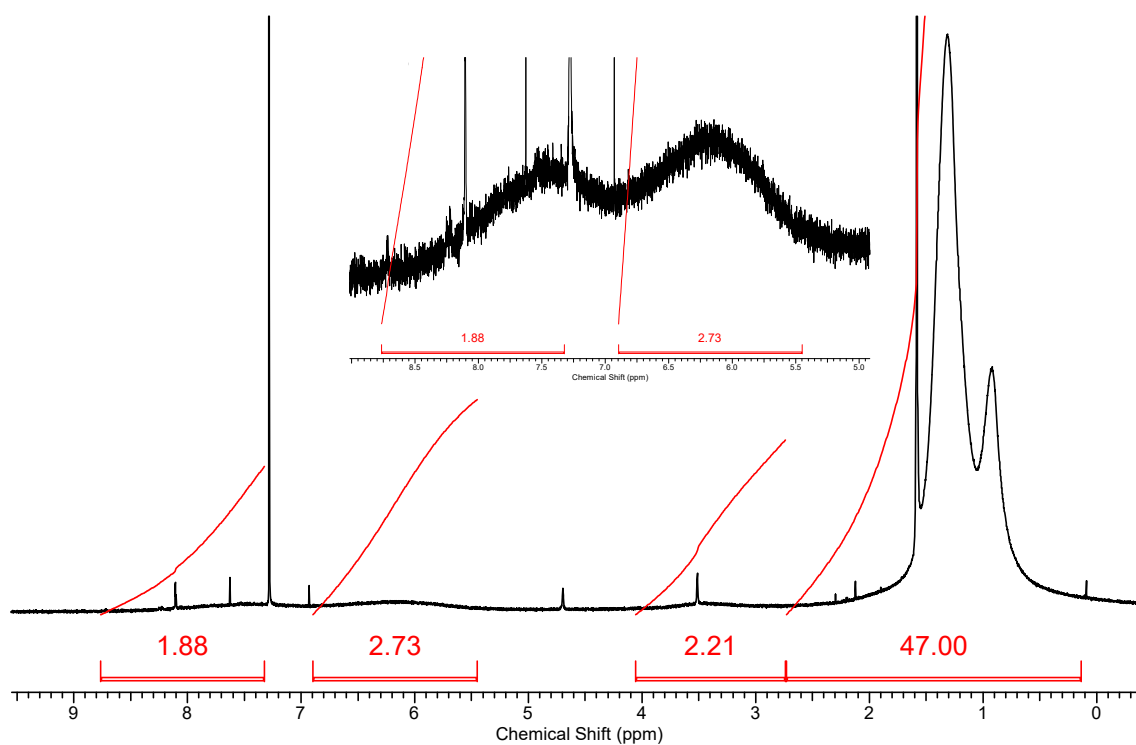


Figure S 7.6. $^1\text{H-NMR}$ spectrum of polymer PTPD[2T]TF₂ in CDCl₃.

2.2 Polymer SEC

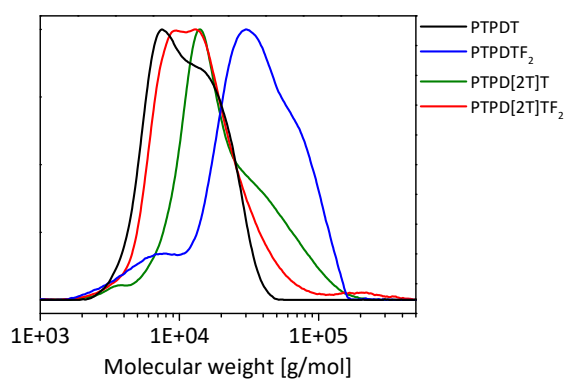


Figure S 7.7. SEC measurements in trichlorobenzene at 160 °C calibrated with PS standards.

3 Thermal properties

3.1 Thermogravimetric analysis

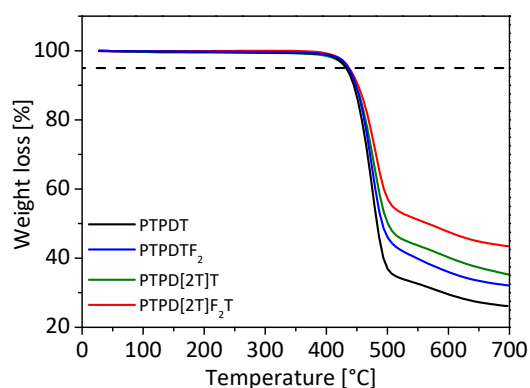


Figure S 7.8. Thermogravimetric analysis of the PTPDs with the decomposition onset ($T_{5\%}$).

3.2 Flash differential scanning calorimetry

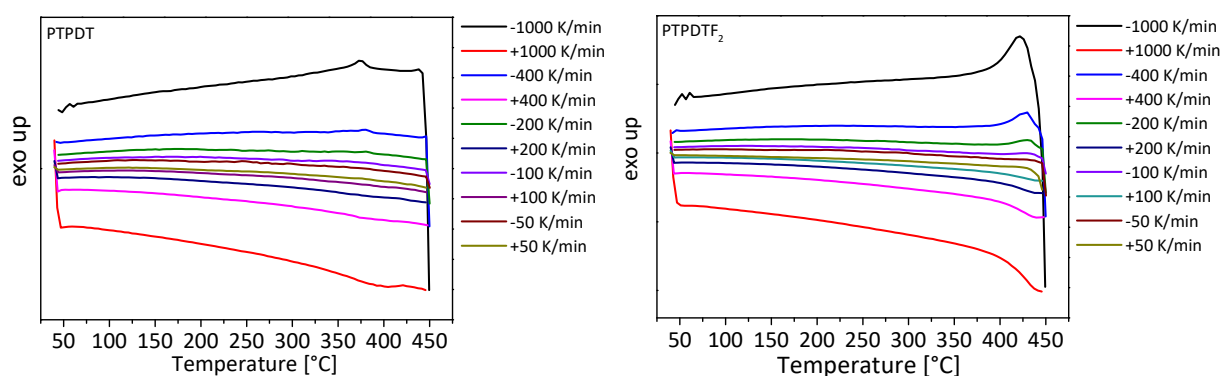


Figure S 7.9. Flash DSC analysis of PTPDT and PTPDTF₂ with scanning rates from 50-1000 K min⁻¹.

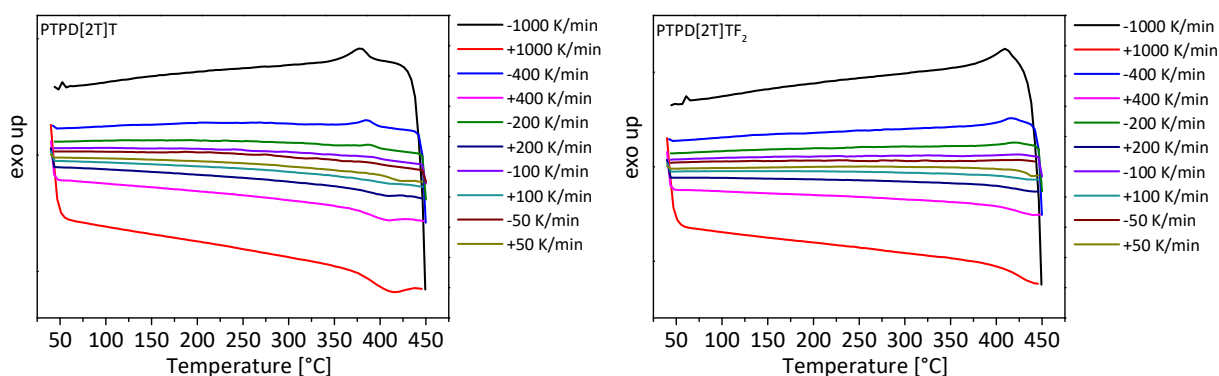


Figure S 7.10. Flash DSC analysis of PTPD[2T]T and PTPD[2T]TF₂ with scanning rates from 50-1000 K min⁻¹.

4 Cyclic voltammetry

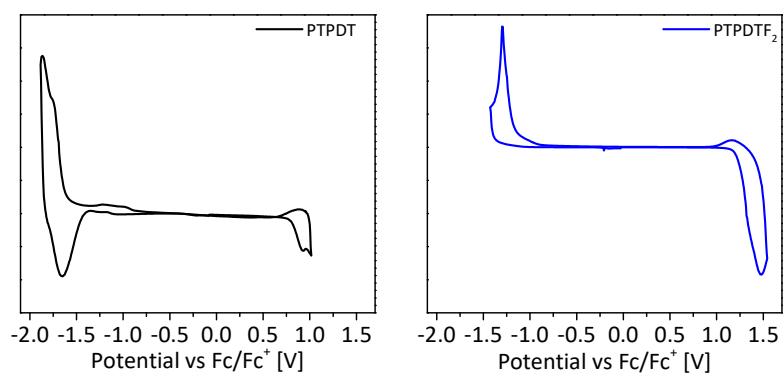


Figure S 7.11. Cyclic voltammetry measurements in thin films of PTPDT and PTPDTF₂.

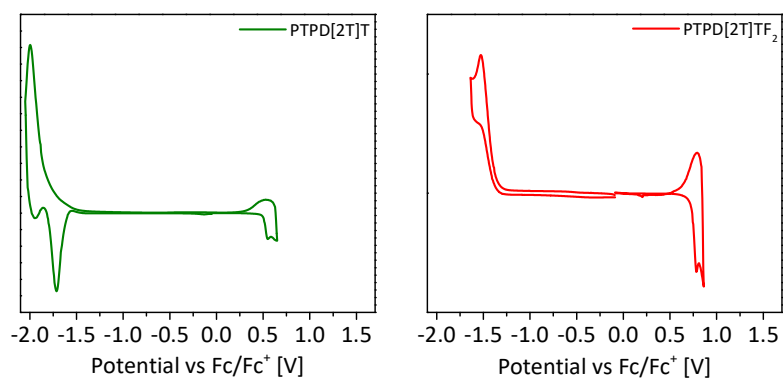


Figure S 7.12. Cyclic voltammetry measurements in thin films of PTPD[2T]T and PTPD[2T]TF₂.

5 UV-Vis and fluorescence spectroscopy

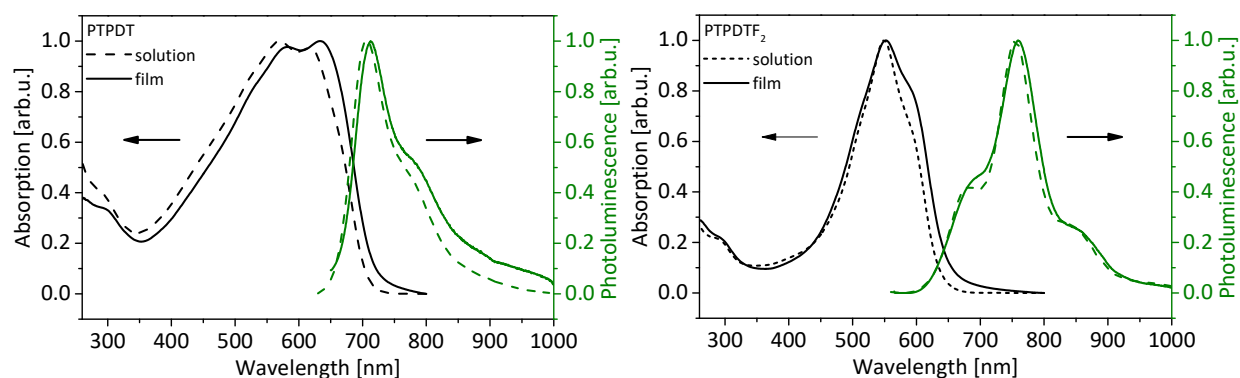


Figure S 7.13. UV-Vis and photoluminescence spectra in solution and thin films for PTPDT and PTPDTF₂.

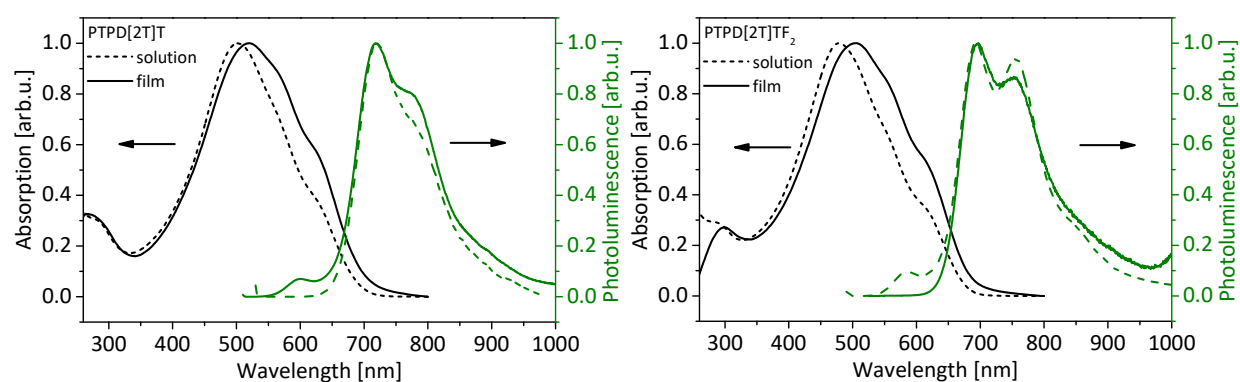


Figure S 7.14. UV-Vis and photoluminescence spectra in solution and thin films for PTPD[2T]T and PTPD[2T]TF₂.

6 OFET I-V curves

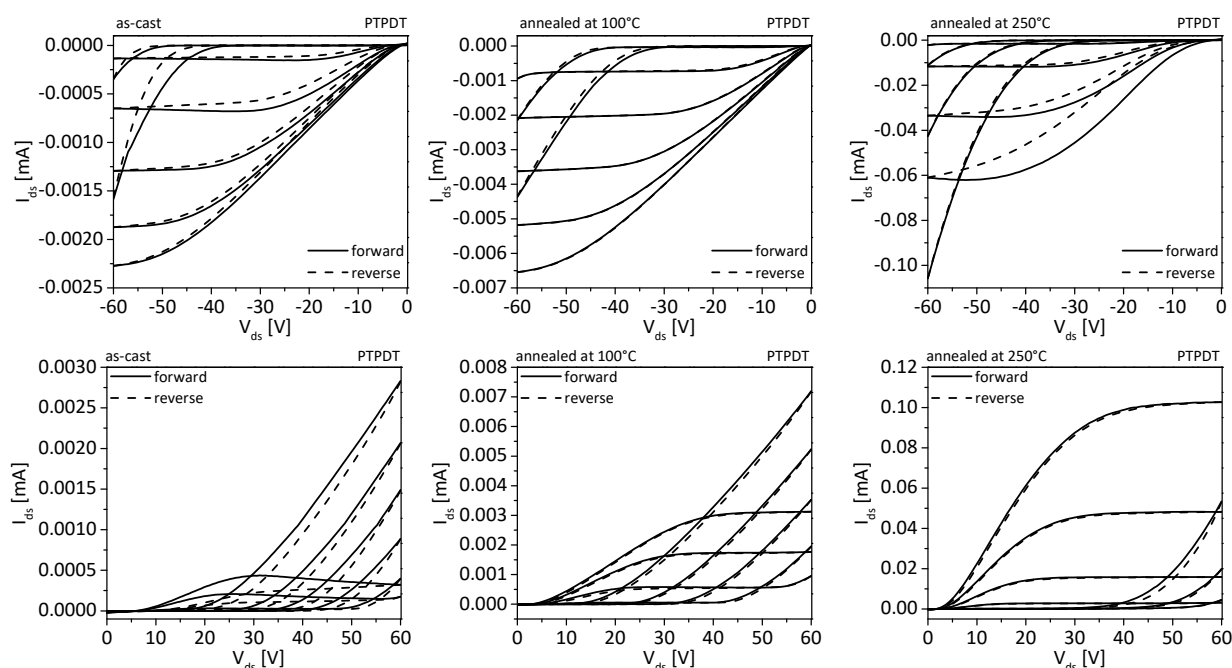


Figure S 7.15. OFET output characteristics: p-channel operation (top) and n-channel operation (bottom) of PTPDT in as-cast films (left), annealed films at 100 °C (middle) and 250 °C (right). Solid lines represent forward scans and dashed lines reversed scans.

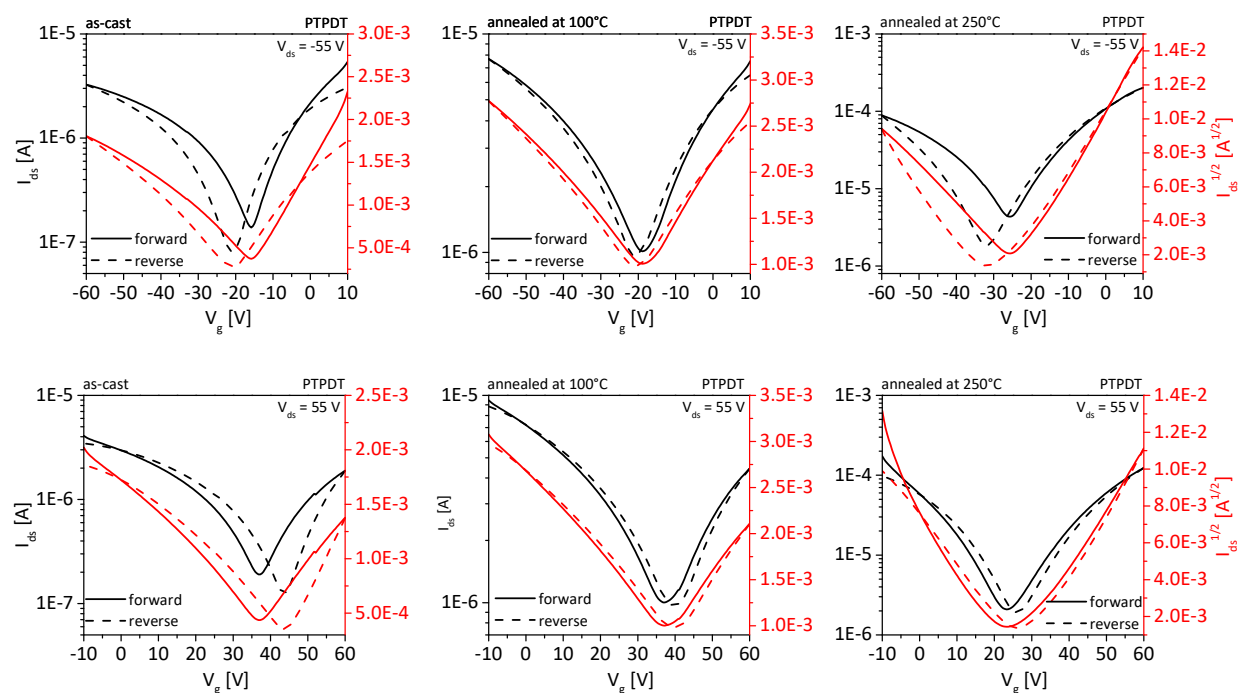


Figure S 7.16. OFET transfer characteristics: p-channel operation (top) and n-channel operation (bottom) of PTPDT in as-cast films (left), annealed films at 100 °C (middle) and 250 °C (right). Solid lines represent forward scans and dashed lines reversed scans.

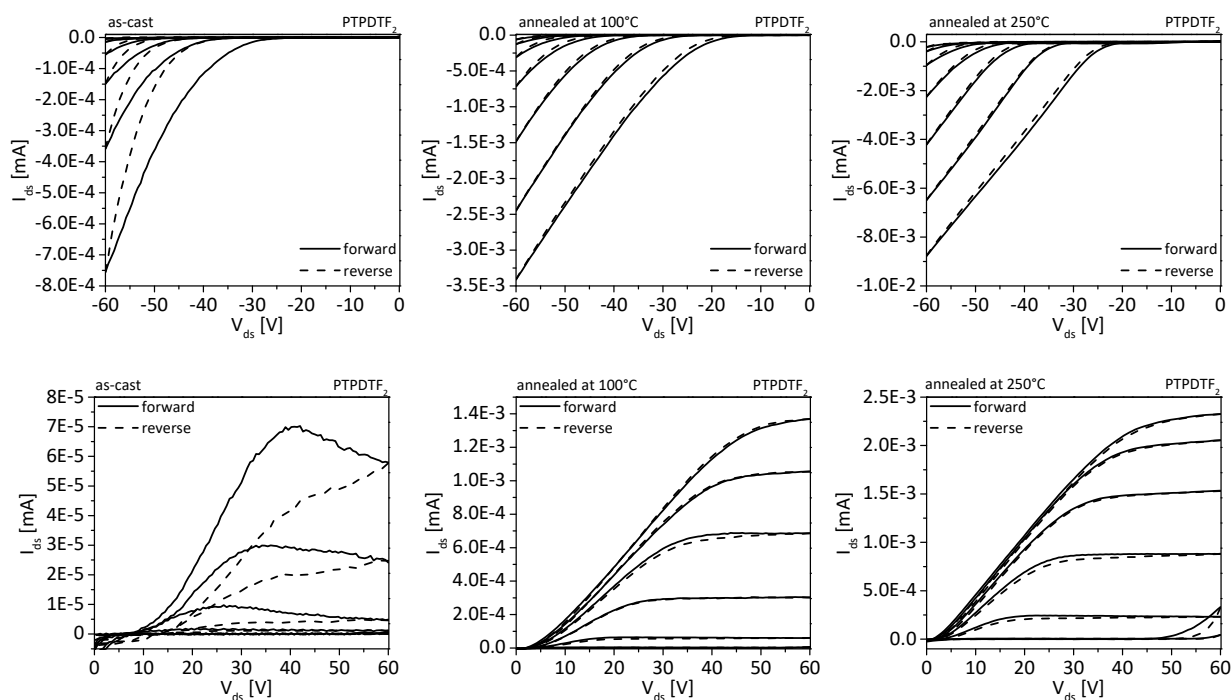


Figure S 7.17. OFET output characteristics: p-channel operation (top) and n-channel operation (bottom) of PTPDTF₂ in as-cast films (left), annealed films at 100 °C (middle) and 250 °C (right). Solid lines represent forward scans and dashed lines reversed scans.

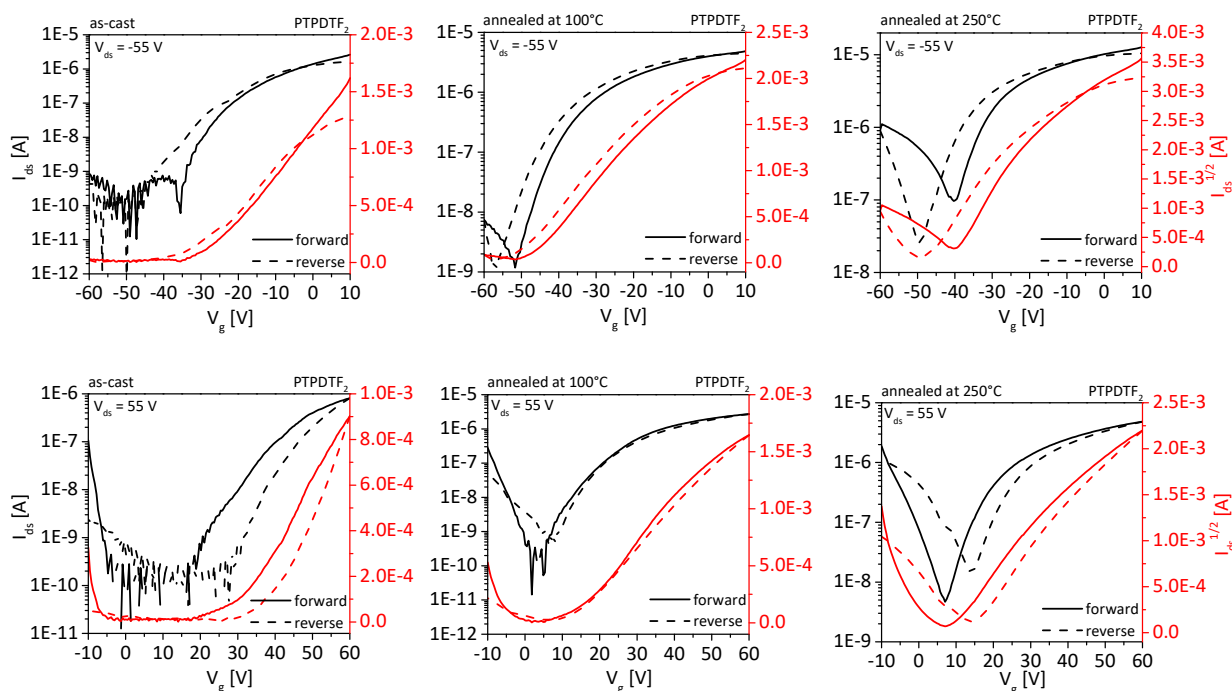


Figure S 7.18. OFET transfer characteristics: p-channel operation (top) and n-channel operation (bottom) of PTPDTF₂ in as-cast films (left), annealed films at 100 °C (middle) and 250 °C (right). Solid lines represent forward scans and dashed lines reversed scans.

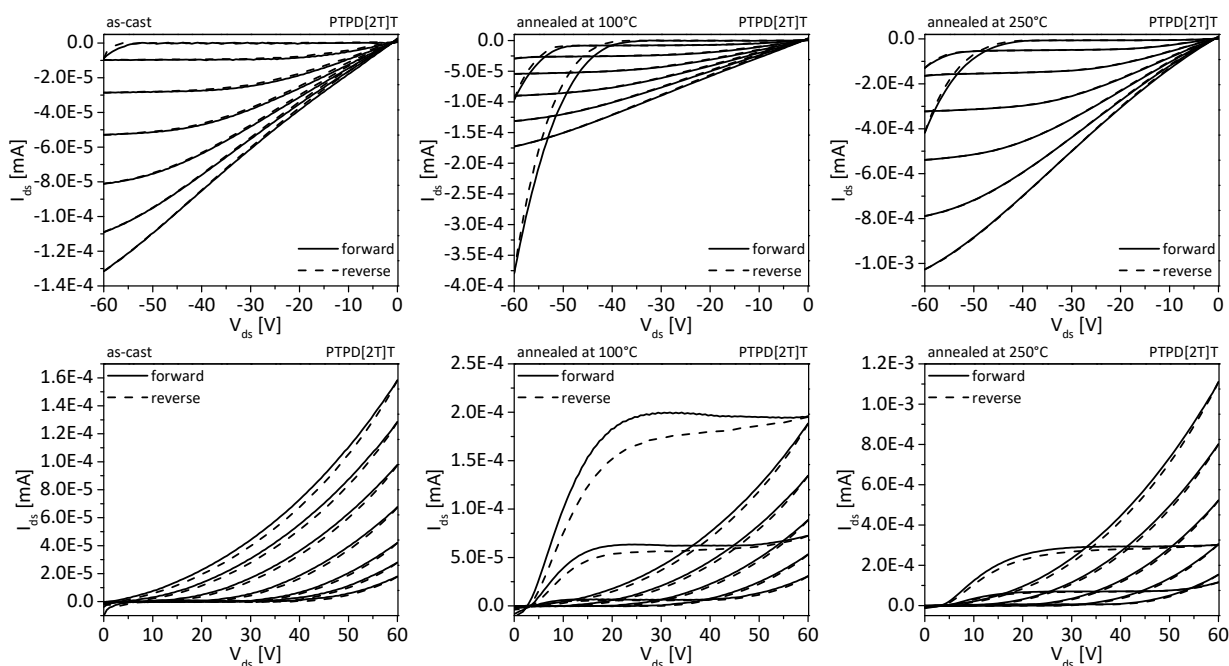


Figure S 7.19. OFET output characteristics: *p*-channel operation (top) and *n*-channel operation (bottom) of PTPD[2T]T in as-cast films (left), annealed films at 100 °C (middle) and 250 °C (right). Solid lines represent forward scans and dashed lines reversed scans.

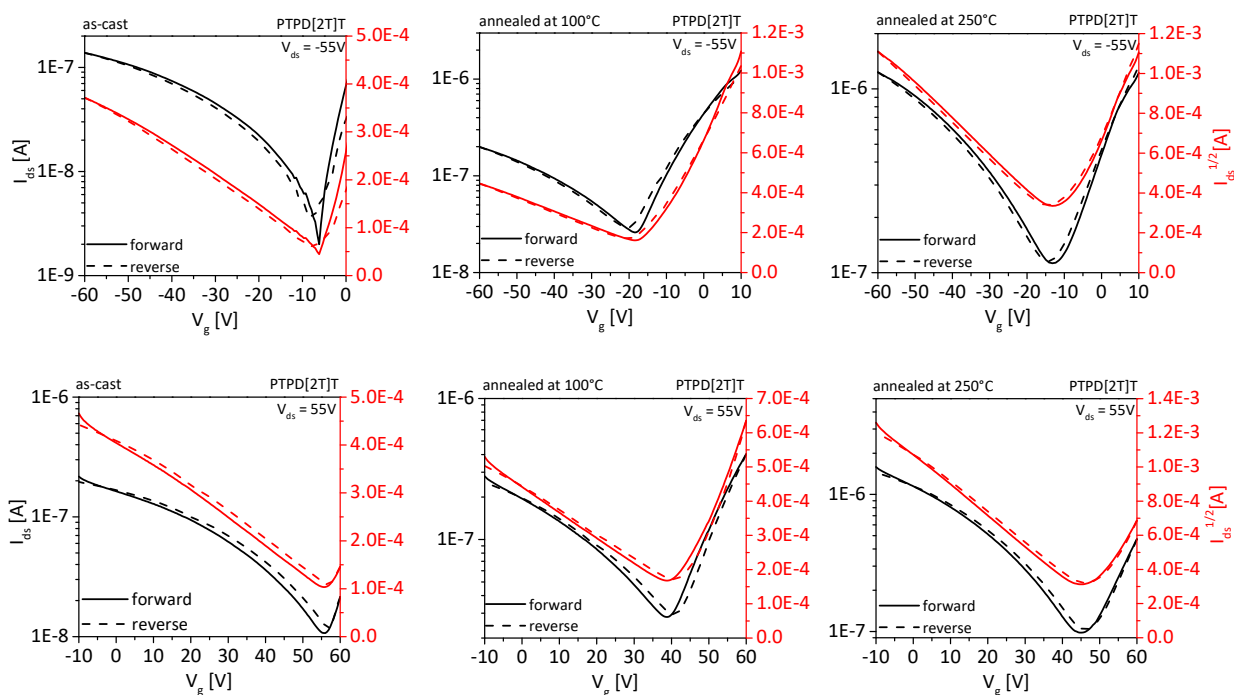


Figure S 7.20. OFET transfer characteristics: *p*-channel operation (top) and *n*-channel operation (bottom) of PTPD[2T]T in as-cast films (left), annealed films at 100 °C (middle) and 250 °C (right). Solid lines represent forward scans and dashed lines reversed scans.

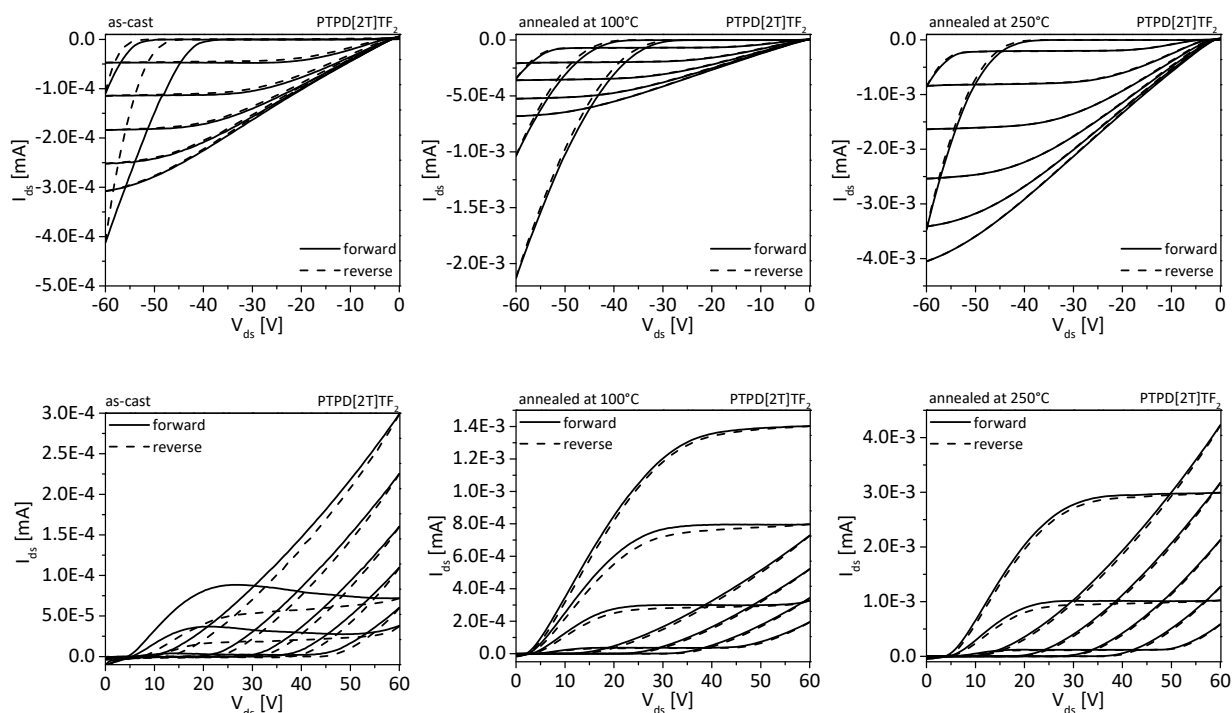


Figure S 7.21. OFET output characteristics: *p*-channel operation (top) and *n*-channel operation (bottom) of PTPD[2T]TF₂ in as-cast films (left), annealed films at 100 °C (middle) and 250 °C (right). Solid lines represent forward scans and dashed lines reversed scans.

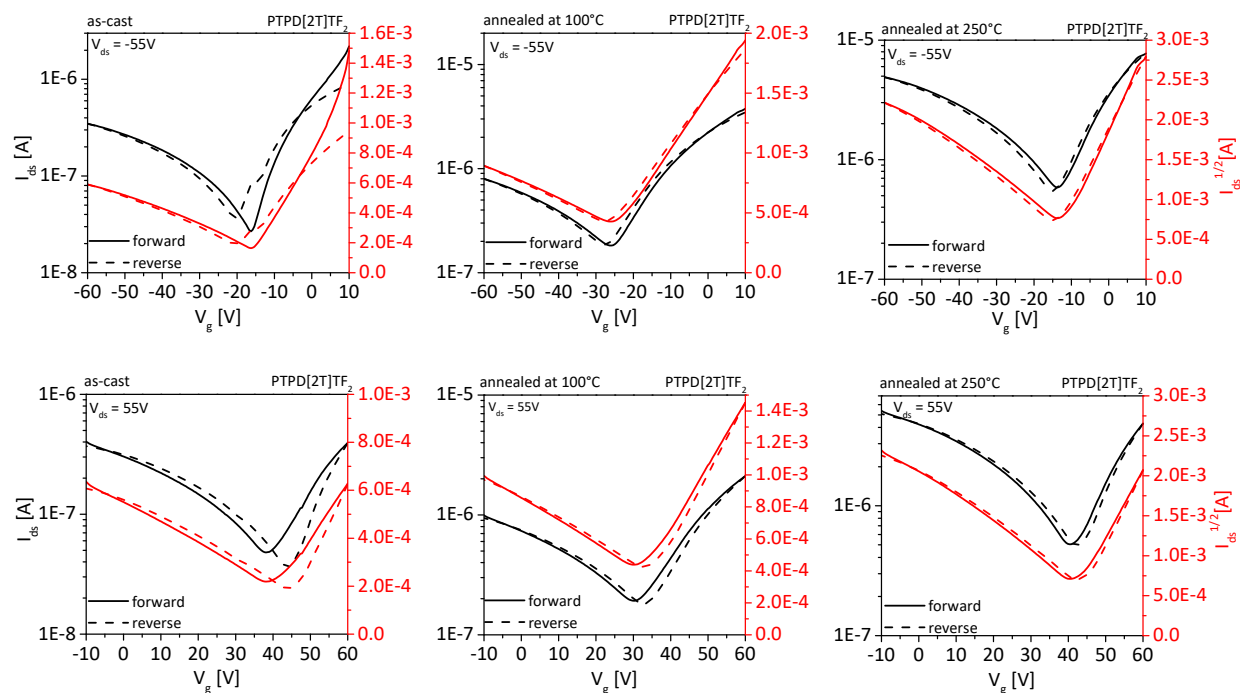


Figure S 7.22. OFET transfer characteristics: *p*-channel operation (top) and *n*-channel operation (bottom) of PTPD[2T]TF₂ in as-cast films (left), annealed films at 100 °C (middle) and 250 °C (right). Solid lines represent forward scans and dashed lines reversed scans.

Table S 7.1. Threshold voltages for as-cast films and after thermal annealing.

	as-cast		100 °C		250 °C	
	p-type	n-type	p-type	n-type	p-type	n-type
	V_T	V_T	V_T	V_T	V_T	V_T
	[V]	[V]	[V]	[V]	[V]	[V]
PTPDT	-5	27	1	23	-12	30
PTPDTF ₂	-	32	-	18	-	9
PTPD[2T]T	3	-	1	35	0	39
PTPD[2T]TF ₂	-1	30	2	23	-2	30

7 References

- [1] A. Najari, P. Berrouard, C. Ottone, M. Boivin, Y. Zou, D. Gendron, W.-O. Caron, P. Legros, C. N. Allen, S. Sadki and M. Leclerc, *Macromolecules* **2012**, *4*, 1833.
- [2] X. Guo, R. P. Ortiz, Y. Zheng, Y. Hu, Y.-Y. Noh, K.-J. Baeg, A. Facchetti and T. J. Marks, *J. Am. Chem. Soc.* **2011**, *5*, 1405.
- [3] C. J. Mueller, C. R. Singh, M. Fried, S. Huettner and M. Thelakkat, *Adv. Funct. Mater.* **2015**, *18*, 2725.

8 List of publications

Publications which are part of this thesis:

- [1] T. Weller, M. Breunig, C. J. Mueller, E. Gann, C. R. McNeill, M. Thelakkat; Fluorination in thieno[3,4-c]pyrrole-4,6-dione copolymers leading to electron transport, high crystallinity and end-on alignment; *Journal of Materials Chemistry C* **2017**, *5*, 7527.
- [2] T. Weller, K. Rundel, G. Krauss, C. R. McNeill, M. Thelakkat; Highly efficient and balanced charge transport in thieno[3,4-c]pyrrole-4,6-dione copolymers: Dramatic influence of thieno[3,4-b]thiophene comonomer on alignment and charge transport; *Journal of Physical Chemistry C* **2018**, *122*, 7565.

Further publications:

- [3] R. Schmidt, M. Pärs, T. Weller, M. Thelakkat, J. Köhler; Trapping on demand: External regulation of excitation energy transfer in photoswitchable smart matrix, *Applied Physics Letters* **2014**, *104*, 013304.
- [4] J. Maier, M. Pärs, T. Weller, M. Thelakkat, J. Köhler; Deliberate switching of single photochromic triads, *Scientific Reports* **2017**, *7*, 41739.

Danksagung

An dieser Stelle möchte ich all denjenigen danken ohne die das Gelingen dieser Doktorarbeit nicht möglich gewesen wäre. Zuallererst möchte ich mich bei meinem Betreuer Prof. Dr. Mukundan Thelakkat für die Möglichkeit meine Doktorarbeit in seinem Arbeitskreis zu schreiben bedanken. Zudem danke ich ihm für die Bereitstellung dieses interessanten und abwechslungsreichen Themas, für ein perfekt ausgestattetes Labor sowie für die gute Zusammenarbeit.

Many thanks to my cooperation partner Prof. Dr. Chris McNeill for the fruitful collaboration and the opportunity for a research stay in his group at the Monash University in Melbourne. Thank you for your supervision, support, and the many discussions. Especially I want to say thanks to his PhD student, Kira Rundel, for the perfect collaboration, which resulted in two manuscripts. Hope to see you some time again in Germany. For the AFM measurements, I also want to thank Adam Welford, a further PhD student in the McNeill group.

Bei meinen vielen Praktikanten und wissenschaftlichen Hilfskräften, die ebenfalls einen Beitrag zu dieser Arbeit geleistet haben, möchte ich mich ganz herzlich bedanken. Vielen Dank an Gabriela Hahn, Ferdinand Seibold, Markus Drummer, Marion Breunig, Gert Krauss, Tobias Lauster und Anne Burger. Ganz besonders möchte ich an dieser Stelle Marion Breunig und Gert Krauss danken, die einen wesentlichen Beitrag zu zweier meiner Publikationen geleistet haben.

Für die Mithilfe bei vielen Synthesen sowie Laborarbeiten möchte ich mich bei Martina Fried bedanken sowie bei Jonas Mayer für die Unterstützung bei allen Arbeiten im PNS sowie für den IT Support gemeinsam mit Alexander Kern. Bei unseren beiden lieben Sekretärinnen Christina Wunderlich und Petra Weiss möchte ich mich für jegliche Unterstützung bei allen organisatorischen und administrativen Aufgaben sowie für eure Fürsorge bedanken.

Ein großer Dank geht auch an Windfried Kretschmer und Martin Friedrich aus der AC II für die Hochtemperatur-GPC sowie GC-MS Messungen.

Für das viele Korrekturlesen dieser Arbeit bedanke ich mich bei Alexander Krimalowski, Gert Krauss und Paul Reichstein.

Vielen Dank an den gesamten Lehrstuhl MC I für die gute Zusammenarbeit und die schöne Zeit während meiner Doktorarbeit. Ich möchte mich sowohl bei der „alten“ als auch „neuen“ MC I für die vielen gemeinsamen Abende im Kaffeezimmer bedanken, ohne die ein Durchstehen der Doktorarbeit nur schwer möglich gewesen wäre. Auch möchte ich mich bei dem B6 Team für die gute Zusammenarbeit im Exil bedanken, insbesondere bei meinen beiden Bürokollegen Christian Müller und Gert Krauss für die einzigartige Atmosphäre im Büro sowie Labor. Danke auch an Eva Fürsattel für den sportlichen Ausgleich zur Promotion sowie die vielen gemeinsamen Aperol Spritz.

Zuletzt danke ich meiner Familie für die großartige Unterstützung nicht nur während der Doktorarbeit, sondern während meines gesamten Studiums. Ihr habt mir ein sorgenfreies Chemiestudium ermöglicht und mich stets motiviert und vorangetrieben. Danke!

(Eidesstattliche) Versicherungen und Erklärungen

(§ 9 Satz 2 Nr. 3 PromO BayNAT)

Hiermit versichere ich eidesstattlich, dass ich die Arbeit selbständig verfasst und keine anderen als die von mir angegebenen Quellen und Hilfsmittel benutzt habe (vgl. Art. 64 Abs. 1 Satz 6 BayHSchG).

(§ 9 Satz 2 Nr. 3 PromO BayNAT)

Hiermit erkläre ich, dass ich die Dissertation nicht bereits zur Erlangung eines akademischen Grades eingereicht habe und dass ich nicht bereits diese oder eine gleichartige Doktorprüfung endgültig nicht bestanden habe.

(§ 9 Satz 2 Nr. 4 PromO BayNAT)

Hiermit erkläre ich, dass ich Hilfe von gewerblichen Promotionsberatern bzw. -vermittlern oder ähnlichen Dienstleistern weder bisher in Anspruch genommen habe noch künftig in Anspruch nehmen werde.

(§ 9 Satz 2 Nr. 7 PromO BayNAT)

Hiermit erkläre ich mein Einverständnis, dass die elektronische Fassung meiner Dissertation unter Wahrung meiner Urheberrechte und des Datenschutzes einer gesonderten Überprüfung unterzogen werden kann.

(§ 9 Satz 2 Nr. 8 PromO BayNAT)

Hiermit erkläre ich mein Einverständnis, dass bei Verdacht wissenschaftlichen Fehlverhaltens Ermittlungen durch universitätsinterne Organe der wissenschaftlichen Selbstkontrolle stattfinden können.

.....
Ort, Datum, Unterschrift